Signal Specificity Amongst STAT1- and STAT3- Inducing Cytokines in the Context of Th17 Differentiation

By

Kevin D. Fowler

B.ChE, University of Minnesota – Twin Cities, 2004
M.S. Chemical Engineering Practice, Massachusetts Institute of Technology, 2007

SUBMITTED TO THE DEPARTMENT OF CHEMICAL ENGINEERING IN PARTIAL FULFILLMENT OF THE REQUIREMENTS FOR THE DEGREE OF

DOCTORATE OF PHILOSOPHY IN CHEMICAL ENGINEERING
AT THE
MASSACHUSETTS INSTITUTE OF TECHNOLOGY

FEBRUARY 2012

Signature of Author: _____
Department of Chemical Engineering
January 26, 2012

Certified by: _____
Arup K. Chakraborty
Robert T. Haslam Professor of Chemical Engineering
Professor of Chemistry
Professor of Biological Engineering
Thesis Supervisor

Accepted by: _____
William M. Deen
Professor of Chemical Engineering
Chairman, Committee for Graduate Students

Signal Specificity Amongst STAT1- and STAT3- Inducing Cytokines in the Context of Th17 Differentiation

By

Kevin D. Fowler

Submitted to the Department of Chemical Engineering
On January 26, 2011 in Partial Fulfillment of the Requirements for the Degree of Doctor of Philosophy in Chemical Engineering
At the Massachusetts Institute of Technology

Abstract

The adaptive immune response is very important for our survival in that it gives us the capability of detecting a wide variety of foreign material, allows for the elimination of pathogens, and provides memory to protect against future attacks by the same pathogen. Key mediators of the adaptive immune response are CD4+ T cells, which depending on the cytokine milieu, and the activating conditions during antigen recognition, can differentiate into different effector T cells. One particular type of effector T cell, Th17, is highly inflammatory and has been implicated in various autoimmune diseases, such as Multiple Sclerosis. Three chapters within this thesis investigate the conditions which lead to Th17 differentiation and the mechanisms involved in their regulation. Th17 cells can be obtained *in vitro* by culturing naïve CD4+ T cells with IL-6 and TGF-β under activating conditions. IL-6 was thought to primarily activate the transcription factor STAT3, which has been shown to be necessary for Th17 differentiation. Numerous cytokines activate STAT3, but IL-6 is the most potent inducer of Th17 cells, so we sought to find out what is special about IL-6's induction of STAT3. In the first of these three chapters, we propose a simple genetic network which is capable of translating IL-6's high amplitude, transient STAT3 signal into a pro-inflammatory response and IL-10's low amplitude, sustained STAT3 signal into an anti-inflammatory response. This network is able to predict that IL-6 and IL-10 would induce an indistinguishable anti-inflammatory response in SOCS3-/- cells where IL-6's STAT3 signal is sustained. In the second of these chapters, we continue our research into the origin of signal specificity in cytokine signaling by systematically characterizing the activation of STAT1 and STAT3 by IL-6, IL-10, IL-21, IL-27, and different combinations of cytokines in CD4+ T cells. In this analysis we find that the ratio of STAT3 to STAT1 activated is the important quantity in determining whether or not a cytokine will be an inducer of Th17 differentiation (IL-6, IL-21) or an inhibitor (IL-27). We show that in the absence of STAT1, that IL-6 and IL-27 are both potent inducers of Th17 differentiation since they have similar STAT3 activation profiles. In the third of these chapters, we develop a simple algorithm for clustering gene activation profiles for intermediate numbers of genes measured (10-50) and use it to analyze a 96-hour time course of gene activation during Th17 differentiation for a number of genes of interest.

In order for T cells to differentiate into effector cells, they must first recognize antigen which is presented on the surface of an antigen presenting cell by a membrane-bound extracellular complex called MHC. The MHC have a groove which peptide fragments (antigen) are bound in. Without peptide loaded in the pocket, the MHC are quite unstable so they are synthesized with a generic peptide fragment loaded. A protein, DM, is responsible for stabilizing the MHC while the generic peptide is ejected and the peptide fragment of interested is loaded. Two chapters within this thesis investigate the role of DM in peptide loading / unloading and attempt to characterize the interaction of DM with MHC.

Thesis Supervisor: Arup K. Chakraborty
Robert T. Haslam Professor of Chemical Engineering
Professor of Chemistry
Professor of Biological Engineering

Table of Contents

List of Figures

List of Tables

Acknowledgements

This thesis is dedicated to my parents, Mary and Larry, and my sister, Kelly. I would never have made it through all these years of school without your constant support, uplifting spirit, and willingness to listen. I am truly blessed to have been given such a wonderful family.

I would like to thank my advisor, Arup Chakraborty for his willingness to give me the latitude to follow where the science led me. In this case, the science led me to do experiments in someone else's lab for the last 3 years of my doctoral research. This was an invaluable opportunity for professional development that not all advisors would have allowed. Arup also deserves much credit for converting someone who proudly proclaimed that he couldn't stand the field of biology into someone who will likely spend their entire career in the field just by giving an inspirational and charismatic 40 minute talk about his research. People with the skill to motivate others with such ease are few and far between and I was lucky enough to have one as my advisor.

I would like to thank Vijay Kuchroo who has been my surrogate advisor for the last 3 years and who allowed me to do experiments in his lab. Vijay is another individual who was willing to let the science go where it led us. In this case, it was allowing a student with no experimental background in biology to join his top-tier research lab. He was incredibly supportive during my time in his lab and took me under his wing even though I was not an official member of his group. He provided me with any resource I asked for and knew exactly who to refer me to when he did not have something I needed. It was a luxury being in someone's lab filled with top notch individuals.

I would like to thank many of the members of the Chakraborty lab during my time here. First and foremost, I would like to thank Jayajit Das. During my first few years in the lab, Jayajit tolerated me constantly thinking aloud about problems and constantly running things by him. I really appreciate his patience and all of the quality advice he gave me during those pivotal years. Second, I'd like to thank Mikhail Wolfson, who deserves all the credit for maintaining our computer cluster over the years. It is unsung work, but his dedication has made so much research in our group possible.

I would like to thank all the members of the Kuchroo lab who welcomed me with open arms. It is probably the most comfortable I have ever felt in any work environment, which is a testament to the high character individuals in the lab and all of their personalities. I thank Hulin Jin for his patience in being dealt the task of teaching someone with no experimental skills how to do impactful experimental research. I'd like to thank Amit Awasthi, Andrew Sutherland, and Chen Zhu for much guidance and their willingness to go through my data with me whenever I asked. I'd like to thank my social advisor, Nicole Joller for all of her advice about both life and work in the lab. I'd like to thank my collaborator over the last few months, Anneli Peters, whose skills and insight made it possible to do experiments that I could have never done myself. I'd like to thank Deneen Kozoriz for teaching me how to use instrumentation and for sorting my cells. I'd like to thank Loise Francisco for giving me the FACS protocol for STAT measurement which finally allowed me to make some progress. Thanks to my fellow grad student, Youjin Lee, for helping me with experiments. Thanks to Ana Anderson for likely finding me my first post grad school job. Also, thanks to Manu Rangachari for his friendship.

I would like to thank my friends back in Minneapolis, Andrew Smith, Aaron Kuznia, Chris Muellner, and John Wappel II. You guys have always been there for me and I couldn't have made it through grad school without all of your continued friendship. I'd also like to thank Erin Bell, Daniel Schmidt, Kevin Carlson, Michael Harper, Aleksander Radovic-Moreno, Karthik Viswanathan, Alex Rewald, Jared DeMaster, Rachel Dobbs and Tim Hallett for their friendship and support.

I'd like to thank my committee members, Paul Barton and Darrell Irvine. Your input at my committee meetings was invaluable. Thanks so much for taking the time to be on my committee.

I'd also like to thank other people who have contributed to my professional development over the years. My high school chemistry teacher, Hans Andresen, went out of his way to give me a pamphlet on chemical engineering one day after class since he thought I would be interested. From that instant on, I have never had any doubts that I was going to be a chemical engineer. Manoj Nirmal, a fellow MIT alum, gave me my first job in the field as a technical aide at 3M. Lon Chubiz, a fellow student at the University of Minnesota-Twin Cities, gave me a famous pep talk one night that convinced me to go to grad school. Prodromos Daoutidis allowed me to do research in his lab and showed me the options that I would have in choosing a grad school. Michael Baldea took me on as a UROP my last semester in Minnesota and gave me my first exposure to academic research.

Finally, I would like to remember my grandparents, Ike and Helen, who both passed away during my time here at MIT. I will always continue working to the best of my abilities in honor of you.

Chapter 1: Introduction

1.1 Introductory Remarks

All of the topics covered in this thesis involve questions regarding the inner workings of the adaptive immune system. Before jumping into the specific nature of these questions, I think it is important to introduce some general immunology concepts in the following subsections of the introduction. A description of these general concepts is by no means intended to be a comprehensive review of the literature. Rather, I will discuss the concepts in more broad, "common knowledge" terms, giving references where needed. Intertwined throughout this discussion I will introduce all of the questions to be addressed in this thesis and the motivation behind investigating such questions. In the next to last section of the introduction, I will give an overview of the remaining chapters.

1.2 Adaptive Immunity

The adaptive immune response is very important for survival in that it gives the host organism the capability of detecting a wide variety of foreign material, allows for the elimination of pathogens, and provides memory to protect against future attacks by the same pathogen. Key mediators of the adaptive immune response are CD4+ T cells, which detect antigen presented on the surfaces of antigen presenting cells (APC). The APCs break down both endogenous and foreign material internally and load these fragments into MHC class II molecules forming peptide-MHC complexes, which are transported to the surface for interaction with T cell receptors (TCR) expressed on the surface of T cells. Upon ligation of the TCR with a foreign peptide-MHC complex (pMHC), the T cell can be activated. After activation, the T cell undergoes extensive proliferation and eventually differentiates into an effector cell which mediates the immune response.

1.3 TCR Signaling

The process of T cell activation involves the transduction of multiple intracellular signaling pathways initiated by the TCR upon ligation with pMHC. One outcome of these signaling pathways is the transcription and secretion of Interleukin 2 (IL-2), which is a cytokine that induces cellular proliferation. The TCR signaling pathway has been well characterized (a schematic of the pathway can be found in Figure 1.1). Upon ligation with a peptide-MHC complex, the kinase Lck is recruited, which then phosphorylates the TCR-ζ chain and the immuno-tyrosine activation motifs (ITAMs). The kinase, ZAP-70 can bind to phosphorylated ITAMs and is activated by Lck. Two methods of regulation for these initial signaling events are phosphatase activity and Cbl-b-mediated degradation. Cbl-b is a ubiquitin ligase that can bind to ZAP-70 and mark it for degradation. The degradation process results in the destruction of both ZAP-70 and the associated TCR[1].

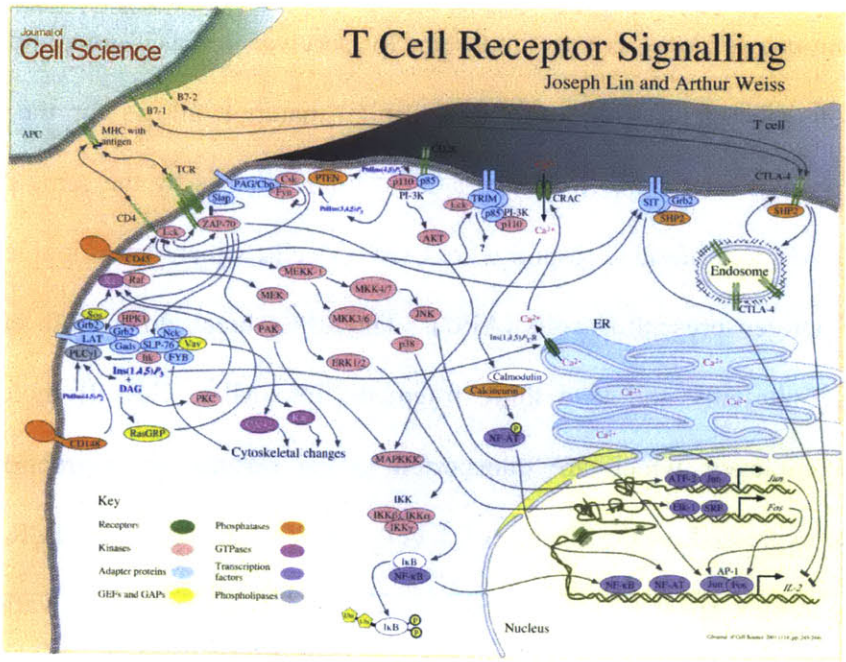

Figure 1.1. T cell receptor signaling pathways (from Lin and Weiss, 2001)[2]

Once activated, ZAP-70 can phosphorylate downstream targets including the membrane-bound adapter molecule LAT, which spatially organizes downstream signaling pathways. LAT contains a phosphorylation site that can bind the phospholipase PLCγ, and multiple phosphorylation sites that can bind the adaptor molecules Grb2 and GADS. PLCγ cleaves membrane bound PIP_2 molecules into IP_3 and DAG. IP_3 leads to both the release of intracellular Ca^{2+} stores and an influx of Ca^{2+} into the cell. This, in turn, results in the activation of NFAT, an IL-2 transcription factor. DAG leads to the activation of PKC, which subsequently leads to NF-kB activation, another IL-2 transcription factor. The adaptor molecule GADS binds to the scaffold SLP-76 and can stabilize the interaction of PLCγ with LAT when the two molecules are bound to adjacent phosphorylation sites. The Tec kinase Itk binds to SLP-76 and is thought to activate PLCγ. Additionally the MAPK pathway can be initiated by the binding of Grb2 to LAT by the following mechanism. Grb2 recruits the guanine exchange factor, Sos, which can catalyze the conversion of RasGDP to its activated form, RasGTP. Sos contains an allosteric site that can be occupied by either RasGDP or RasGTP, which increases its catalytic ability. RasGTP can activate the MAPKKK Raf, which ultimately leads to the production of the third IL-2 transcription factor, AP-1. Ras can also be activated by RasGrp, which is activated in the PLCγ pathway through DAG. The primary difference between the two methods of Ras activation is that activation through Sos is cooperative, while activation through RasGrp is not[3].

1.4 Loading of peptides by DM

In Section 1.2 it was described that T cells have receptors which interact with pMHC on APCs, which give the T cells the ability to scan for foreign material and ultimately set off a response if any is detected. Therefore, the ability of APCs to take in material from their surroundings, break it up into peptide fragments, load it into MHCs, and display the pMHC on their surface is an

integral part of the adaptive immune system. MHCs that do not have peptide loaded in them are unstable and either collapse or form aggregates of multiple empty MHCs (Grotenbreg). To avoid this issue, they are synthesized loaded with a generic peptide, CLIP. Somehow, the APCs need to be able to remove CLIP and load in a peptide fragment from engulfed material without the pocket on the MHC collapsing or the formation of MHC aggregates. This is the role of the protein, DM. DM's role is to eject the CLIP peptide, stabilize the empty MHC, and load the peptide of interest.

Having a protein specialize in the removal and additions of peptides seems contradictory, since it would be assumed that DM would eject the peptide that it has just loaded. The precise role of DM in this process is investigated in Chapter 2 using photocleavable peptides. These are peptides that when exposed to UV light, get cleaved and dissociate from MHC. Also in solution during this process is a labeled peptide which can be measured using a technique called fluorescence polarization where the signal is indicative of whether or not the labeled peptide is bound to the much larger MHC molecule. This experimental technique allows for the analysis of the kinetics of MHC aggregation and peptide loading in the absence of DM, which when compared to the same experiment done in the absence of UV and presence of DM, allows for analysis of the role of DM. We further characterize the interaction between pMHC and DM in Chapter 3 using a Biacore instrument. This is another tool for analyzing the kinetics of association and dissociation between two molecules.

1.5 Modeling cell signaling networks

During the early years of immunology research in the Chakraborty group, much focus was placed on studying different problems involving the T cell receptor (TCR) signaling network discussed in a previous subsection. The TCR pathway had been studied extensively and therefore most of the relevant pathways were known. Using estimated parameters found throughout the literature and also heuristic estimates, computer simulations of the TCR pathway could be performed by treating the pathway as a series of chemical reactions. As an example, ZAP70 binding to LAT would be one reaction, ZAP70 phosphorylating a tyrosine residue on LAT would be another reaction, ZAP70 unbinding from LAT would be another reaction. Simulations could show how downstream markers like ZAP70 activation varied as the strength of the TCR – pMHC interaction varied.

Due to length scale that these intracellular interactions occur and due to the relatively small number of molecules involved, the reaction network could not simply be solved using an Ordinary Differential Equation (ODE) solver like MATLAB. Solving ODEs gives the mean concentrations that are the solutions at various time points. One could imagine a scenario where a threshold is imposed on the number of activated ZAP70 molecules which constitutes a T cell being activated. For a range of parameters, it may appear that the T cell would not be activated since the ODE solution does not show the number of activated ZAP70 molecules crossing the threshold at any time point. However, this is just the average solution. Stochastic simulation allows for the visualization of many different trajectories since it takes into account the stochastic nature of equations involving small numbers of molecules. In practice, numerous trajectories could cross the threshold of activated ZAP70 molecules at numerous time points

without the average of all the trajectories ever crossing that threshold. Any conclusions made based on the ODE solution would be flawed for this reason.

A very useful algorithm, known as the Gillespie algorithm is used throughout the Chakraborty group to simulate interactions in signaling networks due to its ability to take into account stochastic effects associated with small numbers of molecules in an easily programmable manner[4]. For all the reactions in a network, a rate equation can be written in the form of

$$a_i = k_i C_{i\ldots j} \qquad \text{(Equation 1.1)}$$

Equation 1.1 where the propensity of reaction i (a_i) is equal to the rate constant (k_i) multiplied by the concentrations of all the reactants ($C_{i\ldots j}$). At every time step in the algorithm, the total propensity (a_0) is computed by summing all of the individual reaction propensities. Next, two random numbers are generated according to a uniform distribution from 0 to 1. The first random number (r1) is used to compute the time that has elapsed since the last reaction occurred at the previous time step (τ) using Equation 1.2.

$$\tau = \frac{1}{a_0} \ln\left(\frac{1}{r1}\right) \qquad \text{(Equation 1.2)}$$

A variable in the algorithm keeps track of the total time elapsed by summing the individual time steps. Now that the time that the next reaction will occur has been computed, the other random number (r2) is used to determine the identity of the next reaction (μ) which satisfies the inequality in Equation 1.3.

$$\sum_{\nu=1}^{\mu-1} \frac{a_\nu}{a_0} < r_2 \leq \sum_{\nu=1}^{\mu} \frac{a_\nu}{a_0} \qquad \text{(Equation 1.3)}$$

After the identity of the next reaction is determined, the numbers of molecules for all species are changed according to the stoichiometry of whichever reaction has occurred. At the next time step, all of the propensities are recalculated, two new random numbers are generated and the process continues until the desired reaction time is reached. In practice, Equation 1.3 favors the occurrence of reactions with the highest propensities, but the random element allows for the occurrence of reactions with small propensities as well.

Our group has used these methods to investigate a number of problems involving TCR signaling. The site of interaction between a T cell and an APC during TCR – pMHC binding is known as the immunological synapse. After early signaling events through the TCR, costimulatory receptors and signaling molecules begin to congregate in the middle of the synapse, while adhesion molecules begin to congregate on the edge of the synapse. A series of papers by former members of the group investigated the role of the synapse in T cell activation[5,6,7]. Another standing problem in immunology at the time was how a TCR could find a small amount of foreign antigen in a sea of many endogenous peptides and initiate an activation signal. A model known as the dimer model was illustrated using simulation[8]. In this model, it was proposed that the sea of endogenous pMHC could be used to amplify the signal generated by an antigenic pMHC through localization of CD4. LCK bound to the cytoplasmic tail of CD4 associated with the antigenic pMHC – TCR interaction could then activate the ITAMs of neighboring TCR's bound to endogenous pMHC.

Ashok Prasad, a post doc in the group, added more detail to the basic TCR models by adding in the downstream signals which are localized by LAT. He used this model investigate the origin of the sharp boundary that discriminates the positive and negative selection of thymocytes[9]. Jayajit Das used modeling to investigate properties of RAS signaling[3]. Dennis Wylie expanded

our algorithms from spatially homogenous systems (a well-mixed system) to spatially inhomogeneous systems where spatial effects of signaling matter[10].

1.6 Cytokines

All of the previous models in our group, as discussed in the previous subsection, focused on TCR signaling. However, T cells receive many more signals than just through their TCRs. T cells have various costimulatory receptors on their surface, such as CD28 and CTLA-4, which interact with ligands, B7-1 and B7-2, on the APCs. These signals further regulate whether or not a T cell gets activated by providing either a supplemental signal (CD28) or an inhibitory signal (CTLA-4).

In addition to costimulatory receptors, there are also cytokine receptors on the surface of T cells. Cytokines are extracellular signaling molecules which help skew the immune response towards whatever is needed locally. Many of the cytokines are members of the interleukin family and all have names in the form of Interleukin # (IL-#). Many of these signal through the Jak-STAT pathway and may also activate a MAPK pathway. Frequently in the literature the term, cytokine milieu, appears which is in reference to the composition of cytokines that are present locally. During T cell differentiation into various effector types, the cytokine milieu often determines which type of effector T cells will dominate. As an example, if primary T cells are in the presence of IL-4 during differentiation, the resulting effector cells will be Th2 cells (described in the next subsection). IL-4 is secreted by Th2 cells which serves to further induce the T cells around them to become Th2 and also to inhibit the development of Th1 or Th17 cells. In this manner, cytokines serve as an additional means of shaping the nature of the immune response.

1.7 Effector T cells

Effector cells arise when naïve T cell get activated and have undergone differentiation over the course of several days. Up until recently, it was thought that there were only two main categories of effector T cells, T helper 1 cells (Th1) or T helper 2 cells (Th2). Now, several new effector types have been described including Th17 cells, Th9 cells, Tr1 cells, etc. In this section, I will focus on three of the major types, Th17, Th1 and Th2, which can be seen in Figure 1.2. Th17 cells were discovered in the context of Multiple Sclerosis where it was discovered that there was a lot of the cytokine IL-17 present in the lesions. It was found that the IL-17 was coming from a previously uncharacterized effector cell, which became known as Th17 cells, due to their ability to secrete IL-17. Soon two groups, including Vijay Kuchroo's group, found that Th17 cells could arise *in vitro* by added TGF-β and IL-6 in the presence of some form of TCR stimulation.

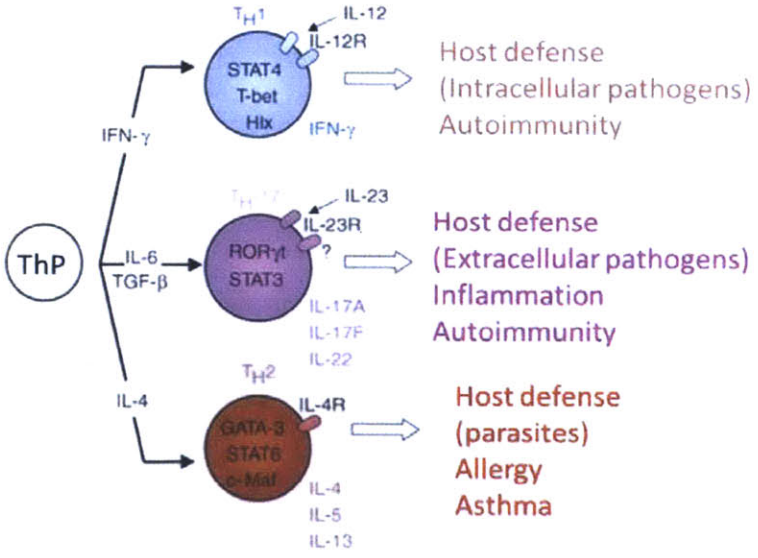

Figure 1.2. T cell differentiation into different effector types. Figure modified from (Bettelli, 2007)[11].

As seen in Figure 1.2, effector cell types are classified according to the cytokines that they secrete, which in turn dictate the nature of the immune response. Each expresses a master transcription factor which drives its lineage: T-bet for Th1, RORγt for Th17, and GATA-3 for Th2. It is thought that Th1 cells specialize in the defense against intracellular pathogens, while Th17 cells specialize in the defense against extracellular pathogens. Th2 cells specialize in defense against parasites. These are not strict definitions of function, rather they are summations of some different functions observed by the given effector type. Th17 cells are highly inflammatory and have been implicated in numerous autoimmune diseases, including multiple sclerosis as described above. Th17 cells are currently a hot topic in research due to their involvement in autoimmune disease as well as their relatively new status within the field. The remainder of the introduction will revolve around problems involving Th17 differentiation.

1.8 Th17 versus Treg differentiation

There are two types of regulatory T cells, iTreg and nTreg, which both serve as a check on the immune system in the periphery. They are characterized by their expression of the transcription factor Foxp3 and their ability to inhibit the proliferation of T cells. nTregs arise during thymic selection and are thus are beyond the scope of this thesis. Inducible Tregs (iTregs) arise from primary T cells after several days of TCR stimulation in the presence of TGF-β (Figure 1.3). The differentiation conditions for Tregs are surprisingly similar to that of Th17 cells, which arise from primary T cells in the presence of TCR stimulation, TGF-β, and IL-6. Determining how the addition of IL-6 can change a Treg-inducing TGF-β signal into a Th17-inducing signal began as the primary focus of this thesis.

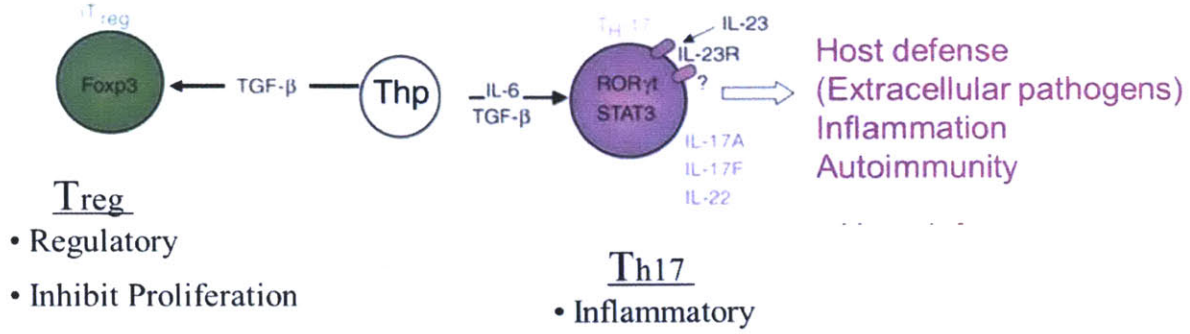

Figure 1.3. T cell differentiation into either Tregs or Th17 cells. Figure modified from Bettelli, 2007.

We were recruited by Vijay Kuchroo (thesis committee member) to use our computational skills to determine how the signaling pathways of IL-6 and TGF-β overlap to give Th17 cells. The obvious place to start was to look at the components of the TGF-β signaling pathway (Figure 1.4) and the IL-6 signaling pathway (Figure 1.5). TGF-β induces the activation of SMADs. Upon activation, the SMADs form a trimer which allows for access to the nucleus. This is about the simplest signaling network possible in that the transcription factor is induced at the receptor without any signaling cascades. Through the Jak-STAT pathway, IL-6 induces what we believed to be mainly pSTAT3. Upon activation, pSTATs form a dimer which reveals a nuclear targeting sequence and allows for their access into the nucleus. Given the simplistic nature of these two pathways, it is not obvious how they would overlap at the membrane-proximal level. Thus, they must likely overlap at the transcriptional level. It should be noted that there is also a MAPK pathway induced by both IL-6 and TGF-β, which will not be considered in this thesis.

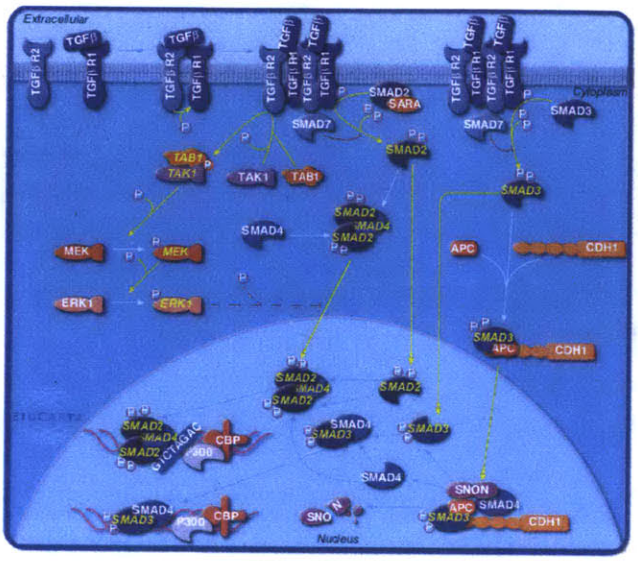

Figure 1.4. TGF-β signaling pathway obtained from BioCarta's website (www.biocarta.com).

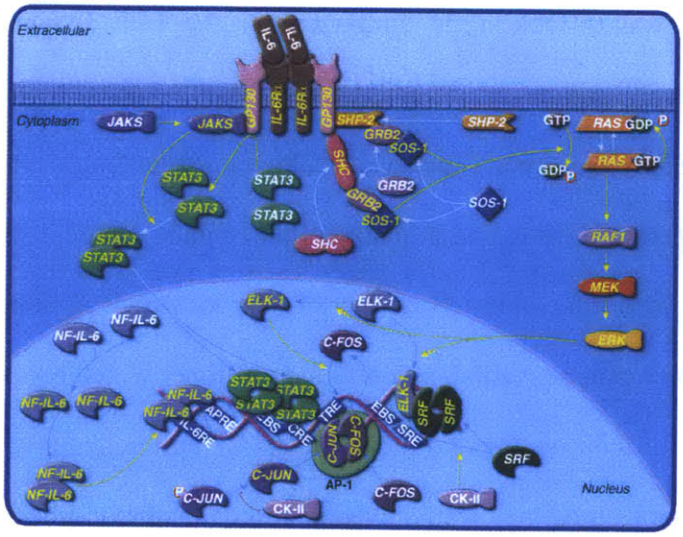

Figure 1.5. IL-6 signaling pathway obtained from Biocarta's website (www.biocarta.com).

1.9 Approach for studying Th17 versus Treg differentiation

With no obvious overlap between the IL-6 and TGF-β pathways on paper, we needed some way to approach the problem of understanding the difference between Th17 and Treg differentiation.

Being a chemical engineer, a good way to start is by constructing a process flow diagram of the problem (Figure 1.6). Through membrane-proximal signaling, IL-6 induces pSTAT3 and TGF-β induces pSMAD. These transcription factors feed into a genetic network, which leads to the differentiation into Th17 cells. In the absence of IL-6, the genetic network leads to Tregs. In the absence of TGF-β, the genetic network leads to a pro-inflammatory response. We focused our research efforts on characterizing the membrane-proximal signaling using flow cytometry (Chapter 5) and characterizing the genetic network by following the activation of numerous genes over the course of several days using PCR (Chapter 6).

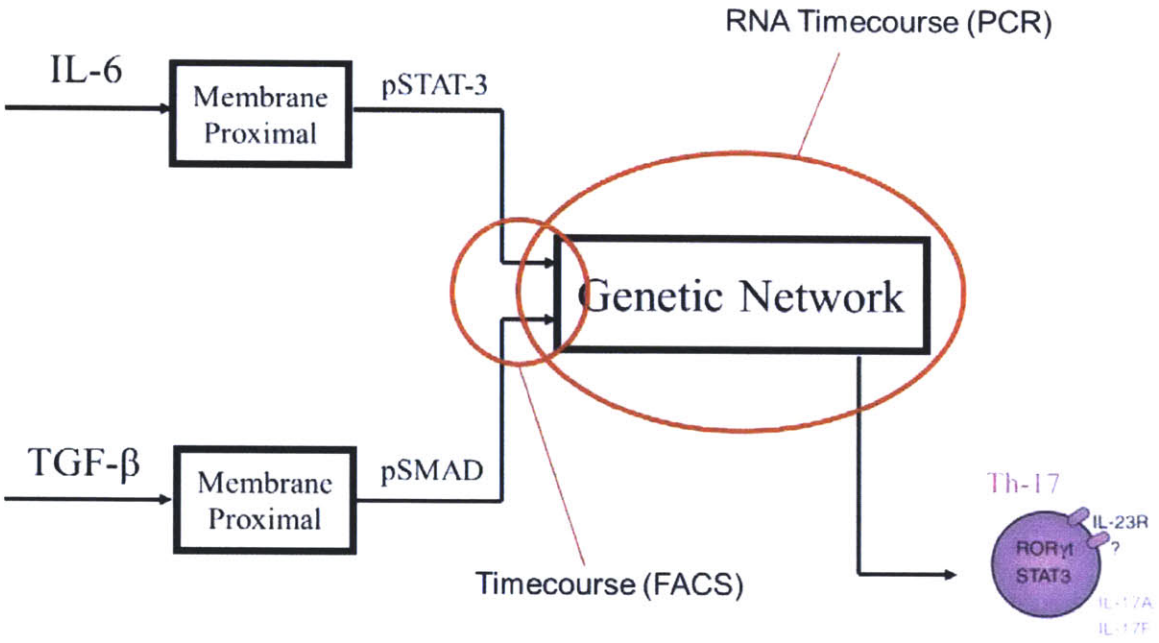

Figure 1.6. Effective process flow diagram of the cytokine signals that lead to Th17 differentiation and the techniques to be used to characterize the important sections of the diagram.

1.10 Cytokine specificity

In the literature, it seemed that the consensus was that IL-6 primarily induced pSTAT3. However, numerous cytokines activate STAT3 and behave very differently to IL-6. We began to appreciate this problem in the context of IL-6 and IL-10 signaling. IL-6 induces a pro-inflammatory response, while IL-10 induces an anti-inflammatory response, despite both signaling through STAT3. Before even approaching the problem of understanding the inner workings of Th17 differentiation, we were faced with the issue that we had no way mathematically to distinguish an IL-6 induced STAT3 signal from an IL-10 induced STAT3 signal. Through a literature review, it was learned that IL-6 induces a transient STAT3 signal, while IL-10 induces a sustained STAT3 signal. In both cases, pSTAT3 is exposed to exactly the same genetic network, but the transient signal leads to a pro-inflammatory response while the sustained signal leads to an anti-inflammatory response. In Chapter 4, we show that a very simple genetic network can use changes in signal duration to lead to two different cellular outcomes. Therefore, cells can utilize signal duration as a means of distinguishing between two different cytokines despite them activating the same transcription factor.

The case considered in Chapter 4 was simpler since it was just two cytokines, IL-6 and IL-10 which had been characterized experimentally in the literature in the same experiment. In the context of Th17 differentiation, we knew of four cytokines of interest, IL-6, IL-10, IL-21, and IL-27 (Figure1.7). These were all chosen due to their effects on Th17 differentiation and because they all activate the same two transcription factors STAT1 and STAT3. As discussed before, IL-6 induces Th17 differentiation when combined with TGF-β. It was generally thought that IL-10 would inhibit Th17 differentiation since it is an anti-inflammatory cytokine, but its

effect had not been observed at the start of this study. IL-21 was known to be secreted during Th17 differentiation, reinforcing the Th17 lineage. In the absence of IL-6, IL-21 is a weak inducer of Th17 cells when combined with TGF-β. IL-27 was known as a main inhibitor of Th17 differentiation.

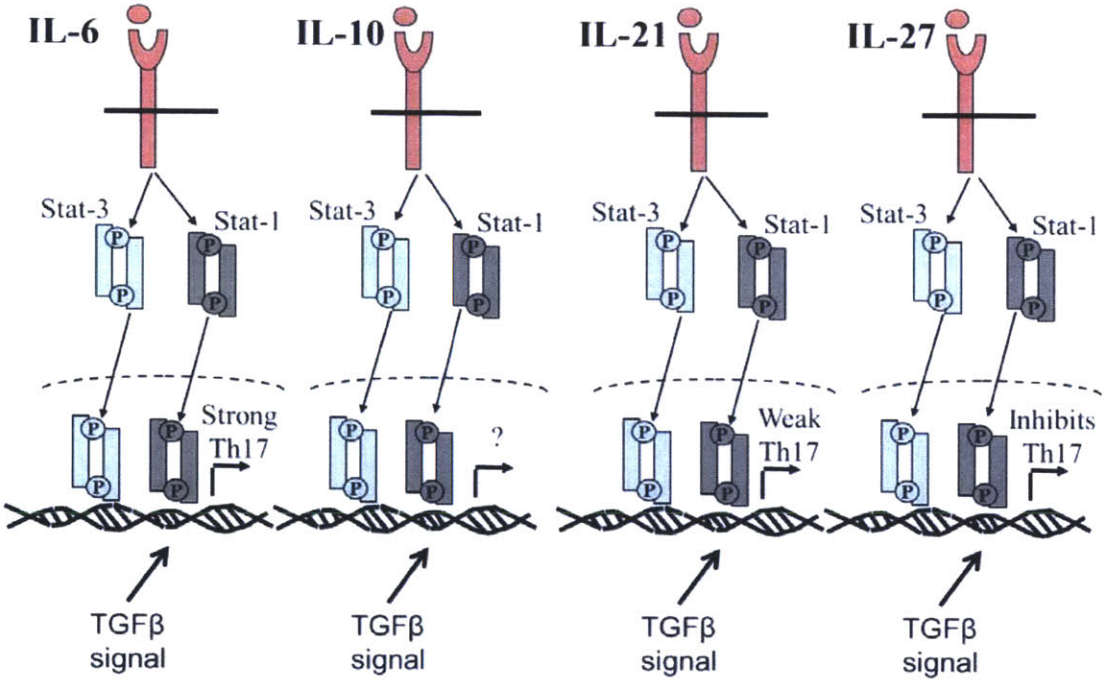

Figure 1.7. Cytokine signaling pathways and their effects on Th17 differentiation when combined with TGF-β signaling. Some of the information used in the construction of this figure is from (Delgoffe, 2011)[12].

In Chapter 5, we explore the origin of signal specificity in the context of Th17 differentiation amonugst pSTAT1 and pSTAT3 inducing cytokines by measuring experimentally in Vijay Kuchroo's lab how each cytokine activates these transcription factors over the first four hours of stimulation. It was very important, in order to compare the cytokines, that we characterize the cytokines in the same study. Other studies had characterized 1 or 2 of the cytokine's STAT

signals at a time, which did not allow for comparing the cytokines. We observe the effects of how these activation profiles change when multiple cytokines are present. We also observe whether or not these cytokines behave similarly when their pSTAT activation profiles are made to be similar.

(It may be confusing to the reader that early in this subsection it is noted that IL-6 primarily activates STAT3 and then in Figure 1.7, it is shown to activate STAT1 as well. This figure is based on our experiments in Chapter 5 and not what we had seen in the literature when the work in Chapter 4 was performed.)

1.11 Overview of experimental techniques to be used

Three main experimental techniques were used in the preparation of Chapter 5, which is the primary results section of this thesis. In the next three subsections, I will briefly describe the techniques. For a more detailed description, refer to Appendix 1.

1.11.1 FACS

Flow cytometry was used to reliably and repeatably measure pSTAT1 and pSTAT3 levels in CD4+ T cells. T cells were stimulated with various cytokines for varying amounts of time in an incubator. After, the cells were collected and fixed. They were then permeabilized and antibodies for pSTAT1 and pSTAT3 were added. The cells were then run on a flow cytometer which measured both pSTAT1 and pSTAT3 levels based on the intensity of the colors on the individual antibodies.

1.11.2 EMSA

A compounding variable in the STAT characterization study was that pSTAT1 and pSTAT3 can exist in homodimers (pSTAT1-pSTAT1, pSTAT3-pSTAT3) or heterodimers (pSTAT1-pSTAT3) which could have different properties. We sought a technique to be able to characterize the ratio of these different forms in the nucleus of the T cells after stimulation with different cytokines for varying amounts of time. FACS cannot give insight into these ratios since there are different antibodies for pSTAT1 and pSTAT3 which may have different affinities or intensities and thus the levels measured using FACS cannot be compared. A technique called electrophoretic mobility shift assay (EMSA) could be used to accomplish this. In this assay, a labeled oligomer that all three dimeric forms can bind to is combined with the nuclear extracts from the T cells of interest. The mixture is then run on a non-denaturing gel using electorophoresis. The labeled oligomer is relatively small and travels with ease through the gel if nothing is bound to it. If any of the dimeric forms binds to the oligomer, it moves slowly. Due to subtle differences in molecular weights, the gel can then be visualized and bands appear with intensities proportional to the relative amounts of the dimeric forms. The oligomer used is part of the C-fos gene known as hSie[13,14]. This technique did not end up being used due to difficulty in interpreting its results. However, since a protocol was developed, it seemed relevant to include it in this thesis.

1.11.3 Th17 differentiation

To compare how different cytokine pairs affected Th17 differentiation, we needed to have a standardized way of performing Th17 differentiations and measuring the results. Naïve CD4+ T cells ($CD62L^{high}$ $CD25^{-}$) were sorted on a FACS ARIA and then plated on flat-bottom 24-well plates coated with α-CD3 / α-CD28 (Note: If APCs were to be used for stimulation, uncoated

plates were used). The cytokines of interest were added along with TGF-β, and neutralizing antibodies for IFN-γ and IL-4 before placing the plate in an incubator for 48 hours. At 48 hours, the cells were moved to a new uncoated plate and IL-23 was added. At 96 hours, the cells were collected and restimulated with PMA and Ionomycin for 3-4 hours in the incubator. The cells were then fixed and stained for measurement of intracellular IL-17a.

1.12 Thesis Overview

All of the chapters were introduced in the previous subsections, but to understand how everything fits together, I will use this subsection to reiterate the content of each of the chapters.

Chapter 2 and 3 are reprints of two manuscripts that resulted from a collaboration with Kai Wucherpfennig's lab to try and further the understanding of the role of DM in the loading and unloading of pMHC (Chapter 2), as well as understanding the nature of the interaction between DM and pMHC (Chapter 3). These were side projects that do not necessarily relate to the central theme of cytokine specificity and Th17 differentiation, but do relate to immunology and did result in two publications and thus are included in this thesis.

Chapter 4 is a reprint of a manuscript where we sought to show that a simple genetic network capable of distinguishing between transient and sustained signals could account for the fact that IL-6 induced pSTAT3 leads to a pro-inflammatory response while IL-10 induced pSTAT3 leads to an anti-inflammatory response without needed to resort to unknown species or receptor specific conformational changes of STAT3. This simple study is how we began to appreciate the nuances of cytokine specificity when two cytokines signal through the same transcription factor but lead to different results. It is a fine illustration of how two cytokines can unexpectedly

behave similarly when their signals are made to be similar. In this case, if IL-6 is made to induce a sustained pSTAT3 signal, it behaves exactly like IL-10 in inducing an anti-inflammatory response.

Chapter 5 is a pre-print of a manuscript that will eventually be submitted for publication. It is also the culmination of my 3 years of doing experiments in Vijay Kuchroo's lab and should be considered the main chapter of the thesis. In this chapter, I seek to characterize IL-6, IL-10, IL-21, and IL-27 signaling and ultimately determine why these cytokines behave differently in the context of Th17 differentiation despite signaling through the same transcription factors. We show that the ratio of pSTAT3 to pSTAT1 induced is the important distinguishing variable between the different cytokines and that only considering that amplitude of one or the other transcription factors leads to faulty conclusions. This ratio is what we believe dictates cytokine specificity in the context of Th17 differentiation. Even though IL-27 is considered an inhibitory cytokine, we show that it is a potent inducer of Th17 cells in the absence of STAT1 since it induces a very similar pSTAT3 profile to that induced by IL-6 in these cells.

In Chapter 6, I present an algorithm that can be used to analyze time courses of gene activation as measured by PCR for intermediate system sizes (10-50 genes). The algorithm is used to analyze the measurements made over the course of 96 hours of Th17 differentiation that was used to be a pilot study to determine points of interest to measure using a gene array. We find different clusters of genes that behave similarly in different phases of the differentiation process. These could then be tested experimentally for their significance. In the time course, we observe that the master transcription factor for Tregs (Foxp3) and the master transcription factor for Th17 cells (RORγt) seem to oppose each other in that if one transcription factor is high, the other is

always low. This study is meant to be an initial attempt at characterizing the genetic network important in Th17 differentiation.

In Chapter 7, I make some concluding remarks.

1.13 References

1. Janeway, CA, Travers, P, Walport, M, Schlomchick, M. Immunobiology, 6th edition, Garland Publishing: New York (2005).

2. Lin, J and Weiss, A. 2001. T cell receptor signaling. *J. Cell Science* **114**:243-244.

3. Das J, Ho M, Zikherman J, Govern C, Yang M, Weiss A, Chakraborty AK, Roose JP. 2009. Digital Signaling and Hysteresis Characterize Ras Activation in Lymphoid Cells. *Cell* **136**:337-351.

4. Gillespie DT. 1977. *J Phys Chem* **81**:2340–2361.

5. Lee K-H *et al.* 2003. The Immunological Synapse Balances T Cell Receptor Signaling and Degradation. *Science* **302**:1218-1222.

6. Cemerski, S, *et al.* 2007. The Stimulatory Potency of T Cell Antigens is Influenced by the Formation of the Immunological Synapse. *Immunity* **26**:345-355.

7. Cemerski, S, *et al.* 2008. The Balance between T Cell Receptor Signaling and Degradation at the Center of the Immunological Synapse is Determined by Antigen Quality. *Immunity* **29**:414-422.

8. Li Q-J, Dinner AR, Qi S, Irvine DJ, Huppa JB, Davis MM, Chakraborty AK. 2004. CD4 enhances T cell sensitivity to antigen by coordinating Lck accumulation at the immunological synapse. *Nat Immunol* **5**:791-799.

9. Prasad A, Zikherman J, Das J, Roose JP, Weiss A, Chakraborty AK. 2009. Origin of the sharp boundary that discriminates positive and negative selection of thymocytes. *Proc Natl Acad Sci USA* **106**:528-533.

10. Wylie, DC, *et al.* 2006. A Hybrid Deterministic – Stochastic Algorithm for Modeling Cell Signaling Dynamics in Spatially Inhomogeneous Environments and under the Influence of External Fields. *J. Phys. Chem. B.* **110**:12749-12765.

11. Bettellii E, Oukka M, Kuchroo VK. 2007. Th-17 cells in the circle of immunity and autoimmunity. *Nat Immunol* **8**:345-350.

12. Delgoffe GM, Murray PJ, Vignali DAA. 2011. Interpreting mixed signals: the cell's cytokine conundrum. *Curr Opin Immunol.* **23**:632-638.

13. Sadowski HB, Shuai K, Darnell JE Jr and Gilman MZ. 1993. A common nuclear signal transduction pathway activated by growth factor and cytokine receptors. *Science* **261**:1739–1744.

14. Costa-Pereira AP, Tininini S, Strobl B, Alonzi T, Schlaak JF, Is'harc H, Gesualdo I, Newman SJ, Kerr IM, Poli V. 2002. Mutational switch of an IL-6 response to an interferon-γ-like response. *Proc Natl Acad Sci USA* **99**:8043-8047.

Chapter 2: The Role of DM in Peptide Association

Portions reprinted from "Empty Class II Major Histocompatibility Complex Created by Peptide Photolysis Establishes the Role of DM in Peptide Association" by Gijsbert M. Grotenbreg, Melissa J. Nicholson, Kevin D. Fowler, Katherine Wilbuer, Leah Octavio, Maxine Yang, Arup K. Chakraborty, Hidde L. Ploegh, and Kai W. Wucherpfennig, *JBC*, **282**, 2007 21425-21436, 10.1074/jbc.M702844200.

2.1 Contributions

My contribution to this work consisted of mathematical modeling to determine the interactions between molecules and the associated rate constants depicted in Figure 2.7 based on the experimental data collected by the other authors on the paper. All of the modeling work described in Section 2.4.7 (and the corresponding associated work in Appendix 2) was performed by myself with some assistance by Leah Octavio and Maxine Yang. Arup Chakraborty assisted in the writing of these sections.

2.2 Introduction

Major histocompatibility complex (MHC) molecules are cell surface proteins that present peptides to antigen-specific receptors on T cells. The Class II MHC products are specialized in sampling endosomal compartments to acquire these peptides. Delivery of newly synthesized and assembled Class II MHC proteins to endo-lysosomal compartments is assured by means of the transient association of the MHC αβ heterodimer with the invariant chain, a protein endowed with both chaperone function and an address code[1, 2]. In endosomal compartments, the invariant chain is destroyed, yielding a Class II MHC product occupied with an invariant chain-derived remnant, the CLIP peptide[3-5]. The HLA-DM (DM) molecule, itself incapable of binding peptide, facilitates replacement of CLIP with antigenic peptides[6-10]. The action of DM is not limited to the Class II MHC/CLIP complex and extends to Class II MHC-peptide complexes more generally.

Such editing by DM favors presentation to CD4 T cells of those peptides that are most resistant to peptide displacement by DM[9, 11-17].

DM is a membrane-anchored heterodimer that belongs to the extended family of proteins with a MHC fold but lacks a functional peptide-binding groove[18, 19]. Mutagenesis experiments identified lateral surfaces on DM and DR molecules that are involved in the interaction between the two proteins. On the DR side, these mutations span the entire length of the ectodomain and are localized to the α1 and β2 domains[20]. On the DM side, an extended interaction surface has been mapped that also spans the entire length of the ectodomain[21]. These data support a model in which lateral interactions between DM and DR molecules induce a conformational change that destabilizes the DR-bound peptide. It has been proposed that DM disrupts one or several hydrogen bonds between the peptide backbone and conserved DR residues, which could account for the fact that DM accelerates dissociation of peptides that are highly diverse in sequence[12, 19, 22]. However, DR-peptide complexes vary substantially in susceptibility to DM and peptide, and DR residues along the entire length of the binding site can affect susceptibility to DM[23]. These data suggest that DM causes a more global conformational change of the peptide-binding site.

High affinity peptides form stable, long-lived complexes with DR molecules that have a half-life of days to weeks[24]. Purified, soluble DM greatly increases the rate at which labeled peptides dissociate from DR molecules at an acidic pH[6, 9, 12]. In such experiments, DM obviously also accelerates the binding of labeled peptides to DR molecules, but it has been difficult to discern whether accelerated peptide binding is solely due to the increased availability of binding sites or also due to a direct contribution of DM to peptide association. The detailed mechanism of DM catalysis has resisted elucidation, partly because of this difficulty of measuring independently the

contributions to peptide dissociation and peptide association. Isolating the contribution of DM to peptide association would require a homogenous population of empty Class II MHC molecules in a peptide-receptive state. In theory, empty Class II MHC molecules could be generated by dissociating bound peptide, but empty molecules tend to aggregate during the prolonged incubation periods that would be required. An alternative approach that has been pursued consists of the production of recombinant molecules refolded from denatured DR chains in the absence of peptide, but the majority of such molecules (~95%) bind peptides only slowly, apparently because conversion to more active conformer(s) is required[25, 26].

Because of these technical challenges, two different models have been proposed regarding the interaction of DM with DR molecules. According to the first model, DM interacts only with DR-peptide complexes but not empty DR molecules and catalyzes the interconversion between transient and stable DR-peptide complexes[26]. The second model proposes that DM interacts with both DR-peptide complexes and empty DR molecules and that DM acts as a molecular chaperone that rescues empty DR molecules at an acidic pH[27, 28]. Resolution of this issue requires a novel approach with which empty DR molecules can be generated rapidly and synchronously. An intriguing new development has been the generation of conditional ligands for Class I MHC molecules. Toebes et al.[29]synthesized photocleavable ligands for Class I MHC molecules and reconstituted the relevant subunits into an assembled Class I MHC complex. UV irradiation resulted in cleavage of the bound peptide and rapid departure of the cleavage fragments from the binding pocket.

Here, we apply this chemistry to generate empty Class II MHC molecules. The experiments make use of a human Class II MHC molecule, the expression of which predisposes its carrier to

multiple sclerosis, HLA-DR2 (DRA, DRB1*1501), and a photocleavable peptide based on a T cell epitope of human myelin basic protein (MBP_{85-99})[30, 31]. Rapid, early binding events were followed with a fluorescence polarization (FP) readout, in which the fraction of emitted fluorescent light that retains polarization is proportional to the amount of MHC-bound fluorescent reporter peptide, because of a slower tumbling speed of the MHC-peptide complex compared with free peptide[32]. The presence of DM substantially accelerated peptide binding to such empty DR molecules under all of the reaction conditions tested. Mathematical models show excellent concordance with the experimental data for a model wherein DM contributes significantly to peptide association through formation of a complex with empty Class II MHC molecules. We propose that this DM-DR complex represents a peptide-loading complex that facilitates antigen presentation by rapid peptide capture, analogous to the MHC class I peptide-loading complex[33].

2.3 Experimental Methods

Peptide Synthesis and Photocleavage

Peptides were constructed manually with the aid of Fmoc (*N*-(9-fluorenyl)methoxycarbonyl)-based solid phase peptide chemistry using standard protocols. The photolabile 3-amino-3-(2-nitro)phenyl-propionic acid (Anp) residue was incorporated at the positions indicated in Fig. 2.1 as described previously[29]. Details of the synthesis of MBP-C647 and MBP-N647 are provided in the Appendix 2. Photocleavage was examined by preparing a stock solution of lyophilized peptide in Me_2SO (10 mg/ml). This stock was diluted in H_2O, and 200-µl aliquots were added to a 96-well plate on ice. Two UV sources were used, both of which induced efficient photolysis: a Stratalinker 2400 UV cross-linker (Stratagene, La Jolla, CA) fitted with lamps emitting at a

wavelength of 365 nm and a dedicated long wavelength UV lamp (Blak Ray B100AP, UVP, Upland, CA; wavelength of 365 nm). Aliquots were taken at different time points to determine the kinetics of photolysis by liquid chromatography/mass spectrometry or matrix-assisted laser desorption/ionization time-of-flight (MALDI-TOF) mass spectrometry. For liquid chromatography/mass spectrometry analysis, an HP/Agilent 1100 HPLC system (UV detection at 214 nm) equipped with an analytical C18 column (2.1 mm × 50 mm, 3.5-μm particle size) was used in combination with buffers H_2O, 0.085% trifluoroacetic acid (A) and MeCN, 0.085% trifluoroacetic acid (B), which was coupled to an LCT mass spectrometer (Waters, Milford, MA) with an electrospray interface. MALDI-TOF mass spectrometry was performed using a Waters MALDI Micromass spectrometer (Waters, Milford, MA) and 3,5-dimethoxy-4-hydroxycinnamic acid as a matrix.

Protein Expression and Purification

Soluble DR2 with covalently linked CLIP peptide (1 μm) was loaded with DNP-labeled photocleavable peptides (10 μm) following linker cleavage with thrombin[34] overnight at 30 °C in 50 mm sodium citrate, pH 5.2, 100 mm NaCl, 1% octylglucoside, protected from light. Free peptide was removed from the protein complex by HPLC gel filtration (Superose 6, GE Healthcare Bio-Sciences Corp, Piscataway, NJ). The fraction containing the DR2-peptide complex was then affinity-purified on an anti-DNP HPLC column[34]. The yields of the purified complexes are listed in Table A2.1 in Appendix 2. Soluble DM was produced from stably transfected *Drosophila melanogaster*-derived S2 cells as described previously[9, 35].

FP Assay

Association of MBP-488 was monitored by FP as described previously[32]. The assay was performed in black polystyrene 384-well flat bottom plates (Corning, Corning, NY) with a nonbinding surface, and the reactions were protected from external light and evaporation with an aluminum foil seal (Excel Scientific, Wrightwood, CA) when the plate was not in the reader. The data were acquired using a Victor^{3}V plate reader (Perkin-Elmer Life Sciences) with 485/20 and 530/30 filter sets to track FP of the Alexa-488 (Invitrogen) label. Typically, the experiments were performed in citrate buffer (50 mm sodium citrate, 150 mm sodium chloride, pH 5.2) in a final volume of 40 μl. FP values were recorded at ambient temperature. The data were acquired from triplicate wells, and wells that contained only the fluorescent MBP-488 peptide were used to determine base-line FP values.

In experiments where FP was monitored in a cuvette, a QM-7 fluorometer was used (Photon Technology International, Lawrenceville NJ). DR2-MBP-P4* was UV-cleaved at the same conditions as above but 7.5-fold concentrated relative to the binding reaction. MBP-488 was added to a quartz cuvette containing 1300 μl of buffer, and the FP followed over time to generate a base line and stabilize the temperature to 20 °C before DR2 and DM addition. Photocleaved DR2 with or without DM was rapidly injected in a volume of 200 μl into the cuvette using a spring-loaded 200-μl Hamilton syringe (CR700-200, Hamilton Company, Reno, NV). A small opening in the cover of the reader allowed the injection to be performed while the FP was being measured. The reaction was under constant mixing with a magnetic stirrer. FP values were measured for 10 min after DR2 addition at a speed of 1 reading/s.

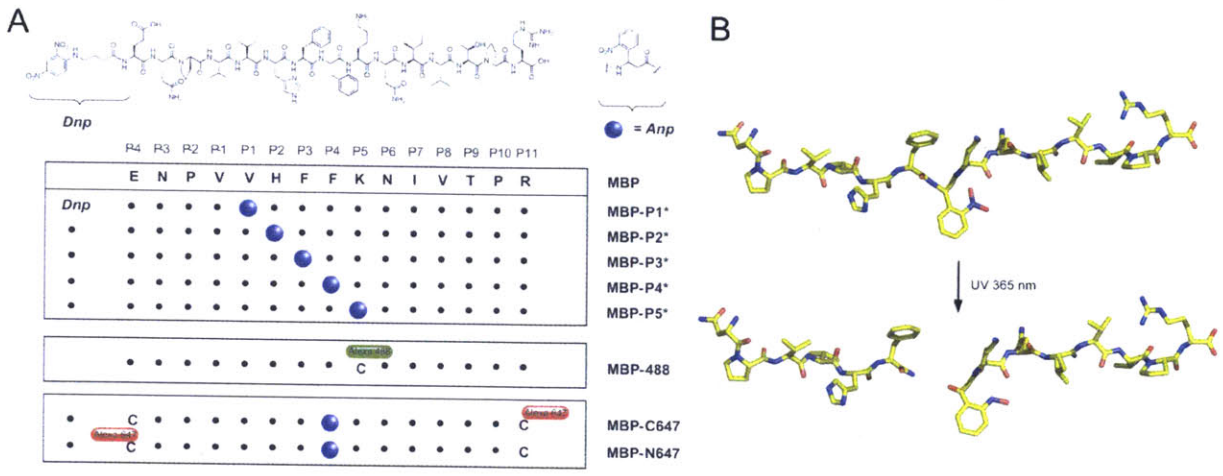

Figure 2.1. Design of photocleavable peptides. (**A**) Peptides based on the MBP_{85-99} sequence were synthesized to contain a nonproteinogenic amino acid (Anp, *blue circles*) that undergoes photocleavage when exposed to 365-nm UV light. MBP-488 is the reporter peptide used throughout, and it carries an Alexa-488 at the P5 Cys residue. MBP-C647 and MBP-N647 are peptides onto which Alexa-647 is appended C- or N-terminally to photocleavable MBP-P4* and were used to monitor the departure of cleavage fragments from DR2. (**B**) Model of MBP-P4* peptide and major cleavage products formed upon exposure to UV light. Cleavage occurs between the P3 and P4 positions, thus separating the major DR2 anchor residues (P1 Val and P4 Phe)[30].

Binding of Photocleavable Peptides to DR2

Freshly cleaved DR2-CLIP complex (final concentration 100 nm) and MBP-488 (final concentration 10 nm) were added to citrate buffer containing 1% octylglucoside. Photocleavable DNP-labeled peptides were added to these reactions at different concentrations (3-fold dilution

series, highest concentration of 250 μm) and incubated overnight at 37 °C. The amount of bound MBP-488 was then determined by FP, and the ability of the photocleavable peptides to compete for binding of MBP-488 to DR2 was compared with the MBP_{85-99} index peptide (Table A2.1).

Photocleavage and Exchange

In a typical experiment, a stock solution of DR2-MBP-P4* was deposited into several wells (maximum volume of 50 μl/well) of a 96-well V-bottom plate (Corning Inc., Corning, NY), placed on ice, and allowed to cool. In a separate 96-well plate (no UV control), the samples were shielded from UV light with aluminum foil but otherwise treated identically. The plates were then placed directly under a preheated UV lamp fitted with a UV source emitting at 365 nm (Blak Ray B100AP, UVP, Upland, CA). After 2-10 min of UV irradiation, the contents of wells were pooled (no signs of solvent evaporation were apparent at this point), and 30 μl were dispensed into appropriate wells of a 384-well plate, preloaded with MBP-488 alone or a mixture of DM and MBP-488. Following mixing, the 384-well plate was transferred to the FP reader. The FP values were measured at regular intervals, and the data was collected in triplicate.

Separation of Empty DR2 Molecules from Cleavage Fragments

DR2-MBP-P4* was photocleaved at a concentration of 3 μm as described above. 1 ml of the photocleaved product was loaded onto a HPLC gel filtration column (Superose 6) with 50 mm sodium citrate, 150 mm sodium chloride, pH 5.2, as the mobile phase to separate free peptide fragments from empty DR2 molecules. The protein concentration in collected fractions was determined using the Coomassie Plus protein assay reagent (Pierce). The purified molecules

were then assayed by FP for their ability to bind MBP-488. In each experiment, the purification and reaction set-up time required 1.5-2 h starting at the end of photocleavage.

2.4 Results

2.4.1 Design and Properties of Photocleavable Peptide Ligands

The structure of DR2 complexed with the MBP_{85-99} peptide[30] served as the point of departure for the design of photocleavable ligands. We applied the strategy first described by Schumacher and co-workers[29] for Class I MHC products and synthesized peptides that contained an Anp residue at the indicated positions (Fig. 2.1A). Peptide binding to Class II MHC molecules is stabilized by cooperative hydrogen bond networks and anchor residues nestled deep into the peptide-binding groove[36]. A panel of peptides was synthesized that placed the Anp residue between the known anchor residues Val_{89} (P1) and Phe92 (P4) and critical hydrogen bonds such that, upon cleavage, two fragments would be generated, neither of which was expected to fulfill the criteria for strong binding on its own. We refer to Class II MHC molecules loaded with a photocleavable ligand as caged Class II MHC products. The peptides (MBP-P1* to MBP-P5*) were further fitted with a DNP group through a 4-aminobutyric acid spacer to allow affinity purification of the properly loaded DR2 complex. A model based on the crystal structure of MBP_{85-99} illustrates the close proximity of the nitro-substituent on the aromatic ring to the backbone of MBP-P4* (Fig. 2.1B), which accounts for the photochemical liberation of the N-terminal amide and C-terminal nitroso-fragments at the relatively long wavelength of 365 nm, at which proteins are essentially transparent.

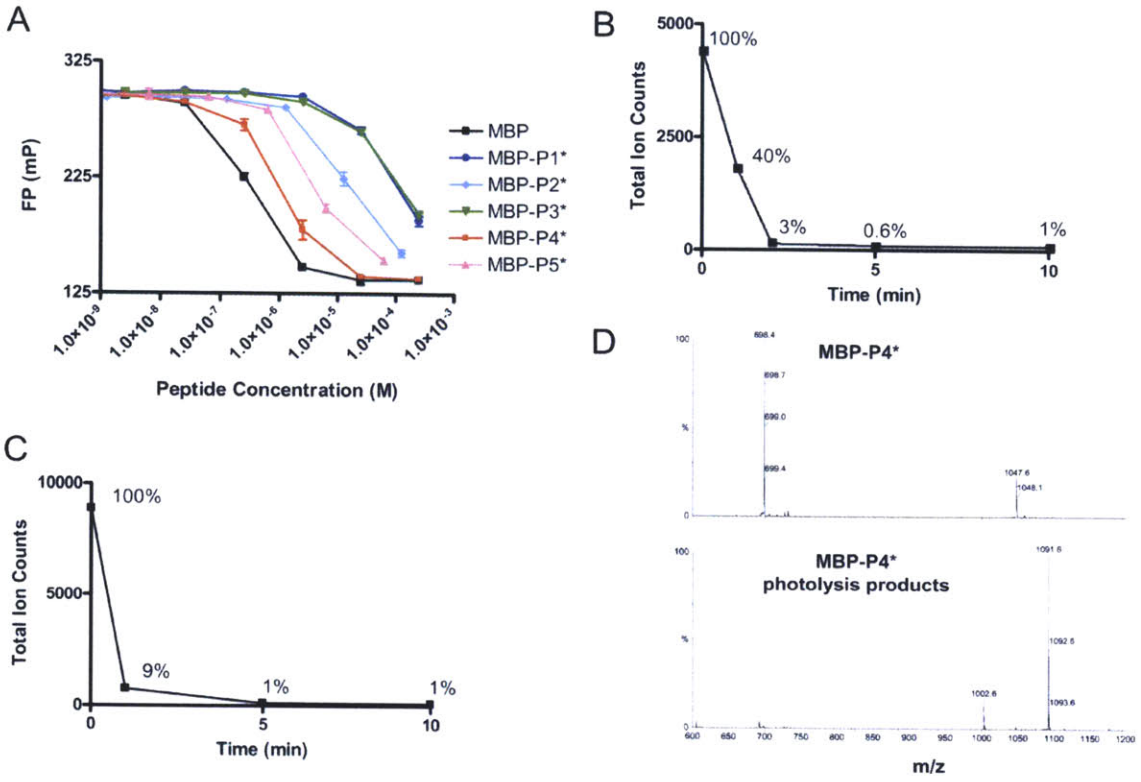

Figure 2.2. Affinity of photocleavable peptides for DR2 and kinetics of MBP-P4* cleavage. (**A**) Photocleavable peptides MBP-P1* to MBP-P5* were examined for their ability to compete with MBP-488 (10 nm) for DR2 binding (100 nm). MBP-P4* bound most tightly. (**B**) and (**C**) Photocleavage of MBP-P4* was rapid both in solution or bound to DR2. (**D**) Mass spectrometry of intact peptide (*top panel*, 2+ and 3+ ions) and photocleaved peptide (*bottom panel*, 1+ ions) showing major cleavage products of molecular weights 1002.6 (C-terminal fragment) and 1091.6 (N-terminal fragment).

2.4.2 Affinity of the Peptide Ligands for DR2 and Efficiency of Photocleavage

The peptide ligands were next used to generate complexes with DR2. A Chinese hamster ovary cell-derived DR2 preparation, in which the CLIP peptide was attached covalently to the DR2 β-chain, was exposed to thrombin, upon which the CLIP peptide could be readily exchanged in

DM-independent fashion for other ligands. To avoid confounding effects of a mixture of DR2 loaded with MBP-P4*, DR2-CLIP, and empty DR2, a DNP moiety installed at the N terminus of the photocleavable peptide was used for retrieval of the correspondingly loaded DR2 molecules on an anti-DNP affinity matrix. This final purification step ensured that all DR2 molecules used as input for subsequent reactions were occupied homogeneously with the photocleavable peptide. We identified one MBP-derived ligand, MBP-P4*, for which the caged DR2 complex could be obtained in yields comparable with the DR2-MBP_{85-99} complex. The affinity of DR2 binding by photocleavable ligands (MBP-P1* to MBP-P5*) was explored by means of a competition assay (Fig. 2.2A and Table A2.1), confirming that the substitution of Phe92 of the MBP_{85-99} peptide (the P4 anchor in context of DR2) for Anp least affected the affinity (3-fold) for DR2. Therefore, the caged complex that contained MBP-P4*, which most closely matched the affinity of the MBP_{85-99} index peptide for DR2, was chosen as substrate for peptide exchange reactions in the following experiments.

Each of the photocleavable peptides was examined individually for its ability to undergo chromatic cleavage. Electron spray ionization mass spectroscopy was used to follow the disappearance of the dominant triple-charged ion species of the parent peptide. In the representative case of MBP-P4* (Fig. 2.2B), photocleavage was largely complete after 2 min of irradiation. Photocleavage proceeded with similar efficiency when the peptide was bound to DR2 (Fig. 2.2C). In addition to the expected reaction products of UV fragmentation that were identified with certainty (Fig. 2.2D), electron spray ionization mass spectroscopy as well as MALDI-TOF spectra showed several additional unidentified cleavage products, whereas the index MBP_{85-99} peptide was unaffected by UV irradiation (data not shown).

2.4.3 Functional Properties of DR2 Molecules Synchronously Liberated from Bound Peptide

The ability to quickly arrive at an empty state allowed us to examine the association of peptides with Class II MHC and revisit the role of DM in peptide loading. This method differs significantly from published procedures that use refolded empty Class II MHC as a starting point[37, 38]. Such preparations contain a mixture of species that actively bind peptide, that slowly convert to an active form, or that are inactive. Furthermore, the conformations that may be accessed by a properly loaded Class II MHC molecule upon loss of its peptide ligand may well differ from those of Class II MHC products generated in the complete absence of a ligand.

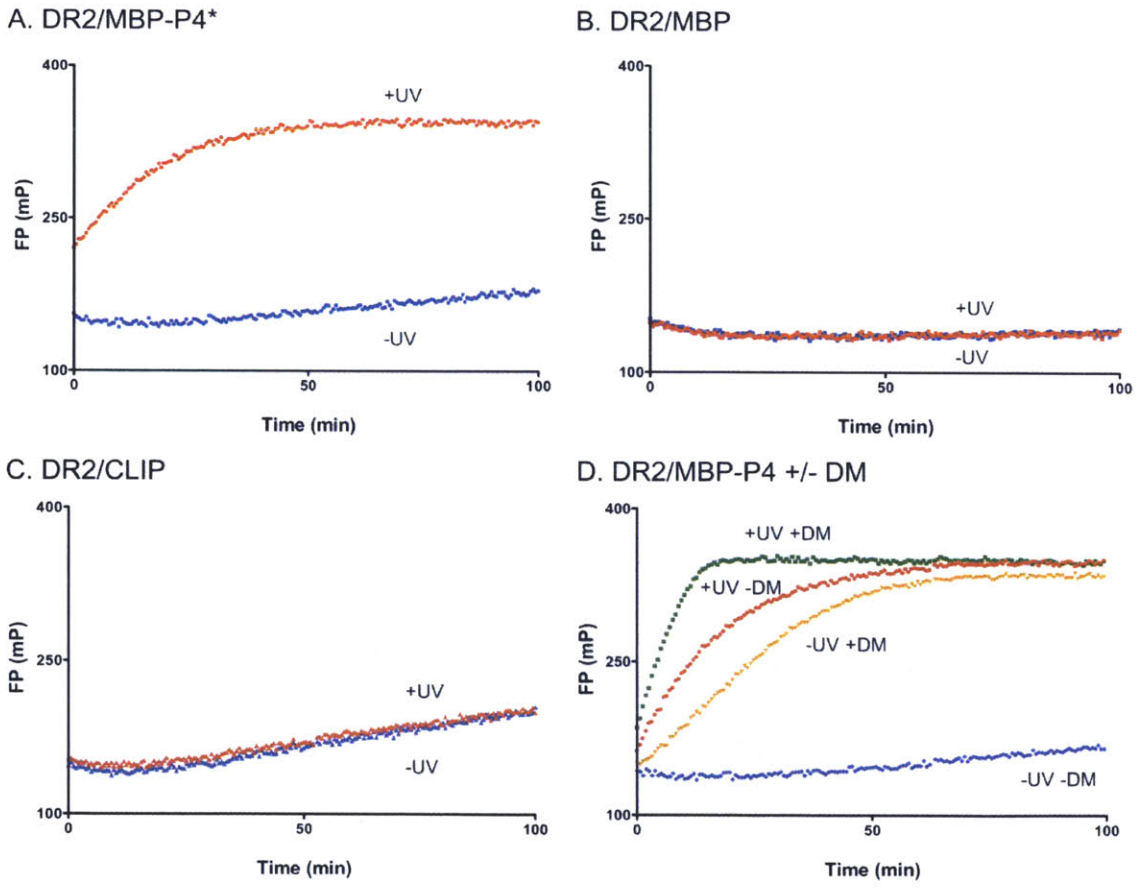

Figure 2.3. Rapid binding of peptide to DR2 following photocleavage of MBP-P4*. Different DR2-peptide complexes (150 nm) were left unilluminated (*-UV*) or exposed to UV light (*+UV*) in the presence of MBP-488 (30 nm) for 2 min. Association of MBP-488 was followed by FP after photocleavage. **(A)** Rapid association of MBP-488 occurs upon UV irradiation of DR2-MBP-P4*, but not in control reactions. **(B)** and **(C)** High affinity MBP_{85-99} peptide could not be displaced **(B)** and slow binding to DR2 molecules with the lower affinity CLIP peptide **(C)** was observed. **(D)** The rate of MBP-488 association was compared for reactions with and without DM. DM was present during photocleavage at an equimolar concentration to DR2, and MBP-488 was added after photocleavage.

Tracking of early stages of peptide association was important for examining the functional properties of DR2 molecules immediately following photocleavage of MBP-P4*. We used an Alexa-488-labeled version of the MBP_{85-99} peptide (MBP-488, Fig. 2.1A) as a fluorescent reporter peptide in the FP assay. In the absence of UV irradiation, the DR2-MBP_{85-99} complex was stable (Fig. 2.3B), showing no evidence for peptide exchange over the time course followed. The DR2-CLIP complex was less stable, with a slow increase in FP values over the 100-min observation window (Fig. 2.3C). In the absence of UV irradiation, the DR2-MBP-P4* complex showed peptide exchange behavior intermediate to that of the DR2-MBP_{85-99} and DR2-CLIP complexes (Fig. 2.3A, *blue curve*), consistent with their affinity rank order (MBP > MBP-P4* > CLIP).

When the identical assay was performed upon UV irradiation, neither peptide binding to the preformed DR2-CLIP nor to the DR2-MBP_{85-99} complex was affected. In contrast, we observed a steep increase in peptide association for the DR2-MBP-P4* complex upon UV exposure (Fig.

2.3A, *red curve*). In this experiment, the MBP-488 reporter peptide was included *during* photocleavage, and the reaction had already proceeded significantly when the first data points could be recorded, even though photocleavage was performed for 2 min on ice. Therefore, in the absence of DM, rapid peptide association occurs to what we propose are newly vacated DR2 molecules.

We then assessed the potential contribution of DM to MBP-488 association following photocleavage of the bound peptide. DM was added before photocleavage at an equimolar concentration relative to DR2 (150 nm), and MBP-488 was then added to measure peptide association. As shown above, the peptide binding reaction proceeded rapidly following photocleavage in the absence of DM, but DM further accelerated the rate of peptide association (Fig. 2.3D). There may be several explanations for this DM-dependent increase in the kinetics of peptide association: removal of residual uncleaved MBP-P4*, removal of cleavage fragments from the peptide-binding site, or, alternatively, a direct contribution of DM to peptide association.

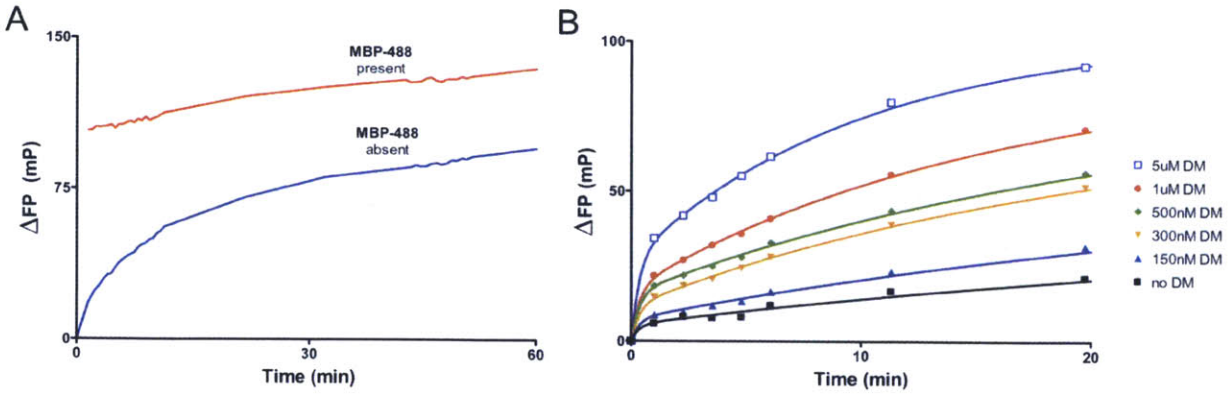

Figure 2.4. Photocleavage generates labile, short-lived DR species that rapidly bind peptide. (**A**) DR2-MBP-P4* (160 nm) was photocleaved for 10 min on ice in the presence (*red line*) or absence (*blue line*) of MBP-488 (220 nm). When peptide was present during photocleavage, the reaction proceeded rapidly (10 min on ice) to ~100 mP, whereas peptide association was slower when the peptide was added following photocleavage (<100 FP after 50 min). Time 0 is defined by the addition of MBP-488 following photocleavage (*blue line*). (**B**) Dose-dependent acceleration of peptide association to empty DR2. DM was present at different concentrations (150 nm to 5 μm) during photocleavage (10 min, 160 nm DR2-MBP-P4*), and MBP-488 was added (330 nm) after photocleavage. Saturation was not observed because of the lower affinity of soluble DM for soluble DR compared with full-length molecules[42].

2.4.4 The DR2 Conformer Created by Peptide Photocleavage Is Short-lived

Mass spectrometry showed that DR2-bound MBP-P4* was cleaved at a rate similar to that of free MBP-P4* (Fig. 2.2, B and C), and incomplete cleavage could thus not account for the increased rate of peptide association in the presence of DM. Acceleration of peptide association was observed even when photocleavage was extended to 10 min (Fig. 2.4B). Extension of photocleavage also demonstrated that the peptide-receptive DR2 conformer created by photocleavage was short-lived (Fig. 2.4A). During UV cleavage, significant quantities of MBP-488 rapidly bound to uncaged DR2 (Fig. 2.4A). In contrast, the reaction kinetics were substantially different when MBP-P4* was photocleaved in the absence of MBP-488. More than 50 min at a more favorable temperature (room temperature) were required to reach 100 mP, a reading reached in less than 10 min on ice when MBP-488 was available in the course of photocleavage in slight molar excess (220 nm MBP-488 to 160 nm DR2). Photolysis of MBP-

P4* thus creates a peptide-receptive intermediate of DR2. This critical conformer is short-lived and converts to other species that bind peptide with substantially slower kinetics.

2.4.5 DM Forms a Complex with Empty DR That Maintains Rapid Peptide Binding Properties over Extended Periods of Time

In the absence of DM, the initial rate of MBP-488 binding was slower when the photocleavage time was extended from 2 to 10 min (compare Fig. 2.3D and Fig. 2.4B). When DM was present *during* the 10-min photocleavage period, peptide binding was more rapid. Association kinetics of MBP-488 were dependent on the DM concentration (Fig. 2.4B), consistent with the modest affinity of soluble DM for DR[39]. Only a fraction of DR molecules would be expected to be bound to DM at a given time at the DM concentrations used here.

To assess the effect of DM on the very early phase of the reaction, we used a cuvette-based system in which FP values could be tracked continuously. The reaction was initiated by the addition of DR2 and DM to a cuvette already containing MBP-488. Although DM clearly accelerated peptide association when added *following* photocleavage, a substantial initial burst of peptide binding was seen only when DM was present *during* photocleavage (Fig. 2.5A). We infer that formation of the DM-empty DR peptide-loading complex in this experimental setting is optimal when DR molecules have just lost their peptide.

How stable is the DM-empty DR peptide-loading complex? We uncaged DR2 molecules in the absence of DM, added DM, and then assessed peptide binding upon delayed addition of the MBP-488 peptide (Fig. 2.5B). DR2 molecules progressively lost activity with longer incubation times in the absence of DM, and only slow kinetics of peptide association were observed with

10-min to 2-h delays following photocleavage (Fig. 2.5B). In contrast, the rapid peptide binding properties of the DM-DR complex were maintained even with prolonged incubation times prior to the addition of peptide (11 min to 2 h) (Fig. 2.5B). The observed differences are inconsistent with the interpretation that DM merely removes residual uncleaved MBP peptide from DR2. Mass spectrometry shows that the vast majority of MBP-P4* is photocleaved even when bound to DR2. Maintenance of the rapid peptide binding properties of the DM-DR complex over extended periods of time is a remarkable trait in view of the rapid decay of active DR in the absence of DM.

2.4.6 The Contribution of DM to Peptide Association Is Not Due to Cleavage Fragments

Could retention of the peptide cleavage fragments affect the results of peptide binding measurements? We considered this explanation unlikely, given the strategic placement of the photocleavage site in the center of the peptide. We nevertheless designed three experiments to directly address this issue. We separated empty DR2 molecules from cleavage fragments by size exclusion chromatography and confirmed removal of fragments by monitoring absorbance of the DNP tag (350 nm) and mass spectroscopy (data not shown). We then compared the contribution of DM to peptide binding (Fig. 2.6, A and B) and obtained comparable results. Could the add-back of cleavage fragments affect the kinetics of peptide association in the presence or absence of DM? Even at a concentration equimolar to DR2 (150 nm), cleavage fragments did not affect the kinetics of peptide association in the presence or absence of DM and regardless of DR:DM ratios (Fig. 2.6, C and D). We conclude that the reaction is primarily dependent on the concentration of DM because of its low affinity for soluble DR2.

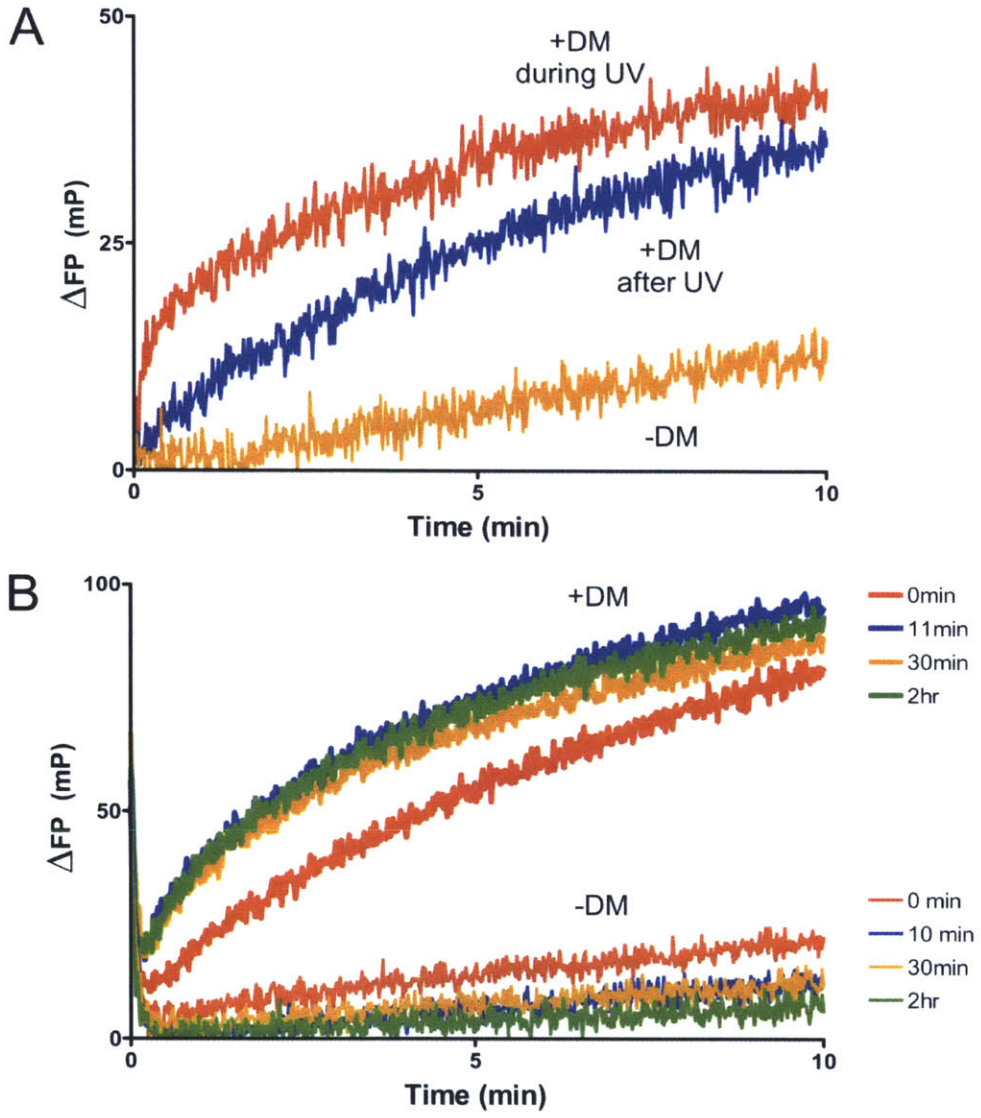

Figure 2.5. Analysis of early, rapid binding events. (**A**) Photocleaved DR2-MBP-P4* (160 nm) ± DM (160 nm) was injected into a cuvette containing 220 nm MBP-488 to monitor the early stages of the peptide binding reaction by FP, immediately upon the addition of DR2. When DM was present during photocleavage, a rapid burst of binding was observed. The rate of MBP-488 association was intermediate when DM was added following photocleavage. Association in the absence of DM was slower. (**B**) Incubation of DM with empty DR2 restores and maintains the highly active DR2 conformer. DR2-MBP-P4* was photocleaved for 10 min in the absence of

DM. Association of MBP-488 was then compared between reactions with or without DM (1 μm). After different preincubation times (0-2 h), the DR/DM mix or DR alone was injected into a cuvette containing 50 nm MBP-488, and the FP values were monitored continuously.

Finally, we synthesized two peptide derivatives based on the MBP-P4* peptide, but onto which an Alexa-647 fluorophore was installed at a single Cys residue either at the N or C terminus of the photocleavable peptide (Fig. 2.1A, MBP-N647 and MBP-C647, respectively). Without UV treatment, the complexes containing MBP-N647 and MBP-C647 were stable for at least 100 min (Fig. A2.1). Upon UV irradiation the decrease in FP is biphasic, with a rapid initial phase that cannot be captured because irradiation and FP measurements must necessarily be conducted in two different geometries. As soon as measurements can be made, the FP signal has already reached nearly plateau levels, with only a slow decay phase that follows for both MBP-N647 and MBP-C647 (Fig. A2.1A). In the same experiment, the association of MBP-488 was recorded. The low FP signal in the 488-nm channel in the absence of UV cleavage indicates that DR2 is firmly loaded with either MBP-N647 or MBP-C647, neither of which are displaced by the mere addition of free MBP-488 (Fig. A2.1B in Appendix 2). Photolysis of these caged MHC molecules enables the loading of MBP-488 in a single phase kinetic fashion. Cleavage of the caged DR2 complex is therefore rapid, and retention of both N- and C-terminal fragments is significantly less than association of MBP-488 with DR2. DM-dependent removal of cleavage products therefore does not appear to be a rate-determining factor for MBP-488 binding.

Displacement of MBP-N647 and MBP-C647 by the addition of DM alone, in the absence of UV irradiation (Fig. A2.1*C*) shows the expected acceleration of exchange for MBP-C647 (compare with Fig. 2.3D). However, the DR2-MBP-N647 is less responsive to inclusion of DM. This

suggests that the presence of the fluorophore at the N terminus of the photocleavable peptide may sterically hinder access of DM[20], whereas a C-terminal addition of a fluorophore does not.

2.4.7 Experimental Observations Are Integrated by a Mathematical Model of the Kinetic Processes

For a deeper mechanistic understanding of the role of DM in facilitating peptide association, we developed mathematical models of the pertinent processes (Fig. 2.7) to fit our experimental observations. Our kinetic data obtained with and without DM can be used to examine the veracity of plausible models for the role of DM after peptide is released from the MHC-binding pocket upon UV irradiation. We developed mathematical models for different hypotheses, and calculations showed whether they do or do not compare well with the experimental data. This allowed us to eliminate certain models from further consideration and led us to a plausible model for how DM may function post-peptide removal. We began by considering whether the following hypothesis could fit the kinetic data when no DM was added during UV irradiation,

$$p\text{MHC} \xrightarrow{k7} p^{*}\text{MHC} \xrightarrow{k8} e\text{MHC} \xrightarrow{k2} fp\text{MHC} \quad \text{(Equation 2.1)}$$

where pMHC is the peptide-loaded DR, p^{*}MHC is the species with the peptide photocleaved, eMHC is the empty DR molecule, and fpMHC is DR loaded with the peptide present in solution. The quantities labeled as k_i are the rate coefficients characterizing the kinetics of the corresponding reactions. Ordinary differential equations describing the kinetics of this simple pathway were then developed (see Appendix 2). A nonlinear regression scheme available as part of the MATLAB suite of programs was used to fit the kinetic constants in this model to the

experimental data. This hypothesis could not fit the experimental data (not shown) because it cannot account for the second slow phase of peptide binding.

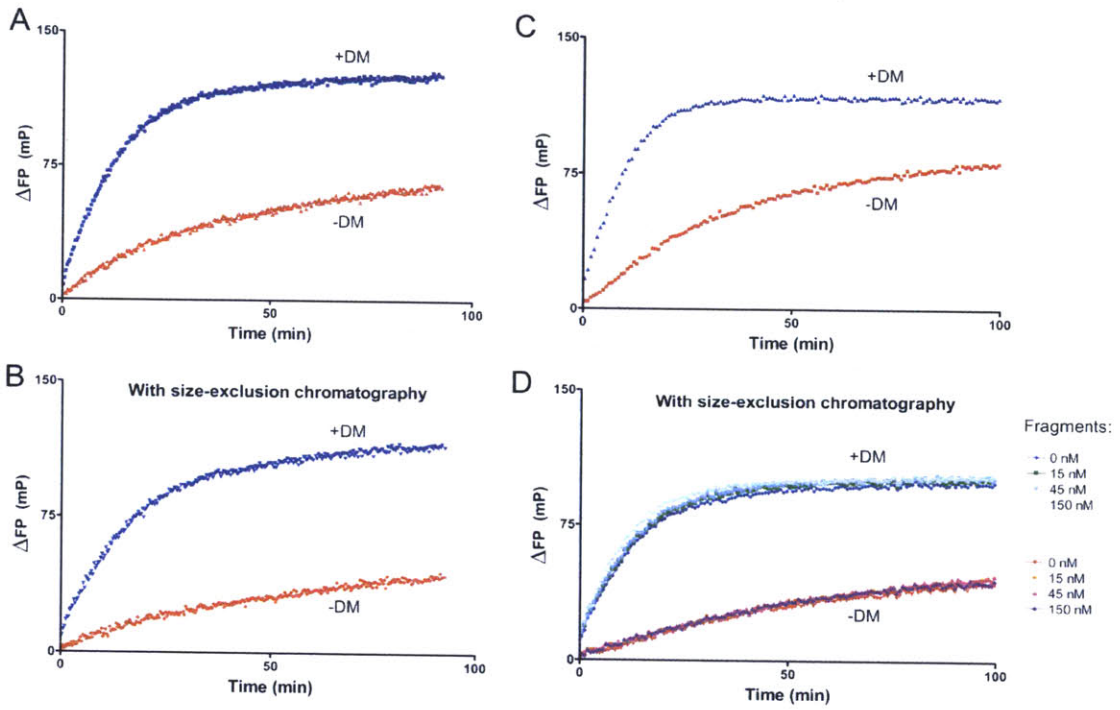

Figure 2.6. Peptide cleavage fragments do not account for DM contribution to peptide association. DR2-MBP-P4* was photocleaved for 5 min, and peptide fragments were removed from DR2 on a HPLC gel filtration column. **(A)** and **(B)** The contribution of DM (1 μm) to the kinetics of MBP-488 (1 μm) association was compared between reactions with photocleaved DR2-MBP-P4* (1 μm) from which cleavage fragments had been removed **(B)** or not removed **(A)** by Superose 6 size exclusion chromatography. **(C)** and **(D)** Cleavage fragments added back at different concentrations **(D)** were without effect on reactions with DR2 molecules not subjected to gel filtration **(C)** at concentrations of 150 nm DR2-MBP-P4*, 150 nm MBP-488, and 1 μm DM. **(D)** Photocleaved peptide fragments were added back at concentrations ranging from 15 nm to 150 nm (DR2 at 150 nm) following purification of DR2 by size exclusion

chromatography. The cleavage fragments also did not affect association of MBP-488 in the absence of DM (*-DM*).

This is not surprising, because this hypothesis does not account for the fact that DR can unfold or aggregate to form species that are not receptive to peptide binding. Thus, we examined the following hypothesis, which includes this feature.

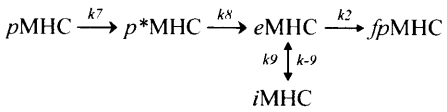

(Equation 2.2)

The symbols are the same as before, except that *i*MHC denotes the inactive conformer or aggregates of DR. It does not make sense to treat aggregates and unfolded conformers of DR as separate species because our experimental data cannot distinguish these species. Fitting this model to the experimental data without DM yields excellent fits as seen in Fig. 2.7B. The best fit parameter values were determined to be: $k_2 = 9.92 \times 10^{-5}$ nm^{-1} min^{-1}, $k_7 = 1.00$ min^{-1}, $k_8 = 1.00$ min^{-1}, $k_9 = 1.24 \times 10^{-4}$ nm^{-1} min^{-1}, $k_{-9} = 1.39 \times 10^{-4}$ min^{-1}, and $n = 2$. n is the effective number of MHC molecules involved in the inactive form. A wide range of k_9, k_{-9}, and n values are capable of producing the same quality of fit. This emphasizes that the experimental data cannot distinguish between unfolding ($n = 1$) and aggregation ($n > 1$). The model is quite sensitive to the value of k_2, because a value very close to 9.00×10^{-5} nm^{-1} min^{-1} is necessary to capture the behavior at the initial times.

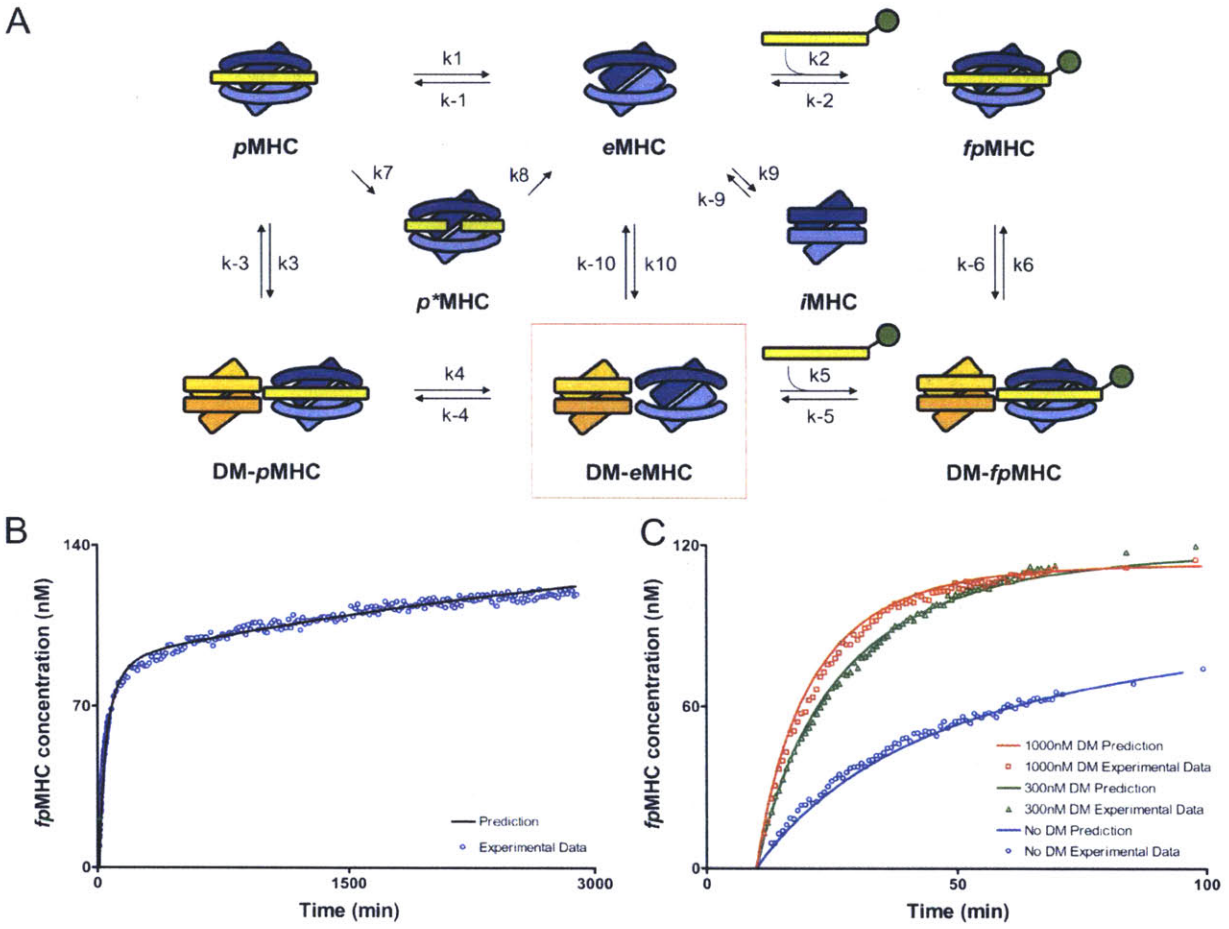

Figure 2.7. Model showing the rate constants used in mathematical models of peptide loading in the presence and absence of DM. **(A)** Peptide-loaded MHC (*pMHC*), empty MHC (*eMHC*), and fluorescent peptide-loaded MHC (*fpMHC*) are shown in the absence of DM (*top row*) and interacting with DM (*bottom row*). Peptide photocleavage creates a short-lived MHC molecule with bound cleavage fragments (p^*MHC), whereas incubation in the absence of peptide creates an inactive form (*iMHC*). *e*MHC remains in a peptide-receptive form only for short periods of time, but *e*MHC bound in the DM-*e*MHC complex (*boxed*) remains active for extended periods of time. **(B)** The hypothesis represented by Equation 2.2 fits the experimental data without DM very well. The initial concentration of *p*MHC was 150 nm, and the amount of MBP-488 added

after 10 min of UV was 200 nm. (**C**) The model represented by Equation 2.3 fits the experimental data well in the presence of variable amounts of DM. The initial concentration of *p*MHC was 150 nm, and the amount of MBP-488 added after 10 min of UV was 200 nm. DM addition occurred at the same time as MBP-488 addition. A summary of the concordance between experimental data and the kinetic model for conditions not shown here is provided in the supplemental information. Because of uncertainties associated with the length of time required to add MBP-488 and to take the first reading, it was assumed that 30 s elapsed during this process for all DM experiments. Because the no DM data were read last, it was assumed that 2 min elapsed before the first reading. The values of the delay times were chosen to improve the quality of the fit. We also carried out the analyses assuming that the elapsed times were negligible. None of the qualitative conclusions changed upon making this assumption; only the quantitative comparisons with experimental data were less precise at short times.

Thus, we conclude that a key aspect of the mechanism is that the aggregated/unfolded DR molecules can slowly revert to the active conformer when peptide is present in excess. This is the origin of the second slow phase of peptide uptake in the data shown in Fig. 2.3D.

The kinetic parameters obtained by fitting this model (Equation 2.2) to the data without DM reflect reactive processes that should proceed in the same way if DM is added. So, we then fixed the values of these parameters to those described above and considered a model for the additional processes that can occur when DM is added. Our experimental findings showed that DM can restore a DR conformer that is peptide-receptive, and we model this by positing that DM binds DR molecules to create a species that can bind peptides. Then, by fitting the experimental data to the following model that includes these processes, we asked whether the DM-bound DR

molecules could bind peptides more or less rapidly than the empty receptive DR molecules in the absence of DM.

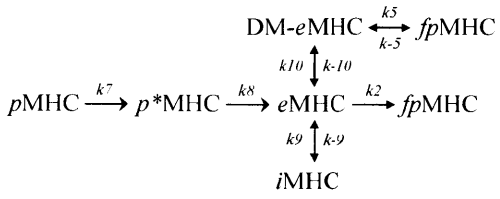

(Equation 2.3)

The model represented by Equation 2.3 fits the experimental data well in the presence of variable amounts of DM (Fig. 2.7C). The parameters, k_2, k_7, k_8, k_9, k_{-9}, and n, were kept constant at values determined previously (Fig. 2.7B), and the new parameters fit the data best for the following values: $k_5 = 5.62 \times 10^{-4}$ nm^{-1} min^{-1}, $k_{-5} = 6.65 \times 10^{-6}$ nm^{-1} min^{-1}, $k_{10} = 0.59$ nm^{-1} min^{-1}, and $k_{-10} = 177.57$ min^{-1}. Multiple combinations of parameter values are capable of producing the same fit; however, k_5 must be at least two times greater than k_2 to capture the observed experimental behavior. We also studied a model where DM could also bind to the inactive form of DR (iMHC) directly and create a stabilized peptide-receptive form. Even in this model, the experimental data can be fit only if k_5 is greater than k_2. Thus, it appears that DM-bound DR molecules bind peptide more rapidly than the receptive conformer of DR alone.

Of course, we are aware that our parameter sensitivity analysis and the space of models we have explored are not exhaustive. Nevertheless, the experimental data and the values of parameters obtained from the kinetic analyses suggest the following mechanistic picture. DM binds DR to stabilize it from unfolding and aggregating. The binding also probably leads to a conformational change in DR. The resulting conformation may be very favorable for peptide binding to the DR groove because it stabilizes the corresponding transition state. This may underlie the faster rate

of peptide binding to the DM-stabilized DR compared with the receptive state of DR alone because peptide binding to the latter may proceed via an induced fit mechanism with associated free energy costs that are no longer relevant for DM-bound DR.

2.5 Discussion

Peptide binding may at first glance appear to be a rather simple process, in which a peptide interacts with an available Class II MHC site. Closer inspection reveals the presence of multiple distinct species of different behavior and stability[12, 26, 40]: (i) stable DR-peptide complexes from which peptides dissociate at very slow rates (half-life of days to weeks); (ii) a transition state induced by DM from which peptide dissociates rapidly; (iii) a labile empty DR conformer that rapidly binds peptide, but is short-lived; (iv) inactive and aggregated forms; and (v) DM-bound empty DR molecules that are stable and bind peptide rapidly.

Two different models of DM action have been proposed: either DM interacts with both empty and peptide-loaded species[27, 28] or only with peptide-loaded Class II MHC molecules[26]. Pulse-chase experiments demonstrated a transient association of DR with DM. When invariant chain degradation was blocked by leupeptin, DM could be retrieved in complex with DR molecules together with a 21-kDa N-terminal fragment of the invariant chain. Furthermore, immunoprecipitation experiments showed that purified DM binds to DR/CLIP[27]. Mass spectrometry-based analysis of bound peptides demonstrated that DM-DR complexes immunopurified from cells were largely devoid of peptides, suggesting that DM continues to interact with DR molecules following peptide dissociation. Furthermore, the presence of DM prevented aggregation of DR molecules at acidic pH. DM was therefore proposed to act as a chaperone that prevents inactivation of empty DR molecules[28]. More recent experiments showed

that DM interacts only with peptide-filled DR molecules and that DM catalyzes peptide exchange by facilitating a conformational change in the peptide-binding complex. This study[26] utilized empty DR molecules refolded from *Escherichia coli* inclusion bodies in the absence of peptide. DM had little or no effect on the conversion between peptide-receptive and -averse DR or on the rapid bimolecular binding reaction between empty DR and free peptide. The stabilization observed previously was attributed to an effect on the peptide binding reaction. DM would prevent inactivation indirectly through catalysis of productive binding in a reaction that competes with inactivation[26].

The dissection of key steps in peptide binding thus requires approaches with which critical, short-lived intermediates can be generated rapidly and synchronously. We created caged Class II MHC molecules from which peptide could be rapidly removed. Chinese hamster ovary cell-produced soluble DR2 molecules were converted, in DM-independent fashion, into DR2 complexes with photocleavable peptide and purified by means of an affinity tag attached to the peptide. This approach ensured that the input population of DR2 molecules was homogeneous with respect to peptide occupancy and ruled out DM contamination of the reactants. With the photocleavable Anp amino acid replacing the Phe92 residue at the P4 anchor position, MBP-P4* retained the highest affinity for DR2. This is a relatively minor change in the overall peptide topology, because the aromatic character of the amino acid side chain is preserved, and the P4 pocket is sufficiently large to accommodate a nitro-substituent on the phenyl side chain. When UV-irradiated, the caged complex is quickly converted into an uncaged peptide-receptive DR2 species. The peptide fragments themselves have negligible affinity for DR2, based on experiments that made use of N- or C-terminally derivatized peptides (MBP-C647 and MBP-N647), in which the departure of both of the anticipated cleavage products was monitored

independently (Fig. A2.1) or when MBP-P4* fragments were added back to empty DR2 purified by size exclusion chromatography (Fig. 2.6D). The cleavage fragments had no effect on the progression of binding of MBP-488 to empty DR2, neither in the presence nor in the absence of DM.

Comparison of peptide binding reactions under different conditions allowed us to identify key factors that determined the magnitude of the DM contribution to peptide association. Acceleration of peptide association by DM was most pronounced with delayed addition of DM, such as experiments in which DM was added following photocleavage (Fig. 2.4), the duration of photolysis was extended from 2 to 10 min in the absence of DM (Fig. 2.5B), or cleavage fragments were removed by gel filtration chromatography (Fig. 2.6D). Thus, DM not only stabilizes an active, peptide-receptive DR2 conformer, but it can also restore such a conformer when the DR molecule lacks contact with peptide for extended periods of time. Restoration of the active conformation of DR by DM may be explained by two mechanisms: DM may bind to multiple DR species and cause the transition from a less active conformer to the active form, or it may bind to active DR species that are short-lived in its absence and indirectly favor the equilibrium toward the active conformer. Particularly notable in these experiments is that reactions with and without DM did not reach the same equilibrium, indicating that a substantial fraction of DR2 molecules is lost to the competing inactivation/aggregation reaction when the active conformer is not restored and maintained by DM. In the presence of DM, the active conformer is stable because near identical peptide association kinetics were observed when peptide addition was delayed for 2 h compared with reactions in which peptide was added directly after photocleavage (Fig. 2.5B).

Could the observed DM contribution be due to the removal of residual intact peptide or even cleavage fragments from the binding site? The following findings argue against this explanation: (i) Mass spectrometry demonstrated rapid cleavage of MBP-P4*, regardless of whether it was free in solution or DR2-bound. (ii) Monitoring of the DNP group based on its unique absorbance at 350 nm during separation of DR2 from cleavage fragments by size demonstrated removal of DNP-tagged peptide. (iii) The FP method measures the fraction of peptide that is DR2-bound *versus* peptide that remains free in solution. At equimolar quantities of peptide and DR, substantial changes in FP thus only occur when a considerable fraction of DR2 molecules bind peptide. (iv) The DM contribution to peptide association is more pronounced with longer photolysis times. If acceleration of peptide association were due to removal of residual peptide or peptide fragments, this effect should be diminished by longer photolysis times.

This study resolves the controversy of whether DM acts only on peptide-loaded DR species[26] or whether it also acts as a chaperone that stabilizes empty DR molecules[27, 28]. We demonstrate that DM forms a complex with empty DR molecules that binds peptide with faster kinetics than DR molecules that just lost their peptide cargo, indicating that DM plays an important role in the peptide association stage. The differences in the conclusions reached by Zarutskie *et al.*[26] and this study are probably related to the DR preparations that were utilized. Zarutskie *et al.*[26] utilized empty DR1 molecules refolded in the absence of peptide from *E. coli* inclusion bodies. The majority of these refolded molecules (~95%) are in a peptide nonreceptive state, apparently resistant to the action of DM. In contrast, newly vacated DR molecules maintain the ability to interact with DM for at least some time.

We propose that DM forms a peptide-loading complex with empty DR that plays an important role in rapid peptide capture. Peptides are short-lived in cells because of proteolytic attack[41], and rapid binding may be essential for display of a diverse array of peptides, many of which contain cleavage sites for proteases present in the peptide-loading compartment.

2.6 References

1. Roche, P.A. and Cresswell, P. (1990) Invariant chain association with HLA-DR molecules inhibits immunogenic peptide binding. *Nature*, **345**, 615-618.

2. Bakke, O. and Dobberstein, B. (1990) MHC class II-associated invariant chain contains a sorting signal for endosomal compartments. *Cell*, **63**, 707-716.

3. Riberdy, J.M., Newcomb, J.R., Surman, M.J., Barbosa, J.A. and Cresswell, P. (1992) HLA-DR molecules from an antigen-processing mutant cell line are associated with invariant chain peptides. *Nature*, **360**, 474-477.

4. Ghosh, P., Amaya, M., Mellins, E., and Wiley, D. C. (1995) *Nature* **378**, 457-462.

5. Wu, S., and Gorski, J. (1996) *Mol. Immunol.* **33**, 371-377.

6. Denzin, L.K. and Cresswell, P. (1995) HLA-DM induces CLIP dissociation from MHC class II alpha beta dimers and facilitates peptide loading. *Cell*, **82**, 155-165.

7. Busch, R., Doebele, R.C., Patil, N.S., Pashine, A. and Mellins, E.D. (2000) Accessory molecules for MHC class II peptide loading. *Curr Opin Immunol*, **12**, 99-106.

8. Busch, R., Rinderknecht, C.H., Roh, S., Lee, A.W., Harding, J.J., Burster, T., Hornell, T.M. and Mellins, E.D. (2005) Achieving stability through editing and chaperoning: regulation of MHC class II peptide binding and expression. *Immunol Rev*, **207**, 242-260.

9. Sloan, V.S., Cameron, P., Porter, G., Gammon, M., Amaya, M., Mellins, E. and Zaller, D.M. (1995) Mediation by HLA-DM of dissociation of peptides from HLA-DR. *Nature*, **375**, 802-806.

10. Morris, P., Shaman, J., Attaya, M., Amaya, M., Goodman, S., Bergman, C., Monaco, J.J. and Mellins, E. (1994) An essential role for HLA-DM in antigen presentation by class II major histocompatibility molecules. *Nature*, **368**, 551-554.

11. Kropshofer, H., Vogt, A.B., Moldenhauer, G., Hammer, J., Blum, J.S. and Hammerling, G.J. (1996) Editing of the HLA-DR-peptide repertoire by HLA-DM. *Embo J*, **15**, 6144-6154.

12. Weber, D.A., Evavold, B.D. and Jensen, P.E. (1996) Enhanced dissociation of HLA-DR-bound peptides in the presence of HLA- DM. *Science*, **274**, 618-620.

13. Lich, J.D., Jayne, J.A., Zhou, D., Elliott, J.F. and Blum, J.S. (2003) Editing of an immunodominant epitope of glutamate decarboxylase by HLA-DM. *J Immunol*, **171**, 853-859.

14. Lovitch, S.B., Petzold, S.J. and Unanue, E.R. (2003) Cutting edge: H-2DM is responsible for the large differences in presentation among peptides selected by I-Ak during antigen processing. *J Immunol*, **171**, 2183-2186.

15. Nanda, N.K. and Sant, A.J. (2000) DM determines the cryptic and immunodominant fate of T cell epitopes. *J Exp Med*, **192**, 781-788.

16. Lazarski, C.A., Chaves, F.A. and Sant, A.J. (2006) The impact of DM on MHC class II-restricted antigen presentation can be altered by manipulation of MHC-peptide kinetic stability. *J Exp Med*, **203**, 1319-1328.

17. Katz, J.F., Stebbins, C., Appella, E. and Sant, A.J. (1996) Invariant chain and DM edit self-peptide presentation by major histocompatibility complex (MHC) class II molecules. *J Exp Med*, **184**, 1747-1753.

18. Fremont, D. H., Crawford, F., Marrack, P., Hendrickson, W. A., and Kappler, J. (1998) *Immunity* **9**, 385-393.

19. Mosyak, L., Zaller, D. M., and Wiley, D. C. (1998) *Immunity* **9**, 377-383.

20. Doebele, C.R., Busch, R., Scott, M.H., Pashine, A. and Mellins, D.E. (2000) Determination of the HLA-DM interaction site on HLA-DR molecules. *Immunity*, **13**, 517-527.

21. Pashine, A., Busch, R., Belmares, M. P., Munning, J. N., Doebele, R. C., Buckingham, M., Nolan, G. P., and Mellins, E. D. (2003) *Immunity* **19**, 183-192.

22. Narayan, K., Chou, C. L., Kim, A., Hartman, I. Z., Dalai, S., Khoruzhenko, S., and Sadegh-Nasseri, S. (2007) *Nat. Immunol.* **8**, 92-100.

23. Belmares, M. P., Busch, R., Wucherpfennig, K. W., McConnell, H. M., and Mellins, E. D. (2002) *J. Immunol.* **169**, 5109-5117.

24. Lanzavecchia, A., Reid, P. A., and Watts, C. (1992) *Nature* **357**, 249-252.

25. Joshi, R.V., Zarutskie, J.A. and Stern, L.J. (2000) A three-step kinetic mechanism for peptide binding to MHC class II proteins. *Biochemistry*, **39**, 3751-3762.

26. Zarutskie, J.A., Busch, R., Zavala-Ruiz, Z., Rushe, M., Mellins, E.D. and Stern, L.J. (2001) The kinetic basis of peptide exchange catalysis by HLA-DM. *Proc Natl Acad Sci U S A*, **98**, 12450-12455.

27. Denzin, L.K., Hammond, C. and Cresswell, P. (1996) HLA-DM interactions with intermediates in HLA-DR maturation and a role for HLA-DM in stabilizing empty HLA-DR molecules. *J Exp Med*, **184**, 2153-2165.

28. Kropshofer, H., Arndt, S.O., Moldenhauer, G., Hammerling, G.J. and Vogt, A.B. (1997) HLA-DM acts as a molecular chaperone and rescues empty HLA-DR molecules at lysosomal pH. *Immunity*, **6**, 293-302.

29. Toebes, M., Coccoris, M., Bins, A., Rodenko, B., Gomez, R., Nieuwkoop, N.J., van de Kasteele, W., Rimmelzwaan, G.F., Haanen, J.B., Ovaa, H. and Schumacher, T.N. (2006) Design and use of conditional MHC class I ligands. *Nat Med*, **12**, 246-251.

30. Smith, K.J., Pyrdol, J., Gauthier, L., Wiley, D.C. and Wucherpfennig, K.W. (1998) Crystal structure of HLA-DR2 (DRA*0101, DRB1*1501) complexed with a peptide from human myelin basic protein. *J Exp Med*, **188**, 1511-1520.

31. Wucherpfennig, K.W., Sette, A., Southwood, S., Oseroff, C., Matsui, M., Strominger, J.L. and Hafler, D.A. (1994) Structural requirements for binding of an immunodominant myelin basic protein peptide to DR2 isotypes and for its recognition by human T cell clones. *J Exp Med*, **179**, 279-290.

32. Nicholson, M.J., Moradi, B., Seth, N.P., Xing, X., Cuny, G.D., Stein, R.L. and Wucherpfennig, K.W. (2006) Small molecules that enhance the catalytic efficiency of HLA-DM. *J Immunol*, **176**, 4208-4220.

33. Cresswell, P., Ackerman, A.L., Giodini, A., Peaper, D.R. and Wearsch, P.A. (2005) Mechanisms of MHC class I-restricted antigen processing and cross-presentation. *Immunol Rev*, **207**, 145-157.

34. Day, C.L., Seth, N.P., Lucas, M., Appel, H., Gauthier, L., Lauer, G.M., Robbins, G.K., Szczepiorkowski, Z.M., Casson, D.R., Chung, R.T., Bell, S., Harcourt, G., Walker, B.D., Klenerman, P. and Wucherpfennig, K.W. (2003) Ex vivo analysis of human memory CD4 T cells specific for hepatitis C virus using MHC class II tetramers. *J Clin Invest*, **112**, 831-842.

35. Busch, R., Reich, Z., Zaller, D.M., Sloan, V. and Mellins, E.D. (1998) Secondary structure composition and pH-dependent conformational changes of soluble recombinant HLA-DM. *J Biol Chem*, **273**, 27557-27564.

36. Stern, L.J., Brown, J.H., Jardetzky, T.S., Gorga, J.C., Urban, R.G., Strominger, J.L. and Wiley, D.C. (1994) Crystal structure of the human class II MHC protein HLA-DR1 complexed with an influenza virus peptide. *Nature*, **368**, 215-221.

37. Altman, J.D., Reay, P.A. and Davis, M.M. (1993) Formation of functional peptide complexes of class II major histocompatibility complex proteins from subunits produced in Escherichia coli. *Proc Natl Acad Sci U S A*, **90**, 10330-10334.

38. Frayser, M., Sato, A.K., Xu, L. and Stern, L.J. (1999) Empty and peptide-loaded class II major histocompatibility complex proteins produced by expression in Escherichia coli and folding in vitro. *Protein Expr Purif*, **15**, 105-114.

39. Vogt, A.B., Kropshofer, H., Moldenhauer, G. and Hammerling, G.J. (1996) Kinetic analysis of peptide loading onto HLA-DR molecules mediated by HLA-DM. *Proc Natl Acad Sci U S A*, **93**, 9724-9729.

40. Rabinowitz, J.D., Vrljic, M., Kasson, P.M., Liang, M.N., Busch, R., Boniface, J.J., Davis, M.M. and McConnell, H.M. (1998) Formation of a highly peptide-receptive state of class II MHC. *Immunity*, **9**, 699-709.

41. Lennon-Dumenil, A.M., Bakker, A.H., Wolf-Bryant, P., Ploegh, H.L. and Lagaudriere-Gesbert, C. (2002) A closer look at proteolysis and MHC-class-II-restricted antigen presentation. *Curr Opin Immunol*, **14**, 15-21.

42. Weber, D.A., Dao, C.T., Jun, J., Wigal, J.L. and Jensen, P.E. (2001) Transmembrane domain-mediated colocalization of HLA-DM and HLA-DR is required for optimal HLA-DM catalytic activity. *J Immunol*, **167**, 5167-5174.

Chapter 3: Further Analysis of the Interaction of DM with pMHC

Portions reprinted from "HLA-DM captures partially empty HLA-DR molecures for caltalyzed removal of peptide" by Anne-Kathrin Anders, Melissa J. Call, Monika-Sarah E. D. Schulze, Kevin D. Fowler, David A. Schubert, Nilufer P. Seth, Eric J. Sundberg, and Kai W. Wucherpfennig, *Nature Immunology*, **12**, 2011 54-61, 10.1038/ni.1967, © 2011 Nature America, Inc.

3.1 Contributions

After the study described in Chapter 2, I continued my collaboration with Kathrin Anders and Kai Wucherpfennig. To further study the interaction of DM with MHC, they designed a 3-stage Biacore experiment. The surface of the instrument was coated with DM. In stage 1, pMHC was run through the system, which caused the binding of the pMHC with DM and the ejection of the peptide leaving a stable MHC-DM complex on the surface. In stage 2, buffer was run through the machine, which led to a slow, linear decline of the signal which corresponded to the off-rate of empty MHC from the DM bound to the surface. In stage 3, free peptide was run through the machine, which rapidly binded to the MHC, causing its release from the DM on the surface and a rapid drop in the signal.

In "normal" Biacore experiments, k_{off} and k_{on} are determined in a two stage process. In stage 1, molecule A is run through the machine which has molecule B on the surface, causing the formation of AB and a rise in the signal. In stage 2, buffer is run through the machine and A is swept away as it unbinds from B. This is a relatively simple analysis that every instrument can do internally since the equation involving the sought parameters is easily derived analytically. The complication with our system is that there are 3 stages and at least 3 species. The signal is directly proportional to molecular weight of what is bound on the surface. DM, empty MHC

(eMHC), and peptide-loaded MHC (pMHC) all have significantly higher molecular weights than the peptide, which makes it difficult to distinguish between eMHC and pMHC. Further complicating the system is that there can be different conformations of these species that have wildly different rate constants associated with them. It is impossible to distinguish between conformations since there is no molecular weight change and thus no signal change.

Extensive attempts to fit a reliable model to their data, which would have allowed the determination of all relevant rate constants of association and dissociation, were unsuccessful due to the inability to distinguish what was actually bound to the surface in terms of conformations, etc. All that could be determined from the modeling was that the basic model in stage 3 of peptide binding to the MHC and detaching from the DM will never fit the data. Stage 3 curves of dissociation were always two exponential in nature, whereas this simple model would never give more than 1 exponential as a solution. Essentially, the peptide needed a fast route to the eMHC-DM complex and then the pMHC-DM would have to break up quickly getting rid of the signal. This fast path to signal decay is 1 exponential in nature. However, there needs to be a slower route to the decay since after a brief strong drop in the signal, there was a slow decay. No adaption to this model could hinder this fast path to decay meaning that steric issues of the peptide binding to eMHC could not be the answer. The most likely solution was that there was an equilibrium between a peptide receptive eMHC bound to DM and a non-peptide receptive eMHC bound to DM. As described earlier, there is no way to distinguish between these two states looking at the signal so anything we came up with was just speculation, which is why it ultimately was not included in the manuscript.

However, my regular meetings with Kathrin about the issues with modeling led to my suggestion that they try to use a linker to secure the peptide in place, which would reduce the number of stages to 2 and the number of species to 2 (DM or pMHC-DM) making conventional Biacore analysis possible. There were concerns that the linker may interrupt binding of pMHC and DM artificially. These discussions though, led them to investigate the role of various anchor residues and lengths of peptide on the binding with DM, which led to the novel results in the paper. This is why I was included as an author. There was a lot of work that was put into the modeling even though it never made it to publication.

3.2 Introduction

Efficient surveillance of the surface of antigen-presenting cells by $CD4^+$ T cells requires long-lived display of peptides bound to major histocompatibility complex class II (MHCII) molecules. High-affinity peptides are kinetically trapped in the peptide-binding groove and dissociate extremely slowly (within days to weeks at 37 °C)[1, 2]. Such stable binding is enabled by a conserved hydrogen-bonding network between the MHC helices and the backbone of bound peptides, as well as by occupancy of MHC pockets by peptide side chains[3, 4].

Empty MHCII molecules quickly lose their ability to rapidly bind peptide and aggregate[5, 6]. Before the arrival of MHCII in the late endosomal peptide-loading compartment, the binding groove is protected by the CLIP (class II–associated Ii peptide) segment of the invariant chain[7]. Cleavage of the invariant chain in the late endosomal compartment leaves the CLIP peptide in the binding groove[8, 9]; CLIP is bound with a wide range of affinities by different allelic forms of MHCII[10]. HLA-DM (human) and H2-DM (mouse) serve a critical role in antigen presentation by MHCII by accelerating the removal of CLIP and by editing the peptide content of MHCII

molecules such that the display of high-affinity peptides is favored[9, 11-20]. HLA-DM also acts as a chaperone that maintains empty MHCII in a highly peptide-receptive state[21-23]. Mass spectrometry analysis of HLA-DM–MHCII complexes purified from antigen-presenting cells has shown them to be largely devoid of peptide[22].

Crystal structures of MHCII, HLA-DM and H2-DM have been available for many years (since 1993 (MHCII) and 1998 (HLA-DM and H2-DM)), but it has been challenging to define the molecular mechanisms of HLA-DM-catalyzed peptide exchange[4, 24, 25]. Comprehensive mutagenesis has identified large lateral surfaces of HLA-DM and HLA-DR required for their interaction; of particular interest are HLA-DR residues in the vicinity of the N terminus of the peptide (Phe51 and Glu40 of HLA-DRα)[26, 27]. The proximity of the HLA-DM-interaction site to the N terminus of the peptide has also been demonstrated by covalent attachment of a peptide to a surface-accessible cysteine residue at position 46 of HLA-DMβ and subsequent loading of this HLA-DM-linked peptide into the HLA-DR1 peptide-binding groove. Such a complex is stable when HLA-DM is linked to the C terminus of the peptide, but HLA-DM catalyzes rapid peptide dissociation when linked to the N terminus of the peptide[28].

Two main models of HLA-DM action have been proposed. The first model suggests that HLA-DM breaks some of the conserved hydrogen bonds between the peptide backbone and the MHC helices[24, 29], whereas the second model proposes more global conformational changes[30]. The first model has been supported by functional data showing that the rate of HLA-DM-induced peptide dissociation is proportional to the intrinsic rate of peptide dissociation for all peptides and MHCII molecules tested[29]. These data suggest that bonds conserved in all peptide-MHCII interactions are targeted by HLA-DM, such as conserved hydrogen bonds formed by HLA-DRα

Phe51, HLA-DRα Ser53 and HLA-DRβ His81 near the N terminus of the peptide[24]. An initial report indicated that HLA-DRβ His81 was the target of HLA-DM action[31], but other studies have shown that substitution of this residue does not result in less susceptibility to HLA-DM[32, 33]. Furthermore, individual substitution of all MHC side chains that form conserved hydrogen bonds to the peptide backbone (nine hydrogen bonds in total) did not identify a substitution that resulted in less susceptibility to HLA-DM[32]. Finally, loss of hydrogen bonds to the main-chain atoms of HLA-DRα Phe51 and HLA-DRα Ser53 enhances susceptibility to HLA-DM rather than diminishing it, which suggests that these hydrogen bonds are not direct targets of HLA-DM[34].

The second model of HLA-DM action proposes that HLA-DM globally distorts the MHCII binding groove rather than breaking a small number of hydrogen bonds. Analysis of a large number of HLA-DR–peptide complexes has shown that the intrinsic stability of any one complex is a poor predictor of susceptibility to HLA-DM and that interactions along the entire length of the groove affect susceptibility to HLA-DM[30]. Dynamic light-scattering and circular-dichroism studies have further indicated that HLA-DR undergoes conformational changes after peptide binding[35].

A central problem in defining the mechanism of HLA-DM-catalyzed peptide exchange is that it remains unknown which HLA-DR–peptide conformers interact with HLA-DM. We report here that the interaction of HLA-DM with HLA-DR was highly dependent on the occupancy of the peptide-binding groove, with high-affinity peptides destabilizing empty HLA-DR–HLA-DM complexes. Furthermore, HLA-DM bound only to HLA-DR–peptide conformers in which key interactions between the N terminus of the peptide and the HLA-DR molecule had already been lost because of peptide motion.

3.3 Methods

HLA-DM expression

Soluble HLA-DM proteins carried a C-terminal BirA tag (GLNDIFEAQKIEWHE; HLA-DMα) or protein C tag (HLA-DMβ) on the extracellular domain. Two N-linked glycosylation sites (HLA-DMα N165D and HLA-DMβ N92D) were removed to diminish heterogeneity, which left the HLA-DMα N15 glycosylation site[47]. Sf9 *Spodoptera frugiperda* insect cells were infected with recombinant baculovirus at a multiplicity of infection of >5, and proteins were purified after 3 d by affinity chromatography with an Anti-Protein C Affinity Matrix (Roche Applied Science); aggregates and impurities were subsequently removed with a Superose 6 gel-filtration column (GE Healthcare Bio-Sciences Corp.).

Site-specific biotinylation of the BirA tag used a protein concentration of 2–3 mg/ml at a molar ratio of 20:1 (HLA-DR to BirA). Reactions proceeded for 2 h at 30 °C in the presence of biotin (100 μM), ATP (10 mM) and protease inhibitors. Excess biotin was removed by dialysis, and biotinylation was confirmed by mobility shift with streptavidin after migration through native polyacrylamide gels.

HLA-DR expression

Peptides were synthesized by Peptide 2.0 and JPT Peptide Technologies. Soluble HLA-DR–CLIP complexes were produced with stably transfected Chinese hamster ovary cell lines in hollow fiber bioreactors, as described[48]. CLIP (PVSKMRMATPLLMQA) was covalently attached via a thrombin-cleavable linker at the N terminus of the appropriate HLA-DRβ chain (DRB1*0101, DRB1*0401 or DRB1*1501).

For covalent attachment of peptides, soluble HLA-DR1 proteins were generated with a cysteine residue at position 58 (G58C) or position 65 (V65C) of HLA-DRα. The low-affinity $CLIP_{low}$ mutant (SKARMATGALAQA; substituted anchor residues underlined) was covalently attached to the N terminus of the HLA-DR1β chain (DRB1*0101) to enable efficient exchange after linker cleavage with human rhinovirus 3C protease (provided by J. Fraser). This protease site enabled cleavage under conditions of low temperature (4 °C) that minimized dissociation of $CLIP_{low}$ before peptide loading. These HLA-DR variants were produced with a baculovirus system. Soluble HLA-DR proteins were purified via affinity chromatography with monoclonal antibody to HLA-DR (L243; American Type Culture Collection); aggregates and impurities were removed with a Superose 6 gel-filtration column. Depending on the construct, covalently linked CLIP or $CLIP_{low}$ was cleaved with thrombin (Novagen; EMD Chemicals) or 3C protease. The former cleavage used 20 units thrombin per mg of protein for 1.5 h at 25 °C; the latter used 50 μg 3C protease per mg of protein under reducing conditions (2 mM reduced glutathione) for 2 h at 4 °C. Protein purity and completeness of cleavage were assessed by SDS-PAGE.

Peptide loading and production of disulfide-linked HLA-DR–peptide complexes

The key aspects of covalent linkage of very low-affinity peptides to DR1 were as follows: use of an HLA-DR1–peptide complex with very low affinity as the input protein (HLA-DR1–$CLIP_{low}$); accelerated dissociation of this low-affinity peptide from HLA-DR1 by the small molecule J10-1 that accelerates peptide loading; and use of redox conditions that enabled efficient formation of a disulfide bond between the HLA-DRα helix and incoming peptide. Most peptides with a DNP group were labeled via a lysine side chain at the peptide C terminus; HA(306–318) C-terminal truncation variants were labeled via the lysine side chain at position P–1. DNP-labeled peptides

were exchanged overnight at 25 °C, 30 °C or 37 °C (depending on the HLA-DR and peptide) onto cut HLA-DR–CLIP complexes (5 μM) at a 10- to 20-fold molar excess of peptide in citrate-phosphate buffer (pH 5.3) in the presence or absence of the J10-1 small molecule[49]. Unbound peptide was removed with a Superose 12 gel-filtration column (GE Healthcare Bio-Sciences) and loaded complex was separated from other HLA-DR species by affinity chromatography with an anti-DNP-1 column (Biotrend Chemikalien). The absorbance of DNP and protein was monitored at 350 nm and 280 nm, respectively[49].

DNP-labeled HA peptides with a cysteine at position P3 or P6 were reduced in 500 μM glutathione and were added to 3C-cleaved HLA-DR1 protein with cysteine substitution; reactions were then incubated for 2 h in the presence of 50 μM J10-1 and 750 μM glutathione. Reactions were then shifted for 2 h to oxidizing conditions (950 μM oxidized glutathione) to promote disulfide bond formation. Unbound peptide and unloaded complex were removed by gel filtration and DNP affinity chromatography as described above. Disulfide linkage of HA peptides was confirmed on the basis of lower motility of HLA-DRα by SDS-PAGE.

SPR

Streptavidin chips (GE Healthcare) were primed and normalized before immobilization of ligand. Biotinylated HLA-DM proteins (ligand) were diluted to a concentration of 0.5 μg/ml in HBS-EP buffer (GE Healthcare), and 500 RU protein (usually HLA-DM Mut2 and wild-type HLA-DM) was immobilized in two consecutive flow cells on a streptavidin chip at a flow rate of 2–10 μl/min at 25 °C unless indicated otherwise. A BIAcore 3000 (GE Healthcare) was used for SPR experiments at 25 °C (range, 20–37 °C). For experiments at a different temperature, the chip was again normalized after the change in temperature was complete. HLA-DR–peptide

complexes were purified by gel-filtration chromatography before SPR experiments for the removal of aggregates. HLA-DR–peptide complexes (analyte) were diluted into the running buffer just before injection and were injected in the appropriate concentrations and conditions (stage 1). This was followed by buffer (stage 2) and injection of peptide (stage 3). Chips were regenerated by injection of 50–100 μM high-affinity peptide for the respective HLA-DR. Experiments were done in degassed 50 mM citrate-phosphate buffer (pH 5.35) with 150 mM NaCl and 0.06% $C_{12}E_9$ detergent (Calbiochem; EMD Chemicals) unless indicated otherwise. Results were calculated by subtraction of binding in the reference flow cell (HLA-DM Mut2 in most cases) from binding in the wild-type HLA-DM flow cell.

Peptide-binding assay

FP assays were done as described[47]. MBP(85–99) was labeled at position P5 (lysine-to-cysteine substitution) with a maleimide derivative of Alexa Fluor 488 (Molecular Probes)[47]. HLA-DR–peptide complexes were incubated with Alexa Fluor 488–labeled MBP(85–99) or HA(306–318) in a volume of 40 μl in black polystyrene 384-well flat-bottomed plates (Corning) in the appropriate conditions and binding of labeled peptide was measured with a Victor^3 V multilabel plate reader (PerkinElmer). Measurements were made in triplicate.

3.4 Results

3.4.1 Peptide destabilizes HLA-DR–HLA-DM complexes

HLA-DM-catalyzed peptide exchange is a multistep process that has been difficult to study mechanistically because most assays do not isolate individual steps but instead represent a mixture of multiple rates. We developed a real-time surface plasmon resonance (SPR) assay to

directly study the individual steps of the interaction of HLA-DR with HLA-DM (Fig. 3.1). We oriented HLA-DM on streptavidin chips through C-terminal site-specific biotinylation so that the large lateral surface required for binding to HLA-DR was fully accessible. We generated soluble HLA-DR–CLIP complexes with a cleavable CLIP linker. In SPR experiments, it is critical to use suitable control proteins to ensure the specificity of binding; we therefore identified HLA-DM and HLA-DR mutants with loss of activity in a real-time peptide-binding assay based on fluorescence polarization (FP; Fig. 3.1 a, c). Substitution of one arginine residue at position 98 of HLA-DMα with alanine (R98A; called 'HLA-DM Mut1' here) resulted in less HLA-DM activity, whereas an additional substitution of the arginine residue at position 194 of HLA-DMα with alanine (R98A and R194A; called 'HLA-DM Mut2' here) resulted in loss of activity (Fig. 3.1a). The SPR binding data closely correlated with those functional data, showing little binding of HLA-DR to HLA-DM Mut1 and no binding to HLA-DM Mut2 (Fig 3.1b). Also, an HLA-DR2 (DRB1*1501) mutant with substitution of the serine residue at position 53 with aspartic acid (HLA-DRα S53D) that was unresponsive to HLA-DM in the FP assay (Fig. 3.1c) failed to bind to HLA-DM, as assessed by SPR (Figure 3.1d and Fig. A3.1 in Appendix 3). This mutant HLA-DR2 bound peptide with kinetics similar to those of wild-type HLA-DR2 (Fig. 3.1c), which indicated correct folding.

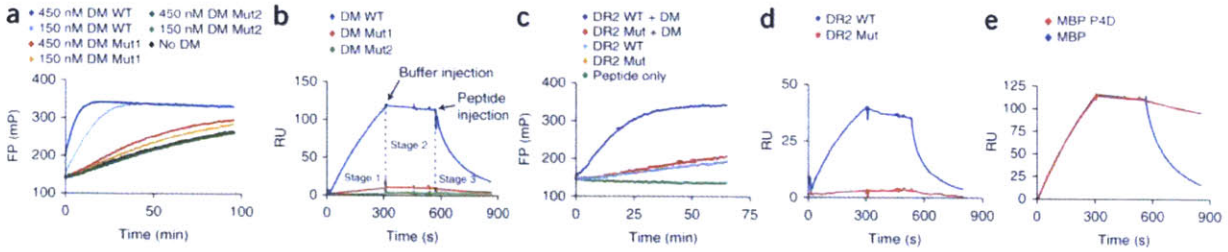

Figure 3.1. Peptide disrupts the long-lived complex of empty HLA-DR and HLA-DM. (**a–d**) Specificity of the SPR assay. (**a**) Effect of wild-type HLA-DM (DM WT), HLA-DMα R98A (DM Mut1) and HLA-DMα R98A-R194A (DM Mut2) on the binding of Alexa Fluor 488–labeled MBP(85–99) (30 nM) to HLA-DR2 (150 nM), measured by FP and presented in millipolarization units (mP). (**b**) SPR analysis of the binding of HLA-DR2–CLIP (2 μM) by wild-type and mutant HLA-DM (pH 5.35, 25 μl/min, 30 °C) injected for 5 min (stage 1), followed by buffer (stage 2) and 1 μM MBP(85–99) (stage 3), presented in resonance units (RU) as HLA-DM flow cell – reference flow cell (reference is streptavidin here). (**c**) Binding of labeled MBP(85–99) to wild-type HLA-DR2 (DR2 WT) or the HLA-DRα S53D mutant (150 nM; DR2 Mut) with (+ DM) or without HLA-DM (25 nM). (**d**) Binding of HLA-DM by wild-type or mutant HLA-DR2–CLIP (1 μM) injected for 5 min, followed by buffer and 10 μM CLIP peptide of amino acids 87–101 (CLIP(87–101)). (**e**) Dissociation of the HLA-DM–HLA-DR2 complex by peptide, assessed by injection of high-affinity MBP(85–99) (MBP) or the MBP P4D analog (1 μM). Data are representative of two (**a**,**c**,**d**) or more than three (**b**,**e**) independent experiments.

In these SPR experiments, we injected HLA-DR–CLIP complexes over the HLA-DM surface (stage 1), followed by injection of buffer (stage 2; Fig. 3.1b,d). Unexpectedly, the dissociation of HLA-DR from HLA-DM during stage 2 was very slow, even though soluble HLA-DM and

HLA-DR are thought to interact only weakly[36]. We reasoned that the catalytic activity of HLA-DM removed the HLA-DR-bound CLIP, which exited with the buffer flow, whereas peptide remains available for rebinding in typical tube-based experiments. We therefore postulated that injection of peptide would destabilize the complex of HLA-DM and empty HLA-DR. Indeed, injection of a high-affinity peptide of myelin basic protein amino acids 85–99 (MBP(85–99)) induced dissociation of HLA-DR2 from HLA-DM (Fig. 3.1e). A single amino–acid mutant of MBP(85–99) with very low affinity for HLA-DR2 (substitution of phenylalanine at position P4 with aspartic acid (MBP P4D)) induced minimal dissociation at the same peptide concentration (1 μM; Fig. 3.1e). We obtained similar binding profiles at flow rates of 15–50 μl/min (Fig. A3.2), which indicated that rebinding (mass transport) was negligible. Injection of an antibody to the DNP group on peptides showed that the complex of HLA-DM and HLA-DR in stage 2 did not contain bound peptide (Fig. A3.3).

The rate of peptide-induced dissociation of HLA-DM–HLA-DR (stage 3) correlated closely with the affinity of these peptides for the HLA-DR2-binding site, both for sets of CLIP mutants (Fig. 3.2a-d) and for sets of MBP(85–99) mutants (Fig. 3.2e,f), regardless of which peptide anchors were replaced. Peptides with high affinity for HLA-DR2, such as CLIP P4F (CLIP with substitution of the alanine residue at position P4 with phenylalanine; Fig. 3.2c) or MBP(85–99) (Fig. 3.2f), induced faster dissociation of HLA-DM–HLA-DR than did peptides of lower affinity. Peptides with very low affinity, such as MBP P4D, did not induce dissociation at low concentrations (such as 1 μM; Fig. 3.1e) but led to some dissociation at higher concentrations (10 μM; Fig. 3.2e).

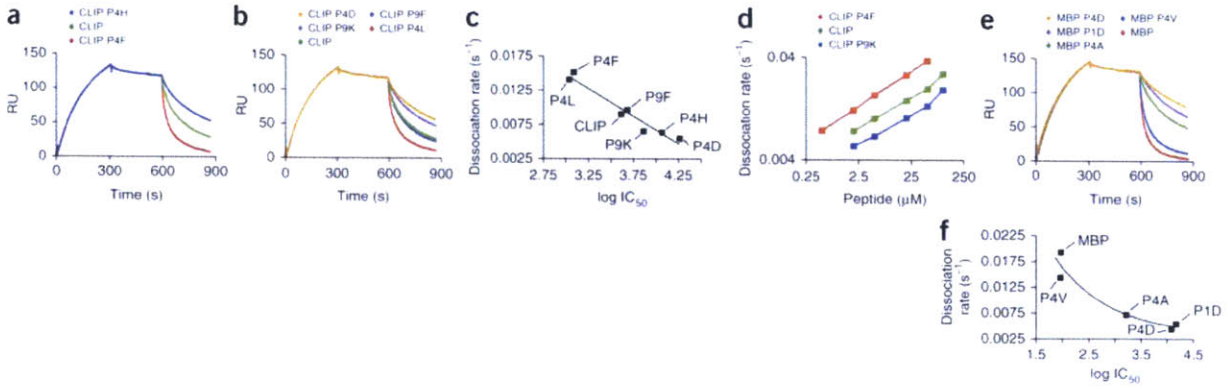

Figure 3.2. Rate of HLA-DM–HLA-DR complex dissociation is determined by peptide affinity. (**a**,**b**) Effect of CLIP and mutant CLIP on the dissociation of HLA-DM–HLA-DR, assessed by injection of 5 μM HLA-DR2–CLIP (5 min, pH 5.35, 15 μl/min, 30 °C), followed by buffer and wild-type or mutant CLIP (10 μM). (**c**) Competition assay of the binding of CLIP peptides (threefold dilution: 10 μM to 14 nM) to HLA-DR2 (100 nM) versus Alexa Fluor 488–labeled MBP(85–99) (10 nM); the median inhibitory concentration (IC_{50}) is plotted against the rate of peptide-induced dissociation of HLA-DM–HLA-DR (from **a**,**b**). (**d**) Effect of CLIP and two CLIP mutants, injected in stage 3 (0.5–100 μM), on the rate of dissociation of HLA-DR from HLA-DM. (**e**) Effect of MBP(85–99) and mutants on HLA-DM–HLA-DR dissociation, injected in stage 3 as in **a**. (**f**) Effect of MBP peptide affinity on the HLA-DM–HLA-DR dissociation rate, presented as the median inhibitory concentration determined by competition assay (as in **c**) versus dissociation rate (from **e**). Data are representative of two independent experiments (**a**–**f**) and more than three additional independent experiments under similar conditions (**a-c**,**e**,**f**; triplicate samples in **c**,**f**).

3.4.2 Slow binding to HLA-DM by high-affinity complexes

The fact that peptide binding induces dissociation of HLA-DM–HLA-DR complexes suggests that the HLA-DR-bound peptide probably also has a considerable effect on the reverse process; that is, the binding of HLA-DR to HLA-DM (Fig. 3.3). Initial experiments showed that HLA-DR molecules with covalently bound peptides did not bind to HLA-DM (Fig. 3.3); this was true for both HLA-DR2–CLIP and HLA-DR1 (DRB1*0101) linked to a low-affinity CLIP variant (HLA-DR1–$CLIP_{low}$), even though binding was readily detectable after linker cleavage (Fig. 3.3a,b). These results could be explained either by steric hindrance caused by the linker attached to the N terminus of the HLA-DRβ chain or by a substantial affinity gain resulting from covalent peptide attachment (rebinding of peptide is probably extremely rapid). The linker is flexible and also not in the immediate proximity of the predicted HLA-DM-interaction site, which makes the latter explanation more plausible.

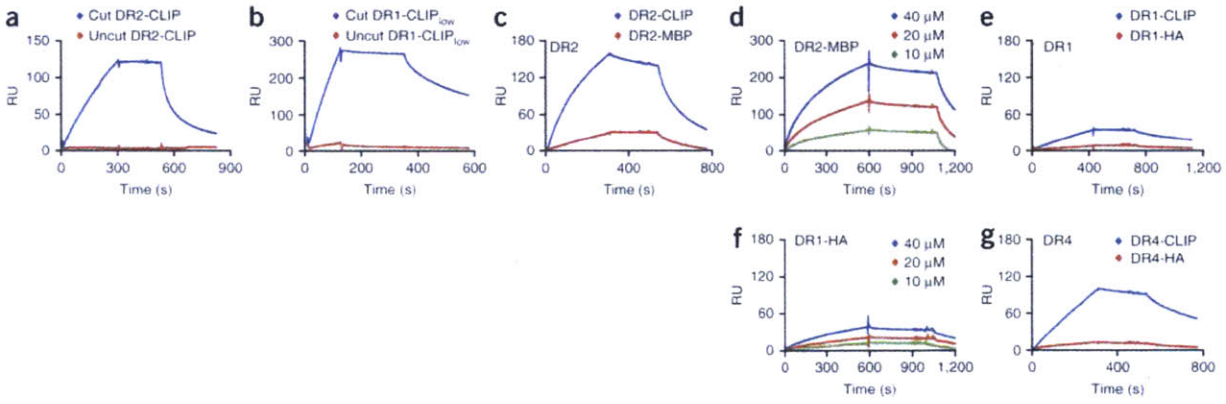

Figure 3.3. High-affinity HLA-DR–peptide complexes interact slowly with HLA-DM. (**a**) SPR assay of the binding of HLA-DM by HLA-DR2–CLIP (5 μM), with (Cut DR2-CLIP) or without (Uncut DR2-CLIP) cleavage of the peptide linker by thrombin, injected for 5 min, followed by buffer (stage 2) and 20 μM CLIP(87–101) (stage 3). (**b**) SPR assay of the binding of HLA-DM

by HLA-DR1–$CLIP_{low}$ (5 μM), with (Cut DR1-$CLIP_{low}$) or without (Uncut DR1-$CLIP_{low}$) cleavage by the 3C protease, injected for 2 min, followed by buffer and HA(306–318) (50 μM). (**c**) SPR assay of the binding of HLA-DM by HLA-DR2 preloaded with CLIP or MBP (2 μM) and injected for 5–7 min, followed by buffer and 10 μM CLIP(87–101). (**d**) SPR assay of the binding of HLA-DM by HLA-DR2 preloaded with high-affinity MBP(85–99) and injected for 10 min, followed by buffer (stage 2) and 5 μM MBP(85–99) (stage 3). (**e**) SPR assay of the binding of HLA-DM by HLA-DR1 preloaded with CLIP or HA (10 μM) and injected for 5–7 min, followed by buffer and 50 μM HA(306–318). (**f**) SPR assay of the binding of HLA-DM by HLA-DR1 preloaded with high-affinity HA(306–318) and injected for 10 min, followed by buffer (stage 2) and 50 μM HA(306–318) (stage 3). (**g**) SPR assay of the binding of HLA-DM by HLA-DR4 preloaded with CLIP or HA (2 μM) and injected for 5–7 min, followed by buffer and 50 μM HA(306–318). Assays were done at 25 °C (**a**,**b**) or 37 °C (**c**–**g**) and at a pH of 5.35 and a rate of 15 μl/min. Data are representative of three (**a**,**c**,**e**) or two (**b**,**d**,**f**,**g**) independent experiments.

We next examined the effect of peptide affinity on the association of HLA-DR with HLA-DM using HLA-DR molecules loaded with single peptides; we synthesized peptides with a dinitrophenol (DNP) tag for affinity isolation of homogenous HLA-DR–peptide complexes. There was strong binding of HLA-DM by the low-affinity HLA-DR2–CLIP complex, but much slower binding by the high-affinity HLA-DR2–MBP(85–99) complex (Fig. 3.3c,d). We also observed this effect for HLA-DR4 preloaded either with low-affinity CLIP or high-affinity influenza hemagglutinin peptide of amino acids 306–318 (HA(306–318); Fig. 3.3g). CLIP binds with high affinity to HLA-DR1[37], and binding of the HLA-DR1–CLIP complex to HLA-DM was also slow (Fig. 3.3e). Nevertheless, there was concentration-dependent binding to HLA-DM by

the high-affinity HLA-DR2–MBP(85–99) and HLA-DR1–HA(306–318) complexes (Fig. 3.3d,f), which indicated that both low-affinity and high-affinity HLA-DR–peptide complexes bound to HLA-DM in this SPR assay, but with different rates. In a functional peptide-binding assay, the rate of HLA-DM-catalyzed binding of a fluorescence-labeled peptide was 8.5% when the high-affinity HLA-DR2–MBP(85-99) complex rather than the low-affinity HLA-DR2–CLIP complex was used as input protein. In the SPR assay, the rate of binding of HLA-DM by HLA-DR2–MBP(85–99) was 11.5% compared with the rate of binding by HLA-DR2–CLIP (Fig. A3.4), which demonstrated overall agreement between the SPR and peptide-binding assays. Published studies with full-length HLA-DR and HLA-DM molecules isolated from cells have reported a stronger interaction of HLA-DM with HLA-DR–CLIP than with HLA-DR–peptide complexes[21, 38]; also, a published SPR experiment has shown stronger binding of immobilized soluble HLA-DM to detergent-solubilized full-length HLA-DR–CLIP than to HLA-DR–peptide complexes[39]. In both sets of experiments, a complex mixture of peptides was bound to these cell-derived HLA-DR–peptide complexes. In the experiments we have reported here, the differences in binding were much greater because we used purified low-affinity and high-affinity HLA-DR–peptide complexes. Comparison of the HLA-DR–CLIP binding data for these three allelic forms (HLA-DR1, HLA-DR2 and HLA-DR4) also showed large differences in the HLA-DM-binding kinetics. HLA-DR2–CLIP bound with the fastest kinetics and HLA-DR1–CLIP bound with the slowest kinetics (Fig. 3.3c,e,g). We also observed large differences among these allelic forms in peptide-induced dissociation of HLA-DM–HLA-DR complexes, with complexes containing HLA-DR2 being more sensitive to peptide-induced dissociation than those containing HLA-DR1 or HLA-DR4 (Fig. 3.3c,e,g).

3.4.3 Binding to HLA-DM requires partial peptide dissociation

The results obtained with covalently linked peptides (Fig. 3.3a,b) raised the questions of whether HLA-DR molecules with fully bound peptides do not bind to HLA-DM and whether partial release of the bound peptide is actually required to generate a HLA-DM-sensitive conformer. To investigate this, we generated HLA-DR1 molecules to which peptides could be covalently attached in one of the pockets so that peptide termini could be truncated without peptide loss (Fig. 3.4). We covalently linked mutant hemagglutinin peptides either in the P6 pocket or the P3 site by replacement of the HLA-DRα valine at position 65 or glycine at position 58 with cysteine; both residues are located on the HLA-DRα-chain helix. We made these complexes with an HLA-DR1 molecule with a very low-affinity peptide as the input protein, and we chose redox conditions that enabled efficient formation of a disulfide bond between the peptide and the HLA-DRα-helix. We generated a large set of such complexes (Table 3.1) that we affinity-purified with DNP affinity tags on the peptides to ensure the absence of empty HLA-DR or HLA-DR species loaded with other peptides (Fig. A3.5). We named these peptides according to the site of covalent linkage (HA_6 and HA_3 for linkage in the P6 pocket or the P3 site, respectively) and the length of the peptide, with full-length HA spanning from the P–2 to the P11 positions (HA P_{-2}-P_{11}; Table 3.1). We confirmed full occupancy by monitoring the ratio of absorbance at 280 nm (HLA-DR) to that at 350 nm (DNP group on peptide). Also, we immunoprecipitated HLA-DR1 molecules with linked HA_6 P_2-P_{11} peptide by conformation-sensitive antibodies to HLA-DRα and HLA-DRβ (Fig. A3.6).

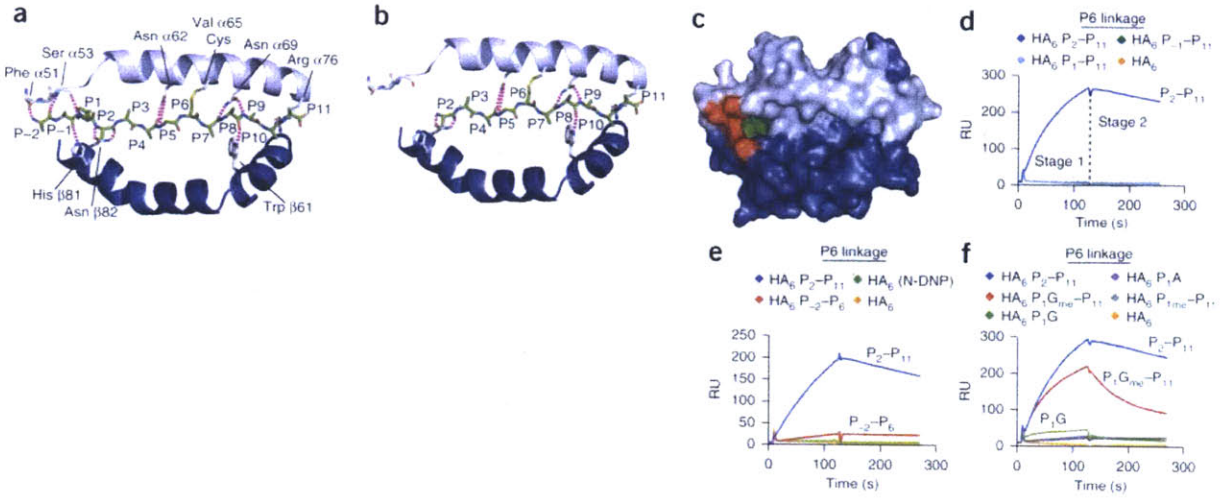

Figure 3.4. HLA-DM binds with fast kinetics to HLA-DR–peptide complexes without an engaged peptide N terminus. (**a**,**b**) Hydrogen-bonding network between HLA-DR1 and full-length, covalently linked HA(306–318) (**a**) or a linked HA mutant peptide lacking three N-terminal residues (**b**). Numbers along peptide 'backbone' (P_{-2} to P_{11}; between HLA-DR helices) indicate peptide position. The valine at position 65 in the HLA-DRα chain was replaced with cysteine to enable the formation of a disulfide bond with a cysteine at position P6 of HA (HA_6). (**c**) Space-filling model of the empty HLA-DR1 groove showing residues contacted by two N-terminal peptide residues (red) and the P1 anchor (green). (**d**–**f**) Binding to HLA-DM by HLA-DR1 with linked HA_6 peptides (5 μM), injected for 2 min (pH 5.35, 15 μl/min, 25 °C), followed by injection of buffer. Data are representative of at least three (**d**,**f**) or two (**e**) independent experiments.

Table 3.1. HA-P_6 and HA-P_3 cysteine peptide variants.

Name	Sequence	Change or substitution
HA-P_6Cys (cysteine residue at P6)		
HA_6	PKYVKQNCLKLAT	
HA_6 P_1A	PKAVKQNCLKLAT	P1 Tyr-to-Ala substitution
HA_6 P_1G	PKGVKQNCLKLAT	P1 Tyr-to-Gly substitution
HA_6 P_{-1}-P_{11}	KYVKQNCLKLAT	P–2 truncation
HA_6 P_1-P_{11}	YVKQNCLKLAT	P–2 and P–1 truncation
HA_6 P_{1me}-P_{11}	Me-YVKQNCLKLAT	P–2 and P–1 truncation; N-methylation of P1 Tyr
HA_6 P_1G_{me}-P_{11}[a]	Me-GVKQNCLKLAT	P–2 and P–1 truncation; substitution of P1 Tyr with N-methylated Gly
HA_6 P_2-P_{11}[a]	VKQNCLKLAT	P–2, P–1 and P1 truncation
HA_6 (N-DNP)	PKYVKQNCLKLAT	N-terminal DNP label
HA_6 P_{-2}-P_6	PKYVKQNC	P7, P8, P9, P10 and P11 truncation; N-terminal DNP label
HA-P_3Cys (cysteine residue at P3)		
HA_3	PKYVCQNTLKLAT	
HA_3 P_1G	PKGVCQNTLKLAT	P1 Tyr-to-Gly substitution
HA_3 P_{1me}-P_{11}	Me-YVCQNTLKLAT	P–2 and P–1 truncation; N-methylation of P1 Tyr
HA_3 P_1G_{me}-P_{11}[a]	Me-GVCQNTLKLAT	P–2 and P–1 truncation; substitution of P1 Tyr with N-methylated Gly
HA_3 P_2-P_{11}[a]	VCQNTLKLAT	P–2, P–1 and P1 truncation
HA_3 P_3-P_{11}[a]	CQNTLKLAT	P–2, P–1, P1 and P2 truncation

HA_6 peptides have a threonine-to-cysteine substitution at position 6, and HA_3 peptides have a lysine-to-cysteine substitution at position 3. All peptides except HA_6 (N-DNP) and HA_6 P_{-2}-P_6 have a DNP group attached through a C-terminal lysine. Underlining indicates P1 anchor residues.

[a]HLA-DR–peptide complexes that bind rapidly to HLA-DM.

Covalent attachment of the high-affinity HA(306–318) peptide in the P6 pocket (HA_6; Fig. 3.4a) yielded a complex that failed to bind to HLA-DM, as assessed by SPR (Fig. 3.4a,d). We then systematically truncated the full-length HA peptide (which spanned from position P–2 to position P11) from the N terminus, which resulted in loss of conserved hydrogen bonds between the peptide backbone and the HLA-DR helices. Removal of the P–2 residue (peptide HA_6 P_{-1}–P_{11}) resulted in loss of hydrogen bonds to Phe51 and Ser53 of HLA-DRα, and further truncation of P–1 (peptide HA_6 P_1–P_{11}) also eliminated a hydrogen bond to His81 of HLA-DRβ (Fig. 3.4a).

Deletion of these two N-terminal peptide residues was not sufficient for binding to HLA-DM (Fig. 3.4d). However, we observed strong binding to HLA-DM after further truncation of the tyrosine at P1 (peptide HA_6 P_2–P_{11}), a critical anchor residue for binding of HLA-DR1[40] (Fig. 3.4b-d). In contrast, truncation of five C-terminal residues (HA_6 P_{-2}–P_6) resulted in little binding to HLA-DM; the small amount of apparent binding was possibly caused by an overall increase in protein mobility due to loss of five peptide residues (Fig. 3.4e).

To determine whether the effect noted above was due solely to removal of the P1 anchor residue, we tested full-length peptides with substitution to alanine or glycine at P1. Replacement of the P1 tyrosine anchor with alanine (HA_6 P_1A) or glycine (HA_6 P_1G) resulted in only a small amount of binding to HLA-DM (Fig. 3.4f). In contrast, substantial binding was enabled by simultaneous loss of the P1 side chain (P1 glycine) and the two N-terminal residues (P_1G_{me}–P_{11}, where 'G_{me}' indicates methylation of the glycine residue at the N terminus; Fig. 3.4f). Substantial binding to HLA-DM therefore requires release of both the P1 anchor and the peptide residues N-terminal to it.

Loss of the P1 anchor could enable dissociation of a longer peptide segment toward the P6 position, which could be required for binding to HLA-DM. To address this possibility, we moved the covalent attachment site from the P6 pocket to the P3 site by replacement of the glycine residue at position 58 of HLA-DRα with cysteine (Table 3.1). Again, removal of positions P–2 and P–1 did not permit binding to HLA-DM (HA_3 P_{1me}–P_{11}; where 'P_{1me}' indicates methylation of the P1 position; Fig. 3.5a) but further removal of the P1 side chain (HA_3 P_1G_{me}–P_{11}) or the P1 residue (HA_3 P_2–P_{11}) resulted in rapid binding of these two complexes to HLA-DM (Fig. 3.5a). Notably, additional truncation of the P2 residue (HA_3 P_3–P_{11}) seemed to slow

the binding to HLA-DM (Fig. 3.5b), which indicated that disengagement of the P1 anchor and two N-terminal peptide residues was sufficient for binding to HLA-DM. The asparagine at position 82 of HLA-DRβ forms bidentate hydrogen bonds to the peptide backbone at position P2, and replacement of this asparagine with alanine increases the intrinsic dissociation rate of the HA peptide >3,000-fold, which indicates that it has a dominant role in stabilizing peptides in the binding groove[32, 41]. Loss of the peptide residue at position P2 may thus result in lower activity of such an HLA-DR–peptide complex due to absence of these critical hydrogen bonds. These results show that HLA-DM binds only to HLA-DR–peptide complexes with a disengaged peptide N terminus but not to complexes in which the peptide is fully bound.

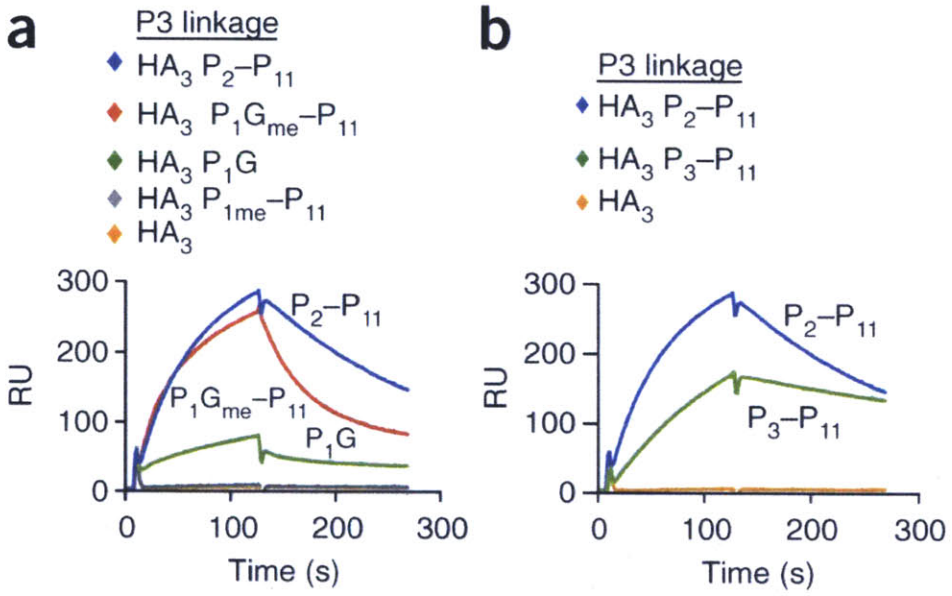

Figure 3.5. Truncated peptides covalently linked through peptide position P3 also bind HLA-DM. (**a**,**b**) Binding of HLA-DM by HLA-DR1–peptide complexes (5 μM) in which the glycine at position 58 of the HLA-DRα chain was replaced with cysteine to permit the formation of disulfide bonds with HA peptides carrying a cysteine at the position P3 (HA_3), assessed as in Figure 3.4. Data are representative of three (**a**) or two (**b**) independent experiments.

3.4.4 Important role for HLA-DRα Trp43 in binding to HLA-DM

The tryptophan at position 43 of HLA-DRα directly interacts with the tyrosine at position P1 and is partially accessible on the lateral surface of the HLA-DRα segment consisting of positions 40–54 (Fig. 3.6a), which has been proposed to be involved in binding to HLA-DM. Conservative substitution of that tryptophan with phenylalanine resulted in much lower susceptibility to HLA-DM in a peptide-binding assay (Fig. 3.6b), and by SPR we observed little binding to HLA-DM by this mutant (Fig. 3.6c). This substitution also accelerated spontaneous release of labeled MBP(85–99) from HLA-DR2 (Fig. 3.6d), a property that would actually be expected to increase binding to HLA-DM, given the data shown above. We also directly compared a panel of four HLA-DR mutants for HLA-DM-catalyzed peptide exchange and binding to HLA-DM (Fig. 3.6e,f). Three HLA-DRα mutants (W43F, S53D and S53H) had much lower activity in both assays, whereas one mutant (G49S) had enhanced activity. These data show that the binding of HLA-DR to HLA-DM as well as HLA-DM-catalyzed peptide exchange require the same HLA-DR residues and hence involve the same binding site on HLA-DR.

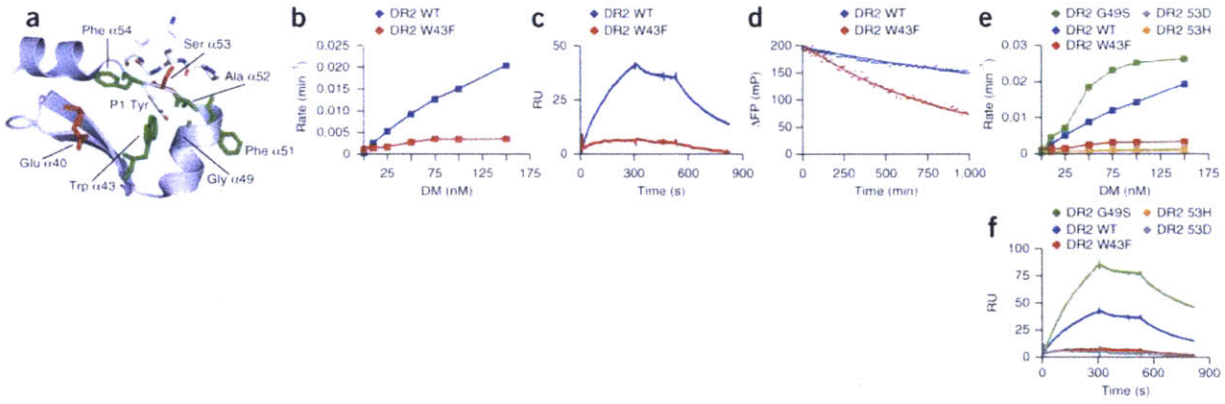

Figure 3.6. HLA-DRα Trp43 is important for interaction with HLA-DM. (**a**) HLA-DRα model showing the surface accessibility of Trp43 and its interaction with the P1 tyrosine of HA(306–

318), as well as the interaction of hydrophobic residues in the HLA-DRα segment of positions 40–54 with the P1 anchor (Trp43, Ala52 and Phe54) and residues associated with the HLA-DM interaction (Glu40, Phe51 and Ser53). The segment of HA(306–318) from P–2 to P2 is presented as a stick model. (**b**) FP analysis of the dissociation of Alexa Fluor 488–labeled MBP(85–99) from wild-type or mutant (W43F) HLA-DR2 over a range of HLA-DM concentrations (horizontal axis). (**c**) Binding of HLA-DM by wild-type or mutant (W43F) HLA-DR2 with bound CLIP (1 μM; pH 5.35, 30 °C, 15 μl/min), followed by buffer and 5 μM CLIP(87–101). (**d**) FP analysis of the dissociation of Alexa Fluor 488–labeled MBP(85–99) from preloaded wild-type or mutant (W43F) HLA-DR2 complexes (100 nM) in presence of 10 μM unlabeled MBP(85–99) competitor peptide (pH 5.4, 25 °C). (**e**,**f**) FP assay (**e**) and SPR assay (**f**) of four HLA-DRα chain mutants in the conditions in **b** (**e**) and **c** (**f**). Data are representative of two independent experiments.

3.4.5 High energy barrier for binding to HLA-DM

Peptide exchange in the presence or absence of HLA-DM is highly dependent on both temperature and pH[11, 12, 42]. HLA-DR1–$CLIP_{low}$ and HLA-DR2–CLIP showed a steep temperature dependence for binding to HLA-DM (Fig. 3.7a and Fig. A3.7) that is unusual for protein-protein interactions. However, binding of HLA-DM by HLA-DR1 with a covalent peptide lacking three N-terminal peptide residues (HA_6 P_2–P_{11}) was much less temperature dependent (Fig. 3.7b,c), which demonstrated that dissociation of the N terminus of the peptide represents an important component of the energy barrier. With peptides of higher affinity, this energy barrier is expected to be even larger. On the basis of the association and dissociation kinetics of the binding of the covalent HLA-DR1–HA_6 P_2–P_{11} complex to HLA-DM, we

calculated a dissociation constant of 1 μM (Fig. 3.7d), which is consistent with the Michaelis constant of ~0.75 μM for the enzymatic reaction executed by HLA-DM[39]. Notably, both on-rates and off-rates increased to a similar extent with temperature, and the affinity was therefore maintained over this temperature range (Fig. A3.8a-c).

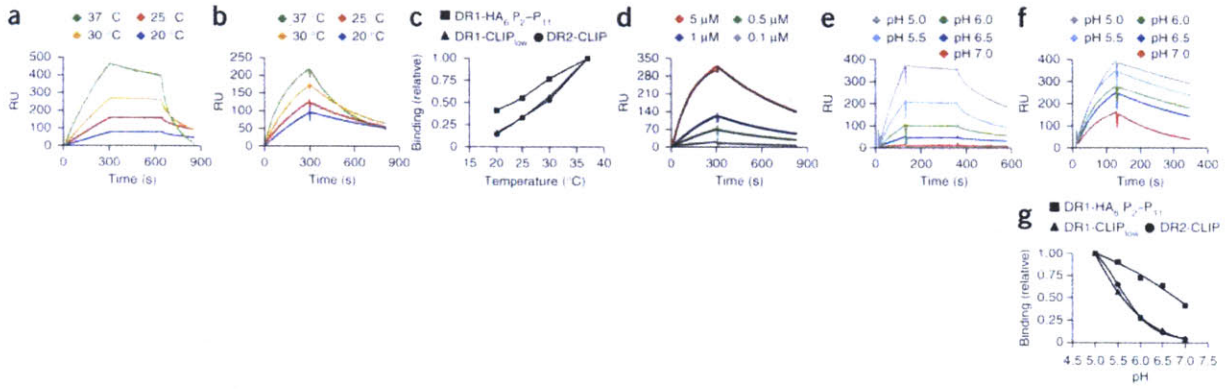

Figure 3.7. Large energy barrier for the binding of HLA-DR–peptide to HLA-DM. (**a**,**b**) Binding of HLA-DM by HLA-DR1–$CLIP_{low}$ (1 μM, **a**) or HLA-DR1–HA_6 P_2-P_{11} (1 μM, **b**) injected at various temperatures (key; 15 μl/min, pH 5.35), followed by buffer and 50 μM HA(306–318). (**c**) Binding at 250–270 s of the association phase in **a**,**b** (Fig. A3.6a), plotted against the corresponding temperature. (**d**) Affinity of HLA-DM for HLA-DR1–HA_6 P_2–P_{11} injected at various concentrations (key) as in **a**; results were fitted with a 1:1 Langmuir binding model by BIAevaluation software. (**e**,**f**) Binding of HLA-DM by HLA-DR1–$CLIP_{low}$ (5 μM; **e**) or HLA-DR1–HA_6 P_2-P_{11} (5 μM; **f**) injected for 2 min at 25 °C as in **a** at various pH values (key). (**g**) Binding at 91–110 s of the association phase in **e**,**f** (and for HLA-DR2–CLIP; not presented in **e**,**f**), plotted against pH, with binding at pH 5.0 set as 1.0. Data are representative of two (**a**,**e**) or three (**b**,**d**,**f**) independent experiments.

HLA-DM has a sharp pH optimum in the acidic range found in late endosomes[11, 12]. As expected, the binding of HLA-DR–CLIP to HLA-DM was increased by lowering of the pH from 5.5 to 4.6

(Fig. A3.9a). However, peptide-binding experiments with HLA-DR2 molecules rendered empty by photocleavage of the bound peptide showed that peptide binding was faster at higher pH[23] (Fig. A3.9b). Consistent with that result, peptide-induced dissociation of the complex was slower at a pH of 4.6 (Fig. A3.9a). HLA-DR1 with a covalent truncated peptide (HLA-DR1–HA_6 P_2–P_{11}) showed 40% of maximal binding to HLA-DM at a pH of 7.0, whereas complexes with a full-length peptide (HLA-DR1–$CLIP_{low}$ and HLA-DR2–CLIP) did not bind to HLA-DM at this pH (Fig. 7e–g). Furthermore, raising the pH during stage 2, at which empty HLA-DR dissociates from HLA-DM, had little to no effect on dissociation rates (data not shown). The pH-facilitated release of the N terminus of the peptide therefore explains in part the low pH optimum of the binding of HLA-DR–peptide to HLA-DM.

3.4.6 Model of interaction between HLA-DM and HLA-DR

The results presented above can be integrated into a new model of DM action (Fig. A3.10) in which HLA-DR molecules with fully engaged peptides do not interact with HLA-DM until the N-terminal part of the peptide dissociates from the HLA-DR–peptide complex because of spontaneous peptide motion. HLA-DM captures this short-lived transition state and peptide quickly departs after binding to HLA-DM. The empty HLA-DM–HLA-DR complex retains the ability to quickly bind a new peptide over extended periods of time. If an interacting peptide has low affinity, HLA-DM may catalyze its removal (editing), whereas binding of a high-affinity peptide is more likely to induce dissociation of the HLA-DM–HLA-DR complex. The resulting high-affinity HLA-DR–peptide complex has a low likelihood of rebinding HLA-DM. This model is consistent with a large body of published work in the field, including the identification of

empty HLA-DR–HLA-DM complexes in cells and the demonstration of an editing function of HLA-DM and H2-DM that drives the selection of high-affinity peptides[14-22, 43].

3.5 Discussion

Our results here have shown that two related mechanisms protect high-affinity peptides from rapid removal by HLA-DM: the binding of such peptides in the HLA-DR groove induces dissociation of HLA-DM, and HLA-DM only slowly rebinds to such high-affinity HLA-DR–peptide complexes. These mechanisms explain how editing by HLA-DM produces HLA-DR–peptide complexes with high intrinsic stability for long-lived display on the cell surface. Forced linkage of HLA-DM and HLA-DR through leucine zipper dimerization domains attached to HLA-DMβ and HLA-DRβ chains results in rapid dissociation of both low-affinity and high-affinity peptides (a half-time of 10 s or 2 min, respectively, for CLIP or HA(306–318) bound to HLA-DR1), which shows the importance of rapid dissociation of the HLA-DR–HLA-DM complex in keeping high-affinity peptides in the binding groove[27].

HLA-DR molecules with full-length peptides covalently linked at position P3 or P6 did not bind to HLA-DM. However, efficient binding resulted after removal of two N-terminal residues (P–1 and P–2) and truncation of the P1 side chain that serves as the main anchor for many HLA-DR-bound peptides[40]. Removal of the peptide side chain at position P1 alone resulted in only weak binding to HLA-DM. The two peptide residues N-terminal to the P1 anchor (P–2 and P–1) form conserved hydrogen bonds to Phe51 and Ser53 of HLA-DRα and His81 of HLA-DRβ[3]; in addition, the side chains of Phe51 and Ser53 of HLA-DRα are critical for the action of HLA-DM. These results show that HLA-DM interacts with HLA-DR molecules only when the P1 pocket is vacant and conserved N-terminal hydrogen bonds to HLA-DR are disrupted; loss of

either set of interactions is not sufficient for substantial binding to HLA-DM. Consistent with those results, it has been shown that filling of the P1 pocket by substitution of the residue at HLA-DRβ position 86 (glycine to tyrosine) results in much lower susceptibility to HLA-DM[44] and that loss of hydrogen bonds between the N terminus of the peptide and Phe51 and Ser53 of HLA-DRα results in greater susceptibility to HLA-DM (six- to ninefold greater)[34]. HLA-DM thus interacts only with HLA-DR conformers in which a critical part of the binding site is already empty.

The segment of HLA-DRα consisting of positions 40–54 not only forms three hydrogen bonds with the backbone of the N-terminal peptide segment (HLA-DRα positions 51 and 53) but also makes substantial hydrophobic contacts that pack against the P1 pocket[3]. Published mutagenesis studies have shown that Phe51 and Glu40 of HLA-DRα are important for susceptibility to HLA-DM[26], and our studies here have shown that the side chains of Ser53 and Trp43 of HLA-DRα are also critical. Trp43 of HLA-DRα is of particular interest because it interacts with the P1 anchor and is also partially solvent accessible in an area that has been linked to the interaction with HLA-DM. Even a conservative substitution, from tryptophan to phenylalanine, resulted in much less binding to HLA-DM, even though this substitution resulted in a moderately higher off-rate of HLA-DR-bound peptide (a change predicted to increase binding to HLA-DM). Phe51 and Ser53 of HLA-DRα (hydrogen bonds to the peptide) and Phe54 and Ala52 of HLA-DRα (hydrophobic contacts with the P1 anchor) are located on an extended strand at the N-terminal side of the HLA-DRα-chain helix that may readily adopt a new conformation when the close interactions with the N terminus of the peptide and the P1 anchor are lost. This specific area of the HLA-DRα chain shows greater flexibility than do the HLA-DR helices, as shown by higher B-factors in crystal structures of MHCII[3, 4]. Molecular-dynamic simulations of the peptide-

occupied state have further shown that the segment of HLA-DRα consisting of positions 50–59 shows greater mobility than do the long helices that flank the peptide-binding groove[45].

All proteins are in constant motion, and local motions may lead to transient loss of interactions in part of the binding groove. We propose that N-terminal truncation of HA(306–318) bound to HLA-DR1 mimics a transient conformation in which part of the peptide has temporarily left the binding site. Structurally, the hydrogen bonds formed by the amino acids at positions 51 and 53 of HLA-DRα and position 81 of HLA-DRβ are surface exposed, whereas other conserved hydrogen bonds to the peptide backbone are sheltered by the helical walls of the binding groove[24]. In the absence of HLA-DM, the most likely outcome is rebinding of this peptide segment in the groove. HLA-DM seems to have a higher affinity for fully empty HLA-DR molecules than for partially peptide-filled HLA-DR molecules, as the dissociation rate of empty HLA-DR–HLA-DM complexes (stage 2) is much lower (~12%) than that of covalent HLA-DR–peptide complexes lacking the N-terminal peptide segment. When HLA-DM senses the loss of interactions surrounding the N terminus of the peptide, its higher affinity for the empty state could shift the equilibrium from a partially peptide-filled form to a fully empty form.

The binding of HLA-DR–peptide to HLA-DM showed a temperature dependence that is highly unusual for protein interactions. The temperature dependence was less steep for truncated HLA-DR–peptide complexes, which suggests that a substantial part of the input energy for binding to HLA-DM is required for dissociation of the N-terminal peptide segment. HLA-DM can catalyze peptide exchange for a wide variety of HLA-DR–peptide complexes, but the enhancement of peptide dissociation by HLA-DM varies substantially among HLA-DR–peptide complexes. In one study, the enhancement of peptide dissociation by HLA-DM for high-affinity HLA-DR–

peptide complexes ranged from 1.4-fold to 227-fold[30]. Our SPR data showed slow binding to HLA-DM by high-affinity HLA-DR–peptide complexes, which suggests that the initial binding event is a rate-limiting step. How frequently such HLA-DR–peptide complexes assume a conformation compatible with binding to HLA-DM is probably influenced by many factors, including the tightness with which the N-terminal peptide segment is bound and how the binding energy is distributed along the groove. Some high-affinity peptides may become almost resistant to the action of HLA-DM because the HLA-DM-interacting conformation is accessed only infrequently.

Finally, we observed that allelic HLA-DR variants showed differences in susceptibility to the action of HLA-DM (fast binding for HLA-DR2–CLIP; intermediate binding for HLA-DR4–CLIP; slowest binding for HLA-DR1–CLIP). These differences in on-rates were explained in part by differences in affinity for CLIP; HLA-DR1 has a high affinity for CLIP, whereas HLA-DR4 binds CLIP with very low affinity[37, 46]. However, additional factors seem to contribute, because HLA-DR4–CLIP complexes bound to HLA-DM with slower kinetics than did HLA-DR2–CLIP complexes. Also, peptide-induced dissociation of the HLA-DM–HLA-DR complex seems to be more efficient for HLA-DR2 than for HLA-DR1 or HLA-DR4. The structural mechanisms that contribute to these differences in HLA-DM-binding kinetics may be complex and will need to be carefully delineated. These results also raise the possibility that MHCII polymorphisms, including those associated with autoimmune diseases, not only change the specificity of MHCII-binding pockets but also broadly affect the peptide repertoire by modifying the kinetics of HLA-DM-catalyzed peptide editing.

3.6 References

1. Lanzavecchia, A., Reid, P.A. & Watts, C. Irreversible association of peptides with class II MHC molecules in living cells. *Nature* **357**, 249-252. (1992).

2. Jensen, P.E. Long-lived complexes between peptide and class II major histocompatibility complex are formed at low pH with no requirement for pH neutralization. *J. Exp. Med.* **176**, 793-798 (1992).

3. Stern, L.J. *et al.* Crystal structure of the human class II MHC protein HLA-DR1 complexed with an influenza virus peptide. *Nature* **368**, 215-221 (1994).

4. Brown, J.H. *et al.* Three-dimensional structure of the human class II histocompatibility antigen HLA-DR1. *Nature* **364**, 33-39 (1993).

5. Germain, R.N. & Rinker, A.G., Jr. Peptide binding inhibits protein aggregation of invariant-chain free class II dimers and promotes surface expression of occupied molecules. *Nature* **363**, 725-728 (1993).

6. Rabinowitz, J.D. *et al.* Formation of a highly peptide-receptive state of class II MHC. *Immunity* **9**, 699-709 (1998).

7. Roche, P.A. & Cresswell, P. Invariant chain association with HLA-DR molecules inhibits immunogenic peptide binding. *Nature* **345**, 615-618 (1990).

8. Riberdy, J.M., Newcomb, J.R., Surman, M.J., Barbosa, J.A. & Cresswell, P. HLA-DR molecules from an antigen-processing mutant cell line are associated with invariant chain peptides. *Nature* **360**, 474-477 (1992).

9. Morris, P. *et al.* An essential role for HLA-DM in antigen presentation by class II major histocompatibility molecules. *Nature* **368**, 551-554 (1994).

10. Stebbins, C.C., Loss, G.E., Jr., Elias, C.G., Chervonsky, A. & Sant, A.J. The requirement for DM in class II-restricted antigen presentation and SDS-stable dimer formation is allele and species dependent. *J Exp Med* **181**, 223-234 (1995).

11. Sloan, V.S. *et al.* Mediation by HLA-DM of dissociation of peptides from HLA-DR. *Nature* **375**, 802-806 (1995).

12. Denzin, L.K. & Cresswell, P. HLA-DM induces CLIP dissociation from MHC class II alpha beta dimers and facilitates peptide loading. *Cell* **82**, 155-165 (1995).

13. Sherman, M.A., Weber, D.A. & Jensen, P.E. DM enhances peptide binding to class II MHC by release of invariant chain-derived peptide. *Immunity* **3**, 197-205 (1995).

14. Nanda, N.K. & Sant, A.J. DM determines the cryptic and immunodominant fate of T cell epitopes. *J Exp Med* **192**, 781-788 (2000).

15. Katz, J.F., Stebbins, C., Appella, E. & Sant, A.J. Invariant chain and DM edit self-peptide presentation by major histocompatibility complex (MHC) class II molecules. *J. Exp. Med.* **184**, 1747–1753 (1996).

16. Lich, J.D., Jayne, J.A., Zhou, D., Elliott, J.F. & Blum, J.S. Editing of an immunodominant epitope of glutamate decarboxylase by HLA-DM. *J. Immunol.* **171**, 853–859 (2003).

17. Lovitch, S.B., Petzold, S.J. & Unanue, E.R. Cutting edge: H-2DM is responsible for the large differences in presentation among peptides selected by I-Ak during antigen processing. *J. Immunol.* **171**, 2183–2186 (2003).

18. Pathak, S.S., Lich, J.D. & Blum, J.S. Cutting edge: editing of recycling class II:peptide complexes by HLA-DM. *J. Immunol.* **167**, 632–635 (2001).

19. Lazarski, C.A. *et al.* The kinetic stability of MHC class II:peptide complexes is a key parameter that dictates immunodominance. *Immunity* **23**, 29–40 (2005).

20. Lazarski, C.A., Chaves, F.A. & Sant, A.J. The impact of DM on MHC class II-restricted antigen presentation can be altered by manipulation of MHC-peptide kinetic stability. *J. Exp. Med.* **203**, 1319–1328 (2006).

21. Denzin, L.K., Hammond, C. & Cresswell, P. HLA-DM interactions with intermediates in HLA-DR maturation and a role for HLA-DM in stabilizing empty HLA-DR molecules. *J Exp Med* **184**, 2153-2165 (1996).

22. Kropshofer, H., Arndt, S.O., Moldenhauer, G., Hammerling, G.J. & Vogt, A.B. HLA-DM acts as a molecular chaperone and rescues empty HLA-DR molecules at lysosomal pH. *Immunity* **6**, 293-302 (1997).

23. Grotenbreg, G.M. *et al.* Empty class II major histocompatibility complex created by peptide photolysis establishes the role of DM in peptide association. *J Biol Chem* **282**, 21425-21436 (2007).

24. Mosyak, L., Zaller, D.M. & Wiley, D.C. The structure of HLA-DM, the peptide exchange catalyst that loads antigen onto class II MHC molecules during antigen presentation. *Immunity* **9**, 377-383 (1998).

25. Fremont, D.H., Crawford, F., Marrack, P., Hendrickson, W.A. & Kappler, J. Crystal structure of mouse H2-M. *Immunity* **9**, 385-393 (1998).

26. Doebele, R.C., Busch, R., Scott, H.M., Pashine, A. & Mellins, E.D. Determination of the HLA-DM interaction site on HLA-DR molecules. *Immunity* **13**, 517-527 (2000).

27. Pashine, A. *et al.* Interaction of HLA-DR with an acidic face of HLA-DM disrupts sequence-dependent interactions with peptides. *Immunity* **19**, 183-192 (2003).

28. Stratikos, E., Mosyak, L., Zaller, D.M. & Wiley, D.C. Identification of the lateral interaction surfaces of human histocompatibility leukocyte antigen (HLA)-DM with HLA-DR1 by

formation of tethered complexes that present enhanced HLA-DM catalysis. *J Exp Med* **196**, 173-183 (2002).

29. Weber, D.A., Evavold, B.D. & Jensen, P.E. Enhanced dissociation of HLA-DR-bound peptides in the presence of HLA-DM. *Science* **274**, 618-620 (1996).

30. Belmares, M.P., Busch, R., Wucherpfennig, K.W., McConnell, H.M. & Mellins, E.D. Structural factors contributing to DM susceptibility of MHC class II/peptide complexes. *J Immunol* **169**, 5109-5117 (2002).

31. Narayan, K. *et al.* HLA-DM targets the hydrogen bond between the histidine at position beta81 and peptide to dissociate HLA-DR-peptide complexes. *Nat Immunol* **8**, 92-100 (2007).

32. Zhou, Z., Callaway, K.A., Weber, D.A. & Jensen, P.E. Cutting edge: HLA-DM functions through a mechanism that does not require specific conserved hydrogen bonds in class II MHC-peptide complexes. *J Immunol* **183**, 4187-4191 (2009).

33. Ferrante, A. & Gorski, J. Cutting edge: HLA-DM-mediated peptide exchange functions normally on MHC class II-peptide complexes that have been weakened by elimination of a conserved hydrogen bond. *J Immunol* **184**, 1153-1158 (2010).

34. Stratikos, E., Wiley, D.C. & Stern, L.J. Enhanced catalytic action of HLA-DM on the exchange of peptides lacking backbone hydrogen bonds between their N-terminal region and the MHC class II alpha-chain. *J Immunol* **172**, 1109-1117 (2004).

35. Zarutskie, J.A. *et al.* A conformational change in the human major histocompatibility complex protein HLA-DR1 induced by peptide binding. *Biochemistry* **38**, 5878-5887 (1999).

36. Weber, D.A., Dao, C.T., Jun, J., Wigal, J.L. & Jensen, P.E. Transmembrane domain-mediated colocalization of HLA-DM and HLA-DR is required for optimal HLA-DM catalytic activity. *J Immunol* **167**, 5167-5174 (2001).

37. Chicz, R.M. *et al.* Predominant naturally processed peptides bound to HLA-DR1 are derived from MHC-related molecules and are heterogeneous in size. *Nature* **358**, 764-768 (1992).

38. Kropshofer, H. *et al.* Editing of the HLA-DR-peptide repertoire by HLA-DM. *Embo J* **15**, 6144-6154 (1996).

39. Vogt, A.B., Kropshofer, H., Moldenhauer, G. & Hammerling, G.J. Kinetic analysis of peptide loading onto HLA-DR molecules mediated by HLA-DM. *Proc Natl Acad Sci U S A* **93**, 9724-9729 (1996).

40. Jardetzky, T.S. *et al.* Peptide binding to HLA-DR1: a peptide with most residues substituted to alanine retains MHC binding. *EMBO J* **9**, 1797-1803 (1990).

41. McFarland, B.J., Katz, J.F., Beeson, C. & Sant, A.J. Energetic asymmetry among hydrogen bonds in MHC class II*peptide complexes. *Proc Natl Acad Sci U S A* **98**, 9231-9236 (2001).

42. Reay, P.A., Wettstein, D.A. & Davis, M.M. pH dependence and exchange of high and low responder peptides binding to a class II MHC molecule. *EMBO J* **11**, 2829-2839 (1992).

43. Sanderson, F., Thomas, C., Neefjes, J. & Trowsdale, J. Association between HLA-DM and HLA-DR in vivo. *Immunity* **4**, 87–96 (1996).

44. Chou, C.L. & Sadegh-Nasseri, S. HLA-DM recognizes the flexible conformation of major histocompatibility complex class II. *J Exp Med* **192**, 1697-1706 (2000).

45. Painter, C.A., Cruz, A., Lopez, G.E., Stern, L.J. & Zavala-Ruiz, Z. Model for the peptide-free conformation of class II MHC proteins. *PLoS One* **3**, e2403 (2008).

46. Patil, N.S. *et al.* Rheumatoid arthritis (RA)-associated HLA-DR alleles form less stable complexes with class II-associated invariant chain peptide than non-RA-associated HLA-DR alleles. *J Immunol* **167**, 7157-7168 (2001).

47. Nicholson, M.J. *et al.* Small molecules that enhance the catalytic efficiency of HLA-DM. *J Immunol* **176**, 4208-4220 (2006).

48. Day, C.L. *et al.* Ex vivo analysis of human memory CD4 T cells specific for hepatitis C virus using MHC class II tetramers. *J Clin Invest* **112**, 831-842 (2003).

49. Call, M.J. *et al.* In vivo enhancement of peptide display by MHC class II molecules with small molecule catalysts of peptide exchange. *J Immunol* **182**, 6342-6352 (2009).

Chapter 4: Signal Duration Can Determine Choice of Gene Transcription Program

Portions reprinted from "A model for How Signal Duration Can Determine Distinct Outcomes of Gene Transcription Programs" by Kevin D. Fowler, Vijay K. Kuchroo, and Arup K. Chakraborty, *In preparation.*

4.1 Introduction

In many examples in biology, a single transcription factor is able to activate multiple genes (1,2,3). Also, different receptors are able to activate the same transcription factor, but each leads to unique outcomes (4,5,6). How signal specificity is attained with all of this redundancy has long interested researchers. Manipulation of signal duration through the use of feedback loops, phosphatases, and ubiquitin ligases is one mechanism by which cells attain signal specificity when multiple receptors utilize the same pathway. For instance, both nerve growth factor (NGF) and epidermal growth factor (EGF) signal through the MAPK pathway, but NGF is able to generate a sustained ERK signal, while EGF generates a transient signal; sustained and transient signals in this case result in two different outcomes through the same pathway (6,7). It was recently discovered that NGF signaling leads to a positive feedback loop in the MAPK pathway, while EGF leads to a negative feedback loop, and this disparity accounts for the differences in signal duration (8). One mechanism cells can use to translate signal duration into different outcomes at the gene transcription level is through manipulation of immediate early gene (IEG) stability (9). ERK induces transcription of the IEG products and then can bind to and phosphorylate them. The phosphorylated form of the IEG is less susceptible to degradation allowing it to further assist in the activation of downstream programs. Transient signals are unable to induce the protected form of the IEG products and the signal degrades. The net result

is that the signal propagates through the genetic network for sustained signals or dies out for transient signals.

A simpler example of two receptors sharing the same signaling pathway, but leading to two different outcomes, is the IL-6 and IL-10 receptor. Both receptors activate signal transducer and activator of transcription 3 (STAT3), which forms dimers upon phosphorylation and enters the nucleus where it acts as a transcription factor. Despite the simplicity of the pathway, the two receptors induce different cellular behaviors: IL-6 elicits a pro-inflammatory response, while IL-10 signaling leads to an anti-inflammatory response (10). The anti-inflammatory response by IL-10 acts on a number of cell types including antigen presenting cells (APCs) and is characterized by the induction of gene products by STAT3, which inhibit the transcription of inflammatory genes (11). One key distinction between the two pathways is that the inhibitor, suppressor of cytokine signaling 3 (SOCS3) induced by STAT3, can bind to the IL-6 receptor, but cannot bind to the IL-10 receptor. This leads to IL-6 inducing a transient STAT3 signal, while IL-10 induces a sustained STAT3 signal (10). Two independent experiments demonstrated that blocking SOCS3's ability to inhibit IL-6 signaling leads to an anti-inflammatory response indistinguishable from that induced by IL-10 in macrophages (12,13).

Recent work by Behar et. al. is an example of how mathematical modeling can be utilized to propose various network architectures in which cells can make decisions by signaling through multiple receptors with shared components, while retaining signal specificity (14,15). These models focus on signal events upstream of transcription. We sought to identify a simple transcriptional model that would allow cells to make decisions based entirely on the duration of the input signal to the transcriptional network. Developed in the context of how signal duration manipulation by SOCS3 can lead to different outcomes from the IL-6 and IL-10 signaling

pathways, our model focuses on the choice whether to produce a generic inflammatory gene product I or a generic anti-inflammatory gene product A when activated by a common transcription factor pSTAT3.

4.2 Model

4.2.1 Transcriptional network model development

A transcriptional network was formulated to allow the cellular decision of whether to be pro-inflammatory or anti-inflammatory to be made by changes in activated pSTAT3 signal duration. The network consists of two genes (I and A) that are activated by the same transcription factor (Figure 4.1). The essential feature of such a network must be that a transient pSTAT3 signal leads to dominant production of the inflammatory gene (I), while a sustained pSTAT3 signal leads to dominant production of the anti-inflammatory gene A. In reality, there are many inflammatory and anti-inflammatory genes, but we will adopt a coarse-grained view of the system where all of these genes will be characterized by generic representative genes I and A, respectively. In the model, pSTAT3 dimers (pSTAT3) are allowed to bind to the promoter region of gene I (I_g) and gene A (A_g)

$$pSTAT3 + I_g \underset{k_{off\_T\_I}}{\overset{k_{on\_T\_I}}{\rightleftarrows}} pSTAT3 - I_g$$

$$pSTAT3 + A_g \underset{k_{off\_T\_A}}{\overset{k_{on\_T\_A}}{\rightleftarrows}} pSTAT3 - A_g$$

where the on and off rates can be different for the two genes. Different epigenetic modifications of the two genes could mean that one gene is more accessible than another, thus the possibility for different rates.

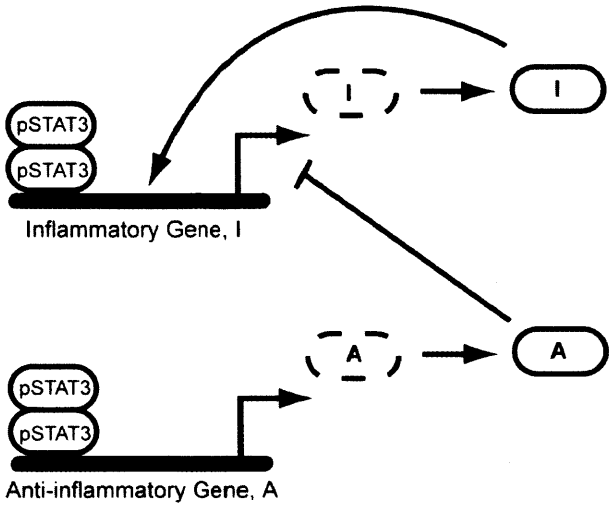

Figure 4.1. Transcriptional network that allows for cellular decisions based on signal duration. The "signal" in this mechanism is the ability of pSTAT3 to induce transcription of I or A. The cellular decision is based on the relative amounts of protein I or A produced. In this mechanism I can induce its own transcription in the absence of signal, pSTAT3. Protein A can bind to inflammatory gene I and inhibit its transcription.

DNA-bound pSTAT3 can induce transcription of I mRNA (I_m) and A mRNA (A_m), via reactions assumed to be assumed first order

$$pSTAT3 - I_g \xrightarrow{k_{trx,I,T}} I_m + pSTAT3 + I_g$$
$$pSTAT3 - A_g \xrightarrow{k_{trx,A,T}} A_m + pSTAT3 + A_g$$

where the rate constants of the form $k_{trx,I,T}$ should be read as the transcription of I in the presence of transcription factor, T (pSTAT3 dimer). It is assumed that the associated transcription factors unbind each time a transcription reaction is carried out. Due to the simplicity of the network, it was easy to also construct a model where transcription factors do not unbind each time mRNA is transcribed to verify that the qualitative behavior would not change. We found multiple combinations of parameters that lead to the same qualitative behavior in both models (Appendix

4), so we will only present results for the case where transcription factors unbind each time the transcription reaction is carried out.

After transcription, the mRNA of I and A can be translated to fully functional proteins in assumed first order processes

$$I_m \xrightarrow{k_{trl\_I}} I$$
$$A_m \xrightarrow{k_{trl\_A}} A$$

where species I and A represent the fully functional proteins.

The model also contains two types of feedback loops, which make the network sensitive to signal duration. Inflammatory protein I is allowed to bind to its own promoter and induce its own transcription in the presence or absence of pSTAT3 as given by

$$I + [pSTAT3]I_g \underset{k_{off\_B,B}}{\overset{k_{on\_I,I}}{\rightleftarrows}} [pSTAT3]II_g \xrightarrow[[k_{trx\_I,T}]]{k_{trx\_I,I}} I_m + [pSTAT3] + I_g + I$$

where [pSTAT3] indicates that pSTAT3 may or may not be present. If pSTAT3 is present, it is assumed that the rate of transcription is governed by whichever rate constant, $k_{trx,I,I}$ or $k_{trx,I,T}$, is greater. The ability of I to induce its own production in the absence of the signal through a positive feedback loop allows for the production of I even for a fast decaying signal as long as the decay rate of I is small enough to allow for the initiation of the positive feeback loop. The A gene has no positive feedback loops so it is entirely dependent on the signal and thus will not be produced in appreciable quantities by transient signals.

The network also contains a negative feedback loop where anti-inflammatory protein A is able to bind to the promoter of gene I and impede its transcription according to

$$A + [pSTAT3, I]I_g \underset{k_{off,..1,1}}{\overset{k_{on,..1,1}}{\rightleftarrows}} [pSTAT3, I]AI_g \xrightarrow{k_{trx,1,..1}} I_m + [pSTAT3, I] + I_g + A$$

where [pSTAT3,I] indicates that either pSTAT3 or I is bound to gene I. The ability of A to negatively regulate I is important in creating a regime where A can win out. If the inhibition is strong enough ($k_{trx,I,A} << 0$), A can shut down the production of I if A is present in great enough quantities. Sustained signaling may permit this scenario.

Another important aspect of the network is that all species, except genes, can decay at assumed first order rates

$$pSTAT3 \xrightarrow{k_{deg,T}} X$$
$$[I, A] \xrightarrow{k_{deg}} X$$
$$[I_m, A_m] \xrightarrow{k_{deg,m}} X$$

where [] represents either I or A. Biologically, the deactivation of I or A would be caused by ubiquitin ligases or phosphatases in the nucleus, which are assumed to be present in large enough concentrations so that the reactions are first order. The parameter, $k_{deg,T}$, is a measure of the duration of the signal. Large values of $k_{deg,T}$ indicate a highly transient signal, whereas small values $k_{deg,T}$ indicate a relatively sustained signal. In the context of IL-6 and IL-10 signaling, $k_{deg,T}$ is modified by ability or inability of SOCS3 to inhibit pSTAT3 signaling. We begin the simulation just after appreciable amounts of SOCS3 have been induced, which means that the signal has reached its maximum value and then begins to decay at time zero. For IL-6, this occurs at about 30 minutes after signaling has begun (13). Deactivation / degradation of I and A is allowed to occur whether or not the proteins are bound to genes. We also considered the case where deactivation / degradation of pSTAT3, I, and A is not allowed to occur when the

molecules are bound to genes and found by sensitivity analysis that this does not significantly affect the qualitative results of the model (Appendix 4).

4.3 Results and Discussion

4.3.1 Genes I and A exhibit different responses to changes in signal duration

Rate laws were written for each of the reactions in the model and the corresponding chemical master equations were solved using the Gillespie algorithm (16). We explicitly considered stochastic fluctuations in the number of molecules in this system via the Master equations because genes are often present in small copy numbers. The solution of the mean field equations could lead to the identification of signaling thresholds that in reality cannot be met due to fluctuations. For instance, the mean field solution to the model equations obtained via MATLAB predicts that the number of I molecules never reaches 50 molecules at any point in time for the set of parameters identified in Table 4.1 using a signal degradation rate of 0 (Figure 4.2A). However, the Gillespie algorithm shows that half of the trajectories of I cross 50; therefore it would be inaccurate to conclude that I never reaches the signaling threshold of 50 molecules (Figure 4.2A).

Table 4.1. Table of parameters used in the model. The results presented were robust to a range of parameters as indicated by the sensitivity analysis (Appendix 4).

$k_{on,T,I}$	0.015 molec^{-1} min^{-1}	$k_{trx,I,I}$	1.0 min^{-1}
$k_{on,T,A}$	0.015 molec^{-1} min^{-1}	$k_{trx,I,A}$	0 min^{-1}
$k_{on,I,I}$	0.015 molec^{-1} min^{-1}	$k_{trl,I}$	0.5 min^{-1}
$k_{on,A,I}$	0.015 molec^{-1} min^{-1}	$k_{trl,A}$	0.5 min^{-1}
$k_{off,T,I}$	0.5 min^{-1}	$k_{deg,T}$	0-10 min^{-1}
$k_{off,T,A}$	0.5 min^{-1}	k_{deg}	0.001 min^{-1}
$k_{off,I,I}$	0.5 min^{-1}	$k_{deg,m}$	0
$k_{off,A,I}$	0.01 min^{-1}	$pSTAT3_o$	100 molec.
$k_{trx,I,T}$	1.0 min^{-1}	I_g	2 molec.
$k_{trx,A,T}$	0.1 min^{-1}	A_g	2 molec.

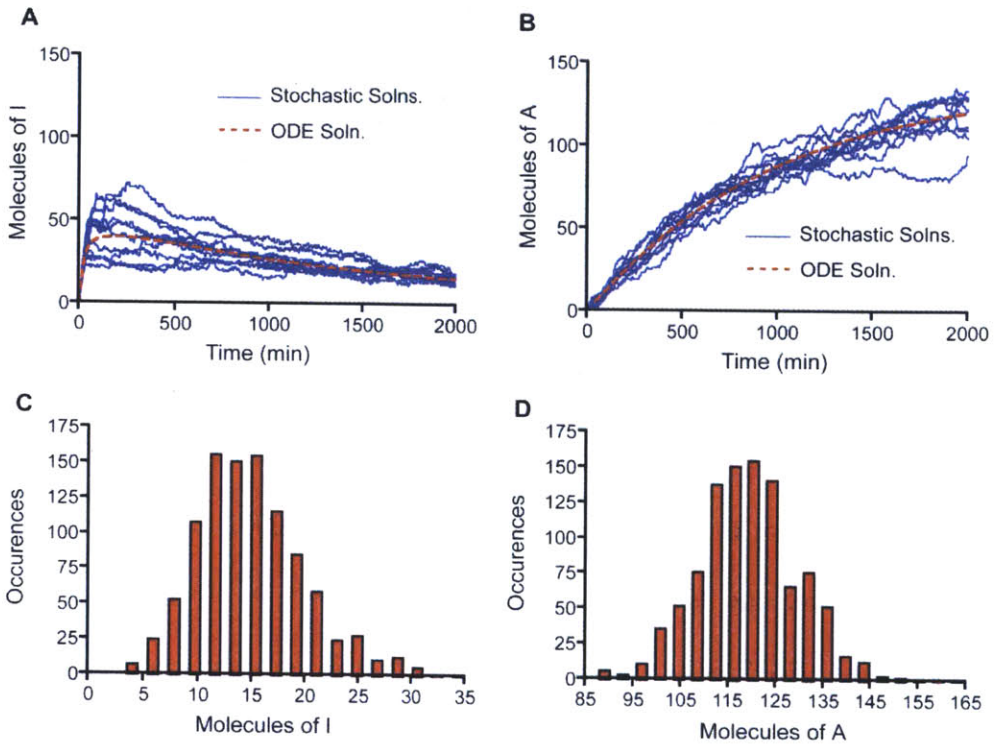

Figure 4.2. A-molecules are expressed in greater numbers for a sustained signal ($K_{deg,T}$ = 0 min^{-1}). (**A**) Time course trajectories for molecule I obtained by solution of the model equations using a mean field ODE solver (red curve) and ten times using the Gillespie Algorithm (10 blue curves). (**B**) Time course trajectories for molecule A obtained by solution of the model equations using a mean field ODE solver (red curve) and ten times using the Gillespie Algorithm (10 blue curves). (**C**) Histogram for molecule I obtained by solving the model equations using the Gillespie Algorithm 1000 times and recording the number of molecules at 2000 min. (**D**) Histogram for molecule A obtained by solving the model equations using the Gillespie Algorithm 1000 times and recording the number of molecules at 2000 min. Parameters for the model were obtained from Table 4.1.

We are more interested in the general qualitative behavior of the genetic network as opposed to fitting the results to actual data, so no attempt was made to use experimentally derived parameters relevant to a specific system. As a result, it is important to use sensitivity analysis to verify that the qualitative results of the model are robust over a range of parameters. Sensitivity analysis was performed according to the procedures outlined in the Appendix 4. The basic procedure was to divide all the parameters into nine different classes and testing all combinations of low, medium, and high values for each parameter class (Table A4.1). We then determined if the response could be switched from pro-inflammatory response to an anti-inflammatory response by changing the signal degradation rate for a given parameter set. In an initial search, 1809 parameter sets were identified that led to the desired qualitative behavior (Appendix 4).

A snapshot of the qualitative behavior of the model can be obtained by considering two values of $k_{deg,T}$ with all other parameters fixed at the values given in Table 4.1. A value of 1 for $k_{deg,T}$ corresponds to a transient signal, whereas a value of 0 for $k_{deg,T}$ corresponds to a sustained signal. Sensitivity analysis revealed that the mRNA degradation rate did not alter the results (Figure A4.6), so the rate of degradation for I and A mRNA was set to 0. We consider the case where the rate of transcription of I is the same whether its induced by pSTAT3 or by itself (i.e. $k_{trx,I,T} = k_{trx,I,I}$) and where the transcription of A is slower than the transcription of I (i.e. $k_{trx,A,T} < k_{trx,I,T}$, $k_{trx,I,I}$). The qualitative results are robust to a range of parameters including the case where the rate of transcription of I and A is the same and the case where the rate of transcription of A is greater than I as determined by parameter sensitivity analysis (Appendix 4).

For sustained signals, the number of I molecules peaks at early times and then degrades, while the number of A molecules increases steadily through time (Figure 4.2A and Figure 4.2B). There are no negative feedback loops on A, and so, for sustained signals, the increase in its

molecular levels is only hindered by its degradation. This is the cause for its steady increase with time. Conversely, I is strongly affected by the negative feedback loop at later times. Protein A is in high concentration at later times and is statistically likely to be bound to both copies of the I genes. In the parameter range chosen, A is able to bind tightly to the I gene and shuts down its production at later times. Once I production is shut down, the level of I gradually decreases due to its degradation / deactivation. The combined effect of the negative feedback loop and the degradation / deactivation reaction causes the peak in the number of I molecules at early times (Figure 4.2A).

An alternative way of viewing the data is to run 1000 trajectories, determine the molecular levels of I and A at "long times" (time = 2000 min), and construct a histogram. For sustained signals, the distributions appear similar in shape; however, I is at much lower levels than A (Figure 4.2C and Figure 4.2D). Therefore, these cells would appear to be producing mostly protein A if assayed at long times. This implies that the cells have made the decision to activate the anti-inflammatory gene program for sustained signals, an idea which will be explored in more detail in the next section.

For transient signals, the molecular levels of I increase gradually with time in some of the trajectories, while A remains at or around zero in all of the trajectories (Figure 4.3A and Figure 4.3B). Protein A is entirely signal-dependent so it is not able to be produced in significant quantities when the signal degrades too quickly. As a result, the negative feedback loop is not effective for highly transient signals and the production of I is limited only by its ability to initiate the positive feedback loop. For this particular degradation rate, $k_{deg,T} = 1$, only some of the trajectories of I led to nonzero amounts, which is clearly observed in the long time histogram (Figure 4.3C). The bistability that results is entirely stochastic in nature, evident by the fact that

the mean field time trajectory for I follows the average of the nonzero curves (Figure A4.1) (17). Bistability results from the "roll of the dice" in determining whether or not the positive feedback loop is initiated before the signal and resulting I molecules degrade. It appears that bistability develops at approximately $k_{deg,T} = 0.4\ min^{-1}$ (Figure 4.4). As the signal becomes more transient in nature, an increasing number of I trajectories remain at I=0. In many biological systems bistability serves as a tool in making cellular decisions, but in this system it is simply a breakdown mechanism that does not have relevance, and may simply be a nuisance (18, 19, 20).

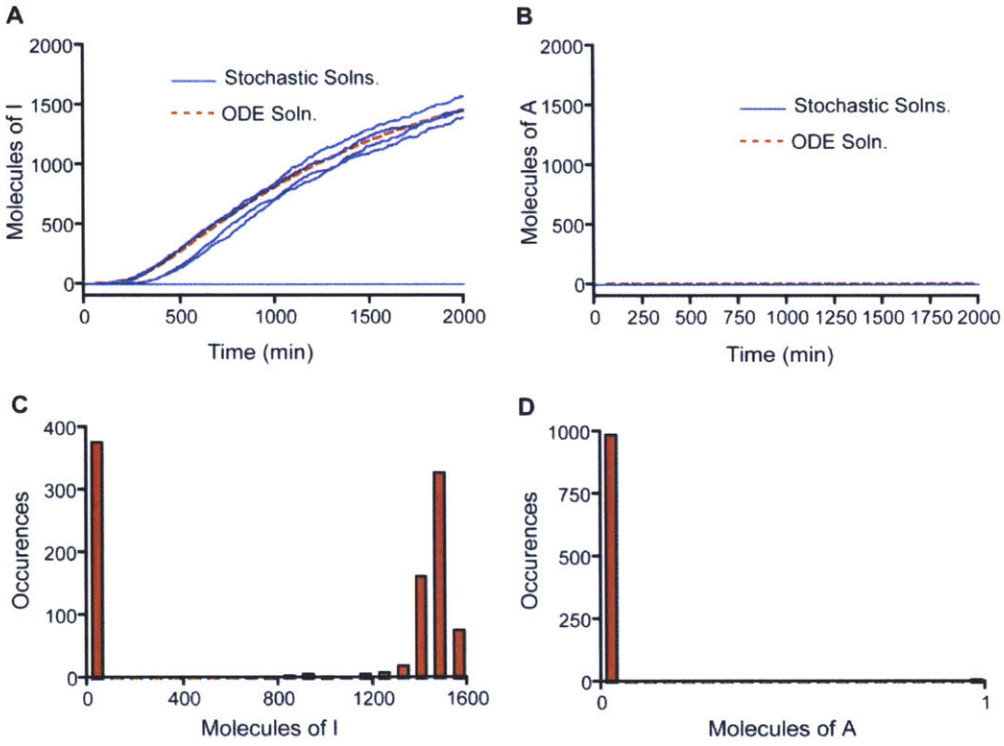

Figure 4.3. I-molecules are expressed in greater numbers for a transient signal ($K_{deg,T}$ = 1.0 min^{-1}). (**A**) Time course trajectories for molecule I obtained by solution of the model equations using a mean field ODE solver (red curve) and ten times using the Gillespie Algorithm (10 blue curves). (**B**) Time course trajectories for molecule A obtained by solution of the model equations using a mean field ODE solver (red curve) and ten times using the Gillespie Algorithm

(10 blue curves). (**C**) Histogram for molecule I obtained by solving the model equations using the Gillespie Algorithm 1000 times and recording the number of molecules at 2000 min. (**D**) Histogram for molecule A obtained by solving the model equations using the Gillespie Algorithm 1000 times and recording the number of molecules at 2000 min. Parameters for the model were obtained from Table 4.1.

In silico knock-out experiments can be performed where either the positive or negative feedback loops are removed. When the positive feedback loop is removed, the results for sustained signals are virtually unchanged since the negative feedback loop dominates (Figure A4.2). For the transient case, both I and A would remain at approximately zero since both would be entirely signal dependent. The end result of blocking the positive feedback loop is that the cell would activate the anti-inflammatory gene program for sustained signals or neither program for transient signals. When the negative feedback loop is knocked out, the results for transient signals remain unchanged since the positive feedback loop dominates the behavior (Figure A4.3). For sustained signals, both I and A would be produced in significant quantities. There would no longer be a peak in I at short times, but a steady increase as a function of time. The end result of blocking the negative feedback loop is that the cell would choose the pro-inflammatory gene program for transient signals. The model predicts that both programs would be initiated for sustained signals, but this is likely not biologically relevant since the ability of anti-inflammatory genes to act "anti-inflammatory" has been removed by the deletion of the negative feedback loop. Therefore, sustained signals would likely lead to pro-inflammatory cells in this system. If both feedback loops were removed, both I and A would be entirely signal dependent and would exhibit similar qualitative behavior (Figure A4.4). The end result of

blocking both the positive and negative feedback loops is that the cell would choose both I and A for sustained signals or neither for transient signals. Again, since the negative feedback has been deleted, it would likely be observed that the cells are pro-inflammatory for sustained signals or neither for transient signals.

4.3.2 Tuning signal duration as a tool for cellular decisions

From the two test values of $k_{deg,T}$, it appears as if this mechanism could be a viable tool for making cellular decisions based entirely on signal duration modification. To further probe this idea, we constructed the following in silico experiment. Thousands of I and A trajectories similar to those obtained in the last section were generated for $k_{deg,T}$ values ranging from 0 to 10 with all other parameters fixed at the values given in Table 4.1. It is assumed that the downstream gene programs (inflammatory or anti-inflammatory) activated by I or A are only initiated when the respective molecules cross a threshold value in molecular number at any point in the time trajectory. To measure this computationally, the maximum point in each trajectory was compared to a threshold value and the number of I and A trajectories crossing the threshold was recorded for each value of $k_{deg,T}$. The percent of I or A trajectories crossing the threshold directly corresponds to the percent of cells that exhibit pro-inflammatory or anti-inflammatory responses in an equivalent biological experiment since each trajectory corresponds to 1 cell.

Cells with sustained signals ($k_{deg,T} < 10^{-3}$) clearly exhibit an anti-inflammatory response while cells with transient signals ($0.02 < k_{deg,T} < 1$) clearly exhibit an inflammatory response (Figure 4.4A and Figure 4.4B). There is a small crossover region for mildly transient signals ($10^{-3} < k_{deg,T} < 0.02$), the behavior in which is determined by the choice in downstream threshold values for I and A. For the given set of parameters, it is clear that I has the capability of attaining a

higher maximal value since its transcription rate is an order of magnitude higher than A and since I has a positive feedback loop (Figure 4.2B and Figure 4.3A). Therefore, one natural choice is to set the downstream threshold higher for I to account for this difference. With different I and A threshold values, the inflammatory and anti-inflammatory response curves overlap such that a mixture of cells exhibiting either response would be observed in the crossover region (Figure 4.4A). An alternative choice is to set the thresholds to be the same for both I and A, which leads to no response in the crossover region (Figure 4.4B). Setting a downstream threshold is an arbitrary process, which merely shifts the inflammatory and anti-inflammatory response curves, but does identify two distinct crossover region behaviors that may both have biological relevance.

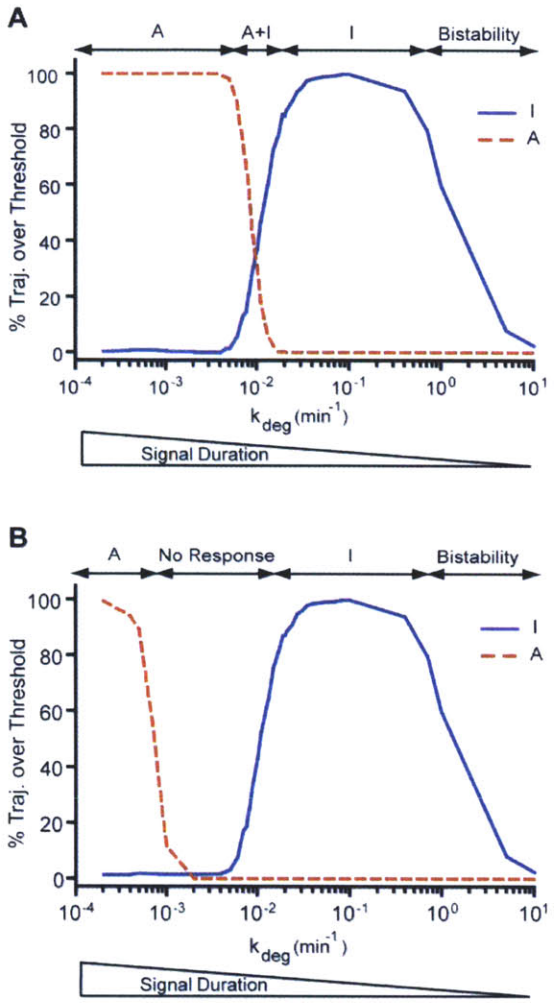

Figure 4.4. Cellular decisions can be made by manipulating signal duration. The maximum amount of I and A observed in 1000 time course trajectories measured out to 2000 min was compared to an arbitrary threshold and the percentage of trajectories crossing the threshold was computed for a wide range of signal degradation rates. (**A**) Different downstream thresholds were chosen for I and A such that both responses are observed in the intermediate crossover region. The I threshold was set to 100 molecules, while the A threshold was set to 20 molecules. (**B**) Using the same downstream threshold for both I and A leads to no response observed in the

intermediate crossover region. The I and A thresholds were taken to be 90 molecules. Parameters for the model were obtained from Table 4.1.

One difficulty in performing this analysis is choosing where to set the long time cutoff for when an inflammatory or anti-inflammatory response can occur. For instance, it would not necessarily be biologically relevant if it takes several days of sustained signaling for A to cross its signaling threshold. For the purposes of this study, we arbitrarily chose this cutoff time to be 2000 minutes (~1.5 days). Immediate early gene transcription is on the order of minutes (21), while Th17 differentiation is on the order of 5 days (22). Choosing 1.5 days as the cutoff seemed like a reasonable intermediate choice. An example of a cellular decision becoming evident after 1 day is in Th17 differentiation, where IL-17 mRNA starts to be transcribed in appreciable quantities at this time (unpublished observations). Using 3.5 days as the cutoff time revealed an important limitation of our model. For any signal with a degradation rate greater than zero, I will eventually be produced in significant quantities if the simulation goes out to long enough times (Figure A4.5A). The cause of this limitation is highlighted by the time course of I for a signal degradation rate of 0 (Figure 4.2). Even with a sustained signal, I does not go to zero since its potent positive feedback loop coupled with the sustained signal are still active in the moments when a given A molecule bound to the I gene unbinds or is deactivated, which can counteract the decrease in I due to its own degradation. For all cases where the signal degradation rate is not zero, A will eventually decay to zero since it is signal dependent. After A has decayed to low enough numbers, it can no longer prevent the few remaining I molecules from initiating the positive feedback loop. Performing the threshold analysis at 3.5 days, I and A thresholds can still be chosen to allow for a cellular decision to be made based on signal duration changes, but

the peak in I is broader and the crossover region occurs at smaller values of the signal degradation rate (Figure A4.5B). One way to deter this limitation is to decrease the degradation rate of A, so that the negative feedback loop will remain active even at long times (Figure A4.5C). We do not believe that this limitation would be relevant under most biological situations since it would take longer than 1.5 days of steady signaling without any other changes within the cell for it to be an issue. Conceivably, once a pro-inflammatory or anti-inflammatory response was selected, the cell would have other means for shutting down the other set of genes. In this sense, the model is not entirely self-contained.

4.3.3 Amplitude only significantly affects cellular decisions in the crossover region

Intracellular signals are generally described by two variables, signal amplitude and duration. Often in the literature, these two variables are combined into one quantity, the strength of signal. One interpretation of the strength of signal is the integrated signal, which is the area under the curve on a plot of signal strength vs. time. The gene transcriptional network depicted in Figure 4.1 was formulated to allow for disparate cellular decisions based strictly on differences in signal duration. To declare the cellular decisions made in the transcriptional model as strictly dependent on signal duration, it was also necessary to study the qualitative effect of modifying the signal amplitude.

The effects of amplitude modification were determined by setting the initial value of pSTAT3 molecules to different amounts and using the same procedure that was used to generate Figure 4.4. We observed that decreasing amplitude from 100 molecules of pSTAT3 to 10 molecules shifted the I and A curves to the left without significantly altering their shape (Figure 4.5). The effects of amplitude modification can be observed within the crossover region from the

inflammatory to anti-inflammatory response in that a 10-fold decrease in signal amplitude would shift the crossover from occurring at a degradation rate of 0.01 min^{-1} to 0.001 min^{-1}. The production of A is entirely signal dependent, so significant decreases in the amount of pSTAT3 molecules translates into significant decreases in the amount of A molecules produced during the lifetime of the signal. As the number of A molecules is reduced, I is less regulated and will eventually win out. The effect of reducing pSTAT3 on the number of A molecules produced during the lifetime of the signal can partially be compensated for by increasing the lifetime of the signal, i.e. decreasing $k_{deg,T}$, which accounts for the shift in the curves to the left. The crossover region is susceptible to these effects since it is at the edges of the inflammatory and anti-inflammatory response regimes.

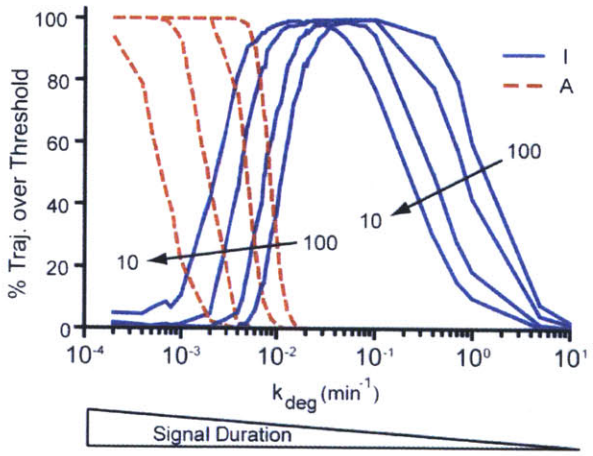

Figure 4.5. Altering the initial signal amplitude shifts the I and A curves, but does not affect their shape. The four sets of curves were generated using initial concentrations of 10, 20, 50, and 100 molecules of pSTAT3, respectively. For each initial concentration, the maximum amount of I and A observed in 1000 time course trajectories measured out to 2000 min was compared to an arbitrary threshold and the percentage of trajectories crossing the threshold was computed for a wide range of signal degradation rates. The I threshold was set to 100 molecules, while the A

threshold was set to 20 molecules. Parameters for the model were obtained from Table 4.1 unless otherwise noted.

Amplitude modification also affects significantly transient signals ($k_{deg,T} > 0.1$ min^{-1}) by shifting the region of bistability to lower $k_{deg,T}$ values as amplitude is decreased. As an example, consider a $k_{deg,T}$ value of 0.2 min^{-1}. At an amplitude of 100 pSTAT3 molecules, 100% of cells assayed would exhibit an inflammatory response. With a 10-fold decrease in amplitude, 50% of cells would exhibit an inflammatory response, while the other 50% of cells would exhibit no response. Therefore, amplitude only affects the number of cells exhibiting a given response for transient signals, but does not affect the type of response. The shift in the bistable region is also due to the fact that a decrease in signal amplitude can be partially compensated for by increasing the lifetime of the signal. Highly transient, low amplitude signals do not lead to any response since they do not have enough strength to kick off the positive feedback loop. Signals that are moderately sustained ($k_{deg,T}<0.001$ min^{-1}) or moderately transient ($0.1 < k_{deg,T} < 0.01$), are unaffected by these changes in amplitude.

Decreasing the amplitude to five or less leads to both inflammatory and anti-inflammatory responses for sustained signals in some of the trajectories, unless the threshold for an inflammatory response is increased from that used to generate Figure 4.5 (data not shown). Since the transcription rate of I is faster than A, I is able to kick off the positive feedback loop before appreciable amounts of A are produced in some of the trajectories. At later times when appreciable amounts of A are produced, the I signal shuts down but had already crossed the inflammatory response threshold leading to an observed inflammatory response starting at early times also an anti-inflammatory response at later times.

4.3.4 Model predicts that IL-6 will promote an anti-inflammatory response in SOCS-/- cells

Another key difference between the IL-10R and the IL-6R, besides their differing interactions with SOCS3, is that the IL-10R has two motifs for STAT3 activation while the gp130 subunit of the IL-6R has four, leading to the IL-6R inducing a higher amplitude STAT3 signal (13,23,24). Given that IL-6 induces a higher amplitude signal than IL-10, one could conclude that strong signals induce an inflammatory response, while weak signals induce an anti-inflammatory response. In this definition of signal strength, amplitude is the defining feature. If an experiment were performed where SOCS3 was no longer able to inhibit IL-6 signaling, the high amplitude signal would go from being transient to sustained, and thus would have even higher signal strength than before. Thinking about this problem in terms of signal strength, one would predict that IL-6 would still induce an inflammatory response when SOCS3 inhibition has been removed.

A revealing experiment performed by Yasukawa et. al. in which they exposed SOCS3-/- macrophages to IL-6 and LPS and measured the concentration of two pro-inflammatory cytokines (TNF and IL-12(p40)) in the supernatant showed just the opposite (12). LPS induces an inflammatory response in macrophages, so a decrease in inflammatory cytokine production would be considered anti-inflammatory. As the dosage of IL-6 was increased, the pro-inflammatory cytokine concentration dropped meaning that IL-6 was acting as an anti-inflammatory cytokine on the SOCS3-/- macrophages. This puzzling result cannot be explained by a signal strength model where signal strength is essentially just a measure of the amplitude of the signal.

Our model is capable of making a prediction for how IL-6 will act on SOCS3-/- by making very few assumptions. We assume that IL-6 induces a moderately transient pSTAT3 signal that can roughly be approximated by a $k_{deg,T}$ value of 0.1 min^{-1} in WT macrophages. The second assumption is that IL-10 induces a slowly decaying pSTAT3 signal that can be approximated by a $k_{deg,T}$ value of 0.003 min^{-1} in both SOCS3-/- and WT macrophages. IL-6 and IL-10 would conceivably induce similarly decaying pSTAT3 signals in SOC3-/- macrophages, so we can use the same $k_{deg,T}$ value. In their experiment, Yasukawa et. al. measure concentrations of secreted inflammatory cytokines, which in our model translates to counting the percentage of trajectories (cells) that cross the imposed threshold value of I at any point for a set value of $k_{deg,T}$, which is characteristic to the macrophage type and the type of cytokine added along with LPS. By carrying out this analysis for a variety of initial amplitudes, we can make a prediction about how the macrophages will respond to increasing dosages of either IL-6 or IL-10. Since LPS induces an inflammatory response on its own, it is assumed that 100% of the cells would be pro-inflammatory in the absence of IL-6 and IL-10. Therefore, until a large enough amplitude is reached where gene A can cause a drop in the number of trajectories which cross the threshold value of I, it is assumed that all the cells will remain pro-inflammatory.

Using these assumptions, it is clear that the model predicts IL-6 will be anti-inflammatory when acting on SOCS3-/- macrophages (Figure 4.6). The model also captures the observed phenomenon that as the pSTAT3 amplitude is increased (i.e. the IL-6 dose is increased), IL-6 has a stronger anti-inflammatory effect. Since there is no distinction between IL-10 acting on SOCS3-/- or WT macrophages, the model predicts that no distinction will be seen experimentally, as was observed (12). For transient signals, the model predicts a pro-inflammatory response, which is why the percentage of inflammatory cells remains at 100% for

all amplitudes when WT macrophages are exposed to IL-6. If it were IL-6 alone, there would be a ramping up of the percentage of inflammatory cells at low amplitudes since a basal level of signaling is required to initial the positive feedback loop. However, since LPS induces an inflammatory response on its own, the ramping up period is not observed in the figure. There is no amplitude range for transient signals where A is capable of decreasing the percentage of inflammatory cells.

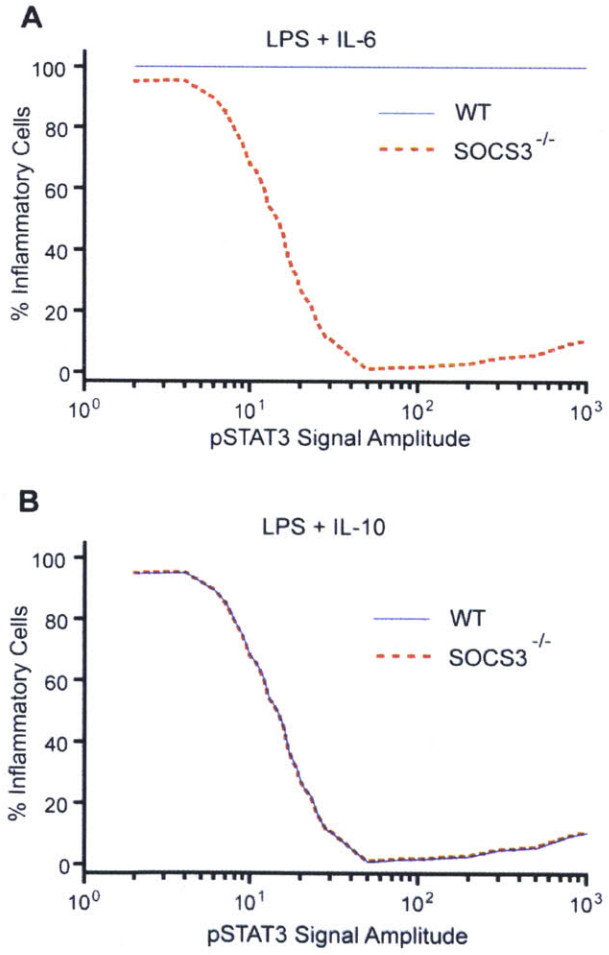

Figure 4.6. Model predicts that IL-6 will be anti-inflammatory in SOCS3-/- cells when given some inflammatory stimulus such as LPS for most pSTAT3 signal amplitudes. (**A**) Percentage of inflammatory cells predicted for transient pSTAT3 signals (WT) and sustained signals

(SOCS3-/-) when the cells are exposed to LPS and IL-6. The value of $k_{deg,T}$ used to represent the WT condition was 0.1 min^{-1}, while a $k_{deg,T}$ value of 0.003 min^{-1} was used to represent the SOCS3-/- condition. (**B**) Percentage of inflammatory cells predicted for sustained pSTAT3 signals (WT and SOCS3-/-) when the cells are exposed to LPS and IL-10. The value of $k_{deg,T}$ used to represent these conditions was 0.003 min^{-1}. For each initial concentration of pSTAT3, the maximum amount of I observed in 1000 time course trajectories measured out to 2000 min was recorded and the percentage of trajectories crossing the inflammatory threshold (100 I molecules) was determined for a value of $k_{deg,T}$ corresponding to the signal duration expected for each condition. Parameters for the model were obtained from Table 4.1 unless otherwise noted.

Yoshimura (10) has proposed that sustained STAT3 signals are essential for anti-inflammatory responses while transient signals promote inflammation, which is consistent with our model. The model serves as a tool for visualizing how the duration of the signal can lead to two different responses from the same genetic network activated by the same transcription factor from two different pathways. As further evidence of signal duration being a defining feature in determining the inflammatory response, El Kasmi et. al. also developed a system for analyzing this problem(13). They transfected macrophages with an altered form of the EPO receptor (EPOR) that activated STAT3 and was not susceptible to SOCS3 inhibition. The unaltered form of the EPOR activates STAT5. This altered form of the EPOR induced an anti-inflammatory response indistinguishable from IL-10, which also supports the hypothesis that signal duration is a determinant of whether or not a response is inflammatory or anti-inflammatory (13).

While it is true that many different cytokines activate STAT3 that may or may not induce an inflammatory or anti-inflammatory response, often these cytokines activate multiple STAT

molecules, such as STAT1 or STAT5, in addition to STAT3. It is beyond the scope of this analysis to determine how genes activated by other STATs affect the decision to be pro-inflammatory or anti-inflammatory. Since different STATs can be activated by the same receptor, heterodimer formation may be prevalent and it is difficult to predict how this may impact a network with this structure.

One could argue that the proposed transcriptional network model cannot easily account for common gene expression. The key wiring in our model that makes it sensitive to changes in signal duration is the positive and negative feedback loops. Common genes would not necessarily need to have the same wiring as the anti-inflammatory / inflammatory genes. As an example, consider the example of a common gene C that is also induced by pSTAT3. If this gene had a positive feedback loop, significant amounts of C would be produced from both transient and sustained signals. Even in the absence of a positive feedback loop, a transient signal still could produce significant amounts of C for high amplitude signals and low values of the C degradation / deactivation.

We have provided the structure of a gene transcriptional network which is sensitive to changes in signal duration. The essential feature of the model is that both genes of interest are activated by the same transcription factor and that one of the genes has a positive feedback loop to sustain itself in the absence of the main signal, but is also negatively regulated by the opposing gene. Even though the model was presented in the context of IL-6 / IL-10 signaling, it may be applicable to a range of biological networks which are sensitive to signal duration. Though most genetic networks are highly complex, this may be an underlying basic structure. We believe that the model may be applicable to IL-6 / IL-10 signaling since all essential steps of the model have been observed except for the positive feedback loop, namely that STAT3 induces both

inflammatory and anti-inflammatory genes and that the anti-inflammatory genes inhibit the inflammatory genes. Experimentation would be necessary to identify a positive feedback loop in the inflammatory gene network in order for the model to be fully validated. Bioinformatic techniques could be used to determine whether inflammatory genes have the potential to bind to the promoter region of other inflammatory genes. Gene array analysis could then be used to verify the binding. Mutations to these promoter sites could then be used to knockout the positive feedback loop. Our model would then predict that IL-6 would not be able to induce an inflammatory response (Figure A4.2). Further analysis will be necessary to identify more systems where the model is applicable.

4.4 References

1. Müller MR, Rao A (2010) NFAT, immunity and cancer: a transcription factor comes of age. *Nat Rev Immunol* **10**:645-656.

2. Li Q, Verma IM (2002) NF-κB regulation in the immune system. *Nat Rev Immunol* **2**:725-734.

3. Boros J, Donaldson IJ, O'Donnell A, Odrowaz ZA, Zeef L, et al. (2009) Elucidation of the ELK1 target gene network reveals a role in the coordinate regulation of core components of the gene regulatory machinery. *Genome Res* **19**:1963-1973.

4. Murray PJ (2007) The JAK-STAT signaling pathway: input and output integration. *J Immunol* **178**:2623-2629

5. Okkenhaug K, Vanhaesebroeck B (2003) PI3K in lymphocyte development, differentiation, and activation. *Nat Rev Immunol* **3**:317-330.

6. Marshall CJ (1995) Specificity of receptor tyrosine kinase signaling: transient versus sustained extracellular signal-regulated kinase activation. *Cell* **80**:179-185.

7. Kholodenko BN (2007) Untangling the signaling wires. *Nat Cell Biol* **9**:247-249.

8. Santos SDM, Verveer P, Bastiaens PIH (2007) Growth factor-induced MAPK network topology shapes Erk response determining PC-12 cell fate. *Nat Cell Biol* **9**:324-330.

9. Murphy LO, MacKeigan JP, Blenis J (2004) Molecular interpretation of ERK signal duration by immediate early gene products. *Mol Cell Biol* **24**:144-153.

10. Yoshimura A, Naka T, Kubo M (2007) SOCS proteins, cytokine signaling and immune regulation. *Nat Rev Immunol* 7:454-465.

11. Murray PJ (2005) The primary mechanism of the IL-10-regulated anti-inflammatory response is to selectively inhibit transcription. *Proc Natl Acad Sci U S A* **102**:8686-8691.

12. Yasukawa H, Ohishi M, Mori H, Murakami M, Chinen T, et al. (2003) IL-6 induces an anti-inflammatory response in the absence of SOCS3 in macrophages. *Nat Immunol* **4**:551-556.

13. El Kasmi KC, Holst J, Coffre M, Mielke L, de Pauw A, et al. (2006) General nature of the STAT3-activated anti-inflammatory response. *J Immunol* **177**:7880-7888.

14. Behar M, Dohlman HG, Elston TC (2007) Kinetic insulation as an effective mechanism for achieving pathway specificity in intracellular signaling networks. *Proc Natl Acad Sci U S A* **104**:16146-16151.

15. Behar M, Hao N, Dohlman HG, Elston TC (2007) Mathematical and computational analysis of adaptation via feedback inhibition in signal transduction pathways. *Biophys J* **93**:806-821.

16. Gillespie DT (1977) Exact stochastic simulation of coupled chemical reactions. *J Phys Chem* **81**:2340-2361.

17. Artyomov MN, Das J, Kardar M, Chakraborty AK (2007) Purely stochastic binary decisions in cell signaling models without underlying deterministic bistabilities. *Proc Natl Acad Sci U S A* **104**:18958-18963.

18. McClean MN, Mody A, Broach JR, Ramanathan S (2007) Cross-talk and decision making in MAP kinase pathways. *Nat Gen* **39**:409-414.

19. Losick R, Desplan C (2008) Stochasticity and cell fate. *Science* **320**:65-68.

20. Das J, Ho M, Zikherman J, Govern C, Yang M, et al. (2009) Digital signaling and hysteresis characterize Ras activation in lymphoid cells. *Cell* **136**:337-351.

21. Sun H, Charles CH, Lau LF, Tonks NK (1993) MKP-1 (3CH134), an immediate early gene product, is a dual specificity phosphatase that dephosphorylates MAP kinase in vivo. *Cell* **75**:487-493

22. Bettelli E, Carrier Y, Gao W, Korn T, Strom T, et al. (2006) Reciprocal developmental pathways for the generation of pathogenic effector Th17 and regulatory T cells. *Nature* **441**:235-238.

23. Moore KW, de Waal Malefyt R, Coffman RL, O'Garra, A (2001) Interleukin-10 and the interleukin-10 receptor. *Annu Rev Immunol* **19**:683-765.

24. Kamimura D, Ishihara K, Hirano, T (2003) IL-6 signal transduction and its physiological roles: the signal orchestration model. *Rev Physiol Biochem Pharmacol* **149**:1-38.

Chapter 5: Signal specificity amongst STAT1 and STAT3 inducing cytokines in the context of Th17 differentiation

Portions reprinted from "Clever Title About Signal Specificity" by Kevin D. Fowler, Anneli Peters, and Vijay K. Kuchroo, *In preparation.*

5.1 Introduction

Key orchestrators of the adaptive immune system are CD4+ T cells. Depending on activation conditions and the cytokine milieu, these cells can differentiate into a variety of effector cells which are often characterized by the cytokines that they secrete. It was originally believed that there were two types of effector cells, Th1 and Th2 cells[1, 2]. It was later discovered in the context of autoimmune inflammation that there was another lineage of effector cells, Th17 cells[3, 4, 5]. These pro-inflammatory effector cells can be induced *in vitro* by culturing naïve CD4+ T cells under activating conditions in the presence of Interleukin-6 (IL-6) and transforming growth factor-β (TGF-β)[6, 7]. How these two pathways overlap to lead to the induction of the Th17 differentiation program remains an outstanding problem in the field of immunology. The first place to look for overlap between the two cytokines is at the membrane-proximal signaling level. IL-6 primarily signals through the JAK/STAT pathway[8] while TGF-β signals primarily through the SMAD pathway[9], so there is no obvious overlap in their signaling pathways.

IL-6 is thought to primarily activate Signal Transducer and Activator of Transcription-3 (STAT3)[10], so it is likely that its primary input to the genetic network governing Th17 differentiation is STAT3. It has been shown quite clearly that STAT3 is necessary for induction of Th17 cells as evidenced by a nearly complete loss of IL-17 secretion in its absence[11]. IL-6 is just one of a number of cytokines that activate STAT3, but yet it remains the most potent inducer

of IL-17 producing cells. IL-10, an anti-inflammatory cytokine, induces pSTAT3 (the active form of STAT3)[12, 13]. IL-21 activates STAT3[14] and induces weak, but noticeable, IL-17 secretion in the presence of TGF-β[15]. IL-27 is an anti-inflammatory cytokine[16, 17, 18] which activates STAT3[19] and is a potent inhibitor of Th17 differentiation[21].

How four different STAT3-inducing cytokines can cause such a large range of effects on Th17 differentiation is another standing question in the field[22]. There is another STAT protein induced by these four cytokines, STAT1[22], which adds another layer of complexity to their signaling pathways and may help account for the differences observed. It has been shown that IL-27 completely loses its ability to inhibit Th17 differentiation in STAT1 knockout mice (S1KO)[20, 22]. Therefore STAT1 must be an inhibitory transcription factor in the Th17 differentiation pathway. A simple theory to account for all of these observations would be that IL-6 induces mostly pSTAT3, IL-27 induces mostly pSTAT1, and IL-21 and IL-10 induce some combination of the two. One way to test this theory would be to comparatively measure STAT1 and STAT3 activation amongst the four cytokines. Previous studies have used Western blots or flow cytometry to measure STAT activation by IL-21[23], IL-6 and IL-10[12, 24], and IL-6 and IL-27[19], in a variety of cell types, but not in the same study or same cell type so it is impossible to compare the amplitude of STAT activation for all four cytokines.

We sought to investigate the issue of cytokine specificity in the context of Th17 differentiation by measuring the STAT1 and STAT3 activation profiles for the four different cytokines of interest (IL-6, IL-10, IL-21, and IL-27) in a systematic way. After obtaining the single cytokine activation profiles, we will measure the activation profiles for pairs of cytokines to see how the single cytokine profiles would change upon addition of other cytokines. Next, we see how the STAT3 activation profiles change for some cytokines in the absence of STAT1. These three

experiments combined will allow us to see how different STAT1 and STAT3 activation profiles affect Th17 differentiation and ultimately allow us to assess how the cytokines of interest can behave differently despite activating the same two transcription factors.

5.2 Results

5.2.1 Normalization method allows for cytokine comparison

We sought to find a method which would allow us to reproducibly and reliably characterize the signaling pathways of four cytokines of interest (IL-6, IL-10, IL-21, and IL-27) at early times in order to gain insight into why the cytokines behave differently despite activating the same two transcription factors, STAT1 and STAT3. Measurements of pSTAT1 and pSTAT3 levels were made only during the first 3-4 hours for two reasons. First, we wanted to be able to isolate CD4+ T cells, culture them with the various cytokines, stain the cells, and measure the STAT activation using FACS comfortably in one day, which less than 3-4 hrs of cytokine stimulation allowed. Second, we wanted to be sure that the STAT activation levels were entirely attributable to the cytokine of interest and not the sum of activation by the cytokine of interest and other uncontrolled amounts of secreted cytokines. Measuring at times less than 3-4 hours allowed us to comfortably neglect the effect of secreted cytokines. While in culture with the various cytokines, the cells were also exposed to plate-bound α-CD3 / α-CD28 since we were ultimately interested in comparing these cytokines of interest in the context of Th17 differentiation, which requires the presence of TCR stimulation.

Given all of the conditions we sought to measure to perform a good comparison of the differences in STAT activation amongst the cytokines of interest, it became apparent that using Western Blots would not be feasible. The measurement of band intensity is only semi-quantitative and it would be impossible to put all the conditions onto one membrane to allow for a good comparison. While it may be feasible to devise a way to normalize using some standard blot intensity, it was clear that flow cytometry was the better choice due to ease of measurement and the availability of a more quantitative result. It was impractical to do all of the flow cytometry measurements in one day so we devised a way to put all of our data collected over several months of separate experiments onto the same curve. Using the MFI (mean fluorescence intensity), we were able to extract just one number from each FACS measurement that could be plotted and compared to other samples. Daily variations in FACS measurements and mouse to mouse variations could be corrected for by measuring a set condition which gave a high signal and a set condition which gave a basal signal every day that measurements were taken. After taking measurements at numerous conditions, it became clear that the maximum signal obtained for both pSTAT1 and pSTAT3 was from cells that received 15 minutes of IL-6 stimulation while the minimum observed signal for both pSTATs was from unstimulated cells (Figure 5.1). Therefore, in every experiment we always had at least 2 wells of cells that received 15 minutes of IL-6 stimulation and 2 wells of cells that received no supplemental cytokine stimulation. That days measurements could then be normalized to all other measurements using Equation 5.1.

$$Normalized\ pSTAT = 100 * \frac{(MFI_{Sample} - MFI_{Untreated})}{(MFI_{IL6,15min} - MFI_{Untreated})} \quad \text{(Equation 5.1)}$$

In each experiment, IL-6 at 15 minutes will have a value of 100 for both pSTAT1 and pSTAT3, whereas a value of 0 indicates a basal level of STAT activation. It is important to note that pSTAT1 and pSTAT3 are normalized using different values so a value of 100 for pSTAT1 and a value of 100 for pSTAT3 does not necessarily indicate that there are equivalent levels of the two transcription factors at the molecular level. The values observed for $MFI_{IL6,15min}$ / $MFI_{untreated}$ were typically 1.5-2.0 for pSTAT3 and 8.0-15.0 for pSTAT1. As a result, significantly less variation was observed in the normalized pSTAT1 measurement since there was much greater separation between the max signal and the background than that observed with pSTAT3.

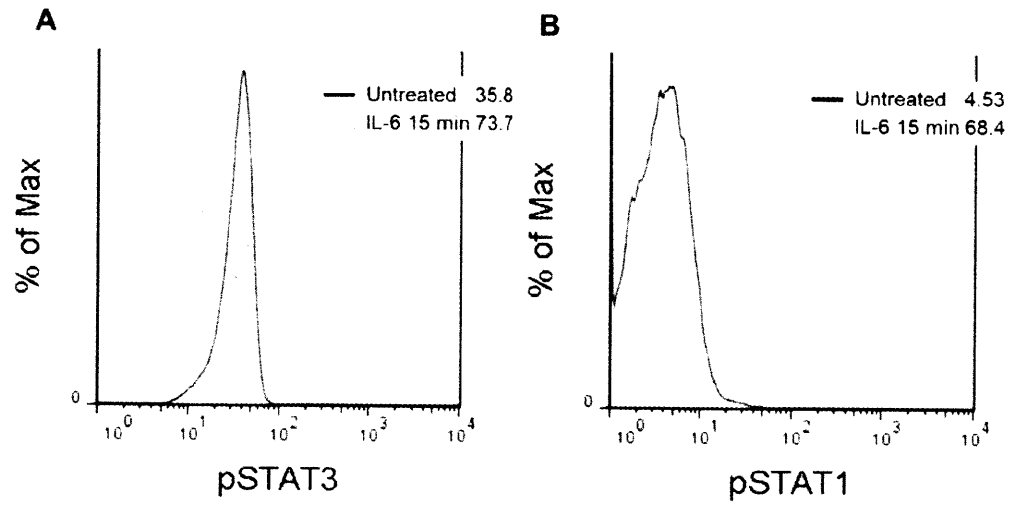

Figure 5.1. Maximum observed signal to noise ratios for pSTAT1 and pSTAT3. (**a**,**b**) Flow cytometry measurement of (**a**) pSTAT3 and (**b**) pSTAT1 in bulk CD4+ T cells purified from the lymph nodes and spleen after being cultured with α-CD3 / α-CD28 for one hour and then IL-6 or no cytokine for 15 minutes. Results are representative of multiple experiments.

5.2.2 Cytokines induce different STAT activation profiles

STAT activation profiles for the different cytokines of interest were measured and normalized using the method described in the previous section. There are a couple ways that the data can be visualized. One way is to compare the cytokines' activation of STAT1 and STAT3 separately (Figure 5.2). Another way is to create a "fingerprint" of a given cytokine's signaling pattern by plotting the time course of pSTAT1 and pSTAT3 levels on the same graph and then comparing the fingerprints of the various cytokines (Figure 5.3).

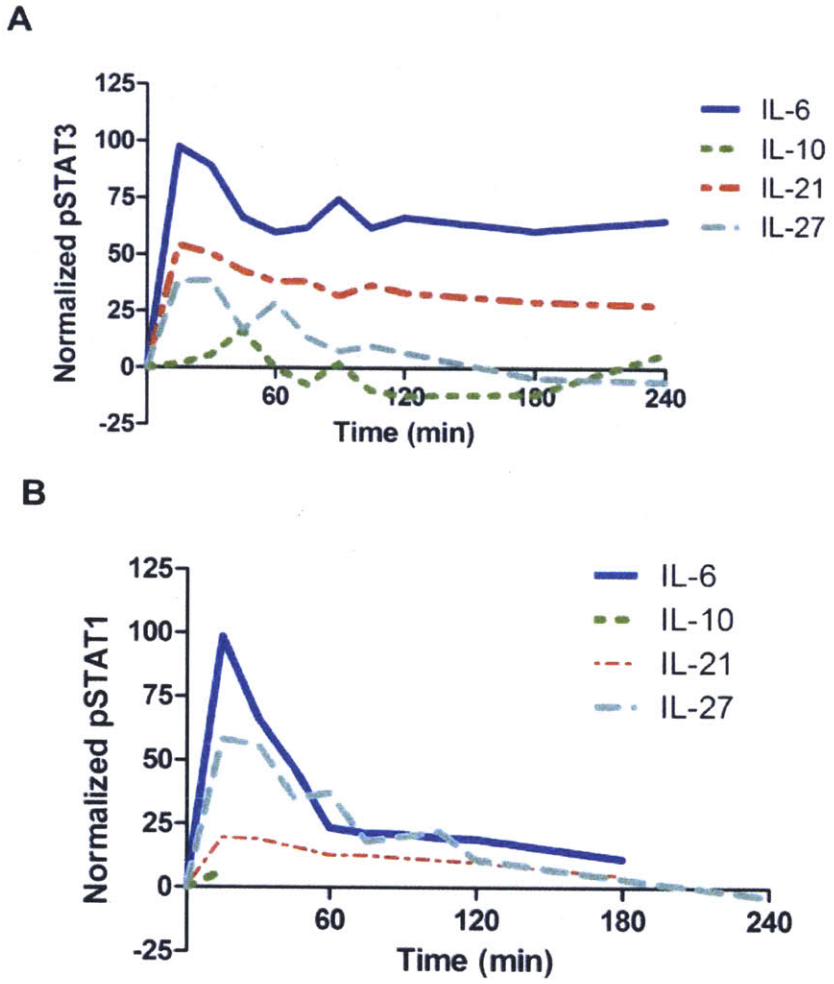

Figure 5.2. Cytokines of interest induce different time course profiles of pSTAT1 and pSTAT3. (**a**,**b**) Flow cytometry measurement of (**a**) pSTAT3 and (**b**) pSTAT1 in bulk CD4+ T cells and in some experiments sorted naïve CD4+ T cells (CD4+CD25-CD62L^{HI}) purified from the lymph nodes and spleen after being cultured with α-CD3 / α-CD28 for one hour and then IL-6 (10 ng/mL), IL-10 (10 ng/mL), IL-21 (20 ng/mL), or IL-27 (25 ng/mL) at different time points for up to 4 hours . Results are the averages of all of the MFIs (mean fluorescence intensities) measured at a given time point and a given condition, which have been normalized using Equation 5.1 using the MFI of either (**a**) pSTAT3 or (**b**) pSTAT1 induced by IL-6 at 15 minutes on the day

that a given data point was collected. Data points were collected over the course of several months and the average MFIs for a given point are the average of anywhere from 4 to 13 measurements.

IL-6 clearly induces the most pSTAT3 out of the 4 cytokines at all time points measured in the first 4 hours (Figure 5.2A). Comparatively, IL-21 activates roughly half the amount of STAT3 during that time period. IL-27 has a peak activation of STAT3 at 15-30 minutes reaching roughly 33% of that activated by IL-6 at those time points. IL-27's activation of STAT3 then drops off to basal levels steadily during the remainder of the first two hours. Given that STAT3 is vital to Th17 differentiation[11], it is logical that IL-6 is the best inducer of Th17 cells (in combination with TGF-β) since it induces the most pSTAT3. IL-21 is a weak inducer of Th17 cells and it induces roughly half the amount of pSTAT3 as IL-6. IL-10 and IL-27 do not induce Th17 cells and they had the lowest induction of pSTAT3. Perhaps there is simply a threshold of pSTAT3 induction below that of IL-21 and above that of IL-27 which allows a cytokine to induce Th17 cells.

Before these experiments, it was generally believed that IL-27 is a strong inducer of pSTAT1 which accounts for its inhibitory effects on Th17 differentiation since IL-27 does not inhibit Th17 differentiation in *STAT1-/-* mice[20, 22]. Thus we were surprised to observe that IL-6 induced more pSTAT1 at almost all time points in the first 4 hours than IL-27 (Figure 5.2B). At its peak induction of pSTAT1 at 15 minutes, IL-27 only induced roughly 60% of the amount induced by IL-6. This raises an important question. If pSTAT1 is inhibitory of Th17 differentiation, how can IL-6 induce the most pSTAT1 and still be able to be a strong inducer of Th17 cells. Visualizing the data in the form of cytokine fingerprints can possibly assist in addressing this question. For completeness, IL-21 induced relatively small amounts of pSTAT1 and IL-10

induced only trace amounts. Given that IL-10 did not produce very strong measurements of either pSTAT1 or pSTAT3, and since its effects on Th17 differentiation was not known, we chose to discontinue our analysis of IL-10 in this study.

Visualizing the data as cytokine fingerprints allows for a comparison of the relative amounts of pSTAT3 and pSTAT1 induced at all the time points for a given cytokine (Figure 5.3). Though it was described in the previous section that the values of pSTAT1 and pSTAT3 cannot be directly compared, it is still instructive to plot them on the same curve. Regardless of the absolute number of STAT1 or STAT3 molecules, it is still valid to compare the ratio of pSTAT3 and pSTAT1 over time between the different cytokines since all the data has been normalized the same way. On this scale, IL-6 has a pSTAT3:pSTAT1 ratio of 1 at 15 minutes. At all time points after that, the ratio of pSTAT3:pSTAT1 increases to 5 at 3 hours. IL-21 has a pSTAT3:pSTAT1 ratio of 2 to 3 during the first 3 hours. On this scale, IL-27 was the only cytokine to have a higher amount of pSTAT1 than pSTAT3 at any time point. In fact, at all time points it has more pSTAT1 than pSTAT3. These observations suggest that the ratio of pSTAT3 to pSTAT1 is an important quantity in determining whether or not a cytokine will induce Th17 differentiation since on this particular scale, the two cytokines which have a ratio of pSTAT3:pSTAT1 that is greater than 1 at most or all time points (IL-6 and IL-21) promote Th17 differentiation while the cytokine which had a ratio of pSTAT3:pSTAT1 less than 1 at all time points inhibits Th17 differentiation.

A

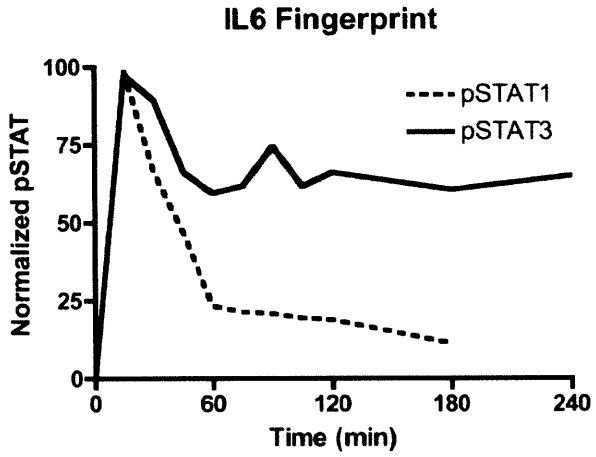
IL6 Fingerprint
pSTAT1
pSTAT3
Normalized pSTAT
100
75
50
25
0
0
60
120
180
240
Time (min)

B

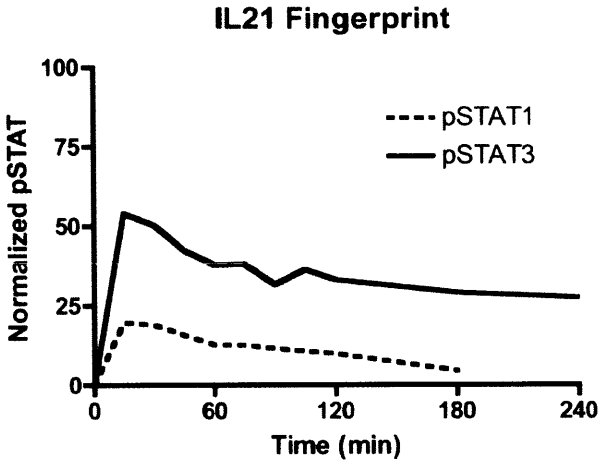
IL21 Fingerprint
pSTAT1
pSTAT3
Normalized pSTAT
100
75
50
25
0
0
60
120
180
240
Time (min)

C

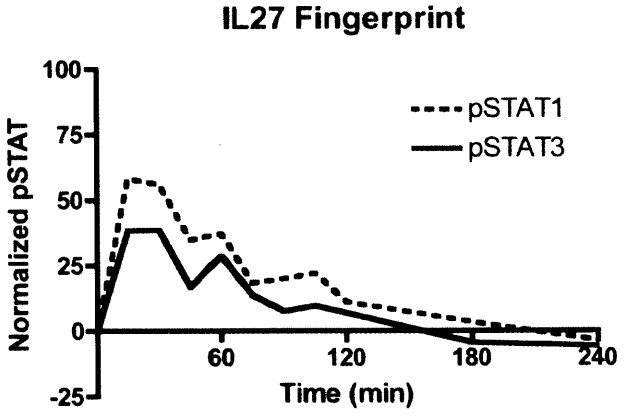
IL27 Fingerprint
pSTAT1
pSTAT3
Normalized pSTAT
100
75
50
25
0
-25
60
120
180
240
Time (min)

Figure 5.3. Cytokine fingerprints illustrate how the relative amounts of pSTAT1 and pSTAT3 vary over the first 4 hours. (**a**,**b**,**c**) Flow cytometry measurement of pSTAT3 and pSTAT1 in bulk CD4+ T cells and in some experiments sorted naïve CD4+ T cells (CD4+CD25-CD62L^{HI}) purified from the lymph nodes and spleen after being cultured with α-CD3 / α-CD28 for one hour and then (**a**) IL-6 (10 ng/mL), (**b**) IL-21 (20 ng/mL), or (**c**) IL-27 (25 ng/mL) at different time points for up to 4 hours . Results are the averages of all of the MFIs (mean fluorescence intensities) measured at a given time point and a given condition, which have been normalized using Equation 5.1 using the MFI of either pSTAT3 or pSTAT1 induced by IL-6 at 15 minutes on the day that a given data point was collected. Data points were collected over the course of several months and the average MFIs for a given point are the average of anywhere from 4 to 13 measurements.

5.2.3 Ratio of pSTAT1 to pSTAT3 determines whether or not a pair of cytokines inhibits or induces Th17 cells

To further investigate the impact of the ratio of pSTAT3:pSTAT1 on a cytokines ability to induce Th17 differentiation, we began looking at STAT activation profiles for pairs of cytokines. We were interested in the STAT activation profiles for pairs of cytokines for three reasons. First, in experiments which show that IL-27 inhibits Th17 differentiation, IL-27 is added in addition to IL-6 and TGF-β at time 0. Therefore, the cell is exposed to both IL-6 and IL-27 at the same time, so their individual profiles are not directly applicable. Second, we can possibly gain some mechanistic insight by seeing how individual profiles add. If the sum of the individual profiles does not equal that of the cytokine pair's profile, then there is either a saturating effect or there could be some inhibition. Finally, by looking at cytokine pairs, it gives us additional profiles which we can then compare to see which profiles lead to Th17 differentiation and which do not.

We measured the fingerprints of IL-6 (Figure 5.4A), IL-6 with IL-21 (Figure 5.4B), and IL-6 with IL-27 (Figure 5.4C). All measurements were normalized as before with untreated cells as the baseline and IL-6 at 15 minutes as the maximum. One consequence of this was that it was possible for the pairs of cytokines to induce pSTATs with values higher than 100 if the profiles were at all additive since IL-6 is present in all pairs and they are normalized to IL-6 at 15 minutes. The addition of either IL-21 or IL-27 to IL-6 increased the value of pSTAT1 over 100 at 15 minutes and shifted the IL-6 alone curve upwards in value at all time points while still maintaining the same shape. Interestingly, the pSTAT1 profiles for IL-6 with IL-21 and IL-6 with IL-27 are nearly identical. Since it was known that IL-27 inhibits Th17 differentiation, we hypothesized that adding IL-21 at time 0 may also inhibit differentiation due to the similarity in pSTAT1 profiles. We measured IL-17a producing CD4+ T cells using FACS for TGF-β with IL-6 (Figure 5.4D), TGF-β with IL-6 and IL-21 (Figure 5.4E), and TGF-β with IL-6 and IL-27 (Figure 5.4F). All samples received IL-23 at 48 hours and were collected on day 4, restimulated with PMA and Ionomycin, and stained for intracellular cytokines. It is quite clear from these measurements that IL-27 is a potent inhibitor of Th17 differentiation, while IL-21 does not inhibit. How can this be when they have almost identical pSTAT1 profiles?

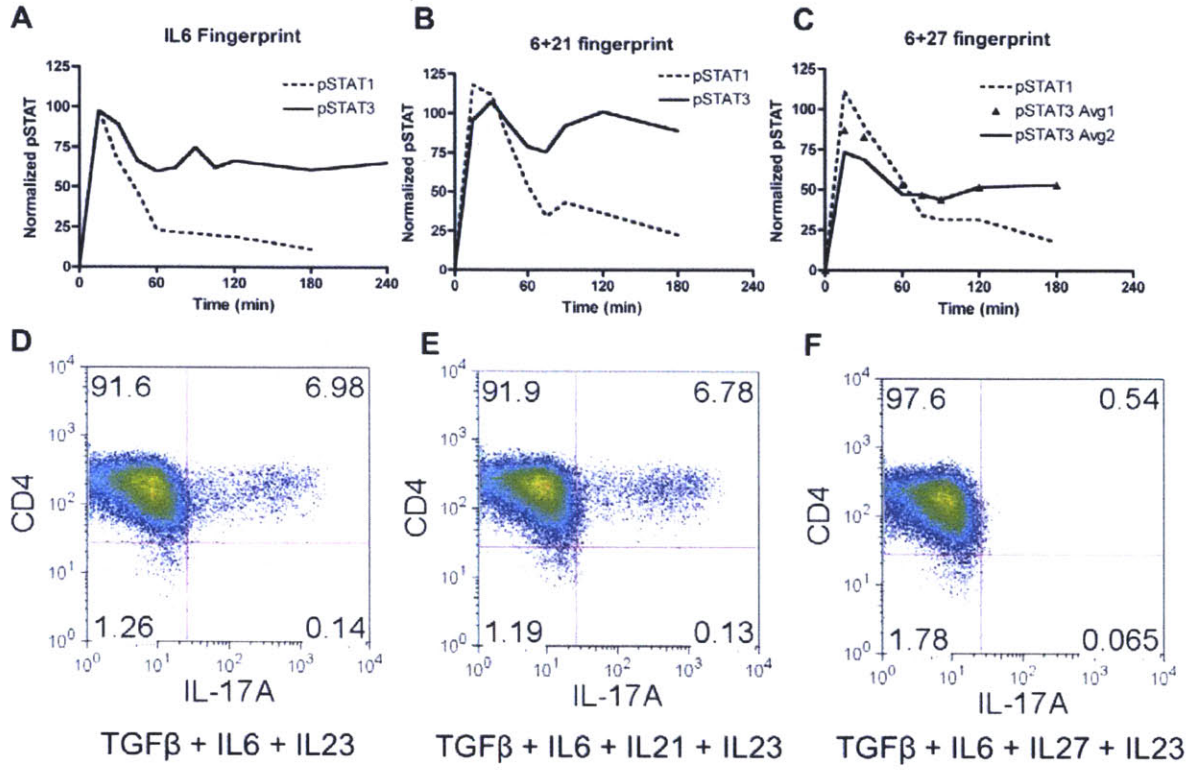

Figure 5.4. The ratio of pSTAT1 to pSTAT3 induced is important in determining whether or not a pair of cytokines inhibit or induce Th17 differentiation. (**a**,**b**,**c**) Flow cytometry measurement of pSTAT3 and pSTAT1 in bulk CD4+ T cells and in some experiments sorted naïve CD4+ T cells (CD4+CD25-CD62L^{HI}) purified from the lymph nodes and spleen after being cultured with α-CD3 / α-CD28 for one hour and then (**a**) IL-6 (10 ng/mL), (**b**) IL-6 (10 ng/mL) and IL-21 (20 ng/mL), or (**c**) IL-6 (10 ng/mL) and IL-27 (25 ng/mL) at different time points for up to 4 hours . Results are the averages of all of the MFIs (mean fluorescence intensities) measured at a given time point and a given condition, which have been normalized using Equation 5.1 using the MFI of either pSTAT3 or pSTAT1 induced by IL-6 at 15 minutes on the day that a given data point was collected. Data points were collected over the course of several months and the average MFIs for a given point are the average of anywhere from 4 to 13 measurements. (**d**,**e**,**f**) Flow

cytometry of naïve CD4+ T cells cultured for 4 d in the presence of (**d**) IL-6 or (**e**) IL-6 and IL-21 or (**f**) IL-6 and IL-27, TGF-β, anti-IL-4 and anti-IFN-γ with subsequent IL-23 treatment at 48 h, then stimulated for 4 h with PMA and ionomycin, followed by intracellular cytokine staining with anti-IL-17A and anti-CD4.

The answer can likely be obtained by observing the relative pSTAT3 profiles. The addition of IL-21 to IL-6 shifts the pSTAT3 curve upward, while the addition of IL-27 to IL-6 shifts the pSTAT3 curve downward. In the case of adding IL-21 to IL-6, both pSTAT1 and pSTAT3 are shifted upwards resulting in a similar pSTAT3:pSTAT1 ratio for most times to that of IL-6 alone. When IL-27 is added to IL-6, pSTAT1 is shifted upward and pSTAT3 is shifted downward resulting in a significant change in the pSTAT3:pSTAT1 ratio. Thus looking at just the pSTAT1 curve alone is misleading since one would infer that IL-21 should be inhibitory to Th17 differentiation. This experiment further suggests that he ratio of pSTAT3:pSTAT1 is what is important and not just the individual profiles themselves.

5.2.4 IL-6 and IL-27 induce similar pSTAT3 profiles in *STAT1-/-* T cells

It has been shown that IL-27 is unable to inhibit Th17 differentiation in *STAT1-/-* (S1KO) T cells since cells stimulated with TGF-β, IL-6, and IL-27 gives a very similar percentage of IL-17 producing cells when compared to TGF-β and IL-6 alone[20, 22]. Based on our previous results and given the similarity in Th17 induction, we expected IL-6 with and without IL-27 to induce similar pSTAT3 profiles in S1KO T cells. To test this, we measured pSTAT3 in wild-type (WT) (Figure 5.5A) and S1KO (Figure 5.5B) T cells after stimulation with either IL-6, IL-27, or IL-6 and IL-27 for up to 3 hours. In WT cells, IL-6 induced the most pSTAT3 at all times and IL-27 induced the least amount of pSTAT3. As early as 15 minutes, less pSTAT3 was observed upon

addition of IL-27 to IL-6. The IL-6 with IL-27 time course of activation for STAT3 fell in between the time courses of activation by the cytokines alone. However, as predicted in S1KO cells, the STAT3 activation profiles for IL-6 and IL-6 with IL-27 are quite similar implying that the presence of STAT1 is somehow able to reduce the level of activation of STAT3. Another observation that can be made is that IL-27 induces a similar, albeit slightly less, amount of pSTAT3 in S1KO compared to the other two conditions. In the absence of STAT1, the ratio pSTAT3:pSTAT1 is no longer relevant. As suggested by Figure 5.2A, the absolute level of pSTAT3 induced may correlate with Th17 differentiation.

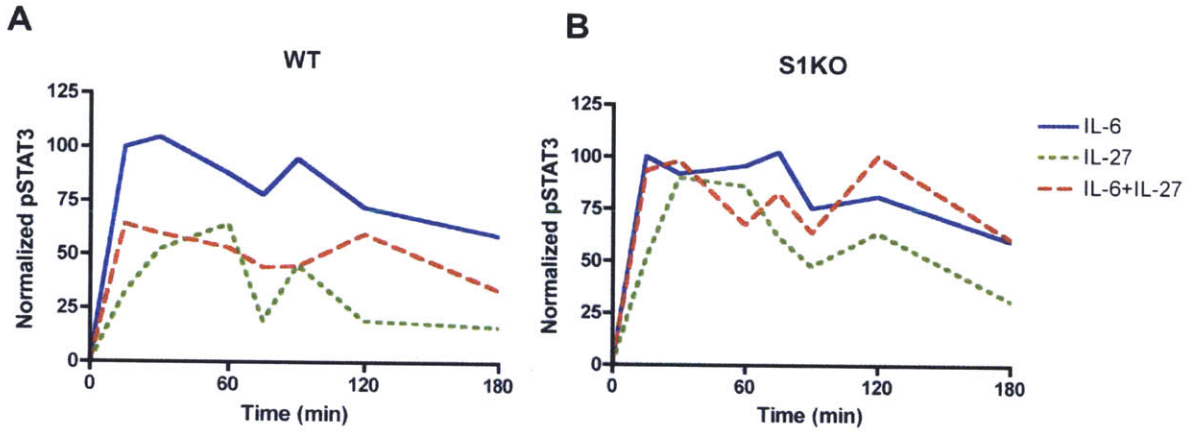

Figure 5.5. IL-6 and IL-27 induce similar pSTAT3 profiles in *STAT1-/-* T cells. (**a**,**b**) Flow cytometry measurement of pSTAT3 and pSTAT1 in sorted naïve CD4+ T cells (CD4+CD25-$CD62L^{HI}$) purified from the lymph nodes and spleen of either (**a**) 129S6/SvEvTac mice (WT) or (**b**) 129S6/SvEv-Stat1(tm1Rds) mice (S1KO) after being cultured with α-CD3 / α-CD28 for one hour and then IL-6 (10 ng/mL), or IL-27 (25 ng/mL), or IL-6 (10 ng/mL) and IL-27 (25 ng/mL) at different time points for up to 3 hours. Results are the MFIs (mean fluorescence intensities) measured at a given time point and a given condition, which have been normalized using Equation 5.1 using the MFI of either pSTAT3 or pSTAT1 induced by IL-6 at 15 minutes.

5.2.5 IL-27 with TGFβ induces Th17 cells in *STAT1-/-* T cells

Given the similarity between the pSTAT3 profiles induced by IL-6 and IL-27, we predicted that in the absence of STAT1 IL-27 could induce Th17 differentiation when combined with TGF-β. If correct, this would be quite surprising since both TGF-β and IL-27 are anti-inflammatory cytokines, so it defies conventional logic that in the absence of one gene, STAT1, these two could induce a highly inflammatory cell type, Th17. To test our prediction, we cultured naïve CD4+ T cells (CD4+CD25-CD62L^{HI}) from either WT or S1KO mice with APCs and with either no cytokines (Th0), TGF-β and IL-6, TGF-β and IL-27, or TGF-β and IL-6 and IL-27, for 4 days,(I did not put any IL-23). At the end of the 4 days, the cells were stimulated with PMA and Ionomycin for 3.5 hours and then stained for intracellular cytokines (Figure 5.6A). RNA from a portion of the cells collected at 4 days for all conditions was used in a TaqMan real-time PCR assay (Figure 5.6B).

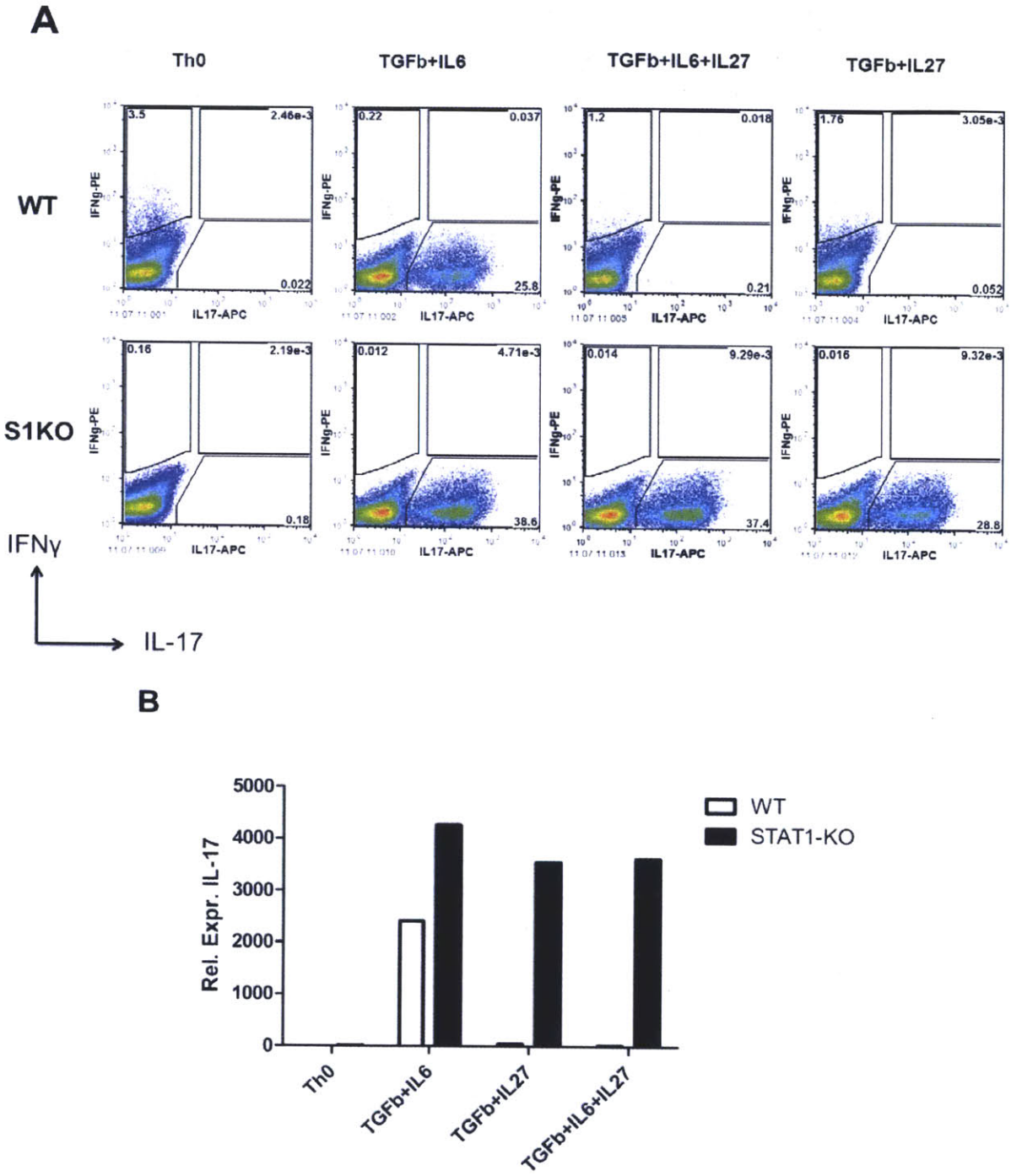

Figure 5.6. IL-27 with TGFβ induces Th17 cells in the absence of STAT1. (**A**) Sorted naïve CD4+ T cells from 129S6/SvEvTac mice (WT) or 129S6/SvEv-Stat1(tm1Rds) mice (S1KO)

were cultured for 4 d in the presence of IL-6+TGF-β, IL-27+TGF-β, IL-6+IL-27+TGF-β, or no cytokines (Th0), and then stimulated for 3.5 h with PMA and ionomycin. Cytokine production was measured by intracellular cytokine staining with anti-IL-17A and anti-IFNγ and subsequent flow cytometry. (**B**) mRNA levels of IL-17a were measured by Taqman PCR for cells collected under the same conditions as (**A**). Data are representative of (**A**) 2 independent experiments or (**B**) 3 independent experiments.

As previously observed in other studies, IL-27 potently inhibits Th17 differentiation in WT cells, but has no effect in S1KO cells[20, 22] (Figure 5.6A). In WT cells, IL-27 and TGF-β do not induce any Th17 cells. However, IL-27 and TGF-β induce a substantial portion of Th17 cells in the S1KO cells as we predicted from observing the pSTAT3 profiles. This same result can also be observed using real-time PCR (Figure 5.6B). This observation supports the hypothesis that cytokines do not have an innate ability to be anti-inflammatory or pro-inflammatory. Instead their properties can be derived based on the ratio of pSTAT3:pSTAT1 induced over time. Once the ratio is skewed entirely to pSTAT3, as is the case in S1KO cells, then cytokines should behave similarly whether or not they are regarded as anti-inflammatory or pro-inflammatory in WT cells as long as their amplitudes of pSTAT3 induced over time is similar.

5.2.6 IL-27 exacerbates EAE in *STAT1-/-* mice

We sought to further study IL-27's ability to induce Th17 cells in the presence of TGF-β by developing an *in vivo* experiment. In WT mice which have been immunized to develop EAE (Experimental Autoimmune Encephalomyelitis), injections of IL-27 will ameliorate disease. Based on previous studies[20, 22], it would be predicted that injections of IL-27 should have no effect on the severity of disease in immunized S1KO mice. However, if IL-27 can induce Th17

cells in the presence of TGF-β, then we would predict that IL-27 injections should increase the severity of disease in these mice.

To test this prediction we immunized mice on the 129 background in order to induce EAE[25]. Our lab had not tried to induce EAE in mice on this background before, so we were not sure how much peptide to inject in order to make the mice sick in a reasonable amount of time. In our first experiment, we injected the mice with a lot of peptide in order to increase the chances of them getting sick. We had four separate cages with 5 mice in each. Cage 1 contained WT mice, each of which was injected with IL-27 every other day after immunization. Cage 2 contained S1KO mice that also received the IL-27 injections. Cage 3 and Cage 4 contained WT and S1KO mice, respectively, that received PBS injections. As can be seen in Figure 5.7, the WT mice on average had scores of less than 0.5 when the experiment ended on day 15. The S1KO mice given the PBS injections got sick on day 11, while the S1KO mice given the IL-27 injections got sick one day earlier and had died by day 15. There is not a very strong difference between the S1KO mice receiving IL-27 versus PBS, but our results do suggest that IL-27 may make disease worse, as predicted. However, it is apparent that we injected the mice with far too much peptide in an effort to make them sick. This experiment will be repeated in the coming weeks, but was not completed in time to be printed in this thesis.

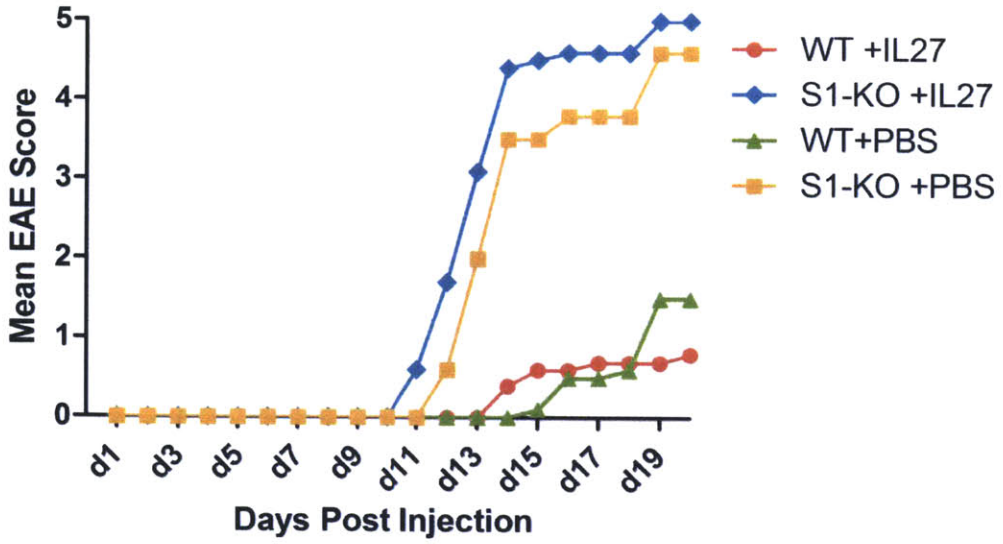

Figure 5.7. Addition of IL-27 exacerbates EAE in *STAT1-/-* mice. WT and STAT1-/- mice were immunized with MOG in CFA and received PT for the development of EAE. Mice were treated with 250ng IL-27 or PBS every other day from day 0 until day 14. Data shown represent 5 mice per group.

5.3 Discussion

We are not the first to characterize STAT activation in IL-6[12, 19, 24], IL-10[12, 24], IL-21[23], and IL-27[19], but we are presumably the first to systematically measure the profiles for all four cytokines in the same study. This allowed us to be able to directly compare the signals activated by each of the cytokines. IL-6 activated the most STAT3 of the four, followed by IL-21 which appeared to correlate with their relative abilities to induce Th17 differentiation. In this analysis, we are making the assumption that STAT activation in the first 4 hours is relevant in determining a cytokine's ability to induce Th17 differentiation, which is a several day process. However, two

IL-6 induced genes, STAT3 and IL-21R peak around 2 hours during Th17 differentiation and quickly drop off to basal levels for the remainder of the differentiation process (Chapter 6). Therefore it is relevant to consider STAT activation at early times.

We observed that IL-6 induced the most pSTAT1 out of all the cytokines tested during the first four hours. This was unexpected since IL-6 is the best inducer of Th17 cells and STAT1 is entirely responsible for IL-27's ability to potently inhibit Th17 differentiation[20, 22]. This is certainly contradictory to the theory that IL-27 induces a lot of pSTAT1; therefore it is inhibitory to Th17 cell development. We saw that only considering the total amount of pSTAT1 induced leads to faulty conclusions when we predicted that adding IL-21 to IL-6 and TGF-β would inhibit Th17 differentiation since the pSTAT1 profile for IL-6 with IL-21 is the same as the pSTAT1 profile for IL-6 with IL-27. IL-21 was not inhibitory and therefore we were missing something. When adding IL-21 to IL-6, the total amount of pSTAT1 induced increased, but so did the total amount of pSTAT3. Thus, the ratio of the two did not significantly change from IL-6 alone, so IL-21 did not change the amount of IL-17 producers induced. When adding IL-27 to IL-6, the total amount of pSTAT1 is increased, while the amount of pSTAT3 is decreased, leading to a significant change in the ratio. It would appear from this analysis that the important variables in determining whether or not a cytokine will induce or inhibit Th17 differentiation is the total amount of pSTAT3 induced and the ratio of pSTAT3 to pSTAT1. Of the cytokines tested, IL-27 was the only one which had a higher amount of pSTAT1 induced loosely compared to pSTAT3 on the normalized scale.

There are actually three forms of pSTAT1 and pSTAT3 that can exist in the nucleus as a result of JAK/STAT signaling. STAT proteins form dimers after they are phosphorylated which reveals a nuclear targeting sequence that allows for transport into the nucleus. These two particular

pSTATs can either form homodimers (pSTAT1-pSTAT1, pSTAT3-pSTAT3) or a heterodimer (pSTAT1-pSTAT3)[26, 27, 28]. Ultimately what we are alluding to when we say the ratio of pSTAT3 to pSTAT1 is the resulting distribution of these three dimeric forms. Conceivably the highest relative amount of heterodimer will be observed when pSTAT1 and pSTAT3 are present near the membrane in similar quantities. The relative amount of heterodimer will decrease as one of the STATs starts dominating in numbers over the other and the homodimeric form of the dominant STAT will be present in the highest relative amount. An assay which allows for the comparison of the relative amounts of transcription factors present in the nucleus is an electrophoretic mobility shift assay (EMSA). A labeled oligonucleotide that all of the transcription factors can bind to is necessary to allow for comparison. A part of the c-FOS promoter referred to as the hSIE sequence[29, 30] is capable of binding all 3 dimeric forms theoretically allowing for the determination of the relative amounts present in the nucleus as has been done in several studies[26, 27, 31]. We attempted to use this technique to characterize the relative amounts of the dimeric forms induced by the different cytokines of interest, but were unable to reliably come to any conclusions.

The observation that IL-6 and IL-27 induce similar pSTAT3 profiles in CD4+ T cells from S1KO mice led to our prediction that IL-27 would be able to induce Th17 differentiation in these cells when added under activating conditions in the presence of TGF-β. Indeed, IL-27 and TGF-β could potently induce Th17 differentiation in the absence of STAT1. IL-27 is widely observed to be an anti-inflammatory cytokine[16, 17, 18] and an inhibitor of Th17 differentiation[20, 22] so according to conventional wisdom, this is a very surprising result. In order to reiterate this point, just consider the fact that in the absence of just one transcription factor, two anti-inflammatory cytokines (TGF-β and IL-27) when added together are capable of inducing one of the most

inflammatory effector cells. This unexpected result of two cytokines behaving similarly in the absence of just protein is reminiscent of two independent studies that showed that IL-6 and IL-10 induce an indistinguishable anti-inflammatory response in SOCS3-/- cells[12, 24]. Combined these two results suggest that there is likely nothing inherently special about cytokine receptor for the cytokines of interest. In other words, induction of unique conformations of the STATs and other unknown pathways do not need to be invoked to explain why there are circumstances where cytokines induce similar behaviors or behave completely differently despite activating the exact same transcription factors.

A built-in assumption in this analysis is that there are no other relevant STATS induced or MAPK pathways activated that further account for differences. We believe that our results and verified predictions can be explained by simply considering STAT1 and STAT3, but we agree that this is a simplification. An alternative analysis of our IL-27 based induction of Th17 differentiation is that Th17 differentiation is more accessible in S1KO cells since IFNγ, a potent inhibitor of Th17 differentiation and activator of STAT1, is unable to inhibit these particular cells. To test this alternative hypothesis, we measured intracellular IL-17a in IFNγ-/- cells after 4 days of stimulation with IL-27 and TGF-β and saw no IL-17 producers compared to a positive control of this type of cell that had been exposed to normal Th17 differentiation conditions (unpublished observation).

IL-27 injection is a viable way to inhibit EAE disease progression due its potent ability to inhibit Th17 differentiation. Simply based on previous results, one would conclude that in patients with STAT1 defects, that IL-27 treatment would have no effect since S1KO cells stimulated with IL-6, IL-27, and TGF-β secrete similar amounts of IL-17 as WT cells stimulated with IL-6 and TGF-β[20, 22]. However, our results would suggest that the therapy could actually exacerbate

disease in these patients. There have been at least two reports of patients that were born with a defect in STAT1 signaling[32, 33]. Thus if someone had this defect it would be dangerous for them to try the therapy according to our initial EAE results.

Further experimentation is required to further understand how the ratio of pSTAT3 to pSTAT1 is an important determinant of whether or not a cytokine will be an inducer or inhibitor of Th17 differentiation. It would be a useful contribution for the field for a group with extraordinary skill in performing EMSA assays to characterize the homodimer vs. heterodimer distribution for these cytokines of interest. Additional experimentation will also be necessary to determine the mechanism for how this distribution translates into induction or inhibition of the Th17 differentiation program. We feel that this information will lead to a much better understanding of how STAT inducing cytokines attain signal specificity.

5.4 Methods

Mice

The mice used to perform the experiments which led to Figures 1-4 were 6-8 week old C57BL/6J mice obtained from Jackson Laboratories.

The mice used to perform the experiments in Figures 5-7 were 6-8 week old 129S6/SvEvTac mice (WT) and 129S6/SvEv-Stat1(tm1Rds) mice (S1KO)[34] obtained from Taconic. Mice were housed in a specific pathogen-free, viral Ab-free animal facility at the Harvard Institutes of Medicine. All breeding and experiments were reviewed and approved by the Institutional Animal Care and Use Committee of Harvard Medical School.

Intracellular staining of pSTAT1 and pSTAT3

In a given experiment, cells were plated in a 96-well plate and various wells were given cytokines at different time points. As an example, if measurements at 30 minutes, 60 minutes, and 90 minutes were desired in an experiment, the cytokine was added to the 90 minute wells at time 0, to the 60 minute wells after 30 minutes, and to the 30 minute wells after 60 minutes. This way all the cells could be collected and fixed after 90 minutes. The rest of the details can be found in Appendix 1.

Th17 differentiation *in vitro*.

Our procedure for Th17 differentiation can be found in Appendix 1.

Real-time PCR

RNA was extracted from cells using the RNeasy Kit (Qiagen) according to the manufacturer's instructions. 1 μg RNA was then transcribed into cDNA using the iScript^{TM}cDNA Synthesis Kit (BIO-RAD) according to the manufacturer's instructions. Quantitative PCR primers and probes were purchased from Applied Biosystems (IL-17A: Mm00439619_m1, β-Actin: 4352341E).

EAE

WT and STAT1-/- mice were immunized s.c. with 150ug MOG35-55 in Complete Freund's adjuvants containing 8mg/ml of *Mycobacterium tuberculosis H37 RA* (DIFCO Laboratories). Mice also received 200 ng of pertussis toxin i.v. (List Biological Laboratories) on day 0 and day 2 post immunization. Mice were injected i.v. with 250 ng of recombinant murine IL-27 (BioLegend) or PBS every other day from day 0 until day 14. Mice were monitored daily for development of disease and scored according to the following criteria: 0, no disease; 1, decreased

tail tone; 2, hind limb weakness or partial paralysis; 3, complete hind limb paralysis; 4, front and hind limb paralysis; 5, moribund state.

5.5 References

1. Szabo SJ, Sullivan BM, Peng SL, Glimcher LH. 2003. Molecular mechanisms regulating Th1 immune responses. *Annu Rev Immunol* **21**:713-758.

2. Murphy KM and Reiner SL. 2002. The lineage decisions of helper T cells. *Nat Rev Immunol* **2**:933-44.

3. Langrish CL, Chen Y, Blumenschein WM, Mattson J, Basham B, Sedgwick JD, McClanahan T, Kastelein RA, Cua DJ. 2005. IL-23 drives a pathogenic T cell population that induces autoimmune inflammation. *J. Exp. Med.* **201**, 233–240.

4. Harrington LE, Hatton RD, Mangan PR, Turner H, Murphy TL, Murphy KM, Weaver CT. 2005. Interleukin 17-producing $CD4^+$ effector T cells develop via a lineage distinct from the T helper type 1 and 2 lineages. *Nature Immunol.* **6**, 1123–1132.

5. Park H, Li Z, Yang XO, Chang SH, Nurieva R, Wang YH, Wang Y, Hood L, Zhu Z, Tian Q, Dong C. 2005. A distinct lineage of CD4 T cells regulates tissue inflammation by producing interleukin 17. *Nature Immunol.* **6**, 1133–1141.

6. Bettelli E, Carrier Y, Gao W, Korn T, Strom T, et al. 2006. Reciprocal developmental pathways for the generation of pathogenic effector Th17 and regulatory T cells. *Nature* **441**:235-238.

7. Mangan PR, Harrington LE, O'Quinn DB, Helms WS, Bullard DC, Elson CO, Hatton RD, Wahl, SM, Schoeb TR, Weaver CT. 2006. Transforming growth factor-β induces development of the Th17 lineage. *Nature* **441**:231-234.

8. Gorelik L and Flavell RA. 2002. Transforming growth factor-β in T-cell biology. *Nat Rev Immunol* **2**:46-53.

9. Murray PJ. 2007. The JAK-STAT signaling pathway: input and output integration. *J Immunol* **178**:2623-2629

10. Kamimura D, Ishihara K, Hirano, T. 2003. IL-6 signal transduction and its physiological roles: the signal orchestration model. *Rev Physiol Biochem Pharmacol* **149**:1-38.

11. Yang XO, Panopoulos AD, Nurieva R, Chang SH, Wang D, Watowich SS, Dong C. 2007. STAT3 regulates cytokine-mediated generation of inflammatory helper T cells. *JBC* **282**:9358-9363.

12. El Kasmi KC, Holst J, Coffre M, Mielke L, de Pauw A, et al. 2006. General nature of the STAT3-activated anti-inflammatory response. *J Immunol* **177**:7880-7888.

13. Moore KW, de Waal Malefyt R, Coffman RL, O'Garra, A. 2001. Interleukin-10 and the interleukin-10 receptor. *Annu Rev Immunol* **19**:683-765.

14. Spolski R and Leonard WJ. 2008. Interleukin-21: Basic Biology and Implications for Cancer and Autoimmunity. *Annu Rev Immunol* **26**:57-79.

15. Korn T, Bettelli E, Gao W, Awasthi A, Jäger A, Strom TB, Oukka M, Kuchroo VK. 2007. IL-21 initiates an alternative pathway to induce proinflammatory Th17 cells. *Nature* **448**:484-487.

16. Villarino, A. *et al.* 2003. The IL-27R (WSX-1) is required to suppress T cell hyperactivity during infection. *Immunity* **19**:645–655.

17. Batten, M. *et al.* 2006. Interleukin 27 limits autoimmune encephalomyelitis by suppressing the development of interleukin 17-producing T cells. *Nat. Immunol.* 7:929–936.

18. Awasthi, A. *et al.* 2007. A dominant function for interleukin 27 in generating interleukin 10-producing anti-inflammatory T cells. *Nat. Immunol.* **8**:1380–1389.

19. Stumhofer JS, Silver JS, Laurence A, Porrett PM, Harris TH, Turka LA, Ernst M, Saris CJM, O'Shea JJ, Hunter CA. 2007. Interleukins 27 and 6 induce STAT3-mediated T cell production of interleukin 10. *Nat Immunol* **8**:1363-1371.

20. Stumhofer JS, Laurence A, Wilson EH, Huang E, Tato CM, Johnson LM, Villarino AV, Huang Q, Yoshimura A, Sehy D, Saris CJM, O'Shea JJ, Hennighausen L, Ernst M, Hunter CA. 2006. Interleukin 27 negatively regulates the development of interleukin 17-producing T helper cells during chronic inflammation of the central nervous system. *Nat Immunol* 7:937-945.

21. Delgoffe GM, Murray PJ, Vignali DAA. 2011. Interpreting mixed signals: the cell's cytokine conundrum. *Curr Opin Immunol.* **23**:632-638.

22. Neufert C, Becker C, Wirtz S, Fantini MC, Weigmann B, Galle PR, and Neurath MF. 2007. IL-27 controls the development of inducible regulatory T cells and Th17 cells via differential effects on STAT1. *Eur J Immunol* **37**:1809-1816.

23. Zeng R, Spolski R, Casas E, Zhu W, Levy DE, Leonard WJ. 2007. The molecular basis of IL-21-mediated proliferation. *Blood* **109**:4135-4142.

24. Yasukawa H, Ohishi M, Mori H, Murakami M, Chinen T, et al. 2003. IL-6 induces an anti-inflammatory response in the absence of SOCS3 in macrophages. *Nat Immunol* **4**:551-556.

25. Buch T, Uthoff-Hachenberg C, Waisman A. 2003. Protection from autoimmune brain inflammation in mice lacking IFN-regulatory factor-1 is associated with Th2-type cytokines. *Int Immunol* **7**:855-859.

26. Qing Y and Stark GR. 2004. Alternative activation of STAT1 and STAT3 in response to Interferon-γ. *JBC* **279**:41679-41685.

27. Costa-Pereira AP, Tininini S, Strobl B, Alonzi T, Schlaak JF, Is'harc H, Gesualdo I, Newman SJ, Kerr IM, Poli V. 2002. Mutational switch of an IL-6 response to an interferon-γ-like response. *Proc Natl Acad Sci USA* **99**:8043-8047.

28. Lillemeier BF, Köster M, Kerr IM. 2001. STAT1 from the cell membrane to the DNA. *EMBO J* **20**:2508-2517.

29. Sadowski HB, Shuai K, Darnell JE,Jr and Gilman MZ. 1993 A common nuclear signal transduction pathway activated by growth factor and cytokine receptors. Science **261**:1739–1744.

30. Horvath CM, Wen Z, Darnell JE, Jr. 1995. A STAT protein domain that determines DNA sequence recognition suggests a novel DNA-binding domain. *Genes and Dev* **9**:984-994.

31. Ehret GB, Reichenbach P, Schindler U, Horvath CM, Fritz S, Nabholz M, Bucher P. 2001. DNA binding specificity of different STAT proteins. *JBC* **276**:6675-6688.

32. Chapgier A, Wynn RF, Jouanguy E, *et al.* 2006. Human complete STAT-1 deficiency is associated with defective Type I and II IFN responses in vitro but immunity to some low virulence viruses in vivo. *J Immunol* **176**:5078-5083.

33. Chapgier A, Kong X-F, Boisson-Dupuis S, *et al.* 2009. A partial form of recessive STAT1 deficiency in humans. *J Clin Invest* **119**:1502-1514.

34. Meraz MA, White JM, Sheehan KC, Bach EA, Rodig SJ, Dighe AS, Kaplan DH, Riley JK, Greenlund AC, Campbell D, Carver-Moore K, DuBois RN, Clark R, Aguet M, Schreiber RD. 1996. Targeted disruption of the Stat1 gene in mice reveals unexpected physiologic specificity in the JAK-STAT signaling pathway. *Cell* **84**:431-442.

Chapter 6: A clustering algorithm analysis of Th17 differentiation

Portions reprinted from "A clustering algorithm analysis of Th17 differentiation" by Kevin D. Fowler, Hulin Jin, Arup K. Chakraborty and Vijay K. Kuchroo, *In preparation.*

6.1 Introduction

Several years ago a new lineage of helper T cells, Th17 cells, was discovered which brought about a change to the classic Th1 / Th2 paradigm[1,2,3]. These cells were characterized by their ability to secrete IL-17 and IL-22, as well as their highly inflammatory nature. Shortly after their discovery, two groups concurrently determined that *Th17* cells could be obtained *in vitro* by adding the cytokines Interleukin-6 (IL-6) and transforming growth factor-beta (TGFβ) in culture with naïve CD4+ T cells along with some form of T cell receptor (TCR) / CD28 stimulation[4,5]. However, since their discovery, the precise mechanisms governing Th17 differentiation have remained elusive.

To determine Th17-important genes, frequently researchers just measure gene expression after differentiation. Measuring gene expression in Th17 cells only after differentiation could miss out on some genes of interest, since it tells us nothing about changes in gene expression throughout the differentiation process. Thus we sought to follow all genes involved in Th17 differentiation as a function of time. It is impossible to follow the expression of all genes continuously over several days so we needed to choose time points at which to measure. It would be ideal to do gene array at as many time points as possible, but it is an expensive technique so we needed to get an idea of which time points are most important. We chose to use real-time PCR to measure the relative mRNA levels of five transcription factors (RORγt[6], RORα[6], Cmaf[7], STAT3[8], and Foxp3[9]), six cytokines (IL-9[10], IL-10[11], IL-17a[12], IL-17f[12], IL-21[13],

and IL-22[14]) and two cytokine receptors (IL-21R[13] and IL-23R[1]), which are all genes of known interest in Th17 differentiation, at eighteen different time points over 4 days. While possibly not directly linked to Th17 differentiation, IL-10 was chosen since it is a prevalent anti-inflammatory cytokine[11]. Our goal of these measurements was to identify time points to be used in the array in a future study, observe the time course of transcription of numerous genes of interest, and to determine as much information as possible from the data set using a method for determining correlations between time series of intermediate system size, which is ideally suited to analyze PCR time courses. Determining clusters of genes that behave similarly can give insight into the mechanisms involved in Th17 differentiation. Ultimately, understanding the mechanisms governing Th17 differentiation would lead to a better understanding of inflammatory autoimmune disease progression and would aid in the development of suitable pharmaceutical therapies.

6.2 Methods

Mice.

C57BL/6J mice obtained from Jackson Laboratories were used in this study.

Th17 Differentation.

The Th17 differentiation protocol can be found in Appendix 1.

Real-time PCR.

RNA was extracted with the RNAeasy columns (Qiagen), then cDNA was transcribed as recommended (Applied Biosystems) and was used as template for quantitative PCR[15]. Expression of RORγt, RORα, STAT3, Foxp3, c-MAF, IL-9, IL-10, IL-17A, IL-17F, IL-21, IL-

22, IL-21R and IL-23R was assessed with specific primers and probes (Applied Biosystems)[15]. The Applied Biosystems 7500 Fast system was used for Taqman analysis. Gene expression was normalized to expression of the 'housekeeping' gene *Actb* (encoding β-actin or GAPDH)[15]. Most of this excerpt was taken verbatim from a previously published paper by co-author Hulin Jin[15]. The experiments were performed by him and because he has since moved to Germany, I was unable to obtain the exact protocol for this thesis. However, the method presented here is what he used.

6.3 Results

6.3.1 Normalization of real-time PCR measurement data of genes during Th17 differentiation allows for comparison of expression levels

T cells were cultured under Th17 conditions and were collected at a number of time points during four days of differentiation. Real-time PCR was used to measure the expression of levels of numerous genes. A wide range of relative expression between all of the genes of interest was observed over the course of differentiation (Figure 6.1). The relative expression of IL-17f peaked at close to 200,000, while the relative expression of IL-22 peaked around 25. Therefore, peak expression levels varied as much as four orders of magnitude, making it difficult to interpret trends in expression by plotting them all on the same graph. Several observations can be made by plotting the time courses on four different scales of expression (Figure 6.1). The cytokines, IL-17a, IL-17f, IL-9, and IL-21 are all expressed at higher levels than the measured transcription factors. In general, secreted cytokines are expressed at higher levels than transcription factors, since transcription factors can have functional relevance at low expression levels. Measurements were made with and without IL-23 added after 48 hours, but it only made a significant impact on

the expression of IL-23R. This implies that there is some positive feedback loop between IL-23 signaling and the expression of the IL-23R. The effects of IL-23 on all other genes of interest are not plotted since it does not significantly affect the shape of their curves.

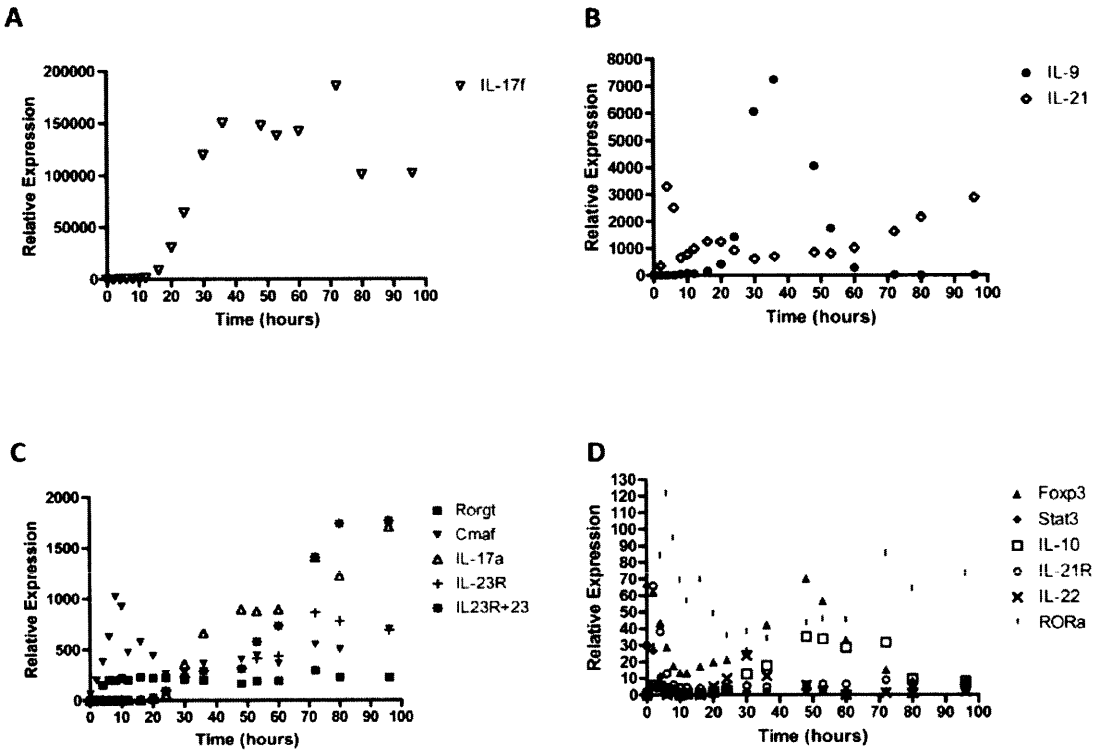

Figure 6.1. Relative expression levels of the genes of interest in Th17 differentiation plotted in four different scales to better visualize the shapes of the trajectories. Measurements were made using real-time PCR with the method described in the Methods section.

In addition to just looking at the profiles of all the genes of interest, we wanted a means of observing similar trends of behavior just by looking at the curves. As previously stated, the expression levels vary too much to compare the time courses of the different genes. It is possible

that some highly expressed cytokine is regulated by the same machinery as a transcription factor expressed at low levels. To compare these curves, we must normalize the data. All of the time courses were normalized by dividing by the maximum relative expression level observed within a given time course and multiplying by 100, which allowed ready comprehension of expression irrespective of the level. Each gene expression time course is normalized by a different constant since all of the trajectories have different peaks expression levels. Once all of the time courses are on the same curve after normalization it is easier to look for trends in expression level (Figure 6.2). Three genes, Cmaf, IL-21, and RORα, peak in the first ten hours, drop down to lower levels, and then steadily increase throughout the next 70 hours. Two genes, IL-21R and STAT3 peak in the first few hours and then rapidly decay to low expression levels and remain low throughout the differentiation. Three genes, IL-9, IL-22, and Foxp3, remain low during the first day, peak between 24 and 48 hours and then decay. Most of the rest of the measured genes start off low during the first day and then steadily increase across the differentiation.

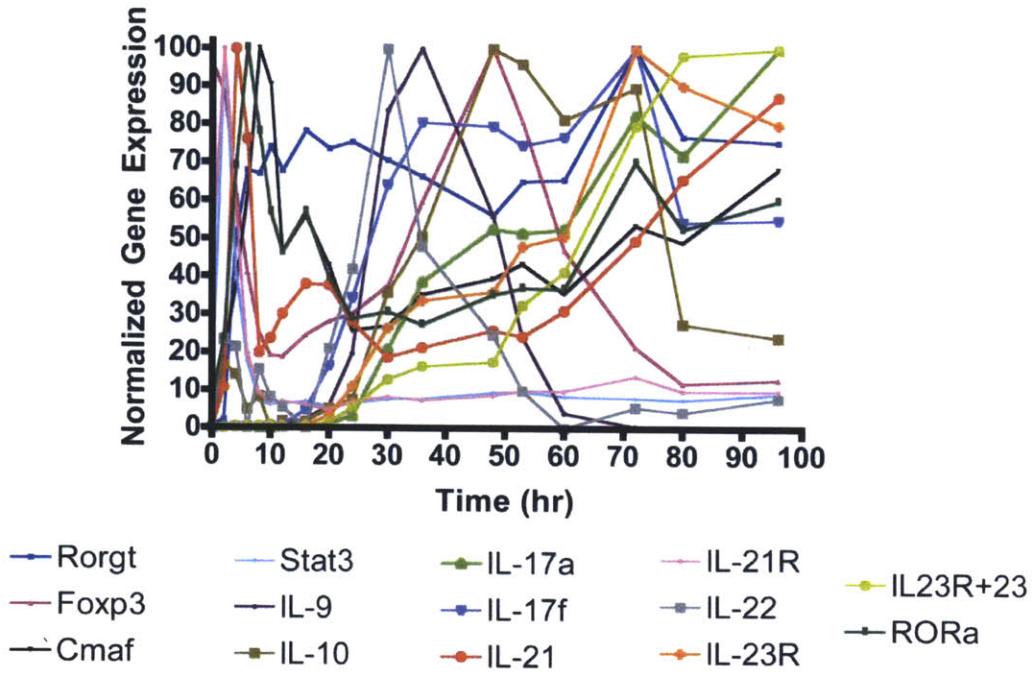

Figure 6.2. Normalized expression levels of the genes of interest in Th17 differentiation. All trajectories were normalized by dividing the relative expression levels at all times for a given gene by the maximum observed relative expression and multiplying by 100.

To get a better view of the behavior of a few important genes, we plotted their time courses separately (Figure 6.3). The interplay between Foxp3 and RORγt is easily visualized. At time zero, Foxp3 is up and RORγt is down. Foxp3 then decreases and remains low while RORγt increases and remains relatively constant throughout day 1. During day 2, RORγt decreases, while Foxp3 increases. During day 3, RORγt increases while Foxp3 decreases down to low levels. It is known that these two transcription factors can interact so it is interesting to observe the opposing nature of nature of their expression during the differentiation process[9,16]. One could argue that the observation that RORγt reaches a local minimum at 48 hours is just an artifact due to experimental error. However, we repeated measurements around this point

numerous times and regularly found that there was a minimum around 48 hours. STAT3, which is induced by IL-6 peaks early and then levels out at low expression levels by hour 10. IL-17a does not start to be expressed at significant quantities until the end of day 1. After the first day it steadily increases over the next 3 days.

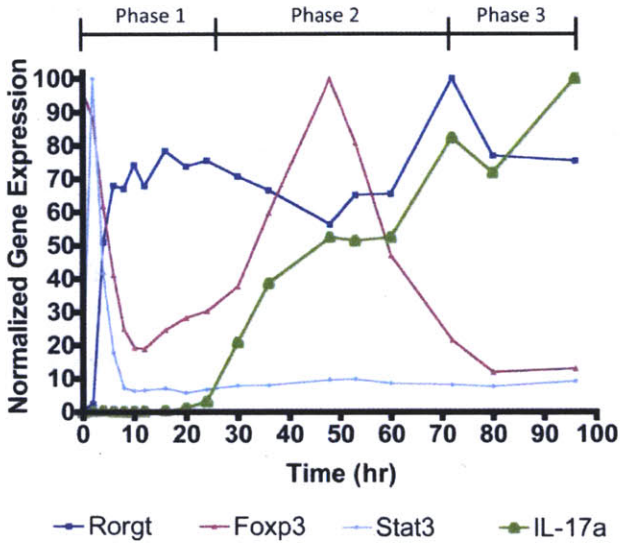

Figure 6.3. Normalized expression levels of a few genes of interest in Th17 differentiation along with an indication of the three different assumed phases of differentiation.

6.3.2 Simple algorithm allows for determination of correlations between genes during Th17 differentiation

We sought to attain a more quantitative measure to determine the degree of similarity in the time courses of various genes in a given phase of the differentiation process. One possible way to analyze correlations between genes would be to use random matrix theory, which was first applied in the field of physics to study the spectra of heavy atoms[17]. More recently it has been

applied in the analysis of stock correlations[18], responses in the brain to auditory stimuli[19], and mutations in HIV[20]. The first step in random matrix theory is to determine the correlation matrix which has pairwise correlations of all the time series as elements. Next, the eigenvalues are of the correlation matrix are computed and compared to the eigenvalues of a random matrix of equivalent size. The corresponding eigenvectors of any eigenvalue larger than the largest eigenvalue of the random matrix contain information about significant correlations between different time series.

To obtain a measure of the correlation between two genes (gene i and gene j), we calculate the elements of the correlation matrix C_{ij} using the expression

$$Cij = \frac{\sum_{\alpha}\left[S_i(t_\alpha) - \langle S_i \rangle\right] \times \left[S_j(t_\alpha) - \langle S_j \rangle\right]}{\sqrt{\sum_{\alpha}\left[S_i(t_\alpha) - \langle S_i \rangle\right]^2 \sum_{\beta}\left[S_j(t_\beta) - \langle S_j \rangle\right]^2}} \qquad \text{(Equation 6.1)}$$

where $S_i(t_\alpha)$ is a measure of the relative expression of gene i at time α and $S_j(t_\alpha)$ is a measure of the relative expression of gene j at time α (Kwapian et al.). In the equation, the summations run over all of the time points in the time series. The net result is a matrix whose elements give the relative correlation between the various genes computed over numerous time points. It is important to note that computing one pairwise correlation between two genes using the full 96 hour time courses would not be instructive since the two genes could be highly correlated at early times and highly uncorrelated at later times which would average out to no correlation. For this reason, separate correlation matrices are computed for each of the different phases indicated in Figure 6.3.

A sample histogram of the correlation matrix components for significant genes in the first ten hours of activation is given in Figure 6.4A. A significant gene in a given phase is defined as a gene that attains at least 20% of its maximum normalized expression level within the phase. Non-significant genes are ignored since small fluctuations at low expression levels are amplified in this analysis and can lead to spurious correlations. A positive correlation means that the genes are behaving similarly during a given phase, while a negative correlation means that the genes are behaving oppositely. A negative pairwise correlation of -1.0 for example would mean that the genes are moving in the opposite direction at every point in time (e.g. one is increasing while the other is decreasing). A correlation of zero indicates that there is no significant similarity in how a pair of genes is expressed.

For random matrix theory to be useful the histogram of the correlation matrix components is generally centered on low correlations with only relatively few correlations being high in magnitude. Inspection of Figure 6.4A shows that there are two main peaks at high magnitude correlations and one at roughly zero. Essentially by choosing genes that we knew were relevant in Th17 differentiation, we biased the study towards genes that would likely be correlated strongly. As a result, random matrix theory is not useful because of our small, biased data set.

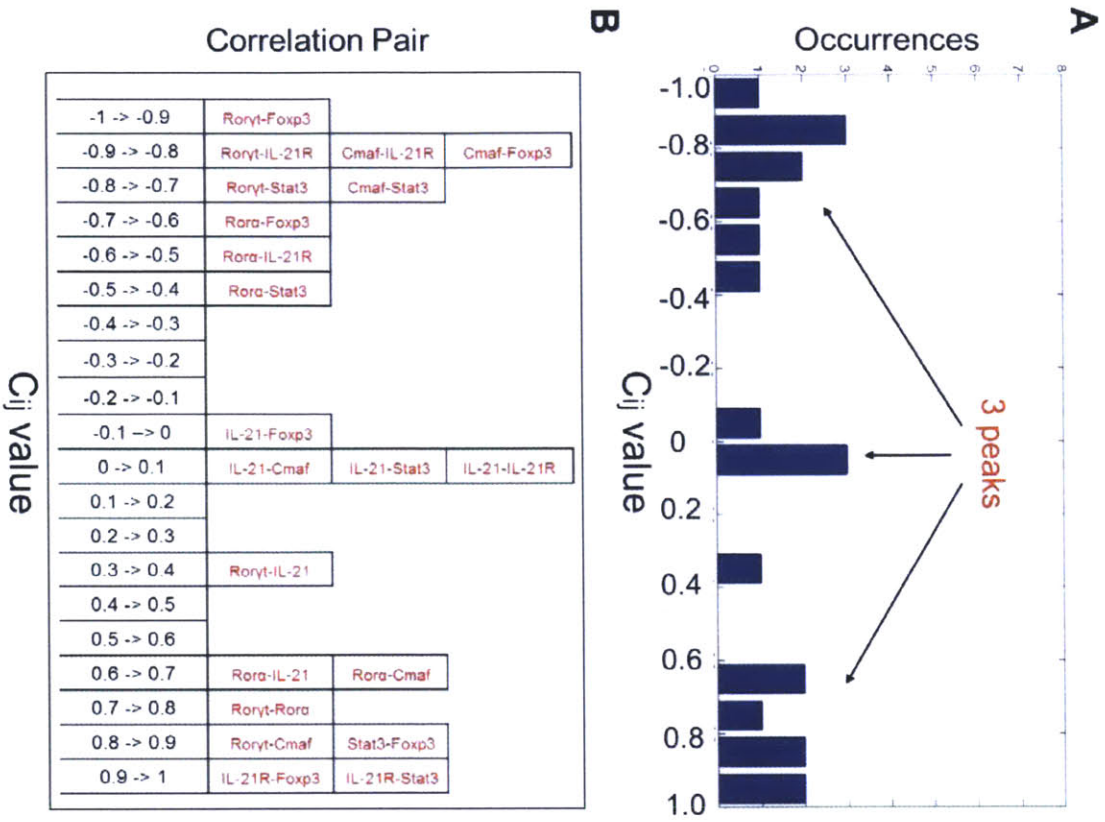

Figure 6.4. Pairwise correlation results for significantly expressed genes in the first ten hours. Genes are determined to be significant if they increase above a normalized expression of 20 at any point during the period of interest. (A) Distribution of the correlation matrix elements for significant genes. (B) Identity of the pairwise correlations corresponding to the distribution of the correlation matrix elements.

Any "higher-powered" technique used to identify clusters of correlated genes would involve operations on the correlation matrix. In the case of intermediate numbers of time courses, as is often the case in collections of real-time PCR time courses, it is easy to construct clusters strictly by looking at the correlation matrix. One simply must define a threshold correlation value,

above which all correlations are considered significant. In Figure 6.4A, an obvious choice is 0.5. In Figure 6.4B, all of the pairwise correlations are sorted according to their C_{ij} value. A cluster diagram can then be constructed by writing down all of the genes appearing in pairwise correlations with C_{ij} values greater than 0.5 and then drawing lines between the various genes which have a significant C_{ij} value. The resulting cluster diagram for the first ten hours would have a connection between Foxp3, STAT3, and IL-21R, and also a connection between IL-21, RORγt, Cmaf, and RORα. IL-21 would only be associated with the RORγt, Cmaf, and RORα cluster through a connection to RORα. The connectivity of these two clusters makes sense since they have high positive correlations within the cluster and high negative correlations between the clusters. We carried out this analysis on both phase 1 (Figure 6.5) and phase 2 (Figure 6.6). It was not instructive to study correlations in phase 3, since we only have two data points for each gene.

6.3.3 Clustering algorithm allows for grouping of genes during Th17 differentiation

In phase 1, we identified three clusters of genes (Figure 6.5a). The first cluster consists of IL-17f and IL-22. Both of these genes remain at relatively low levels until 16 hours when both are steadily rising up until the end of phase 1 (Figure 6.5b). They are both Th17 cell secreted cytokines so it is not surprising that their expression would be correlated at some point during the differentiation process. The second cluster consists of Foxp3, IL-21R, and STAT3. The biological reason for the connection between IL-21R and STAT3 is clear in that they are both IL-6 induced genes[21]. Their behavior at each time point is nearly identical. The mathematical reason for the connection between Foxp3 and IL-21R / STAT3 is also clear in that their behavior

over time after the second time point is quite similar until the end of phase 1. The biological reason for this connection is not clear. There may be similar regulation of these genes in phase 1 or it could just be a coincidence that they behave similarly. This technique only shows the eye where to look for significant correlation between genes. It does not guarantee that such significant correlations are biologically relevant and not just a coincidence. Further experimental testing would be necessary to test connections within clusters. The other cluster in phase 1 consists of IL-21, RORγt, RORα, and a loose connection to RORγt. It is termed a loose connection since the correlation value is right on the edge of not being significant. Biologically, the connection between Cmaf and IL-21 is clear in that Cmaf has been shown to transactivate IL-21 (Apetoh, 2010). The order of the curves would suggest that IL-21 induces Cmaf, but Cmaf is present at nonzero levels at time 0, so there could still be some feedback between these two. A three component v-shaped cluster can be indicative of very similar shaped curves that are shifted in such a way that Curve 1 is correlated with Curve 2 which is then correlated with Curve 3. Curve 1 and Curve 3 are not correlated since they are separated sufficiently. This appears to be the case with IL-21, RORα, and Cmaf in that they are similarly shaped curves separated slightly in time.

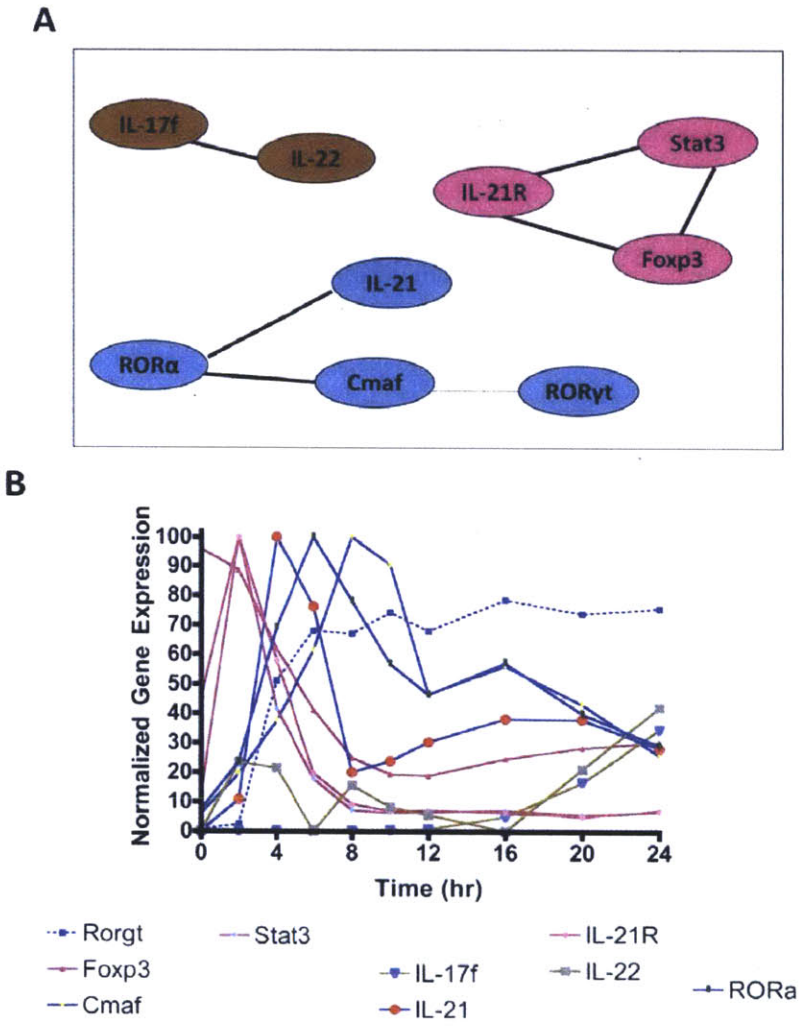

Figure 6.5. Clustering results for significant genes in phase 1 of Th17 differentiation. (A) Cluster diagram of significant genes. All lines represent a pairwise correlation greater than 0.5. (B) Color-coded plot indicating the time courses of the different genes that are in a given cluster.

In phase 3, we identified three different clusters (Figure 6.6A). The first "cluster" consists only of Foxp3, which was significantly expressed in phase three but not significantly correlated with any of the other genes. The second cluster consists of IL-9 and IL-22. Upon inspection of the

time courses of the genes in cluster 1 and cluster 2, it is clear that the shapes of these curves are all the same, only shifted in time, suggesting all 3 genes should be in the same cluster (Figure 6.6B). However, Foxp3's curve is wider than the other two and shifted in such a way that it does not have significant overlap with IL-9 and IL-22. Cluster 3 consists of eight total genes. Six of these genes all have significant connections between each other, which is indicated on the diagram by having all of these genes touch a circle (Figure 6.6A). RORγt has significant connections with three of the genes on the circle and IL-10 has significant connections with the other three. Most of these genes steadily increase throughout phase 3, particularly after 48 hours, which is when Foxp3 begins to decline.

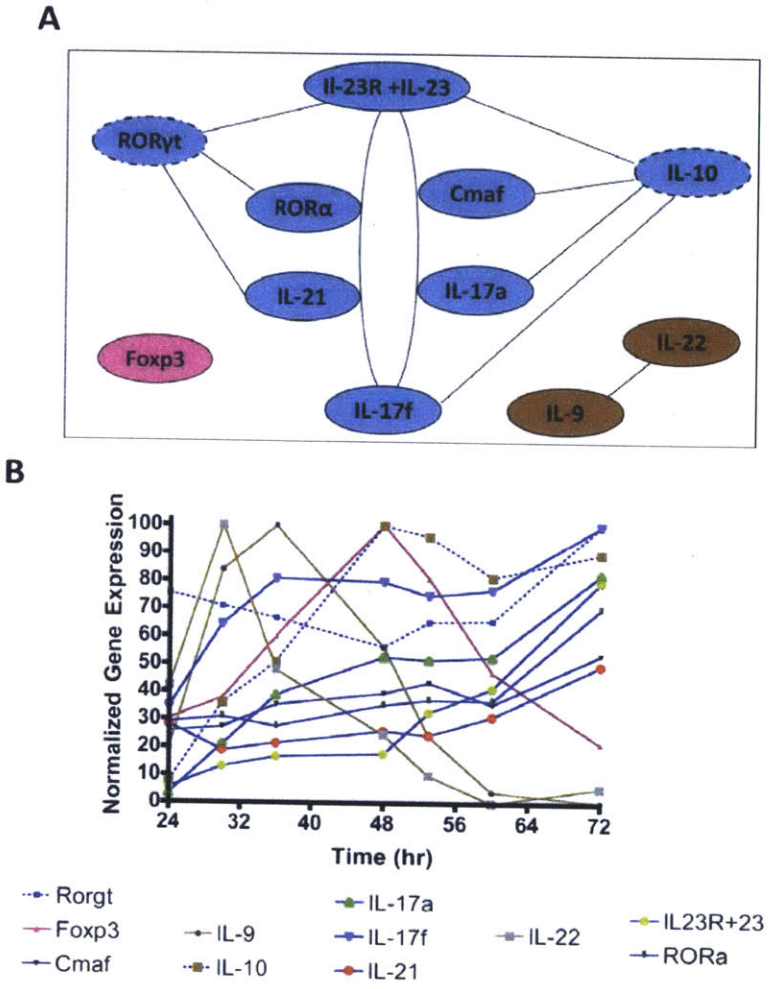

Figure 6.6. Clustering results for significant genes in phase 2 of Th17 differentiation. (A) Cluster diagram of significant genes. All lines represent a pairwise correlation greater than 0.5. Any gene touching the circle in the cluster diagram has significant pairwise correlations with all other genes touching the circle. (B) Color-coded plot indicating the time courses of the different genes that are in a given cluster.

6.4 Discussion

Great emphasis was placed on presenting the clustering algorithm and describing the results obtained from the analysis of the real-time PCR-measured Th17 differentiation gene activation profile for numerous genes of interest. It is likely obvious to the reader that not many conclusions were drawn other than presenting the possible gene clusters in the different phases. Further experimentation would be required in order to validate whether or not the expression of the genes in a given cluster are really related. For instance, in phase 1, we observed that Foxp3, IL21R, and STAT3 were highly correlated since at every time point they behaved exactly the same way, except at time 0. The connection between IL-21R and STAT3 is likely since they are both IL-6 induced genes. It is not apparent that Foxp3, which is induced by TGF-β, should or should not be associated with these two. It may just be a coincidence that they are behaving similarly and they could be controlled by different mechanisms. The experiments required to test these sorts of thing are beyond the scope of this thesis.

Several main conclusions can be drawn from these results. It is clear that RORγt and Foxp3 have opposing functions since any time one of them is highly expressed the other is expressed at low levels, which fits in nicely with the observation that these two transcription factors can interact[9,16]. We also observed that there appears to be three main phases that can be defined during the four days of differentiation. Each phase has a characteristic set of significant genes and a characteristic set of gene clusters. We observed that the addition of IL-23 at 48 hours only significantly affected the expression of a few genes, namely IL-22 and IL-23R. Finally, our clustering algorithm and normalization method may help others analyze their time course data for intermediate system sizes (10-50 genes).

6.5 References

1. Langrish CL, Chen Y, Blumenschein WM, Mattson J, Basham B, Sedgwick JD, McClanahan T, Kastelein RA, Cua DJ. 2005. IL-23 drives a pathogenic T cell population that induces autoimmune inflammation. *J. Exp. Med.* **201**, 233–240.

2. Harrington LE, Hatton RD, Mangan PR, Turner H, Murphy TL, Murphy KM, Weaver CT. 2005. Interleukin 17-producing $CD4^+$ effector T cells develop via a lineage distinct from the T helper type 1 and 2 lineages. *Nature Immunol.* **6**, 1123–1132.

3. Park H, Li Z, Yang XO, Chang SH, Nurieva R, Wang YH, Wang Y, Hood L, Zhu Z, Tian Q, Dong C. 2005. A distinct lineage of CD4 T cells regulates tissue inflammation by producing interleukin 17. *Nature Immunol.* **6**, 1133–1141.

4. Bettelli E, Carrier Y, Gao W, Korn T, Strom T, et al. 2006. Reciprocal developmental pathways for the generation of pathogenic effector Th17 and regulatory T cells. *Nature* **441**:235-238.

5. Mangan PR, Harrington LE, O'Quinn DB, Helms WS, Bullard DC, Elson CO, Hatton RD, Wahl, SM, Schoeb TR, Weaver CT. 2006. Transforming growth factor-β induces development of the Th17 lineage. *Nature* **441**:231-234.

6. Yang XO, Pappu BP, Nurieva R, Akimzhanov A, Kang HS, Chung Y, Ma L, Shah B, Panopoulos AD, Schluns KS, Watowich SS, Tian Q, Jetten AM, Dong C. 2008. T helper 17 lineage differentiation is programmed by orphan nuclear receptors ROR alpha and ROR gamma. *Immunity* **28**:29-39.

7. Apetoh L, Quintana FJ, Pot C, Joller N, Xiao S, Kumar D, Burns EJ, Sherr DH, Weiner HL, Kuchroo VK. 2010. The aryl hydrocarbon receptor interacts with c-Maf to promote the differentiation of type 1 regulatory T cells induced by IL-27. *Nat Immunol* **11**:854-861.
STAT3 Good:

8. Yang XO, Panopoulos AD, Nurieva R, Chang SH, Wang D, Watowich SS, Dong C. 2007. STAT3 regulates cytokine-mediated generation of inflammatory helper T cells. *JBC* **282**:9358-9363.

9. Zhou L, Lopes JE, Chong MMW, Ivanov II, Min R, Victora GD, Shen Y, Du J, Rubtsov YP, Rudensky AY, Ziegler SF, Littman DR. 2008. TGF-β-induced Foxp3 inhibits Th17 cell differentiation by antagonizing RORγt function. *Nature* **453**:236-240.

10. Nowak EC, Weaver CT, Turner H, Begum-Haque S, Becher B, Schreiner B, Coyle AJ, Kasper LH, Noelle RJ. 2009. IL-9 as a mediator of Th17-driven inflammatory disease. *J Exp Med* **206**:1653-1660.

11. El Kasmi KC, Holst J, Coffre M, Mielke L, de Pauw A, *et al.* 2006. General nature of the STAT3-activated anti-inflammatory response. *J Immunol* **177**:7880-7888.

12. Bettellii E, Oukka M, Kuchroo VK. 2007. Th-17 cells in the circle of immunity and autoimmunity. *Nat Immunol* **8**:345-350.

13. Korn T, Bettelli E, Gao W, Awasthi A, Jager A, Strom TB, Oukka M, Kuchroo VK. 2007. IL-21 initiates an alternative pathway to induce proinflammatory T(H)17 cells. *Nature* **448**:484-487.

14. Liang SC, Tan X-Y, Luxenberg DP, Karim R, Dunussi-Joannopoulos K, Collins M, Fouser LA. 2006. Interleukin (IL)-22 and IL-17 are coexpressed by Th17 cells and cooperatively enhance expression of antimicrobial peptides. *J Exp Med* **203**:2271-2279.

15. Bauquet AT, Jin H, Paterson AM, Mitsdoerffer M, Ho I-C, Sharpe AH, Kuchroo VK. 2008. The costimulatory molecule ICOS regulates the expression of c-Maf and IL-21 in the development of follicular T helper cells and Th17 cells. *Nat Immunol* **10**:167-175.

16. Ichiyama K, Yoshida H, Wakabayashi Y, Chinen T, Saeki K, Nakaya M, Takaesu G, Hori S, Yoshimura A, Kobayashi T. 2008. Foxp3 inhibits RORγt-mediated IL-17A mRNA transcription through direct interaction with RORγt. *J Biol Chem* **283**:17003-17008.

17. Wigner EP. 1967. Random matrices in physics. *SIAM Rev* **9**:1-23.

18. Drozdz S, Grummer F, Gorski AZ, Ruf F, Speth J. 2000. Dynamics of competition between collectivity and noise in the stock market. *Physica A* **287**:440-449.

19. Kwapien J, Drozdz, S, Ioannides AA. 2000. Temporal correlations versus noise in the correlation matrix formalism: An example of the brain auditory response. *Physical Review E* **62**:5557-5564.

20. Dahirel V, Shekhar K, Pereyra F, Miura T, Artyomov M, Talsania S, Allen TM, Altfeld M, Carrington M, Irvine DJ, Walker BD, Chakraborty AK. Coordinate linkage of HIV evolution reveals regions of immunological vulnerability. *Proc Natl Acad Sci USA* **108**:11530-11535.

21. Kamimura D, Ishihara K, Hirano, T. 2003. IL-6 signal transduction and its physiological roles: the signal orchestration model. *Rev Physiol Biochem Pharmacol* **149**:1-38.

Chapter 7: Concluding Remarks

In the previous chapters, we looked at a range of problems involving different components of the adaptive immune system. Chapters 2 and 3 addressed the nature of the interaction between DM and pMHC, as well as DM's role in the loading and unloading of peptides from MHC. These two manuscripts resulted from a collaboration between experimentalists (Hidde Plough's lab and Kai Wucherpfennig's lab) and computation / theory people (Arup Chakraborty's Lab). I believe that these are both fine examples of the work that can be done from such collaborations. The conclusions made in both studies likely would not have been reached otherwise.

Chapter's 4 and 5 were both examples of cytokines behaving "unexpectedly" similarly in their effects on immune cells when one gene has been removed. In Chapter 4 we saw that the anti-inflammatory responses induced by IL-6 and IL-10 were indistinguishable in SOCS3-/- cells, despite IL-6 being a pro-inflammatory cytokine. Conventional wisdom that IL-6's high amplitude, transient STAT3 signal is a "strong signal", while IL-10's low amplitude, sustained STAT3 signal is a "weak signal", led to the association of strong STAT3 signals with a pro-inflammatory response and a weak STAT3 signal with an anti-inflammatory response. This led to the conclusion that if a strong STAT3 signal was made even stronger by converting it from a transient signal to a sustained signal, it should induce an even more potent signal pro-inflammatory response. Therefore, it was quite unexpected when this resulted in a conversion to an anti-inflammatory response. This result would not have been unexpected if one de-convolutes amplitude and signal duration from the definition of a strong signal. This would lead to the correct conclusion that sustained signals lead to anti-inflammatory responses, while transient

signals lead to pro-inflammatory responses. Even though IL-6 and IL-10 are different cytokines they can behave the same if you make their STAT3 signals equivalent in duration.

Another example of cytokines behaving unexpectedly similar was seen in Chapter 5 where IL-6 and IL-27 were both potent inducers of Th17 differentiation in STAT1 knockout mice in the presence of TGF-β. This was "unexpected" since IL-27 has the reputation of being inhibitory towards Th17 differentiation through a mechanism involving STAT1. Conventional wisdom would suggest that the removal of STAT1 should just remove IL-27's inhibitory properties. However, we showed that removing STAT1 resulted in IL-27 inducing a STAT3 signal that is similar in duration and amplitude to IL-6. The fact that IL-27 can potently induce Th17 differentiation in the presence of TGF-β shows that there is nothing inherently different between the IL-6R and IL-27R other than the relative amounts of induced pSTAT1 and pSTAT3 that they lead to. The results from both of these chapters challenge the idea that cytokines induce unique conformations of STATs or other unknown factors in order to make them inherently different from one another. I think this is the main conclusion of this thesis.

In Chapter 6, we showed a simple algorithm that can be used to cluster genes according to their levels of activation over time, and showed its properties in the case of Th17 differentiation. The other main result from this Chapter was that Foxp3 and RORγt behaved completely opposite throughout Th17 differentiation. Whenever one was highly expressed, the other was expressed at low levels.

In summation, I think this thesis showed the benefits of collaboration and the benefits of approaching problems mathematically where species are just variables as opposed to attaching universal properties like "IL-27 is an inhibitory cytokine". Biology is so complex that we need

such classifications to teach the subject, but great caution must be used when attempting to solve complicated problems using strictly conventional wisdom.

Appendix 1: Various Experimental Protocols

A1.1 Flow Cytometry Procedure for pSTAT Measurement

Intracellular staining protocol for signaling molecules and transcription factors – L. Francisco, Sharpe Lab 2009 (With modifications)

1. Fix cells with 4% PFA (EM Grade real PFA) for 12 min at 37C. In each well add 112.5 µL PBS and then 37.5 µL 16% PFA (in hood). Cover with plate seal.
2. Rinse with PBS.
3. Spin down and resuspend cells in 15 µL PBS. Slowly add 135 µL cold 100% methanol drop-wise to result in a 90% methanol solution.
4. Incubate on ice for 30 min.
5. Wash out methanol twice with 1x eBiosciences Perm Buffer.
6. Block with Perm Buffer + 2% FBS and Fc Block (1:100) for 10 min at RT. For 1 antibody staining, this results in adding 87 µL Perm Buffer, 2 µL FBS, and 1 µL Fc block per well.
7. Stain with antibodies in Perm Buffer for 45 minutes, covered, at RT. Add 10 uL of the pSTAT antibody of choice in each well.
   - pSTAT1 – Alexa Fluor® 647 Mouse Anti-STAT1 (pY701) BD Biosciences (#612597)
   - pSTAT3 – PE Mouse Anti-STAT3 (pY705) BD Biosciences (#612569)
   - pSTAT6 – Alexa Fluor® 488 Mouse Anti-STAT6 (pY641) BD Biosciences (#558243)
8. Wash extensively (3x with 100 µL Perm Buffer), 2000 rpm 2-3min.
9. Bring to 280 µL PBS in small FACS tube and read on flow cytometer.

A1.2 EMSA (Electrophoretic Mobility Shift Assay) Procedure

Nuclear Extract Isolation:

1. Isolate CD4+ cells from a mouse's spleen and lymph nodes.
2. Incubate cells under different cytokine conditions.
3. Collect cells and transfer to a FACS plate.
4. Transfer cells from FACS plate into 1.5 mL eppendorf tubes.

5. Spin for 5 minutes at the highest speed.
6. Follow the instructions provided in the NE-PER nuclear and cytoplasmic extraction reagents kit from Pierce (Prod # 78833).
7. Only keep the nuclear extract (this is where the highest concentration of pSTATs is located).
8. Measure concentration using the A260 protein concentration program on the NanoDrop instrument.
9. Freeze at -80C until use.

Oligonucleotide Preparation:

All oligonucleotides were obtained from IDT. Labeled Oligos were 5' end labeled with Li-COR IR-DYE 700 on both complementary strands. Oligos were delivered at 100 µL in IDTE Buffer at pH 8.0. Competitor Oligos were not end labeled.

Sequences:

hSIE - 5'-GTC GAC ATT TCC CGT AAA TC-3'

(From reference chain that begun in Costa-Pereira, A.P. et al, *PNAS*, 2002)

STAT1 competitive oligo (S1 Oligo) – 5'-CAT GTT ATG CAT ATT CCT GTA AGT G-3' (Based on Santa Cruz Biotechnologies #2573)

STAT3 competitive oligo (S3 Oligo) – 5'-GAT CCT TCT GGG AAT TCC TAG ATC-3' (Based on Santa Cruz Biotechnologies #2571)

Labeled Oligo Annealing:

1. Add 10 µL of oligo and 10 µL of complement to an eppendorf tube
2. Place in 100C heating block for 5 min, then turn off heat and allow to cool in block for 75+min.
3. In 15 mL tube, add 2.5mL of nuclease free water and 5 µL of annealed oligo from step 2. This gives a 100 nM / 1 µL solution when added to the 20 µL reaction mixture.

Competitor Oligo Annealing:

1. Add 20 µL of oligo and 20 µL of complement to an eppendorf tube.
2. Place in 100C heating block for 5 min, then turn off heat and allow to cool in block for 75+min.

3. Add 60 µL of nuclease free water to eppendorf tube. This gives a 20 uM / 1 µL solution when added to the reaction mixture, which is 200x the Labeled Oligo concentration.

EMSA Solutions:

Some of these solutions are obtained from the Li-cor Odyssey EMSA Buffer Kit (#829-07910). This kit contains 10 labeled tubes of various solutions, which I will indicate as (tube #) to show it is from the kit and what tube it is found in.

100 mM HEPES – 100 µL 1M HEPES in 900 µL nuclease free water

10 mM EDTA – 5 µL 200 mM EDTA (tube 9) in 95 µL nuclease free water

15 mM MgCl2 – 15 µL 100 mM MgCl2 (tube 8) in 85 µL nuclease free water

20 mg/mL BSA – 0.2g BSA in 10 mL nuclease free water.

"Master Mix"

100 mM HEPES – 2 µL

15 mM MgCl2 – 2 µL

10 mM EDTA – 2 µL

50% Glycerol (Tube 5) – 2 µL

20 mg/mL BSA – 1 µL

25 mM DTT/2.5% Tween 20 (Tube 2) – 2 µL
1 µg/ µL Poly(dI.dC) (Tube 3) – 1 µL

Gel Preparation:

Filtered water – 25.33 mL

5x TBE – 8 mL

30% Acrylamide – 6.67 mL

15% APS – 444 µL

TEMED – 33.35 µL

Mix the above ingredients and add in between two 15 cm glass plates (1.5 mm separation). Place 15 well comb in the top of the gel and let gel form for 30 minutes.

Run the gel in 0.5x TBE for 45 minutes at 150V.

DNA Binding Reaction:

1. Add 12 µL of the "Master Mix" to a small eppendorf tube.
2. The total reaction size should be 20-22 µL. Therefore it is necessary to calculate how much nuclease free water to add (if any to bring up the reaction size to that amount).
3. Add 5 µg of nuclear extract.
4. Let sit for ~10 min so that the poly (di.dc) can take up non-specific binders.
5. Add supershift antibody (~5 ug) if doing supershift or add competitive oligo for 20 min. Listed below are the supershift antibodies I used, and the competitive oligos were described earlier.
6. Add labeled oligo for 30 min (keep in dark). (Note: Steps 5 and 6 can be swapped.)
7. Add 2 µL of orange loading dye (tube 10).

Supershift Antibodies (supplied at 2 ug/ µL):

Monoclonal STAT3 AB (S3m) – Santa Cruz Biotechnologies #8019x

Polyclonal STAT3 AB (S3p) – Santa Cruz Biotechnologies #482x

Monoclonal STAT1 AB (S1m) – Santa Cruz Biotechnologies #464x

Polyclonal STAT1 AB (S1p) – Santa Cruz Biotechnologies #346x

Gel Loading and Measurement:

1. Add 20 µL of the reaction mixture to a lane in the gel.
2. Cover gel apparatus with a box.
3. Run at 150V for 2.5 hours (or until orange loading dye reaches the bottom).

4. Measure results using Li-cor Odyssey instrument.

A1.3 Th17 Differentiation

1. Isolate CD4+ cells using autoMACS instrument (magnetic bead isolation)
2. For 3 mice (~60 million cells), put in 5 mL FACS buffer and stain with:
    a. CD4 PeCy7 – 5.25μL
    b. CD62L Fitc – 3.75μL
    c. CD25 PE – 3.75μL
3. Let sit on ice for 20 minutes
4. Spin at 1500 RPM for 5 min and resuspend in complete medium
5. Spin at 1500 RPM for 5 min and resuspend in complete medium (1mL / mouse used)
6. Filter by pipetting through cell strainer
7. Sort using FACS ARIA – collecting CD4+CD62L^{high}CD25-
8. Rinse 3 times!!
9. Make 24 well plate coated with α-CD3 (4μg/mL) and α-CD28 (2μg/mL) and incubate for 2 hours
10. Prepare Master Mix
    a. 6811.7 μL culture medium, 113.87 μL α-IL-4 (1.23 mg / mL stock), 63.92 μL α-IFNγ (2.19 mg/mL stock), 10.5 μL TGF-β (2μg/mL) stock
11. Split sorted cells into 7, 15-mL tubes, 1 for each well on the 24 well plate and resuspend tubes 2-7 in 1mL Master Mix and tube 1 in 1mL culture medium (control)
12. For wells with IL-6, add 1.2 μL IL-6 (25 μg/mL stock). For wells with IL-21, add 3 μL IL-21 (10 μg/mL stock). For wells with IL-27, add 1.5 μL IL-27 (20 μg/mL stock)
13. Add tubes to respective wells and put in incubator for 48 hours.

14. After 48 hours have passed, carefully remove 500 μL from the top of each well.
15. Prepare Master Mix
    a. 3452 μL culture medium, 28.5 μL α-IL4, 16 μL α-IFNγ, 3.5 μL IL-23 (10 μg/mL stock)
16. Add 500 μL of solutions to each well (Master Mix to wells 2-7 and culture medium to well 1)
17. Transfer cells to a new uncoated 24-well plate
18. Incubate for 48 hours
19. After 48 hours have passed, prepare restimulation solution
    a. 5 μL PMA (1:2000 dilution), 10 μL Ionomycin (1:1000 dilution), 10 μL Golgi stop (1:1000 dilution), 10 mL culture medium
20. Carefully collect 400 μL supernatant and put in 1mL eppendorf tubes and freeze for elisa
21. Add fresh medium and transfer to 5mL coered FACS tubes
22. Spin down and resuspend in restimulation solution
23. Incubate for 3.5 hours (129 mice) or 4 hours (B6 mice)
24. Spin down and rinse a few times.
25. Transfer cells into FACS plate and split into 4-5 samples
26. Resuspend in PBS: 89 μL PBS, 1 μL FC block in each well and place in fridge for 10min
27. Add 10 μL of (6 μL PBS, 1 μL CD4-Fitc, 3 μL 7AAD (FL3)) and place in fridge for 25min
28. Rinse 2 times in PBS
29. Fix in 100 μL BD Cytofix/cytoperm on ice for 25-30min
30. Rinse 2 times in 1x perm buffer

31. Block with 87 μL perm buffer, 2 μL FBS, 1 μL FC block per well and place in fridge for 10 min
32. Stain with 1:200 IL-17a APC (0.5 μL/well) and 1:300 IFNγ PE (0.33 μL/well) for 25-30 min in fridge.
33. Rinse 2 times with 1x perm buffer
34. Resuspend in FACS buffer and measure on 4-channel FACS Calibur

Appendix 2: Supplemental Materials for Chapter 2

Figure A2.1

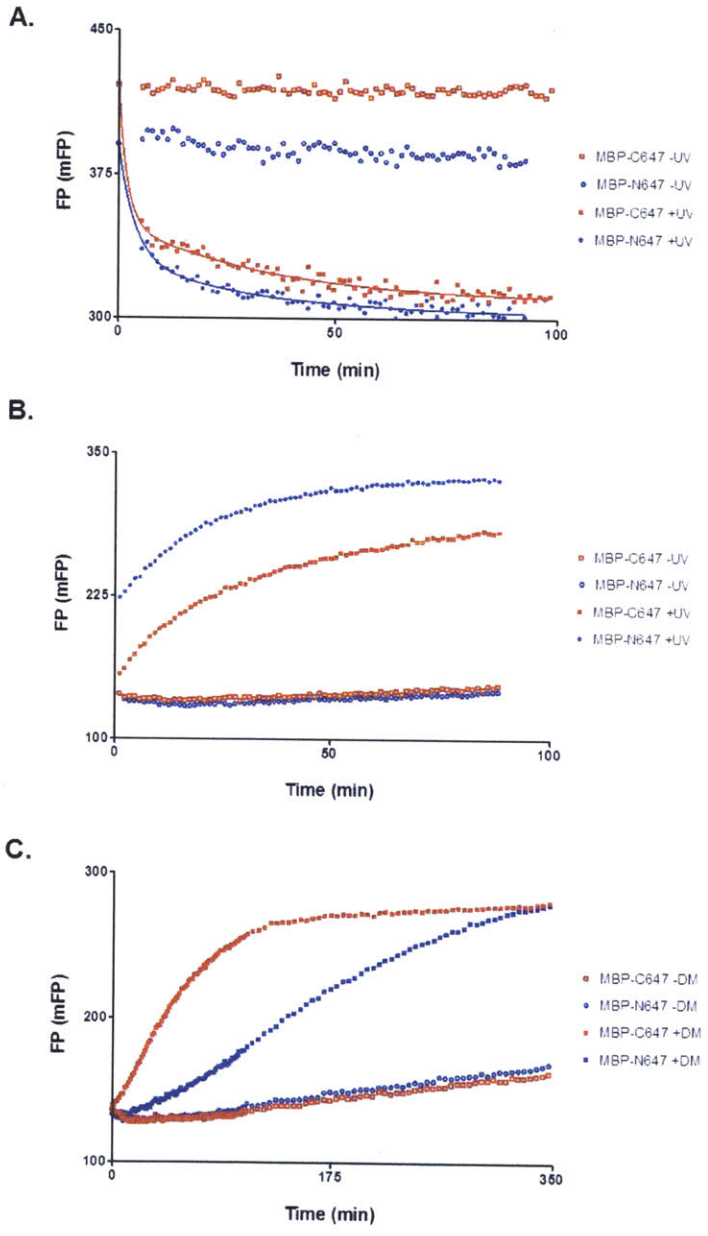

Figure A2.1. (A) Monitoring dissociation of photocleavage products with an N-terminal or C-terminal Alexa647 fluorescent group on the photocleavable peptides **MBP-C647** and **MBP-N647**. (B) Association of **MBP-488** was followed in the 488nm channel. Open symbols represent complexes without UV irradiation (□ = **MBP-C647**, ○ = **MBP-N647**), closed symbols complexes with UV irradiation (■ = **MBP-C647**, ● = **MBP-N647**). The **MBP-488** association phase following cleavage of **MBP-N647** mirrored the early rapid dissociation kinetics of the N-terminal **N647** fragment (A). A higher FP reading was observed following cleavage of DR2 loaded with **MBP-N647**, due to more efficient photocleavage of this peptide. (C) Effect of DM on displacing **MBP-N647** or **MBP-C647**, monitored by binding of **MBP-488**. DM accelerated exchange of the **MBP-N647** and **MBP-C647** peptides by **MBP-488**, but the N-terminal Alexa647 group in the **MBP-N647** peptide reduced the activity of DM on this complex compared to the **MBP-C647** peptide, consistent with mutagenesis data that mapped the DM binding site close to the peptide N-terminus (Doebele et al., 2000).

Table A2.1: Yield of DR2-peptide complexes and affinity of peptides for DR2

	MBP_{85-99}	**MBP-P1***	**MBP-P2***	**MBP-P3***	**MBP-P4***	**MBP-P5***
Yield complex†	~300 μg	~3 μg	~30 μg	~30 μg	~300 μg	~50 μg
Affinity difference‡	1	306	52	355	3	11

† Recovery after all purification steps
‡ Fold difference affinity for DR2 compared to index MBP_{85-99}

Peptide Synthesis

Standard Fmoc-based solid-phase peptide chemistry was employed for the synthesis of peptides **MBP-P1* - MBP-P5***. N-terminal capping was accomplished by coupling of a 4-aminobutyric acid succinimide ester endowed with a dinitrophenyl (Dnp) moiety. Cleavage from the resin and

concomitant removal of the side-chain protecting groups was followed by HPLC purification and lyophilization of the final products. LC/MS analysis and MALDI TOF MS confirmed the identity and homogeneity of the peptides.

Purified peptides of the sequence Dnp-C(SStBu)NPVVHF-Anp-KNIVTPC were labeled with thiol-reactive maleimide derivatives of AlexaFluor647 C_2-maleimide (Invitrogen, Carlsbad, CA). The attachment of the fluorecent probe to the C-terminal cysteine was accomplished using a modified procedure of the manufacturers instructions. Typically, in an eppendorf tube, shielded from light with alumium foil, 77 μL of a stock solution of peptide Dnp-C(SStBu)NPVVHF-Anp-KNIVTPC in N,N-dimethylformamide (10 mM) was diluted with 77 μL water and 30 μL phosphate buffer (1 M, pH 7) after which a stock solution of AlexaFluor647 C_2-maleimide in water (10 mM) was added. The reaction was allowed to proceed overnight with gentle shaking. LC/MS analysis confirmed quantative consumption of the starting material. The crude mixture was then purified by HPLC. Fractions containing the desired product were pooled and solvents evaporated *in vacuo*. Lyophilization of the final product afforded 1.1 mg, 0.35 □mol of **MBP-N647**.

The N-terminal derivitization with the AlexaFluor647 C_2-maleimide (Invitrogen, Carlsbad, CA) required initial blocking of the C-terminal free thiol, followed by release of thio-*tert*-Butyl protecting group under the agency of tributylphosphine. Therefore, to 65 μL of peptide stock Dnp-C(SStBu)NPVVHF-Anp-KNIVTPC (10 mM in DMF) was added 65 μL water and 7 μL phosphate buffer (1 M, pH 7) as well as 3.25 μL of N-ethylmaleimide (1M in DMF). After shaking for 2 hours, the reaction was quenched by the addition of 4.9 μL of 2-mercaptoethanol (1M in DMF) which was allowed to react for an additional hour. Having exposed the N-terminal free thiol, the peptide was HPLC purified and reacted with AlexaFluor647 C_2-maleimide (Invitrogen, Carlsbad, CA) as described above to furnish 1.0 mg, 0.32 □mol of the final product **MBP-C647**.

Modeling Methods

Each of the three models discussed in the main text were fit to the experimental data using a nonlinear regression package in MATLAB. All of the experiments used for parameter estimation involved the addition of **MBP-488** after 10 minutes of UV exposure to a well containing *e*MHC with or without DM. The relevant ordinary differential equations were solved to determine the concentrations of all species as a function of time and the concentration of *fp*MHC was plotted with the experimental data. In the analyses, the concentration of **MBP-488** was set to 0 nM for the first 10 minutes. After 10 minutes, the concentration was set to 200 nM to simulate the addition of **MBP-488** after the UV exposure. A good initial estimate for the unknown parameters was necessary to get the regression package to converge on a reasonable solution. To obtain a good initial estimate, the unknown parameters were varied manually until the predicted *fp*MHC trajectory overlapped considerably with the experimental data. The nonlinear regression package was then used to refine the parameter estimates.

All reactions were assumed to be elementary, which means that reactions involving one species are first order, two species are second order, etc. A list of all of the possible reactions found in the three proposed models in the main text is shown in **Table A2.2**, along with the corresponding rate expressions. Reaction 2 was assumed to be irreversible because peptide removal to form *e*MHC is slow in the absence of UV and DM. Reactions 7 and 8 involve the UV cleavage of the peptide and the subsequent dissociation of the peptide fragments from DR2, respectively. These two events are assumed to be first order and fast. Reaction 9 is written in a completely general manner using the aggregation number, N, since the number of *e*MHC molecules involved in the reaction is unknown. In the event that the aggregation number is 1, then this reaction represents the reversible unfolding of *e*MHC to an unreactive form. If the aggregation number is greater than 1, then this reaction represents the reversible aggregation of N *e*MHC molecules. All rates are written on a concentration basis, with concentrations in nM.

Table A2.2: List of possible reactions and corresponding rate expressions

Index	Reaction	Rate Expression
2	*eMHC+MBP-488* $\rightarrow$ *fpMHC*	$r_2=k_2$[eMHC][MBP-488]
5	*DM-eMHC+MBP-488* $\leftrightarrow$ *fpMHC*	$r_5=k_5$[DM-eMHC][MBP-488]-k_{-5}[DM][fpMHC]
7	*pMHC* $\rightarrow$ *p*MHC*	$r_7=k_7$[pMHC]
8	*p*MHC* $\rightarrow$ *eMHC*	$r_8=k_8$[p*MHC]
9	*N eMHC* $\leftrightarrow$ *iMHC*	$r_9=k_9$[eMHC]^N-k_{-9}N[iMHC]
10	*eMHC+DM* $\leftrightarrow$ *DM-eMHC*	$r_{10}=k_{10}$[eMHC][DM]-k_{-10}[DM-eMHC]

The set of equations corresponding to model 1 (Eq. 2.1) are given as

$$\frac{d}{dt}[\text{pMHC}] = -r_7 = -k_7[\text{pMHC}]$$

$$\frac{d}{dt}[\text{p*MHC}] = r_7 - r_8 = k_7[\text{pMHC}] - k_8[\text{p*MHC}]$$

$$\frac{d}{dt}[\text{eMHC}] = r_8 - r_2 = k_8[\text{p*MHC}] - k_2[\text{eMHC}][\text{MBP-488}]$$

$$\frac{d}{dt}[\text{fpMHC}] = r_2 = k_2[\text{eMHC}][\text{MBP-488}]$$

$$[\text{MBP-488}] = [\text{MBP-488}]_0 - [\text{fpMHC}] \qquad \text{(A2.1)}$$

where an algebraic species conservation relation is necessary in addition to the ordinary differential equations to calculate the concentration of **MBP-488** at each time point using species

conservation. The values of both k_7 and k_8 were set to 1 min^{-1}, which allowed these reactions to go to completion during the 10 minute UV step as observed in experiments. No value of k_2 was able to capture the experimentally observed behavior at both short and long times.

The set of equations corresponding to model 2 (Eq. 2.2) are given as

$$\frac{d}{dt}[\text{pMHC}] = -r_7 = -\text{k}_7[\text{pMHC}]$$

$$\frac{d}{dt}[\text{p*MHC}] = r_7 - r_8 = \text{k}_7[\text{pMHC}] - \text{k}_8[\text{p*MHC}]$$

$$\frac{d}{dt}[\text{eMHC}] = r_8 - r_2 - r_9 = \text{k}_8[\text{p*MHC}] - \text{k}_2[\text{eMHC}][\text{MBP-488}] - (\text{k}_9[\text{eMHC}]^{\text{N}} - \text{k}_{-9}\text{N}[\text{iMHC}])$$

$$\frac{d}{dt}[\text{iMHC}] = r_9 = \text{k}_9[\text{eMHC}]^{\text{N}} - \text{k}_{-9}\text{N}[\text{iMHC}]$$

$$\frac{d}{dt}[\text{fpMHC}] = r_2 = \text{k}_2[\text{eMHC}][\text{MBP-488}]$$

$$[\text{MBP-488}] = [\text{MBP-488}]_0 - [\text{fpMHC}] \qquad \text{(A2.2)}$$

where an aggregation reaction has been added in order to account for the experimentally observed behavior at short and long times. This model has four parameters, in addition to k_7 and k_8 that were fit to the experimental data. A comparison of the model prediction and the experimental data for one set of parameters is shown in **Fig. 2.7B.**

The set of equations corresponding to model 3 (Eq. 2.3) are given as

$$\frac{d}{dt}[\text{pMHC}] = -r_7 = -\text{k}_7[\text{pMHC}]$$

$$\frac{d}{dt}[\text{p*MHC}] = r_7 - r_8 = \text{k}_7[\text{pMHC}] - \text{k}_8[\text{p*MHC}]$$

$$\frac{d}{dt}[\text{eMHC}] = r_8 - r_2 - r_9 - r_{10}$$

$$= k_8[\text{p*MHC}] - k_2[\text{eMHC}][\text{MBP-488}] - (k_9[\text{eMHC}]^N - k_{-9}N[\text{iMHC}]) - (k_{10}[\text{eMHC}][\text{DM}] - k_{-10}[\text{DM-eMHC}])$$

$$\frac{d}{dt}[\text{iMHC}] = r_9 = k_9[\text{eMHC}]^N - k_{-9}N[\text{iMHC}]$$

$$\frac{d}{dt}[\text{DM-eMHC}] = r_{10} - r_5$$

$$= k_{10}[\text{eMHC}][\text{DM}] - k_{-10}[\text{DM-eMHC}] - (k_5[\text{DM-eMHC}][\text{MBP-488}] - k_{-5}[\text{DM}][\text{fpMHC}])$$

$$\frac{d}{dt}[\text{fpMHC}] = r_2 + r_5$$

$$= k_2[\text{eMHC}][\text{MBP-488}] + (k_5[\text{DM-eMHC}][\text{MBP-488}] - k_{-5}[\text{DM}][\text{fpMHC}])$$

$$[\text{MBP-488}] = [\text{MBP-488}]_0 - [\text{fpMHC}]$$

$$[\text{DM}] = [\text{DM}]_0 - [\text{DM-eMHC}] \qquad \text{(A2.3)}$$

where two additional algebraic species conservation relationships are necessary to calculate the concentrations of DM and **MBP-488** at all time points using species conservation. The values of the parameters obtained from model 2 (used to prepare the curve in **Fig. 2.7B**) were fixed and the additional parameters were fit to experiments where the amount of DM was varied. A comparison of the model predictions and the experimental data for one set of best-fit parameters is shown in **Fig. 2.7C**. Due to the large number of experiments, only a representative set of curves are shown in the figure. A summary of the quality of fit for all experiments can be found in **Table A2.3.** The maximum and minimum percent deviations for each set of conditions were determined by first calculating the percent deviation of the model from the experimental data at all time points using the following equation

$$\%dev(t=\tau) = \frac{[fpMHC]_{predicted}(t=\tau) - [fpMHC]_{experimental}(t=\tau)}{[fpMHC]_{experimental}(t=\tau)} \qquad \text{(A2.4)}$$

where *%dev* is the percent deviation and τ is a generic time value.

Table A2.3: Quality of fit for all DM experiments used for parameter estimation. All quality of fit parameters have been calculated using data points collected within the first 100 minutes of each experiment. The largest magnitude of the percent deviation for all experiments occurred within the first two time points. Values of R^2 are also reported to show that the overall quality of the fit is excellent for all sets of data as in Fig. 7C.

DM Concentration (nM)	R^2	Maximum % Deviation	Minimum % Deviation
0	0.956	18.91	0.14
150	0.988	24.52	0.20
300	0.995	12.66	0.03
500	0.979	61.55	0.03
1000	0.985	31.27	0.00
2000	0.976	24.61	0.01
5000	0.899	24.86	0.17

Parameter sensitivity

As indicated in the main text, we performed parameter sensitivity studies for all models, and found other sets of parameters that also fit the data well. The main mechanistic point derived from the kinetic analyses is that k5 is greater than k2, thereby indicating that DM-bound MHC is more peptide receptive than the receptive state of MHC alone. This result is robust to parameter sensitivity using model 3. As noted in the main text, it is also robust to other models that we explored which were designed such that lower values of k5 might be able to fit the data. For example, we determined the smallest value of *k5* that could predict the large initial slope observed in the experiments where DM was added. To obtain this smallest value, *k-5* and *k-10*

were set to zero since reversible reactions would reduce the initial slope (requiring larger values of *k5*). The value of *k10* was set to a large value since this would create the largest concentration of DM-*e*MHC, which results in the smallest value of *k5* necessary to obtain the same rate. The initial slope of the data for 150 nM DM is the smallest in our experimental data set, and so fitting the initial slope of this data with this model would yield the smallest possible value of k5. The initial slope could only be fit if k5 was at least two times greater than k2. So, even in such a model designed to obtain the smallest possible value of k5, its value must be greater than k2 in order to be in harmony with experimental data.

Appendix 3: Supplemental Materials for Chapter 3

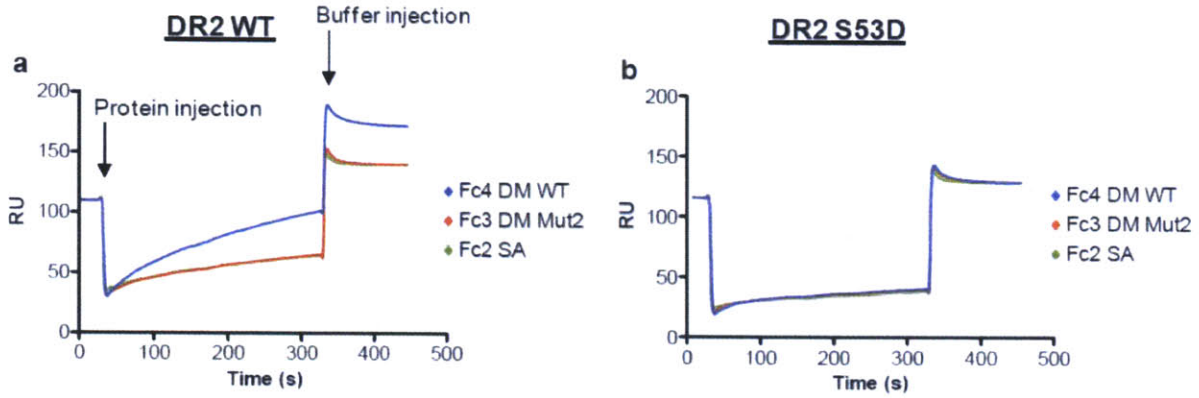

Figure A3.1. Minimal background binding by a HLA-DR mutant compared to the streptavidin surface. In SPR experiments, the sensor detects refractive index changes when only buffer or protein in buffer is injected. Therefore, it is a widely accepted convention in Biacore studies to subtract the response in a control flow cell from the experimental flow cell. Such a control also addresses non-specific binding. We went one step further to rigorously control for non-specific binding: we designed a HLA-DM mutant that closely resembled the biophysical properties of wild-type HLA-DM but which had no catalytic activity and did not bind to HLA-DR–peptide complexes (HLA-DM Mut2). The HLA-DM Mut2 control surface (flow cell 3, Fc3) did not show increased background binding compared to the streptavidin surface (flow cell 2, Fc2) in all experiments that were performed. The two graphs compare results from HLA-DR2 WT (**a**) and the HLA-DR2 S53D mutant (**b**) for three surfaces: HLA-DM WT, HLA-DM Mut2 and streptavidin (SA). HLA-DR2 binding curves were very similar when HLA-DM Mut2 and streptavidin surfaces were compared. Data are representative of more than five (**a**) and of two (**b**) independent experiments, respectively. m – m

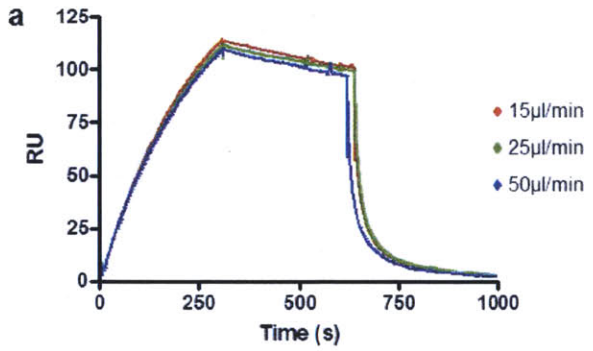

Figure A3.2. Absence of significant rebinding of HLA-DR to HLA-DM (mass transport). (**a**) HLA-DR2–CLIP complexes (2 µM) were run through HLA-DM WT and HLA-DM Mut2 flow cells (1000 RU of immobilized protein) for 5 minutes at the indicated flow rates in a citrate-phosphate buffer with a pH of 5.35 at 30 °C. This was followed by injection of buffer (stage 2) and 20 µM $CLIP_{87\text{-}101}$ (stage 3). Binding in the HLA-DM Mut2 flow cell was subtracted from measurements in the HLA-DM WT flow cell. Data are representative of two independent experiments as shown and of more than three independent experiments under similar conditions.

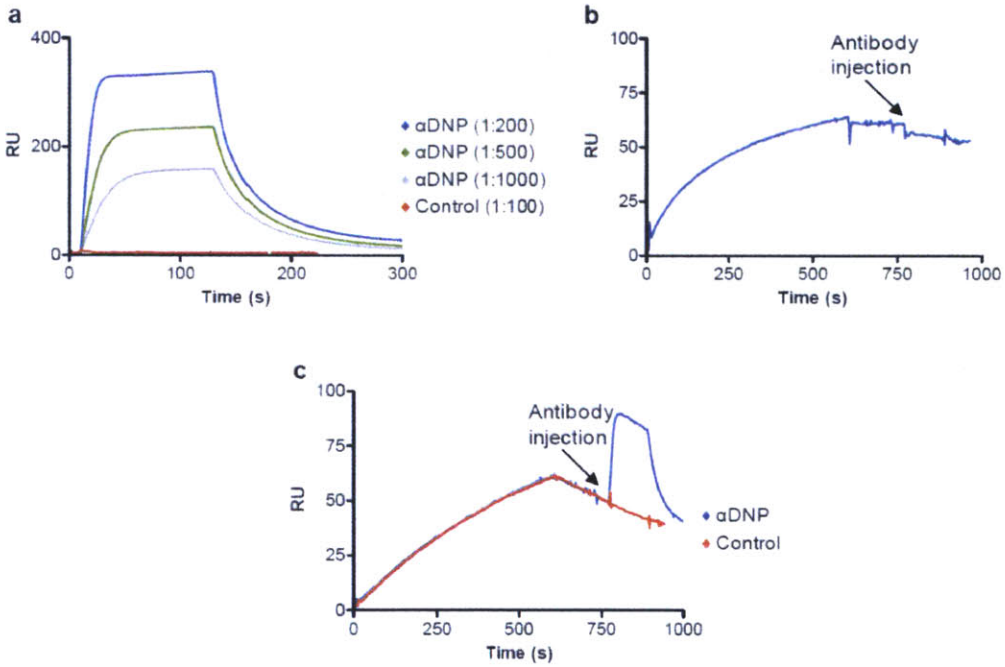

Figure A3.3. The complex of HLA-DR and HLA-DM in stage 2 is devoid of peptide. (**a**) Specific binding of the DNP antibody to a DNP-labeled peptide bound to HLA-DR2. HLA-DR2–CLIP (control, no DNP group on peptide) or HLA-DR2–MBP(85-99)-DNP (500 RU of each protein) were immobilized on a streptavidin chip. DNP or control antibody (at the indicated dilutions) were injected for 2 min (25 °C, 15 µl/min), followed by injection of buffer (citrate-phosphate buffer, pH 6). Binding in the HLA-DR2–CLIP (no DNP) control flow cell was

subtracted from binding in the two experimental flow cells. (**b**) The stable complex of HLA-DM and HLA-DR in stage 2 is devoid of peptide. HLA-DR2–CLIP(87-101)-DNP (5 μM) was injected for 10 minutes (25° C, 15 μl/min), followed by injection of buffer and a 2 minute injection of antibody (DNP or control antibody at 2 μg/ml) in citrate-phosphate buffer (pH6). The SPR assay was carried out in consecutive flow cells with immobilized HLA-DM WT or HLA-DM Mut2 (500 RU of each protein) in citrate-phosphate buffer (pH 5.35). Binding in the HLA-DM Mut2 flow cell was subtracted from measurements in the HLA-DM WT flow cell. Data are representative of two independent experiments. (**c**) The DNP antibody detects the DNP group of a covalently linked peptide. HLA-DR1-HA_6 P_2P_{11} complex (0.5μM) with a C-terminal DNP group on the linked peptide was injected (as in **b**), followed by injection of DNP or control antibody in stage 2.

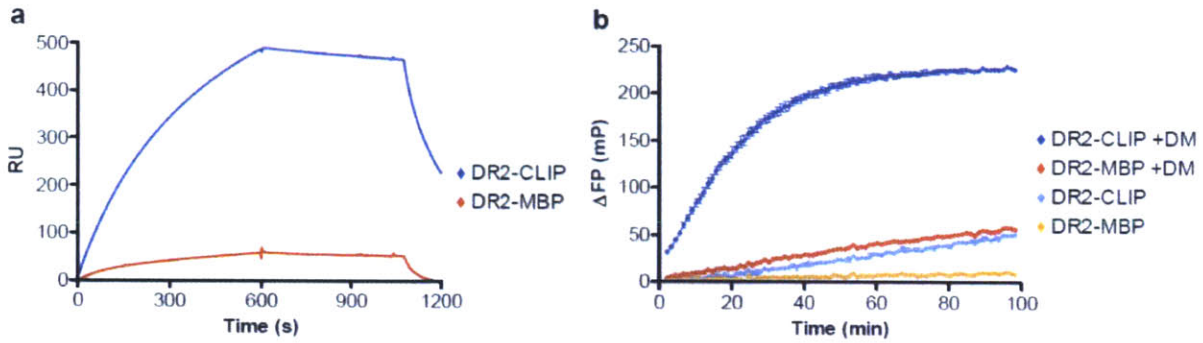

Figure A3.4. Comparison of the kinetics of HLA-DM binding and HLA-DM catalysis for low-affinity versus high-affinity HLA-DR–peptide complexes. (**a**) Comparison of HLA-DM binding by low-affinity HLA-DR2–CLIP and high-affinity HLA-DR2– MBP_{85-99} complexes. HLA-DR2 complexes preloaded with the indicated peptides (10 μM) were injected for 10 minutes (stage 1), followed by injection of buffer (stage 2) and 5 μM MBP_{85-99} (stage 3). The SPR assay was carried out in consecutive flow cells with 500 RU of immobilized HLA-DM WT and HLA-DM Mut2 in a citrate-phosphate buffer (pH 5.35) at 37 °C at a flow rate of 15 μl/min. Measurements from the HLA-DM Mut2 flow cell were subtracted from data obtained from the HLA-DM WT flow cell. HLA-DM binding by HLA-DR2–MBP_{85-99} was 8.7-fold slower compared to HLA-DR2–CLIP, based on measurement of the initial rates. (**b**) Comparison of HLA-DM susceptibility of HLA-DR2–CLIP and HLA-DR2–MBP_{85-99} complexes. Binding of 200 nM Alexa488-labeled MBP_{85-99} to HLA-DR2 (200 nM) preloaded with the indicated peptides was measured in the presence or absence of 100 nM HLA-DM in 50 mM citrate phosphate buffer (pH 5.3) containing 150 mM NaCl. The initial rate of HLA-DM-catalyzed peptide binding was 11.8-fold slower when HLA-DR2–MBP_{85-99} rather than HLA-DR2–CLIP was used as the input protein in the reaction. Data are representative of two independent experiments as shown (**a**, **b**) and of more than three under similar conditions (**a**) (FP assays were performed in triplicates).

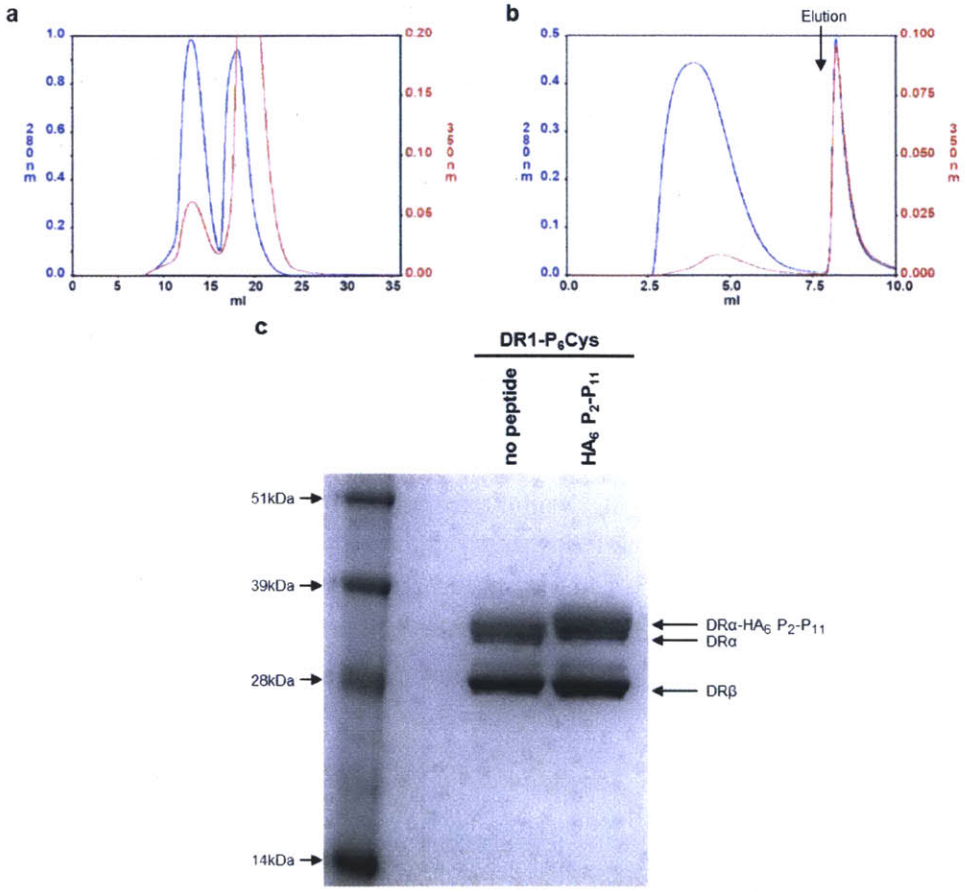

Figure A3.5. Production of homogenous disulfide-linked HLA-DR1–peptide complexes. (**a-c**) Purification of disulfide-linked complexes of HLA-DR1 P_6 Cys and HA_6 P_2P_{11} peptide. (**a**) Removal of excess free DNP-labeled peptide following peptide loading and disulfide bond formation. HLA-DR1–P_6 Cys molecules were separated from DNP-labeled HA_6 P_2P_{11} peptide by gel filtration (Superose 12). The blue trace (280nm) represents protein absorbance, the red trace (350 nm) DNP absorbance. The peak between 11-15ml contains the HLA-DR–peptide complex, the later peak the free peptide. (**b**) Affinity purification of disulfide-linked HLA-DR1–HA_6 P_2P_{11} complexes by DNP affinity chromatography from other HLA-DR species. Protein and peptide are traced as described in (**a**). The earlier peak represents the flow-through, the later peak the peptide-loaded complex (elution with CAPS buffer, pH 11.5). (**c**) Analysis of disulfide linkage of HA_6 P_2P_{11} peptide to the HLA-DRα chain by non-reducing SDS PAGE. Data are representative of at least four independent experiments.

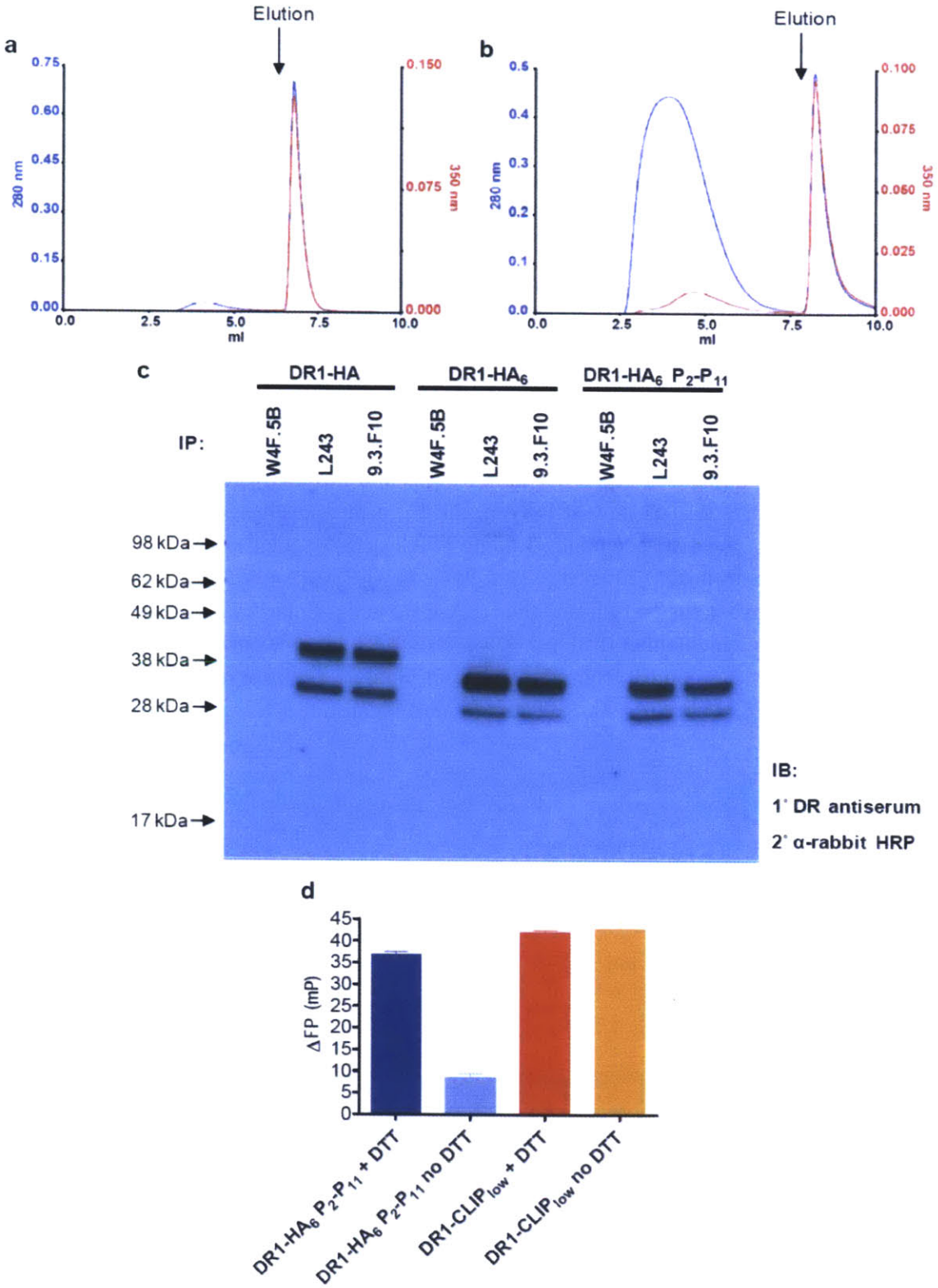
a
Elution
280 nm
350 nm
ml
b
Elution
280 nm
350 nm
ml
c
DR1-HA
DR1-HA6
DR1-HA6 P2-P11
IP:
W4F.5B
L243
9.3.F10
98 kDa
62 kDa
49 kDa
38 kDa
28 kDa
17 kDa
IB:
1° DR antiserum
2° α-rabbit HRP
d
ΔFP (mP)
DR1-HA6 P2-P11 + DTT
DR1-HA6 P2-P11 no DTT
DR1-CLIPlow + DTT
DR1-CLIPlow no DTT

Figure A3.6. Biochemical characterization of HLA-DR1 molecules with covalently linked full length or partial peptides. (**a**, **b**) Affinity purification of disulfide-linked HLA-DR1–HA_6 (**a**) and HLA-DR1–HA_6 P_2P_{11} (**b**) complexes by DNP affinity chromatography from other HLA-DR species. The blue trace (280nm) represents protein absorbance, the red trace (350 nm) DNP absorbance. The earlier peak represents the flow through, the later peak the peptide-loaded complex (elution with CAPS buffer, pH 11.5). The scales of 280 nm and 350 nm readings were adjusted based on prior experiments with affinity purified, fully loaded HLA-DR–peptide complexes such that identical peak heights reflected full occupancy of the peptide binding groove by DNP-labeled peptide. Based on these measurements, the peptide binding groove of both HLA-DR1–HA_6 (**a**) and HLA-DR1–HA_6 P_2P_{11} (**b**) was fully occupied. (**c**) Immunoprecipitation of covalent HLA-DR1-peptide complexes by conformation-sensitive antibodies to HLA-DRα and HLA-DRβ chains. HLA-DR1- $HA_{306-318}$ peptide complexes (without covalent linkage) as well as HLA-DR1–HA_6 and HLA-DR1–HA_6 P_2P_{11} complexes were immunoprecipitated with a control mAb (W4F.5B), mAb L243 (to HLA-DRα chain) or mAb 9.3.F10 (to HLA-DRβ chain). The Western blot was labeled with a polyclonal anti-DR serum, followed by a polyclonal HRP-labeled rabbit IgG antiserum. (**d**) Low-affinity HA_6 P_2P_{11} peptide exchanges quickly from HLA-DR1 upon reduction of the disulfide bond. Binding of Alexa488-labeled $HA_{306-318}$ (65 nM) to the indicated HLA-DR1 complexes (200 nM) was followed by FP with or without prior reduction of the disulfide bond between the peptide and the HLA-DRα helix. Equilibrium binding data are shown for reactions in which either the HLA-DR1–HA_6 P_2P_{11} complex or the HLA-DR1–$CLIP_{low}$ complex (positive control) were used as input proteins. Data are representative of at least two independent experiments (FP assay performed in triplicate).

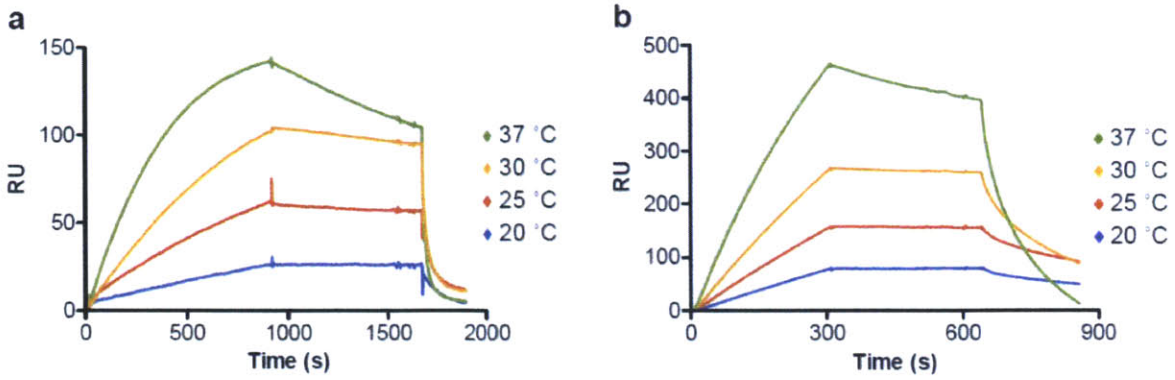

Figure A3.7. HLA-DM binding to HLA-DR loaded with full-length peptide is highly temperature dependent. (**a,b**) Temperature profiles for HLA-DM binding by HLA-DR molecules loaded with CLIP peptide (HLA-DR2–CLIP, **a**) or a low-affinity CLIP variant (HLA-DR1–$CLIP_{low}$, **b**). (**a**,**b**) HLA-DR2–CLIP complexes (0.5 μM, **a**) and HLA-DR1– $CLIP_{low}$ complexes (1 μM, **b**) were run over the HLA-DM WT and HLA-DM Mut2 flow cells (500 RU of immobilized proteins) at a flow rate of 15 μl/min in a citrate-phosphate buffer with a pH of 5.35 at the indicated temperatures. This was followed by injection of buffer and injection of 20 μM CLIP (**a**) or 50 μM $HA_{306-318}$ (**b**). Binding in the HLA-DM Mut2 flow cell was subtracted from measurements in the HLA-DM WT flow cell. Data are representative of two independent experiments shown (**a**, **b**) and of at least four independent experiments under similar conditions (**a**).

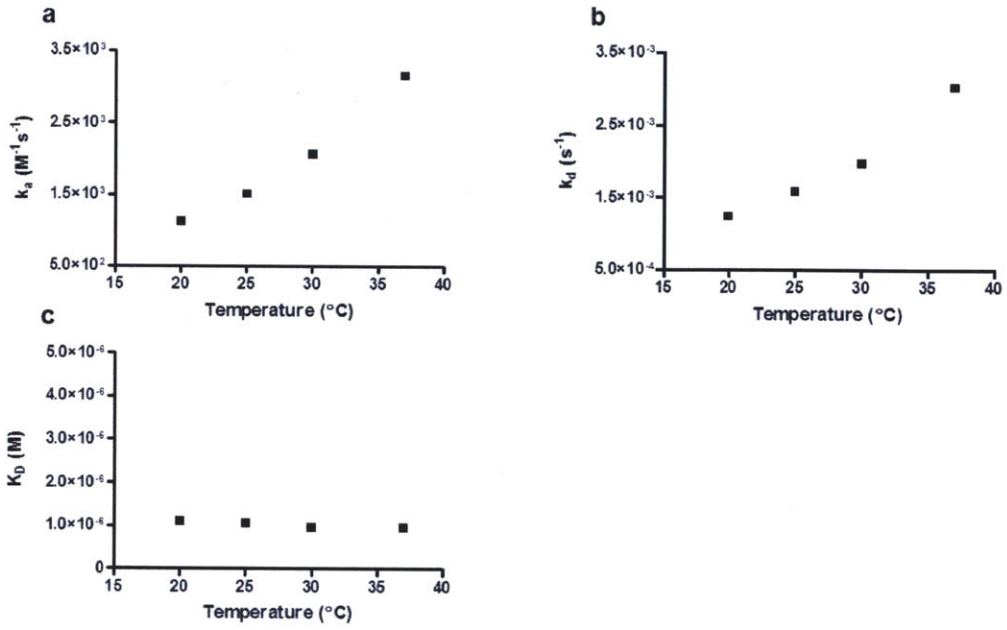

Figure A3.8. Kinetic parameters for HLA-DM binding to HLA-DR1-HA_6 P_2P_{11} complex. (**a-c**) HLA-DR1–HA_6 P_2P_{11} complexes (0.1 to 5 μM) were injected into HLA-DM WT and HLA- DM Mut2 flow cells at temperatures ranging from 20 to 37 °C. The datasets were fitted as in **Fig.** 3.7**c** and k_a, k_d, and K_d values were plotted against the corresponding temperatures. Data are representative of two independent experiments.

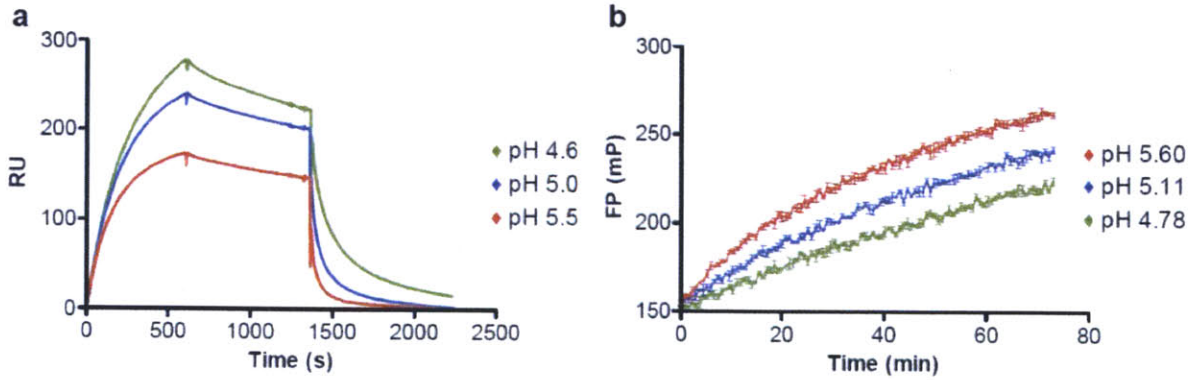

Figure A3.9. Slower dissociation of HLA-DM–HLA-DR complex at lower pH. (**a**) Low pH increases HLA-DM binding to HLA-DR–CLIP and slows dissociation of HLA-DM– HLA-DR complexes. HLA-DR2–CLIP complexes (5 μM) were run over the HLA-DM flow cell (500 RU of immobilized HLA-DM) and the SA flow cell for 10 minutes at a flow rate of 15 μl/min in a citrate-phosphate buffer with the indicated pH at 30°C, followed by injection of buffer (stage 2) and $CLIP_{87\text{-}101}$ at a concentration of 20 μM (stage 3). Binding in the SA flow cell was

subtracted from the measurements in the HLA-DM WT flow cell. (**b**) pH dependent peptide binding to HLA-DR2 molecules after photolysis of bound peptide. HLA-DR2–MBP_{85-99} complexes preloaded with UV-cleavable MBP peptide were UV irradiated for 10 minutes in 10 mM Tris pH 7.0 on ice to generate empty HLA-DR2 molecules. Binding of Alexa-488 labeled MBP_{85-99} (30 nM) to empty HLA-DR2 (150 nM) was measured directly following UV-cleavage using FP at the indicated pH. Data are representative of at least two independent experiments (FP assay performed in triplicates).

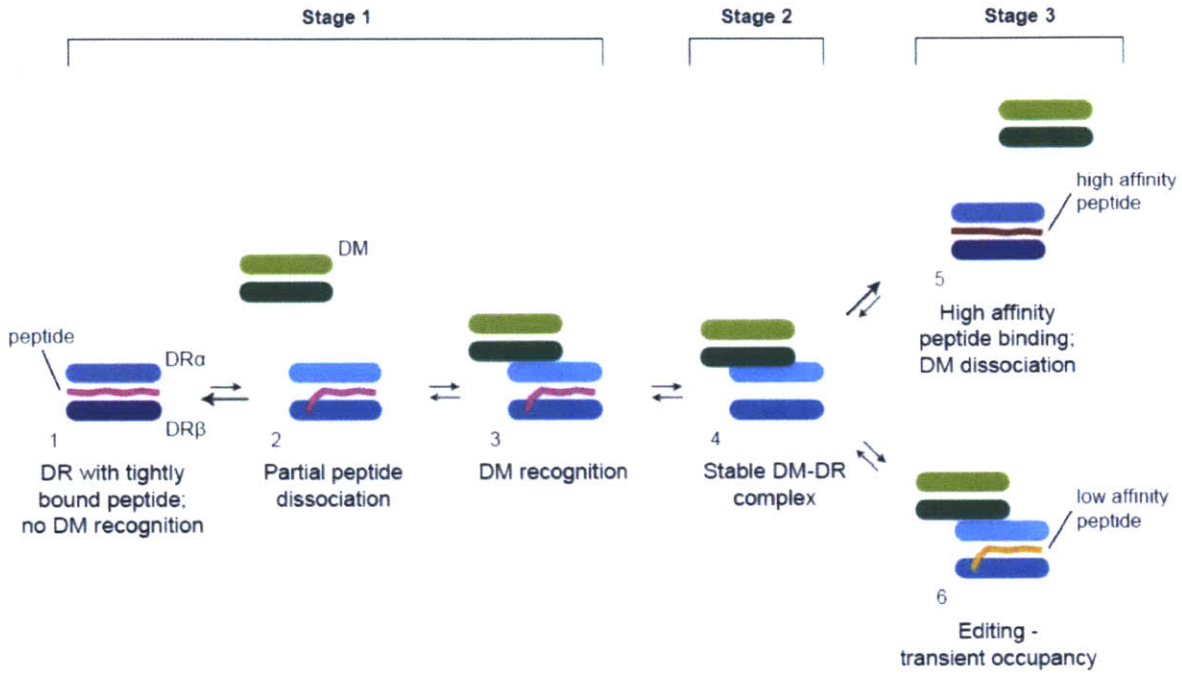

Figure A3.10. Model of the interaction of HLA-DM with HLA-DR. HLA-DR molecules with a fully bound peptide (1) do not interact with HLA-DM. Partial peptide dissociation at the N-terminus (2) enables HLA-DM binding (3). HLA-DM catalyzes peptide removal and forms a long-lived complex with HLA-DR in the absence of peptide (4). Binding of a high-affinity peptide to this complex will most likely result in its dissociation (5), while the HLA- DM–HLA-DR complex is more likely to remain intact upon binding of a low-affinity peptide (6). Low-affinity peptide can be removed by the catalytic action of HLA-DM (editing) and the complex of empty HLA-DR and HLA-DM (4) is then again available for peptide binding. The conformational change in HLA-DR molecules upon release of the N-terminal peptide segment is indicated here by a change in color, compared to HLA-DR molecules with tightly bound peptides. For all individual molecular steps, the corresponding stages of SPR experiments are indicated (stages 1-3).

Appendix 4: Supplemental Materials for Chapter 4

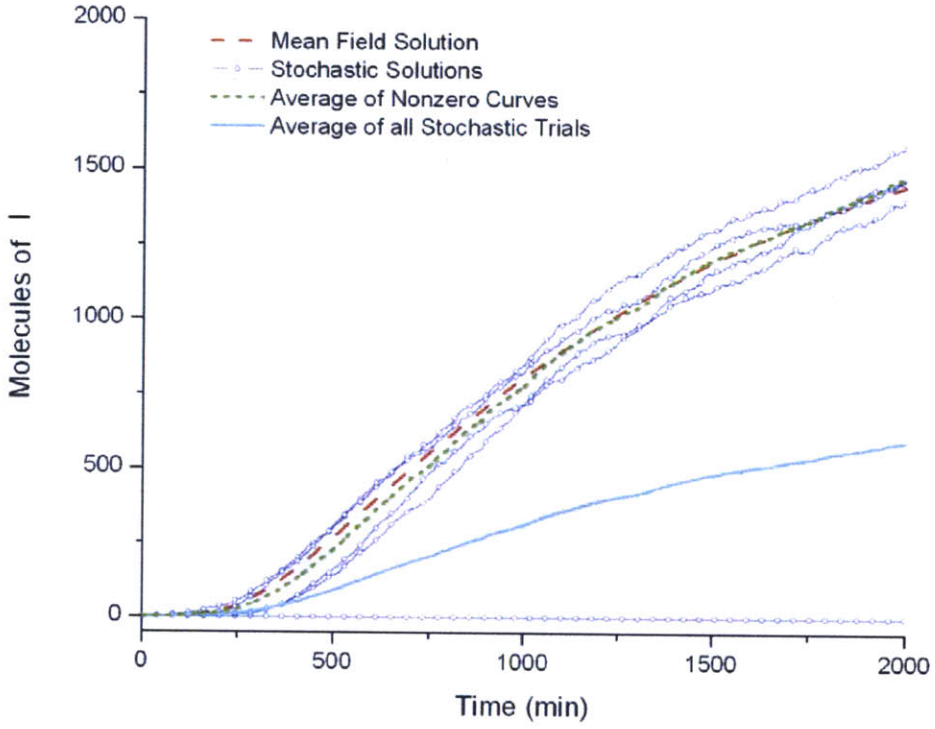

Figure A4.1. Only the nonzero stochastic solution trajectories follow the mean field solution to the model equations for molecule I at a signal degradation rate of 1.0 min^{-1}. Time course trajectories obtained by solution of the model equations using a mean field ODE solver (red curve), ten times using the Gillespie Algorithm (10 blue curves), average at each time point of the nonzero stochastic trajectories (green curve), and average at each time point of all the stochastic trajectories (cyan curve). Parameters for the model were obtained from Table 4.1.

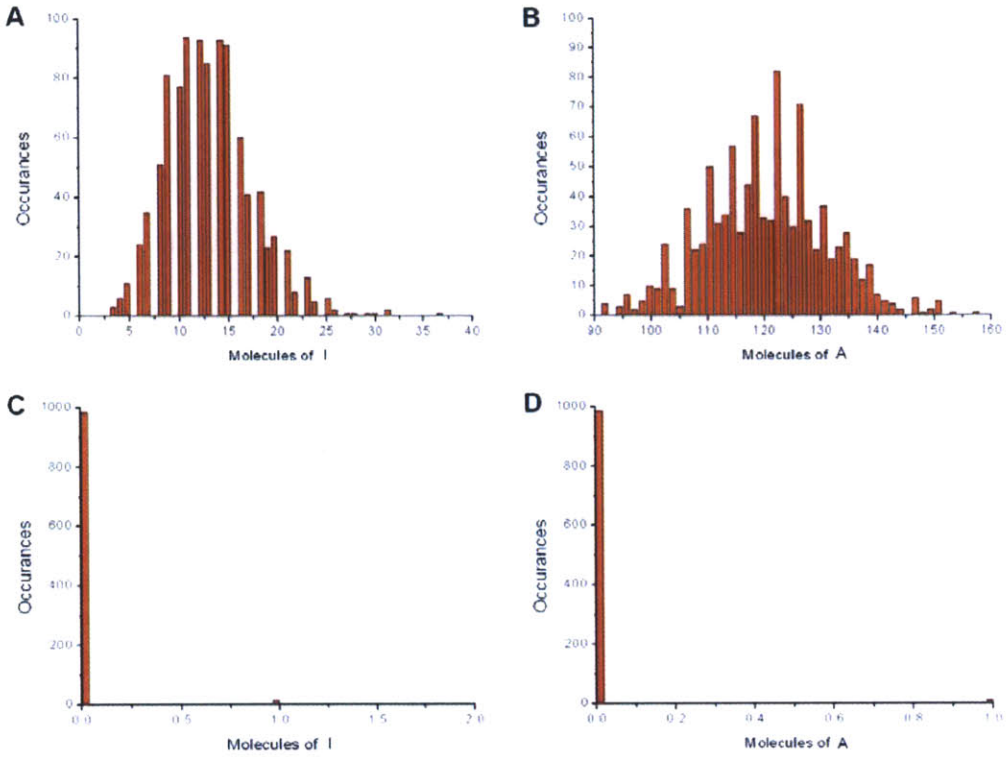

Figure A4.2. Upon deletion of the positive feedback loop, A is produced in greater quantities after 2000 min for sustained signals, while neither is produced in significant quantities for transient signals. Histogram for (A) molecule I and (B) molecule A obtained by solving the model equations for a sustained signal of $K_{deg,T}$ equal to 0.0 min^{-1} using the Gillespie Algorithm 1000 times and recording the number of molecules at 2000 min. Histogram for (C) molecule I and (D) molecule A obtained by solving the model equations for a transient signal of $K_{deg,T}$ equal to 1.0 min^{-1} using the Gillespie Algorithm 1000 times and recording the number of molecules at 2000 min. Parameters for the model were obtained from Table 4.1.

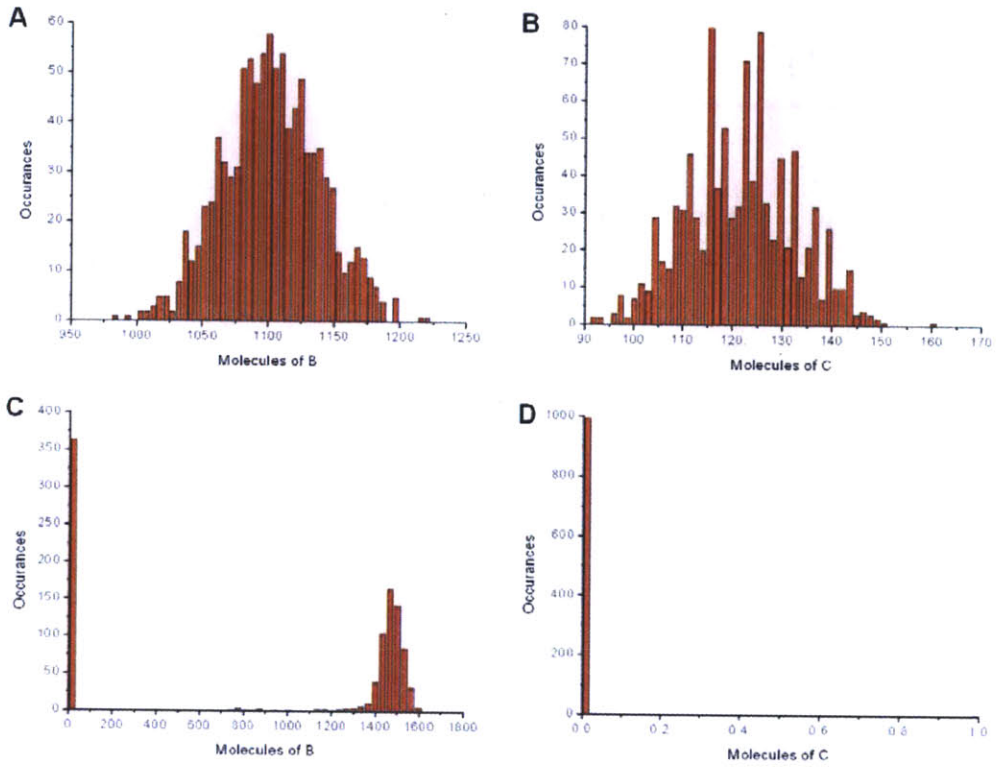

Figure A4.3. Upon deletion of the negative feedback loop, both I and A are produced in significant quantities after 2000 min for sustained signals, while only I is produced in significant quantities for transient signals. Histogram for (A) molecule I and (B) molecule A obtained by solving the model equations for a sustained signal of $K_{deg,T}$ equal to 0.0 min^{-1} using the Gillespie Algorithm 1000 times and recording the number of molecules at 2000 min. Histogram for (C) molecule I and (D) molecule A obtained by solving the model equations for a transient signal of $K_{deg,T}$ equal to 1.0 min^{-1} using the Gillespie Algorithm 1000 times and recording the number of molecules at 2000 min. Parameters for the model were obtained from Table 4.1.

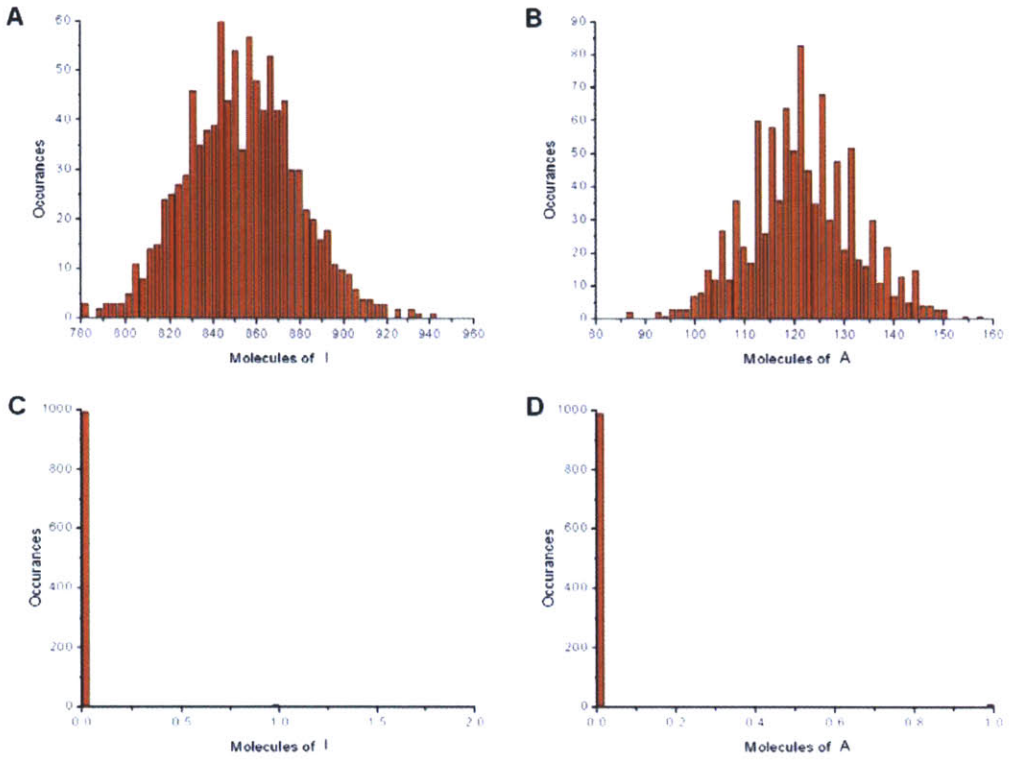

Figure A4.4. Upon deletion of the positive and negative feedback loops, both I and A are produced in significant quantities after 2000 min for sustained signals, while neither is produced in significant quantities for transient signals. Histogram for (A) molecule I and (B) molecule A obtained by solving the model equations for a sustained signal of $K_{deg,T}$ equal to 0.0 min^{-1} using the Gillespie Algorithm 1000 times and recording the number of molecules at 2000 min. Histogram for (C) molecule I and (D) molecule A obtained by solving the model equations for a transient signal of $K_{deg,T}$ equal to 1.0 min^{-1} using the Gillespie Algorithm 1000 times and recording the number of molecules at 2000 min. Parameters for the model were obtained from Table 4.1.

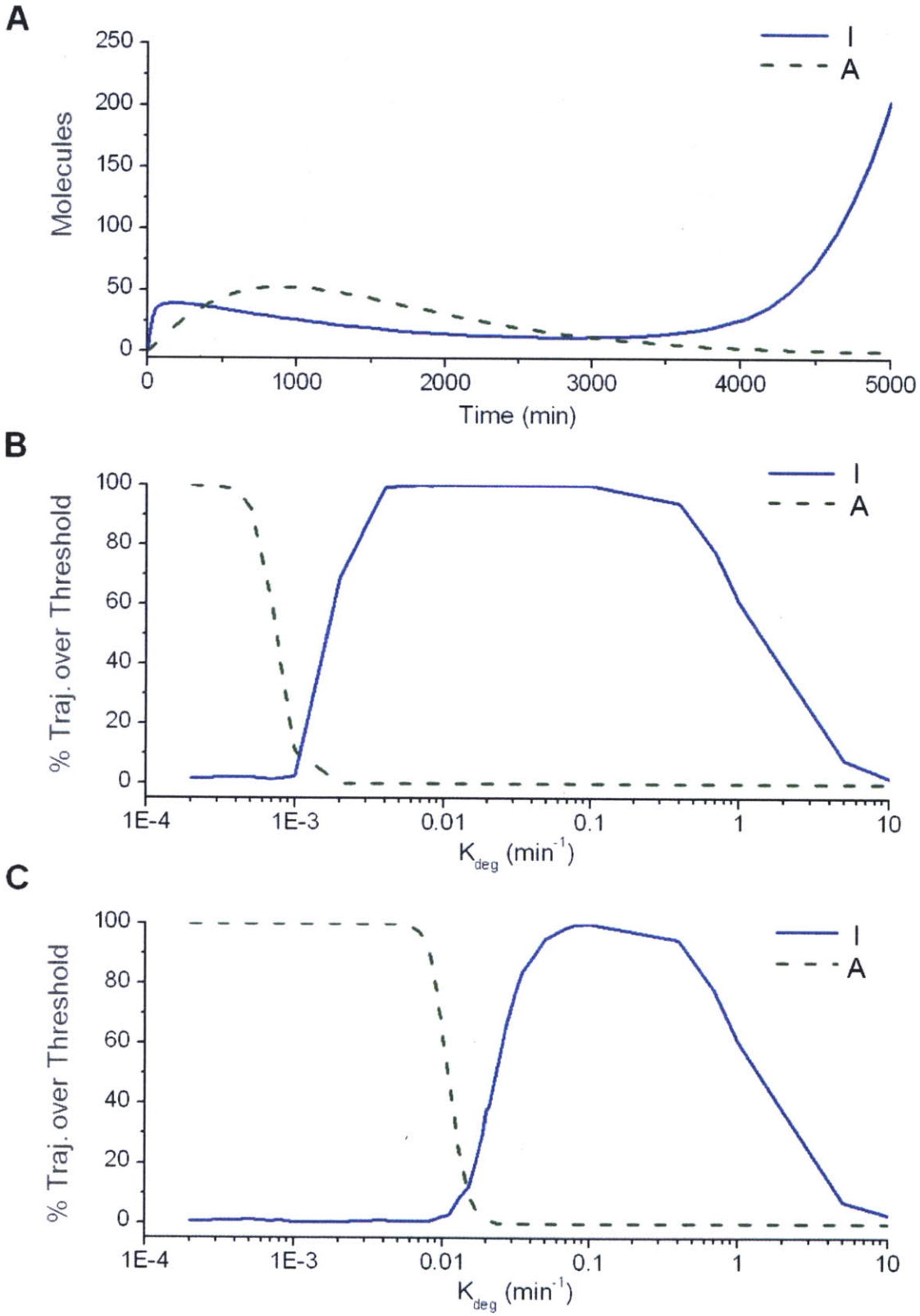
A
Molecules
250
200
150
100
50
0
0
1000
2000
3000
4000
5000
Time (min)
I
A
B
% Traj. over Threshold
100
80
60
40
20
0
1E-4
1E-3
0.01
0.1
1
10
K_deg (min^-1)
I
A
C
% Traj. over Threshold
100
80
60
40
20
0
1E-4
1E-3
0.01
0.1
1
10
K_deg (min^-1)
I
A

Figure A4.5. At long very times model breaks down and I dominates for nonzero signals. This is due to the fact that A is entirely signal dependent, so once the signal is gone it also decays to zero rendering it incapable of inhibiting the production of I. Since I has not decayed to zero, its positive feedback loop allows it to ramp up production when A is incapable of inhibition. (A) Mean field solution for molecule I at a signal degradation rate of 0.002 min^{-1} plotted out to 5000 min. (B) The maximum amount of I and A observed in 1000 time course trajectories measured out to 5000 min was compared to an arbitrary threshold and the percentage of trajectories crossing the threshold was computed for a wide range of signal degradation rates. The I and A thresholds were set to 100 molecules. The parameters given in Table 4.1 were used, thus $K_{deg,A}$ is equal to 0.001 min^{-1}. (C) Reducing the degradation rate of A ($K_{deg,A}$) to a value of 0.0001 min^{-1} counteracts the effect of measuring out to 5000 minutes. The I threshold was set to 100 molecules, while the A threshold was set to 20 molecules. Sampled trajectories were 5000 minutes long.

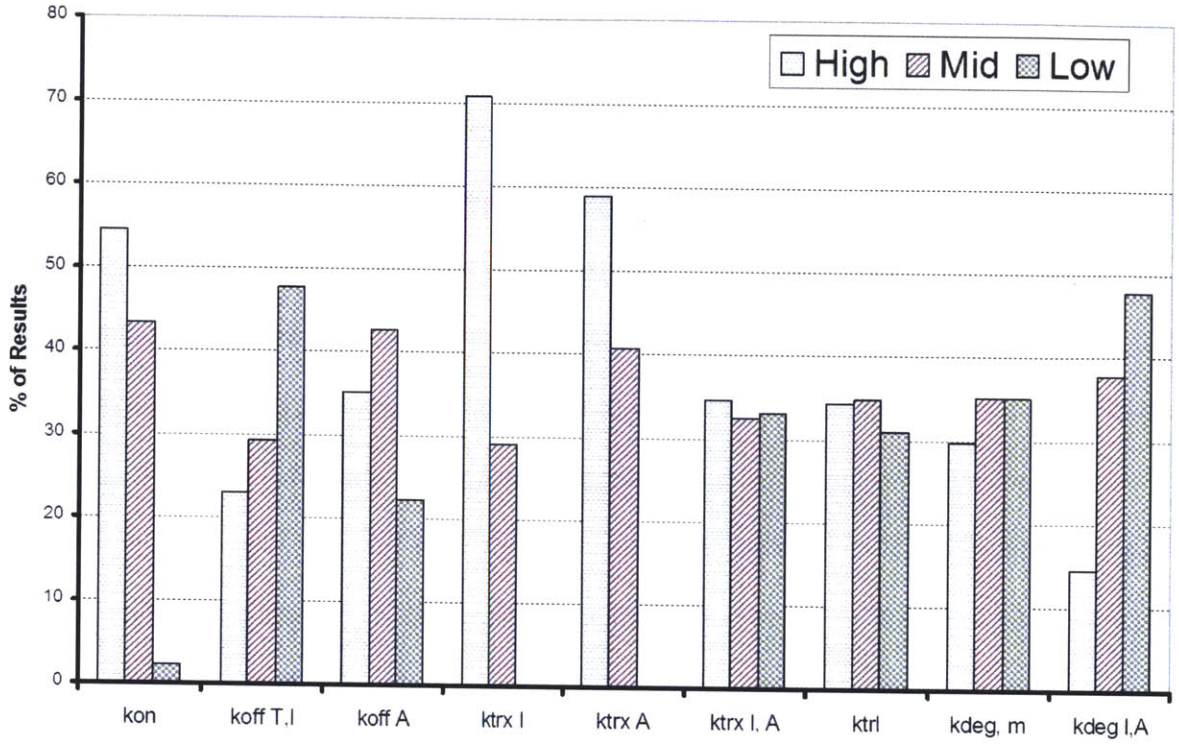

Figure A4.6. Depiction of sensitivity analysis results. Three values were varied for nine different classes of parameters (High, medium, and low), where the description of the classes and their respective high, medium, and low values are defined by Table A4.1. Of all the trajectories leading to a positive result, (i.e. signal duration allows for a decision between I and A), a certain percentage had high, medium, and low values of each parameter, which is depicted in the figure.

Discussion of Sensitivity Analysis

The results presented in this Chapter 4 were generated using the parameters listed in Table 4.1. Since this was just one parameter set, it was important to verify that the qualitative results of the model were the same for a wide set of parameters. The model contains less than 100 reactions so computation times for the Gillespie simulations were quite short. This allowed us to run a great number of simulations over a wide range of parameter sets and actually visualize the effect of varying parameters, which is not feasible for larger networks. Despite there being 91 possible reactions in the network, only 17 of the rate constants were unique, as indicated in Table 4.1. We further reduced this down to nine to make it feasible to test all possible combinations of three different values for each of the nine classes of parameters. The nine parameter classes along with the low, mid, and high values used for the sensitivity analysis of the parameters is given in Table A4.1.

The sensitivity analysis was performed by first generating all 19,683 combinations of the three values for each of the nine parameter classes. Each of these combinations was given a label of the form, LMHLMHLMH, which means parameter 1 (k_{on}) had its low value, parameter 2 ($k_{off\ T,I}$)had its mid value, etc. Twenty trials were run for each parameter set for three different values of signal degradation ($K_{deg,T} = 0.001\ min^{-1}$, $0.01\ min^{-1}$, $0.1\ min^{-1}$). In each individual trial, the program records the maximum value of I and A obtained at any point in the 2000 minute trajectory. At the end of each trial, these max values are compared to the previous trials, such that at the end of all twenty trials, the program records the highest and lowest maximum value of I and A obtained in any trial. Therefore, the output for each parameter set is I_{max}, I_{min}, A_{max}, and A_{min} obtained at three different values of signal degradation ($K_{deg,T} = 0.001\ min^{-1}$, $0.01\ min^{-1}$, 0.1

min^{-1}). Using these 12 values, we can determine whether or not a cellular decision has been made. If I_{min} is greater than A_{max} for one signal degradation rate, and A_{min} is greater than I_{max} at another signal degradation rate, then a signal duration dependent decision has been made. It may be easier to think about this as a comparison of two distributions, I and A. For the A distribution to be great then I, its lowest tail must be greater than the upper tail for I and vice versa. If a decision has been made, the parameter set is given a plus, and if no decision has been made, it is given a minus.

It is also possible for I to be bistable, which would mean that I_{min} would be 0 and using the above procedure it would have been given a minus. However, it is probable that I_{max} would be much greater than A_{min} as observed in the main text. For this reason, we also recorded which parameter sets led to bistable results for the two transient signals ($K_{deg,T}$ = 0.001 min^{-1}, 0.01 min^{-1}). Whenever the positive feedback loop was initiated, it usually resulted in I values much greater than 50, so the test for bistability was whether I_{min} was 0 and I_{max} was much greater than 50. Parameter sets marked bistable may lead to a cellular decision, but it is difficult to test since I_{min} is 0.

The sensitivity analysis revealed that there were 1809 parameter sets that led to a cellular decision, 15529 that did not, and 2345 that were bistable. Even though there were many parameter sets that did not lead to the same qualitative results, we consider the 1809 positive results to indicate that this is a fairly robust qualitative phenomenon for this model considering the range of parameters tested. Also, bistable results may still lead to a cellular decision at lower values of the signal degradation rate. There are various methods for analyzing sensitivity results. We chose to focus our efforts on analyzing the positive results. Within the subset of positive results, we calculated the percentage that had either a low, mid, or high value for each parameter

class (Figure A4.6). The sensitivity of the results to a given parameter can be inferred by the size of the spread in the percentages for that given parameter class. If all of the positive results had an equal spread of low, mid, and high parameter values for a given parameter class, then the results were insensitive to changes in that parameter. The three least sensitive parameter classes were $k_{deg,m}$, k_{trl}, and $k_{trx\ I,A}$. The low sensitivity to $k_{deg,m}$ when one of the values tested was 0 justifies setting this value to 0 in the simulations given in the main text. Clearly the most sensitive parameters are the transcription rates, and the low value for k_{on} and the high value for $k_{deg\ I,A}$ were too extreme.

Some additional information can be obtained by analysis of the sensitivity results. Of the 1809 positive results, 80 had A transcription rates higher than I. Therefore, it is not required for I to have a higher transcription rate than A for this model to be sensitive to signal duration. One assumption used to make the model in the main text was that the transcription factors unbind from the gene after each transcription event. It also may be possible that the transcription factors remain bound and transcription can occur until they unbind according to their respective k_{off} value. We also created a model to test whether or not this type of model would lead to the same qualitative model. As a quick test, we ran the sensitivity analysis program with the parameter set in Table A4.1 and found that 1900 parameter sets led to positive results. This is actually greater than the model presented in the text so the uncertainty about whether transcription factors unbind after each transcription event does not affect the qualitative results of the model. Another assumption made in the model presented in the main text was that molecules pSTAT3, I, and A were able to be deactivated while bound to genes I and A. We tested the effect of this assumption by creating a model where the molecules were not allowed to be deactivated while bound to genes. Using this new model, we ran the sensitivity analysis program with the

parameter set in Table A4.1 and found that 1939 parameter sets led to positive results, indicating that the qualitative results are not significantly affected by the nature of this assumption.

Parameter Class	Description	Low	Mid	High
k_{on} (molec^{-1} min^{-1})	On-rate for all molecules on all genes	0.0015	0.015	0.15
$k_{off\,A,B}$ (min^{-1})	Off-rate of A and B	0.01	0.5	1.0
$k_{off\,C}$ (min^{-1})	Off-rate of C from gene B	0.01	0.5	1.0
$k_{trx\,B}$ (min^{-1})	Transcription rate of B in the absence of C	0.01	0.1	1.0
$k_{trx\,C}$ (min^{-1})	Transcription rate of C	0.01	0.1	1.0
$k_{trx\,B,C}$ (min^{-1})	Transcription rate of B in the presence of C	0	0.001	0.009
k_{trl} (min^{-1})	Translation rate of B and C	0.01	0.5	1.0
$k_{deg,m}$ (min^{-1})	mRNA degradation rate	0	0.001	0.01
$k_{deg\,B,C}$ (min^{-1})	Degradation rate of B and C	0	0.001	0.01

Table S1. Listing of the parameter classes and their corresponding low, mid, and high values used in the sensitivity analysis.